A comprehensive investigation into chemo-mechanical magneto-rheological finishing (CMMRF) process

By
PRABHAT RANJAN
ENGG01201304024

Bhabha Atomic Research Centre, Mumbai

A thesis submitted to the
Board of Studies in Engineering Sciences

In partial fulfillment of requirements
for the Degree of
DOCTOR OF PHILOSOPHY
of
HOMI BHABHA NATIONAL INSTITUTE

February, 2019

Homi Bhabha National Institute[1]

Recommendations of the Viva Voce Committee

As members of the Viva Voce Committee, we certify that we have read the dissertation prepared by PRABHAT RANJAN entitled "A comprehensive investigation into chemo-mechanical magneto-rheological finishing (CMMRF) process" and recommend that it may be accepted as fulfilling the thesis requirement for the award of Degree of Doctor of Philosophy.

Chairman – Dr. B.K. Dutta	BK Dutta	**Date:** 1st February, 2019
Guide / Convener – Dr. R. Balasubramaniam		**Date:** 1st February, 2019
Co-guide - Dr. V.K. Jain		**Date:** 1st February, 2019
Examiner – Prof. P. K. Jain		**Date:** 1st February, 2019
Member 1- Dr. J. Chattopadhyay	J. Chattopadhyay	**Date:** 1st February, 2019
Member 2- Dr. T. A. Dwarkanath		**Date:** 1st February, 2019
Member 3- Dr. I. A. Khan		**Date:** 1st February, 2019

Final approval and acceptance of this thesis is contingent upon the candidate's submission of the final copies of the thesis to HBNI.

We hereby certify that we have read this thesis prepared under my/our direction and recommend that it may be accepted as fulfilling the thesis requirement.

Date: 1st February, 2019

Place: Mumbai

(Dr. V. K. Jain)

Co-guide

(Dr. R. Balasubramaniam)

Guide

---

[1] This page is to be included only for final submission after successful completion of viva voce.

STATEMENT BY AUTHOR

This dissertation has been submitted in partial fulfillment of requirements for an advanced degree at Homi Bhabha National Institute (HBNI) and is deposited in the library to be made available to borrowers under rules of the HBNI.

Brief quotations from this dissertation are allowable without special permission, provided that accurate acknowledgement of source is made. Requests for permission for extended quotation from or reproduction of this manuscript in whole or in part may be granted by the Competent Authority of HBNI when in his or her judgment the proposed use of the material is in the interests of scholarship. In all other instances, however, permission must be obtained from the author.

Prabhat Ranjan

DECLARATION

I, hereby declare that the investigation presented in the thesis has been carried out by me. The work is original and has not been submitted earlier as a whole or in part for a degree / diploma at this or any other Institution / University.

Prabhat Ranjan

List of Publications arising from the thesis

Journal

1. “Development of chemo-mechanical magnetorheological finishing process for super finishing of copper alloy”, Prabhat Ranjan, R. Balasubramaniam, V.K. Suri, *International Journal of Manufacturing Technology and Management*, **2013**, *Vol. 27*, 130-141.

2. “Modelling and simulation of chemo-mechanical magnetorheological finishing (CMMRF) process”, Prabhat Ranjan, R. Balasubramaniam, V.K. Suri, *International Journal of Precision Technology*, **2014**, Vol. 4, 230-246.

3. “Analysis of magnetorheological fluid behavior in chemo-mechanical magnetorheological finishing (CMMRF) process”, Prabhat Ranjan, R. Balasubramaniam, V.K. Jain, *Precision Engineering*, **2017**, Vol. 49, 122-135.

4. “Investigations into the mechanism of material removal and surface modification at atomic scale on stainless steel using molecular dynamics simulation”, Prabhat Ranjan, R. Balasubramaniam, V.K. Jain, *Philosophical Magazine,* **2018**, Vol. 98, 1437-1469.

5. “Analysis, design and synthesis of water-based magnetorheological fluid for CMMRF process”, Prabhat Ranjan, R. Balasubramaniam, V.K. Jain, *Journal of Micromanufacturing*, **2018**, Vol.1, 45-52, 2018.

6. “Molecular Dynamics Simulation of Mechanical Polishing on Stainless Steel Using Diamond Nanoparticles”, Prabhat Ranjan, R. Balasubramaniam, V.K. Jain, *Journal of Manufacturing Science and Engineering*, **2018**, Vol. 141, 014504-014504-4.

7. “Mechanism of material removal during nanofinishing of aluminium in aqueous KOH: A Reactive Molecular Dynamics Simulation study”, Prabhat Ranjan, R. Balasubramaniam, V.K. Jain, *Computational material science,* **2019**, Vol. 156, 35-46.

8. “Molecular Dynamics Simulation of Mechanical Polishing”, Prabhat Ranjan, Anuj Sharma, Tribeni Roy, R. Balasubramaniam, V.K. Jain, *International Journal of Precision Technology*, **2019**, Accepted on 28.12.2018.

Chapter in book

1. "Chapter 12: Chemomechanical Magnetorheological Finishing (CMMRF)", Prabhat Ranjan, R. Balasubramaniam, Vinod K. Suri, Vijay K. Jain, *Nanofinishing Science and Technology, Basic and Advanced Finishing and Polishing Processes*, **2017**, 285-320.

Conferences

1. "Nano-Groove Generation by Diamond Turn Machining and Chemical Processing", Prabhat Ranjan, Anuj Sharma, R. Balasubramaniam, V.K. Suri, *5th International & 26th All India Manufacturing Technology, Design and Research Conference (AIMTDR 2014)*, **2014**, 178, 1-7.

2. "Molecular Dynamics Simulation Of Mechanical Polishing", Prabhat Ranjan, Anuj Sharma, Tribeni Roy, R. Balasubramaniam and V.K. Jain, *10th International conference on Precision, Meso, Micro and Nano Engineering (COPEN 10)*, **2017**, 782-785.

Prabhat Ranjan

Prabhat Ranjan

DEDICATIONS

To my Mother

and

my Wife

ACKNOWLEDGEMENT

First of all, I would like to express my sincere gratitude to my guide Dr. R. Balasubramaniam, Head, Precision Machining Section, Precision Engineering Division, BARC for the encouragement, guidance and support that he has provided during the course of this thesis. He has always given critical and constructive comments, which helped in improving the quality of the thesis. He believes in shaping his student to be able to guide others in course of pursuance of research work of a supreme quality. He has nurtured me to study and analyse in a scientific approach for a deep understanding about a given problem. It was a wonderful experience to work under his guidance.

My deepest gratitude goes to my Co-Guide Dr. V. K. Jain, Retired Professor, I.I.T. Kanpur for permitting me to purse this research work under his supervision. He has been a source of a great inspiration who always advised me to maintain a balance between academic interest and the application aspects of new research. It was an honour to work under his mentorship all these years. I leant various aspects of tools and techniques in field of micro and nano-manufacturing under of his guidance. His constant encouragement and constructive comments have enabled me to focus on key issues related to this research work. In sort, he is a real mentor who has excellent teaching and supervising ability.

I greatly acknowledge the contributions of my doctoral committee members Prof. B. K. Dutta, Prof. J. Chattopadhyay, Prof. T. A. Dwarakanath and Prof. I. A. Khan who spared their valuable time for periodical critical assessment of my work. Their constructive suggestions have greatly enhanced the quality level of my Ph.D. work.

I am extremely thankful to Dr. V.K. Suri former Head, Precision Engineering Division, BARC. He was the key person who had initiated nanofinishing project, and due to this, I could develop CMMRF process. He has an excellent teaching and leadership quality.

I would like to thank Shri Shivam Mishra and Smt. Shrinkhala Ghildiyal, for their scientific advice and positive outlook under all circumstances.

I would also like to thank Shri Anuj Sharma and Shri Tribeni Roy for providing me help in several ways during the course of this thesis.

Direct or indirect support received from BARC is gratefully acknowledged.

I thank with apology all those people whose contributions to this work have escaped my attention and, thus, have gone unnoticed.

Special thanks are due to my wife, without her support, I would not have been able to complete my research work so comfortably. She has always been my biggest strength, who has always shown confidence in me and supported me under all circumstances.

Thanks are due to my parents, brother, sister and elders for their true blessings.

Last but not the least, I would like to thank all my friends and well-wishers wanting me to earn my PhD award.

Prabhat Ranjan

CONTENTS

Page No.

Synopsis i-iii

List of Nomenclatures and Abbreviations iv-ix

List of Figures x-xxi

List of Tables xxii- xxiii

Chapters

1. INTRODUCTION 1-9
   - 1.1 Relevance and Motivation 1
   - 1.2 Objectives 6
   - 1.3 Organisation of the report 8

2. LITERATURE SURVEY 10-34
   - 2.1 Introduction 10
   - 2.2 Conventional finishing processes 10
     - 2.2.1 Grinding process 10
     - 2.2.2 Lapping process 12
     - 2.2.3 Honing process 13
     - 2.2.4 Summary of conventional finishing processes for surface finish quality 14
   - 2.3 Advanced finishing processes (AFPs) 15
     - 2.3.1 Abrasive Flow Machining (AFM) process 17
     - 2.3.2 Magnetic Abrasive Finishing (MAF) process 19
     - 2.3.3 Magnetorheological Finishing (MRF) 22
     - 2.3.4. Chemical Mechanical Polishing (CMP) 24
   - 2.4 Chemo mechanical magnetorheological finishing (CMMRF) 25

2.4.1. MR fluid 26
2.4.2. Summary of literature survey 27
2.5 Modelling and simulation tool for micro and nano-finishing process 28
2.6 Gap areas 31
2.7 Scope of research work 34

3. ANALYSIS OF MAGNETORHEOLOGICAL FLUID FOR CMMRF PROCESS 35-76
3.1. Introduction 35
3.2. Formation of polishing pad 36
3.2.1. Modelling and simulation of magnetism in MR fluid: FEA and CFD simulation 36
3.2.2. Results and discussion 40
3.3. Mechanism to generate polishing pressure 46
3.3.1. Mathematical modelling and simulation 48
3.3.2. Experimentations 54
3.3.3. Results and discussion 55
3.4. Sedimentation behaviour of MR fluid 61
3.4.1. CFD simulation of MR fluid for sedimentation 62
3.4.2. Experiments for sedimentation study of MR fluid 65
3.4.3. Results and discussion for the sedimentation of MR fluid 66
3.5. Synthesis of MR fluid 69
3.5.1. Quantum chemical (QC) modelling and simulation of MR fluid 69
3.5.2. Results and discussion 70
3.6. Summary 75

4. MOLECULAR DYNAMICS SIMULATION OF CMMRF PROCESS 77-141

4.1. Introduction 77

4.2. MD simulation for mechanical finishing 79

4.2.1. MD simulation Methodology 80

4.2.2. Interatomic potentials for simulation 82

4.2.3. Equilibration of MD simulation 84

4.2.4. Analysis Techniques 85

4.2.5. Analysis of mechanical finishing on ductile material (aluminium) 87

4.2.6. Mechanical finishing of brittle material (silicon) 92

4.2.7. Mechanical finishing of stainless steel (*SS304L*) 97

4.2.8. Correlation for material removal 104

4.2.9. Discussion on mechanical finishing 106

4.3. MD simulation for chemical reactions 111

4.3.1. MD simulation for chemical reaction on Aluminium, Silicon and Stainless steel 112

4.3.2. Chemical reaction 113

4.3.3. Effect of chemical reaction on rough surface 113

4.3.4. Effect of chemicals on aluminium 114

4.3.5. Effect of chemicals on silicon 119

4.3.6. Chemical reaction on *SS304L* 123

4.3.7. Comparison of chemical reactions 124

4.4. MD simulation of chemically assisted mechanical finishing (CAMF) 125

4.4.1. CAMF in the presence of chemically reactive slurry 125

4.4.2. CAMF due to chemically active abrasive particles 132
4.4.3. Mechanism of material removal during CAMF 135
4.5. Discussions 136
4.6. Summary 139

5. MATHEMATICAL MODELLING AND SIMULATION OF CMMRF PROCESS 142-174
5.1. Introduction 142
5.2. Modelling of the CMMRF Process for Material Removal and Surface Roughness 143
5.2.1. Modelling of material removal using mechanical abrasion 144
5.2.2. Modelling of CMMRF process 148
5.3. Simulation of CMMRF process 154
5.3.1. Procedure of FEA based simulation for material removal and surface finish 155
5.4. Results and discussion 158
5.4.1 Simulation results 158
5.4.2 Mechanism of material removal for CMMRF process 167
5.5. Summary 173

6. EXPERIMENTAL INVESTIGATIONS 175-213
6.1. Introduction 175
6.2. Experimental setup 175
6.3. Plan of Experiment 180
6.3.1. Experiments on ductile material 181
6.3.2. Experiments on brittle material 183

6.4. Results and discussions 184

6.4.1. Results & discussion on Aluminium alloy 184

6.4.2. Results and discussion on Silicon 192

6.5. Experiments on *SS304L* 200

6.5.1. Results and discussion 202

6.5.2. Comparison between simulation and experimental work 205

6.6. Experiments on copper alloy 206

6.6.1. Plan of experiments 207

6.6.2. Results & discussion on copper 208

6.7. Summary 212

7. CONCLUSIONS AND SCOPE FOR FUTURE WORK 214-217

7.1 Conclusions 214

7.1.1 Scientific contribution 216

7.2 Scope for future work 217

7.2.1 Multi-scale modelling and simulation 217

7.2.2 Optimisation of CMMRF process 217

7.2.3 Experimental and theoretical study to finish 3D surface 218

7.2.4 Sensitivity analysis of CMMRF 219

7.2.5 Theoretical and experimental study of shear stress in CMMRF 219

REFERENECS 220-230

Appendix 231-238

SYNOPSIS

This thesis aims towards comprehensive understanding about chemo-mechanical magneto-rheological finishing (CMMRF) process by studying various aspect of the process. MR fluid is modelled at atomic scale as well as macro-scale to enhance process capability in terms of material removal rate and surface finish of workpiece. Molecular dynamics simulation (MDS) is carried out on few materials under different chemical environment to gain in-depth understanding about the material removal at nanometric scale. MDS results are used to model and simulate CMMRF at macro-scale, and it is also used for the selection of suitable process parameters to achieve defect less and nano-finished surface on both ductile as well as brittle materials.

After carrying out the literature survey in the field of conventional and advanced finishing processes, it is found that (CMMRF) is a comparatively newer and emerging nano-finishing process, which works on the basis of chemical reaction followed by mechanical abrasion controlled by magnetorheological means. This process has capability to modify the surface finish at atomic scale, and it is suitable to generate defect free surface on ductile as well as brittle materials. However, due to limited research in this area, understanding and application of this process for a wider range of engineering materials is limited. To gain a detailed insight about CMMRF process towards its deployment for various engineering materials, following areas of CMMRF are investigated.

MR fluid is an essential element of CMMRF process, which is used to form the polishing pad. Numerical modelling and simulation of MR fluid is carried out to understand its behaviour in the presence of magnetic field, and synthesis of MR fluid using quantum chemical modelling is carried out. In this work, the polishing pressure is computed for various parameters. It is found that the MR fluid based polishing pad of CMMRF process has two zones of working gap to process a wide range of engineering materials for generating defect-less nanofinished surface. For finishing of brittle materials, low working gap (from 0.2 – 0.5 mm), and in case of ductile materials, higher working gap (from 0.5 – 1.5 mm) are identified. Sedimentation of MR fluid is mitigated by using suitable surfactant through nano-coating over CIPs.

To understand the mechanism of material removal and the surface modification at atomic scale, molecular dynamics simulations on steel, aluminium, and silicon have been carried out by applying the polishing pressure which was obtained from the simulation results of the MR fluid. Coefficients for subsequent mathematical modelling of CMMRF process are also obtained from MDS. From MDS, it is found that the stress for material removal at atomic scale is near to theoretical shear stress ($G/2\pi$) which causes scratch lines and sub-surface defect. Sharp peaks of surface roughness profile are removed by using suitable chemical reactions. Chemical reactions also help to protect parent material against the direct abrasion due to abrasive particle, which leads towards generation of defect-fewer surfaces at nanometric scale in both ductile as well as brittle materials. To realise such defect-less surface, four stages of nanofinishing process are identified to bring down the surface roughness from few microns to few angstroms.

Further, CMMRF process has been modelled and simulated using finite element method at macroscopic scale to compute and predict material removal as well as surface finish. Mathematical model of this process is experimentally validated for two materials viz. on aluminium as ductile material and on silicon as brittle material.

In brief, present research work comprises study of CMMRF process by modelling and simulation at atomic scale as well as macroscopic scale. These modelling help to understand the mechanism and science of CMMRF process. This work reports that the type of chemical used is an important attribute of CMMRF process to achieve near to the theoretical value of

surface finish. Moreover, CMMRF process is also demonstrated on copper and stainless steel to explore its capability for these materials as they are commonly used materials in the various field of engineering.

------------x------------

NOMENCLATURES

Symbol	Description
A	Cross-sectional area
Al	Aluminium
Al_2O_3	Alumina
B	Magnetic flux density
c	Crack length
C	Carbon
Cr	Chromium
Cu	Copper
Cv	Specific heat constant in constant volume
d	Diameter of particle
d_{CIP}	Diameter of carbonyl iron particle
E	Young's modulus of elasticity
F	Magnetic force density
F_T	Cutting force form tool on workpiece along tangential direction
F_N	Holding force of tool against workpiece
F_R	Resultant force applied from tool to workpiece
f	Friction force
Fb	Force due to buoyancy
Fe	Iron
Fg	Force due to gravity
F_{IAF}	Inter-atomic force
F_{vf}	Force due to viscosity

Fx	Magnetic force density along X-axis
Fy	Magnetic force density along Y-axis
Fz	Magnetic force density along Z-axis
g	Gravitational constant, i.e. 9.81 m/s^2
G	Bulk modulus of elasticity
$g(r)$	Radial distribution function
H	Magnetic field strength
H_2O	Water
H_2O_2	Hydrogen peroxide
HNO_3	Nitric acid
k	Spring constant of MR fluid
K	Potassium
K_b	Boltzmann constant
K_{chem}	Constant for stress assisted chemical reaction
K_{IC}	Fracture toughness
KOH	Potassium hydroxide
M	Magnetization
MPa	Mega-Pascal
N	Normal force
Na	Sodium
$NaOH$	Sodium hydroxide
NH_4OH	Ammonium hydroxide
Ni	Nickel
nm	Nanometer
nN	Nanonewton

O	Oxygen
P	Pressure
P_f	Pressure due to friction loss
P_s	Pressure due to spring-stiffness of MR fluid
Ra	Average surface roughness in 2-D
Rq	Root mean square surface roughness in 2-D
Rz	Maximum peak to valley distance in 2-D surface profile
R_T	Reaction force form workpiece opposite of cutting direction
R_N	Reaction force form workpiece along normal to cutting direction
R_R	Total reaction force from workpiece on tool
Sa	Average surface roughness in 3-D
Si	Silicon
SiC	Silicon carbide
SiO_2	Silica
Sq	Root mean square surface roughness in 3-D
Sz	Maximum peak to valley distance in 3-D surface profile
t	Time
T	Temperature
u	Velocity
V	Volume of MR fluid
v	Velocity
V_{CIP}	Volume of carbonyl iron particle
Vm	Magnetic potential
W	Work done
Wg	Working gap

$\dot{Y}$	Shear strain rate
ΔQ	Heat input
ΔT	Change in temperature
ΔU	Change in internal energy
$\Delta \xi$	Change in magnetic energy
θ	Angle of peak on rough surface profile
μ_k	Kinematic friction co-efficient
μ_o	Magnetic permeability in vacuum
μ_r	Relative magnetic permeability
μm	Micrometer
ξ	Magnetic energy in MR fluid
ρ	Density
ρ_f	Mass density of liquid medium
ρ_s	Mass density of solid particle
σ_c	Critical stress for crack
τ	Shear stress
τ_o	Yield Shear stress of MR fluid
Υ	Surface energy per unit area
Υ_s	Specific cutting energy
φ	Wave function of single electron
χ_m	Mass magnetic susceptibility of medium
ψ	Wave function

ABBREVIATIONS

Abbreviation	**Full form**
2-D	Two dimension
3-D	Three dimension
ABOP	Analytic bond-order potentials
AFF	Abrasive flow finishing
AFM	Atomic force microscope
AFP	Advanced finishing process
ALE	Arbitrary Lagrangian–Eulerian
B3LYP	Becke 3-parameter, Lee-Yang-Parr
BCC	Body centred cubic
BMH	Born–Mayer–Huggins
CCI	Coherent correlation interferometer
CFD	Computational fluid dynamics
CIP	Carbonyl iron particles
CMMRF	Chemo-mechanical magnetorheological finishing
CMP	Chemo-mechanical polishing
CNA	Common neighbour analysis
CNC	Computer numerical control
CSP	Centro-symmetry parameter
CSV	Comma separated values
DC	Diamond cubic
DTM	Diamond turn machining
EAM	Embedded atom model

EEM	Elastic emission machining
ELID	Electrolytic in-process dressing grinding
FCC	Face centred cubic
FEA	Finite element analysis
FIB	Focused ion beam
FR	Finishing rate
HCP	Hexagonal close packed
IBM	Ion beam machining
IC	Integrated circuit
LAMMPS	Large-scale Atomic/Molecular Massively Parallel Simulator
MAF	Magnetic abrasive finishing
MDS	Molecular dynamics simulation
MEAM	Modified embedded atom model
MFP	Magnetic float polishing
MRF	Magnetorgeological finishing
MRR	Material removal rate
PBC	Periodic boundary condition
PMMA	Poly methyl methacrylate
QC	Quantum chemical
RDF	Radial distribution function
SCF	Self-consistent field
UFF	Universal force field
WEDM	Wire-electrical discharge machining

LIST OF FIGURES

No.	Title	Page No.
Fig. 1.1	Characteristics comparison of CMP, MRF over CMMRF.	4
Fig. 1.2	Various major aspects of CMMRF process, and suitable tools for the process investigations.	6
Fig. 2.1	(a) Schematic of grinding process, (b) material removal during grinding process. (c) Forces involved during material removal by single abrasive particle.	11
Fig. 2.2	Schematic of lapping process. The depth of abrasion (δ) depends on size and orientation of abrasive particles.	13
Fig. 2.3	Schematic of honing process.	14
Fig. 2.4	Micro-nano finishing processes.	16
Fig. 2.5	Schematic of abrasive flow machining process.	18
Fig. 2.6	Schematic of magnetic abrasive finishing. (a) for cylindrical workpiece. (b) for flat workpiece.	19
Fig. 2.7	Schematic of MRF process.	23
Fig. 2.8	Schematic of CMP process.	25
Fig. 2.9	Hierarchy of process modelling at various scales.	30
Fig. 2.10	Research plan.	33

Fig. 3.1 Schematic for the boundary condition of permanent magnet for FEA simulation. (a) Full model. (b) Half model, i.e. axisymmetric model. 36

Fig. 3.2 Lines of magnetic flux distribution in which arrows show the direction. 41

Fig. 3.3 (a) Plot of the magnetic flux density on the surface of PMMA plate (z=0) without MR fluid, (b) Plot of the magnetic flux density on the PMMA surface (z=0) with MR fluid. 41

Fig. 3.4 Plot of magnetic flux density at various places of MR fluid. 42

Fig. 3.5 Distribution of magnetic force density in the MR fluid after applying magnetic field at time, $t = 0$s. 42

Fig. 3.6 (a) Magnetic force density at the interface of magnet and MR fluid (z=0), surface of MR fluid (z=2.5 mm), inside of MR fluid (z=0.5 &1.5 mm), (b) Zoomed view for the radial distance from 6 to 11 mm. 43

Fig. 3.7 (a) Magnetic flux with direction after applying magnetic field, t =0s; (b) Magnetic flux at t =0.2s; (c) Magnetic flux at t =1.0s. 44

Fig. 3.8 Energy optimization of MR fluid in the range of 0.2-0.4s. 44

Fig. 3.9 (a) Final shape of MR fluid (in half of 2D model) due to magnetic force after t =0.4s, (b) shape of the MR fluid in 3-D. 45

Fig. 3.10 (a) Experimentally formed polishing pad of the MR fluid using a permanent magnet, (b) cut section view. 45

Fig. 3.11 Schematic of CMMRF for modelling and simulation of MR fluid. 46

Fig. 3.12 Finite element analysis to understand magnetic field, magnetic force and magnetic energy with varying working gap. 47

Fig. 3.13 (a) Formation of pad of MR fluid under free condition and (b) formation of pad of MR fluid during working condition at a specified working gap. 48

Fig. 3.14 Force due to 0.8 ml of MR fluid at different working gaps. 49

Fig. 3.15 a) Model of CMMRF and b) Free body diagram of polishing pad. 51

Fig. 3.16 Flow chart for simulation of the polishing pressure. 53

Fig. 3.17 Simulated results on polishing pressure due to the effect of volume of MR fluid at three levels of working gap. 53

Fig. 3.18 Experimental plot of pressure with respect to the volume of MR fluid at varying working gap. 55

Fig. 3.19 Comparison between simulated and experimental results. 56

Fig. 3.20. (a) Pressure distribution on MR fluid, (b) Plot for the pressure along radial direction on the work surface at working gap = 0.7 mm, and volume =0.56ml (c) Characteristic plots of polishing pressure. 58

Fig. 3.21 Experimental validation of simulation on MR fluid. 60

Fig. 3.22 Experimental results for surface finish (*Ra*) on *SiC* and *Al* at different working gap. 61

Fig. 3.23 Simulation cell for sedimentation study in MR fluid. 62

Fig. 3.24 Flow chart for CFD simulation to study about the sedimentation phenomenon in MR fluid. 63

Fig. 3.25 (a) Schematic for measurement of sedimentation depth under 650 nm and 5mW laser. (b) Snap-shot of the test tube without laser light. (c) Actual photograph of test tube under laser light. 66

Fig. 3.26 Plot of CFD simulated results for the percentage of sedimentation with respect to time for MR fluid-1, 2, and 3. 66

Fig. 3.27 (a-c) Particles sedimentation with varying time generated by CFD simulation. (d) Trajectories of particles tracing. 68

Fig. 3.28 (a) Atomic model of sodium stearate which is obtained after geometry optimization under universal force field (UFF) using algorithm of ‘steepest descent’; (b) Small cut-portion of sodium stearate to study the quantum chemical calculation. 70

Fig. 3.29 Variation in the change of interaction energy with respect to the inter-atomic distance 72

Fig. 3.30 Chemical interaction between CIPs and sodium stearate in water medium. 74

Fig. 3.31 (a) Model of iron particle with sodium stearate. (b) Model to link multiple iron particles using sodium stearate and *H*-bond. 74

Fig. 4.1 Schematic diagram of nano-abrasion which includes material removal in ductile mode. 77

Fig. 4.2 Flow chart for MD simulation for nano-finishing process. 78

Fig. 4.3 Schematic model of mechanical finishing. 80

Fig. 4.4 (a) Chemical bonding between abrasive particle and workpiece when they have attained sufficient proximity. (b) Removal of material with the help of relative movement between abrasive particles & workpiece. 81

Fig. 4.5 Variation of cohesive energy with time step for (a) workpiece, (b) abrasive particle. 84

Fig. 4.6 Structural variation in aluminium with different levels of finishing time. 88

Fig. 4.7 Finishing force on *Al* along cutting direction or x-axis. 89

Fig. 4.8 Indentation force along normal to *Al* work-surface or z-axis. 89

Fig. 4.9 Potential energy on the asperity of *Al* workpiece. 90

Fig. 4.10 Distribution of von-Mises stress in *Al* during mechanical finishing. 91

Fig. 4.11 Temperature variation during mechanical finishing of aluminium. 92

Fig. 4.12 (a-d) Structural variation at different time intervals of mechanical finishing of silicon at indentation depth equal to 1 nm. 93

Fig. 4.13 Finishing force on *Si* workpiece along cutting direction at different values of indentation depth. 94

Fig. 4.14 Indentation force along normal to *Si* work-surface or Z-axis. 94

Fig. 4.15 Potential energy on the asperity of workpiece during mechanical finishing of silicon at different values of indentation depth. 95

Fig. 4.16 von-Mises stress on silicon workpiece during different time of mechanical finishing at indentation depth equal to 1 nm. 96

Fig. 4.17 Variation in average temperature of the asperity of the silicon workpiece with varying time and different values of indentation depth. 97

Fig. 4.18 Material deformation and chip formation at atomic scale during mechanical abrasion on stainless steel. 98

Fig. 4.19 Finishing force along cutting direction or x-axis on *SS304L*. 99

Fig. 4.20 Finishing force normal to the surface of *SS304L* workpiece. 99

Fig. 4.21 Variation of potential energy of *SS304L* during mechanical abrasion. 100

Fig. 4.22 (a) Atomic distribution of von-Mises stress before initial contact of finishing. (b) Atomic distribution of von-Mises stress during initial contact of polishing. 101

Fig. 4.23 Sub-surface defects during mechanical finishing on stainless steel at different levels of time steps (a-d). 102-103

Fig. 4.24 Temperature variation during the abrasion process with different depth of indentations on *SS304L*. 104

Fig. 4.25 Correlation between indentation force and material removal along depth is made by using MDS results for aluminium, silicon and stainless steel. 106

Fig. 4.26 Effect of finishing force on surface quality, abrasive particle degradation and potential energy due to mechanical finishing. 110

Fig. 4.27 Effect on potential energy per atom and adsorption due to variation of sharing atoms. 111

Fig. 4.28 Schematic of the model for reactive MD simulations to study chemical reactions. 112

Fig. 4.29 Chemical reactions on stainless steel with oxidising agent. 114

Fig. 4.30 Oxidation and removal of *Al*-atom under the presence of aqueous *KOH*. 115

Fig. 4.31 Absorption of atoms from aqueous *KOH* into aluminium workpiece. 116

Fig. 4.32 Oxidation and removal of *Al*-atom under the presence of aqueous H_2O_2. 116

Fig. 4.33 Adsorption and absorption of atoms from aqueous H_2O_2 into aluminium. 117

Fig. 4.34 Oxidation of *Al*-atom under presence of aqueous HNO_3. 118

Fig. 4.35 Absorption of atoms from aqueous HNO_3 into aluminium workpiece. 119

Fig. 4.36 Absorption of atoms from aqueous *KOH* into silicon workpiece. 120

Fig. 4.37 Chemical reaction from aqueous *KOH* on silicon surface workpiece at 1.6 ps. 120

Fig. 4.38 Absorption of atoms from aqueous H_2O_2 into silicon workpiece. 121

Fig. 4.39 Chemical reaction on surface of *Si* under presence of aqueous H_2O_2. 121

Fig. 4.40 Absorption of atoms from nitric acid into silicon workpiece. 122

Fig. 4.41 Chemical reaction on surface of *Si* under presence of nitric acid. 122

Fig. 4.42 Chemical reaction on surface of *SS304L* under presence of oxidiser. 123

Fig. 4.43 Mechanical abrasion of aluminium due to silicon abrasive. 126

Fig. 4.44 Position of atoms before indentation of abrasive particle. 127

Fig. 4.45 Position of atoms/molecules at the time of indentation. 127

Fig. 4.46 Position of atoms/molecules and material removal during abrasion. 128

Fig. 4.47 Material removal after abrasion in case of higher impact during indentation. 129

Fig. 4.48 Material removal during abrasion in the form of oxides/hydroxides. 129

Fig. 4.49 Structure of workpiece and abrasive after finishing process. 129

Fig. 4.50 (a) Normal force of workpiece, (b) abrasion force on workpiece, (c) chemical reaction and material removal of workpiece. 130

Fig. 4.51 Transfer of atoms from aqueous *KOH* into silicon workpiece during indentation of abrasive particle. 131

Fig. 4.52 Chemical reaction on surface under indentation force from abrasive 132

Fig. 4.53 Chemically assisted material removal and chip formation on silicon workpiece. 132

Fig. 4.54 Material deformation and chip formation at atomic scale. 133

Fig. 4.55 Various attributes of CAMF under indentation force of *Fz* and velocity *Vx*. 134

Fig. 4.56 Model for finishing zone of CAMF process. (a) Chemical reaction due to the indentation of abrasive particle. (b) Material removal on ductile material. (c) Material removal on brittle material. 136

Fig. 5.1 Schematic of CMMRF process. 143

Fig. 5.2 Material removal mechanism in the nano-finishing zone of CMMRF process. 144

Fig. 5.3 Schematic of MR fluid while in working condition. 145

Fig. 5.4 Surface profile for modelling of CMMRF process. 147

Fig. 5.5 (a) 3-dimensuonal view of atomic arrangement in a face centred cubic (FCC) lattice structure. (b) 2-dimensional view of atomic arrangement. 152

Fig. 5.6 Schematic diagram of an ideal surface profile at atomic scale. 153

Fig. 5.7 Schematic diagram of work-plan for modelling and simulation to predict material removal and surface finish. 155

Fig. 5.8 Flow chart for the present study of modelling and simulation of material removal and surface finish. 157

Fig. 5.9 Initial surface profile; data is imported from the experimentally measured profile from CCI instrument in the form of CSV format 159

Fig. 5.10 Simulated surface profile of aluminium after 10 min. of CMMRF 160

Fig. 5.11 Surface profile results obtained by simulation and presented on *Al* (a-d) and *Si* (e-h). 161-162

Fig. 5.12 Effect of chemical concentration on material removal of aluminium with respect to time. 163-164

Fig. 5.13 Effect of chemical concentration on material removal of silicon with respect to time. 166-167

Fig. 5.14 Effect of chemical concentration on the improvement in surface finish of aluminium workpiece. 168-169

Fig. 5.15 Effect of chemical concentration on the improvement in surface finish of silicon workpiece. 171-172

Fig. 6.1 Schematic of CMMRF process. 176

Fig. 6.2 Experimental set-up for CMMRF operation. 177

Fig. 6.3 Parameter setting for the CMMRF process which includes flow of slurry, time for slurry flow, stirrer of slurry, spindle speed, and pH. 178

Fig. 6.4 Monitoring window of CMMRF process. 179

Fig. 6.5 Details of finishing head. (a-b) Two different orientation of solid model. (c) Exploded view of parts of the magnetic head. 180

Fig. 6.6 (a) Surface topography of raw surface which made by conventional turning process. Surface finish *Ra*=360 nm (b) Surface of prepared sample after lapping process. *Ra*=45 nm. 181

Fig. 6.7 (a) Surface topography of initial surface with *Ra*=1.38 μm. (b) Surface topography of sample which is generated by mechanical finishing, *Ra*=46 nm. 184

Fig. 6.8 Improvement in surface roughness with finishing time, and different level of working gap and *KOH* concentration. 185-186

Fig. 6.9 Variation in the depth material removal on aluminium alloy with finishing time, and different level of working gap and *KOH* 189-190

Fig. 6.10 (a) Surface of aluminium after turning process, (b) Surface of aluminium after preparation for CMMRF process, and (c) CMMRF finished sample of aluminium at 5% *KOH* and working = 1 mm. 191

Fig. 6.11 Surface topography in 3D which shows nanometric smooth surface and the 2D roughness profile shows *Ra* value equal to 2 nm. 191

Fig. 6.12 Improvement in surface roughness on silicon substrate with finishing time, and different level of working gap and *KOH* concentration 193-194

Fig. 6.13 Variation in the depth material removal on silicon substrate with finishing time, and different level of working gap and *KOH* concentration 196-197

Fig. 6.14 Effect of finishing time at working gap=1mm, 5%*KOH* on silicon 199

Fig. 6.15 (a) Initial etched surface of silicon substrate, (b) Mechanically finished silicon blank, and (c) CMMRF finished surface of silicon 200

Fig. 6.16 Surface topography in 3D which shows *Sa* value equal to 0.14 nm and the 2D roughness profile shows *Ra* value equal to 0.17 nm. 201

Fig. 6.17 CMMRF results on *SS304L* 203-205

Fig. 6.18 Effect of acidic and basic species on critical finishing value of CMMRF on copper. 208

Fig. 6.19 CMMRF finished copper (*Ra* = 28 nm) with 10% ammonia (Sr.N.1) 209

Fig. 6.20 CMMRF finished copper (*Ra* = 9.0 nm) without ammonia and nitric acid 210

Fig. 6.21 CMMRF finished copper (*Ra* = 2.5 nm) with 0.4% nitric acid. 211

Fig. 6.22 CMMRF finished copper (*Ra* = 2.5 nm) with 0.4% nitric acid. Nano-finished surface shows optical reflectivity as compared to initial surface. 211

Fig. A1 Detailed schematic diagram of CMMRF system 234

Fig. A2 Drawing of the CNC stages 234

Fig. A3 Drawing of the spindle assembly 235

Fig. A4 Drawing of the slurry circulatory system 235

LIST OF TABLES

No.	Title	Page No.
Table 2.1	Comparison and observations of various finishing processes	14
Table 2.2	Comparison of AFM, MAF and MRF processes.	24
Table 2.3	Comparison between CMP, MRF and CMMRF	26
Table 3.1	List of assumptions which are used to simulate CMMRF polishing pad behaviour.	40
Table 3.2	Parameters of polishing pad of CMMRF process	54
Table 3.3	Axial force (thrust force) recorded with varying ‘working gap’.	54
Table 3.4	Results of CMMRF for finishing of *SiC* with different working gap	55
Table 3.5	Characteristics of Zone-1 and Zone-2	59
Table 3.6	Composition of MR fluid for CFD simulation.	63
Table 4.1	Parameters of the MD simulation used for mechanical finishing.	82
Table 4.2	MDS results on stainless steel, aluminium and silicon. This result show indentation force (*Fz*) and cutting force (*Fx*) at different depth of material removal.	105
Table 4.3	Selection of materials to study chemical reaction through MD simulation	112
Table 4.4	List of inter-atomic pair potential for chemical reaction.	113

Table 4.5 Effect of chemical reaction on *Al*, *Si* and *SS304L* 124

Table 4.6 List of inter-atomic pair potential for chemical assisted mechanical finishing. 125

Table 4.7 Steps in generating atomically flat surface from a rough surface 138

Table 5.1 Values of parameter for *Al* and *Si* workpiece using MD simulation 150

Table 5.2 List of study area towards understanding of CMMRF process. 154

Table 5.3 FEA parameters to simulate CMMRF process for material removal and *Ra*. 156

Table 6.1 Variable parameters for experimental plan of CMMRF. 182

Table 6.2 List of fixed parameters of CMMRF process. 183

Table 6.3 Process parameters to finish *SS304L* using CMMRF experiments. 201

Table 6.4 Comparison between MDS and experimental works. 206

Table 6.5 Chemical composition, slurry in % volume. 207

Table 6.6 Results of CMMRF on copper 208

Table A1 Sedimentation depth with varying time for different types of MR fluids 231

Table A2 Detailed specifications of CMMRF system 236

Table A3 Experimental results of CMMRF on *Al 6061:T6* 237

Table A4 Experimental results on Silicon substrate 238

Chapter-1

INTRODUCTION

1.1 Relevance and Motivation

Nano-finishing is an emerging and indispensable process for manufacturing technology, which is being used to improve surface finish by reducing average surface irregularities upto a few nanometer or sub-nanometer. Improvement in surface finish (or reduction in surface roughness) from microns to nanometer brings drastic change or enhancement on some specific functional properties like bio-compatibility of medical prosthesis, optical properties for 'general optics, LASER optics and X-ray optics', fabrication density for micro-electronics, i.e., density of Integrated Circuits (IC), flow-ability of fluid in micro-fluidic channels, Q-factor of LINAC cavity, corrosion resistance, mechanical properties of micro-parts, etc. Moreover, nano-finishing (or polishing) is also used for maintaining precision on part's dimensions, e.g., slip-gauges, precision balls of noise-less and ultra-high speed bearings for hard disc drive and aero-space applications.

In present era, technological advancements in engineering and biomedical fields need advanced materials. Nanofinishing of such advanced materials poses challenges to the researchers and engineers of a wide range of industries. There are a few properties of engineering materials which pose challenges for nanofinishing, such as, 'hardness' resists removal of material, ductility & malleability induces surface damages, and brittleness induces surface as well as sub-surface damages. These issues are briefly discussed as follows.

1. Hardness: It allows the surface of workpiece to resist against the indentation of abrasive particles, which affects material removal rate (MRR) during finishing process, and it also

reduces the finishing rate [1]. To overcome this challenge, hard and stiff tools are used along with appropriate techniques to soften the superficial surface of workpiece.

2. Ductility and malleability: These properties allow the material to flow in the zone of plastic deformation and results in generation of defects like scratches, pits, etc. during the abrasive based finishing operation [2,3]. To overcome this problem, hard loop based processes are used; they are, in general, path controlled and deterministic in nature such as diamond turn machining (DTM) process.

3. Brittleness: Fracture toughness [$K_{IC} = \sigma_c(\pi c)^{0.5} = (2\gamma E)^{0.5}$ as per Griffith's theory, where σ_c is critical stress, c is the crack length, γ is the surface energy per unit area and E is the Young's modulus of elasticity] indicates the ability of material to resists generation of surface and sub-surface damages [4]. To avoid such surface damages, ductile mode of machining is preferred while finishing brittle materials. This mode is possible in DTM by adjusting the process parameters like rake angle, cutting edge sharpness, feed rate, etc. [5]. In addition, the soft loop processes need to use spherical abrasive particles to process them under the ductile mode [6].

In general, lapping process does polishing with a force controlled mechanism of the lapping pad. This process does not ensure uniformity of 'force per particle' on abrasive particle as the force/particle depends on the shape and size of the abrasive particle. The variation in the force/particle changes the material removal rate (MRR) which leads to the morphological defects, and hence, the surface finish does not reach upto the nanometric scale. To overcome this problem, flexible nano-finishing processes have been developed in which the polishing medium exhibits some extent of flexibility to gain uniformity on the force/particle. These flexible processes have been developed overtime, and they are known as magnetic abrasive finishing (MAF), abrasive flow finishing (AFF) and magnetorheological finishing (MRF). These processes are capable of generating nanofinished surface in the order of 1-100 nm. The flexible polishing pad has some stiffness value at a given set of finishing parameters, which acts to mitigate variation in the force/particle towards generating near uniform MRR, and results in controlling the uniformity of peaks in the order of few nanometers. Further, removal of these nano-peaks is very difficult. Hence, there is a need to design and develop a process in which the material removal is higher on the nanometric peaks by softening them. The nano-peaks can be softened by few possible techniques as follows;

- Chemical reaction,
- Thermal heating,
- Electrical discharge,
- LASER softening.

In the present research work, a method of chemical reaction has been incorporated to remove the nano-peaks and achieve the surface finish in the atomic scale. The chemical methods are selected in which the species of the chemicals react with nano-peaks in two different ways, namely, (1) chemical reaction on relatively unstable atoms, which is generally possible on sharp peaks, and (2) stress-assisted chemical reaction. After the chemical reaction, the reacted portion (local) of workpiece needs to be softened so that material removal can be precise (in the form of cluster of atoms). In view of this, a hybrid nano-finishing process namely, chemo-mechanical magnetorheological finishing (CMMRF) process, has been developed by the combination of chemo-mechanical polishing (CMP) and magnetorheological finishing (MRF) processes [7].

The motivation behind the development of the CMMRF process is to mitigate the inherent limitations of CMP and MRF processes, and to develop an advanced flexible nanofinishing process for getting ultra-precision surfaces on few engineering materials.

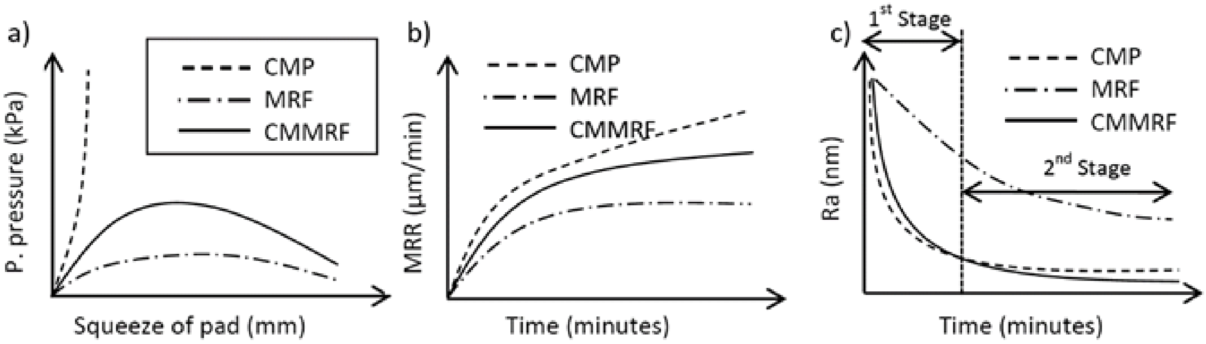

Fig.1.1: Characteristics comparison of CMP, MRF over CMMRF for (a) working gap on polishing pressure, (b) material removal rate (MRR) with time, (c) time on surface finishing.

In addition, theoretical study of various aspects of CMMRF process has become another motivation towards better utilisation of the process for various engineering applications. CMMRF is comparatively a new and emerging nano-finishing process, which works on the basis of chemical reaction followed by mechanical abrasion controlled by magnetorheological effect. In this process, chemo-mechanical polishing (CMP) and magnetorheological finishing (MRF) processes are combined together. By combination of CMP and MRF, following important properties are achieved in CMMRF process, as shown in Figs.1.1 (a-c). Fig.1.1 (a) shows that CMP is highly sensitive (not suitable for fragile as well as 3-D surfaces) for pressure. Whereas, CMMRF is amenable for the working gap variation, and it exerts more pressure compared to MRF. As far as MRR is concerned, Fig.1.1 (b) shows that the MRR is in the following order, CMP ≥CMMRF>MRF. Fig.1.1 (c) shows that the surface finish (or Ra value) during the initial stage of finishing varies in the following order, CMP<CMMRF<MRF. However, the surface finish quality becomes better on CMMRF treated sample in 2nd stage, i.e. CMMRF≤CMP<MRF. Hence, advantages of CMMRF can be written as follows;

1) High material removal rate,
2) Almost ideal surface finish on atomic scale (sub-nanometer level),
3) Tactful polishing of fragile work-surface to avoid damage, and
4) Capable to finish/polish 3-dimensional surfaces.

As far as nano- and sub-nano- finishing of brittle and ductile materials is concerned, CMP, CMMRF and focus ion beam (FIB) finishing are competent processes. FIB shows extremely low finishing rate, due to which this process is not suitable for industrial applications. In case of CMP, generating defect free surface finish at nanometric scale is not possible on ductile materials, and the reasons for the same are as below.

1) Degradation of polishing pad: due to the chemical reaction and mechanical abrasion, polishing pad wears and degrades its texture. This degradation of pad texture results in unwanted abrasion on workpiece and leads to scratches on soft and ductile materials. This problem can be suppressed upto certain extent by applying regular conditioning of polishing pad using diamond dresser.
2) Dislodgment of pad: delamination and dislodgment of polishing pad is an obvious effect observed during CMP process, which gets contaminated with abrasive particle and behaves as a big particle for abrasion. When, such contaminated pad comes into contact with workpiece, sudden rise in the pressure occurs locally which causes the formation of scratches.

These problems are of concern in case of ductile materials [8,9]. However, CMMRF utilises flexible magnetic polishing pad in which such problems will not occur. Thus, CMMRF is an appropriate process for nano and sub-nano finishing of all kinds of engineering materials.

In CMMRF, polishing medium is mainly composed of water based magnetorheological (MR) polishing fluid with suitable chemical, corrosion inhibitors, iron particles, abrasive particles and additives for maintaining pH value and zeta potential.

In general, CMMRF comprises various aspects such as MR fluid, mechanical abrasion using magnetic force, chemical reactions, as presented in Fig. 1.2. This process can be analysed in-depth using the suitable theoretical tools like quantum chemical modelling, reactive molecular dynamics simulation (MDS), classical MDS, CFD and FEA.

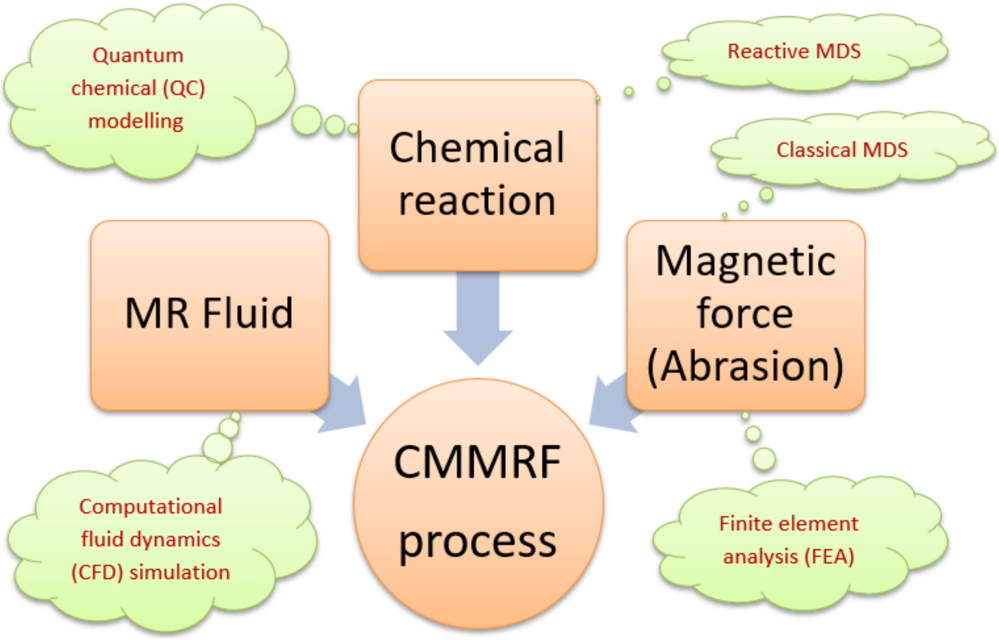

Fig.1.2: Major aspects of CMMRF process, and suitable tools (as presented in cloud callout) for the process investigations.

A set of experimental study on silicon substrate was carried out using CMMRF process in year 2010 [7], which is not enough to understand the process capabilities. It is observed that there is scant information available in the literature for CMMRF and related field. After carrying out extensive literature survey, it is found that there is scarcity of scientific information and understanding about the CMMRF process mechanism for material removal and surface modification at atomic scale on various engineering materials. Hence, research gap areas are identified and summarized as objectives as follows.

1.2 Objectives

One of the objectives of this work is to understand behaviour of magnetorheological (MR) fluid and synthesis of water based MR fluid for CMMRF application. The objective is also to acquire understanding on the mechanism of material removal at atomic scale. Moreover, the present work includes the modelling and simulation of CMMRF process to predict the process outcome like material removal and surface finish.

There are many research papers which deal with finishing of non-ferromagnetic materials, and some are also there which report limitations and applications of magnetic field assisted finishing processes on ferromagnetic materials. Hence, present research work is implemented on non-ferromagnetic materials having different mechanical properties such as *Al* and *SS304L* as ductile materials and *Si* as brittle material. Accordingly, the objectives of the present research work are summarised as follows.

I) Study of MR fluid stability against sedimentation using computational fluid dynamics (CFD) simulation towards the development of a standard water based MR fluid for in-house use.

II) Quantum-chemical modelling of chemical reactions to synthesize physically stable MR fluid.

III) Mathematical modelling of MR fluid, simulation and experimentation to investigate important parameters of CMMRF process. FEA-CFD simulation and experimentation of MR fluid based polishing pad to investigate polishing pressure.

IV) Classical Molecular Dynamics simulation (MDS) for understanding material removal mechanism on stainless steel (multiple alloyed and ductile material) using mechanical, chemical and chemical assisted mechanical abrasion.

V) Reactive MDS on aluminium (ductile material) for chemical, mechanical and chemo-mechanical material removal.

VI) Reactive MDS on silicon (brittle and hard material) for chemical, mechanical and chemo-mechanical material removal.

VII) Mathematical modelling of CMMRF process and FEA based simulation to predict material removal and surface finish.

VIII) Experimental study of on aluminium, and silicon to validate simulated results such as material removal and surface finish.

IX) Experimental study on stainless steel and copper workpiece to demonstrate capability of CMMRF process.

1.3 Organisation of the report

In **Chapter-1**, relevance and motivations are reported with objectives of the present research work. Applications and need of nano-finishing are clearly brought out in this chapter. In addition, challenges and merits of some nanofinishing processes are also summarised with suitable scope for academic research.

Chapter-2 is devoted for the literature survey including understanding of conventional finishing processes, advanced finishing processes such as MRF, CMP, modelling of MR fluid and experimental investigations on CMMRF process. It also discusses about the research gaps and scope of work. This chapter also brings out scope of research work in the field of theoretical as well as experimental aspects.

MR fluid is modelled and simulated in **Chapter-3**. Various parametric investigations have been carried out about MR polishing fluid of CMMRF process. Behaviour of MR fluid is analysed for the magnitude of and nature of the polishing pressure developed at the interface of MR fluid and workpiece, It has also defined the required working gap to process a wide range of engineering materials. In this chapter, chemical reaction is also discussed for synthesis of water based MR fluid using density functional theory.

Molecular dynamics simulations on steel, aluminium, and silicon have been carried out in **Chapter-4** to investigate the mechanism of material removal towards surface modification at atomic scale. In this chapter, finishing force is taken as a parameter from the polishing pressure analysed in chapter-3. This chapter investigates merits and demerits of mechanical finishing and chemical assisted mechanical finishing on aluminium as well as silicon workpiece to understand the behaviour of material removal, and achieving the nanometric level of surface finish in ductile as well as brittle materials. MD simulation is also used to define four types of finishing process to bring down the surface roughness from few microns to few angstroms.

CMMRF process is mathematically modelled and simulated in **Chapter-5**. To simulate mathematical model of CMMRF process, reactive MDS results are used to compute the coefficients for this model. This work helps to predict the process outcome at macro scale. In this chapter, material removal and improvement in surface finish are studied at different levels of parameters.

Chapter-6 discusses experimental investigations on aluminium, silicon, stainless steel and copper as workpiece materials. This chapter also includes results and discussion. In this chapter, the simulated results of mathematical model are also compared and validated. Capability of chemical assisted finishing of CMMRF is studied in this chapter. It is found that the process has capability to finish ductile materials and brittle materials of the order of sub-nanometer.

The concluding remarks on the completed work are summarized in **Chapter-7**. The references and Appendix are appended in the last.

----------x----------

Chapter-2

LITERATURE SURVEY

2.1 Introduction

This chapter deals with various finishing processes including conventional as well as advanced nano-finishing processes. Mechanisms of all such processes are discussed to gain better understanding about the problems associated with them when aimed to achieve surface finish in nanometric scale. In addition, key features are identified with MRF, CMP and CMMRF processes which are known as nano-finishing processes. Thereafter, a list of gap areas and scope of research work are also presented in this chapter.

2.2 Conventional finishing processes

There are mainly three different types of conventional finishing processes which are widely used in industries to improve surface finish, shape and size accuracy, and these processes are grinding, lapping and honing.

2.2.1 Grinding process

Grinding process is the most common and popular abrasive based finishing process in which grinding wheel is used as a cutting tool. It is often used in manufacturing industries. Grinding wheel is made of abrasive particles and bonding material. In this process, material removal takes place with the help of a rotating grinding wheel under the specified normal load and lateral movement against workpiece. Working principle of grinding process is shown in Figs.2.1 (a-c). Material removal mechanisms in grinding was modelled and analysed on the basis of the cutting-edge geometry and kinetics of the process. The model includes the phenomena of friction, ploughing and cutting involved during material removal [10].

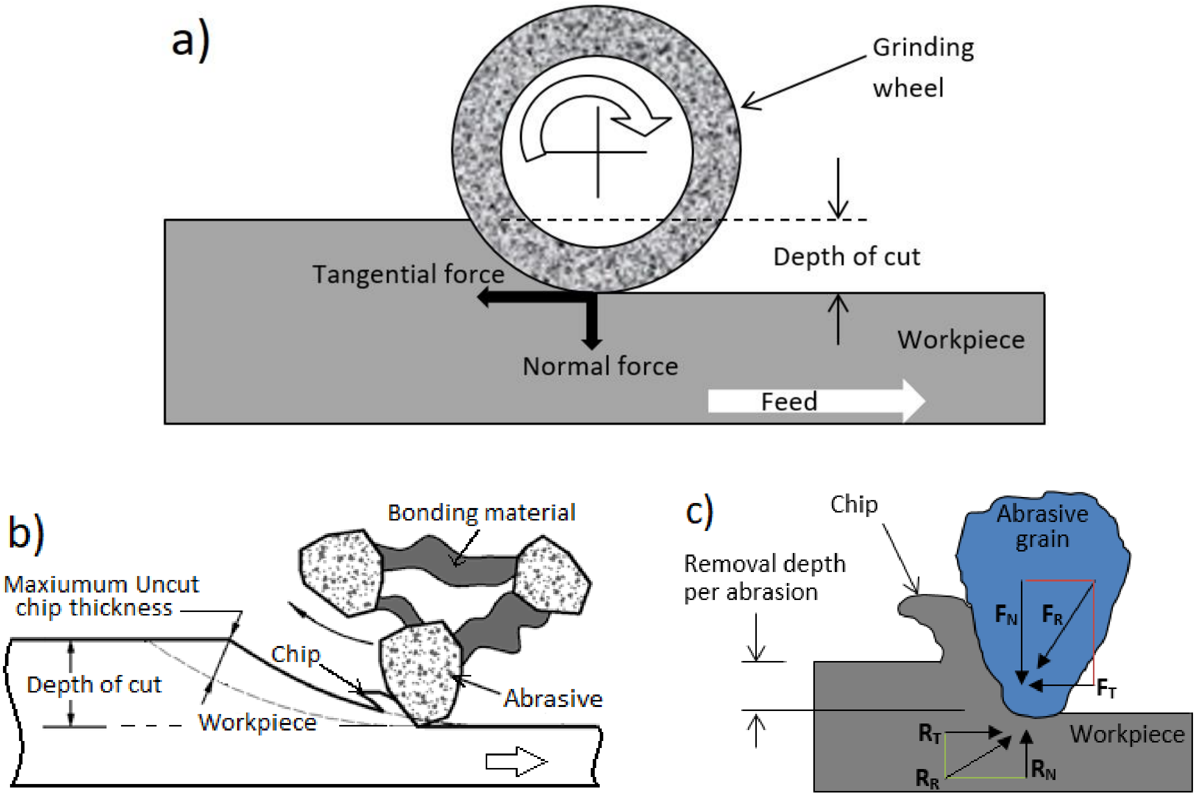

F_N: Indentation force F_T: Cutting force R_R: Net reactive force

Fig.2.1: (a) Schematic of grinding process, (b) material removal during grinding process. (c) Forces involved during material removal by single abrasive particle.

When the abrasive particle interacts with the workpiece material, the material follows the elastic-plastic deformation before the chip formation takes place as shown in Fig. 2.1 (b). This phenomenon repeats continuously with all abrasive grains exposed to the workpiece and results in material removal.

Denkena et. al. [11] have analysed, classified and discussed the fundamentals about the chip formation and material removal mechanisms by means of experimental investigation.

Grinding process has capability for high material removal rate (MRR) as compared with other finishing processes. Hence, it is useful to improve surface finish from very rough surface to finished surface in very small span of the grinding time. However, surface finish of the ground surface becomes few hundreds of nanometers, and it is almost impossible to achieve surface finish less than 100 nm by grinding process. The challenges associated to achieve surface finish less than 100 nm with conventional grinding are wear out of abrasive grits, loading of dislodged abrasive grits on the wheel, loading of debris on the wheel during grinding process, and uncontrolled grinding force variation from one abrasive particle to others, because of random orientation of the abrasive grits in the wheel [12].

Yao et. al. [13] have mathematically modelled the grinding force and grinding temperature. This model was used to investigate the chip formation force, friction force and temperature distribution in contact zone between the workpiece and wheel. When the grinding force and the grinding temperature increase, the workpiece material adheres locally to the grinding wheel. The grinding temperature gets affected mainly because of two reasons, viz. poor thermal properties of grinding wheel and low cooling efficiency. These phenomena cause additional surface damage to the workpiece.

2.2.2 Lapping process

Lapping process is useful to improve the flatness accuracy and surface finish upto few tens of nanometers, in which lapping pad or plate is used to abrade the workpiece using loosely bonded abrasive particles. Schematic of lapping process is shown in Fig. 2.2. Material removal in this process takes place due to relative movement between lapping pad and workpiece, which is described in mathematical model proposed by ‘Preston’ [14].

The material removal mechanisms have been investigated and reported by using an acoustic emission (AE) monitoring technique [15]. It was found that there are two important criteria for describing the material removal mechanisms like ductile vs. brittle machining and two body vs. three body abrasions. Later, the effect of lubricants has been investigated by using various lubricants such as deionized water, hydrocarbon oil, ethanediol, isopropanol, and ethanol to optimise the process performance [16].

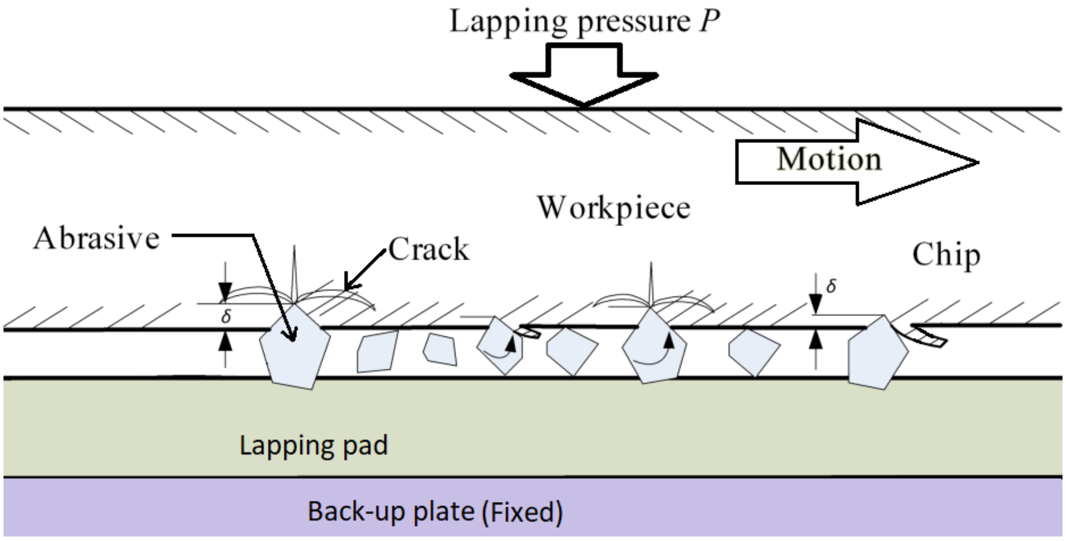

Fig.2.2: Schematic of lapping process. The depth of abrasion (δ) depends on size and orientation of abrasive particles.

In this process, the material removal rate is low as loosely bonded abrasive grits are used to abrade under low polishing pressure with respect to the grinding process.

2.2.3 Honing process

Honing is another finishing process to finish internal surfaces of cylindrical components, in which honing tool rotates and reciprocates along the axis of the cylinder. The honing tool consists of abrasive grits bonded sticks on radially stretchable arm. As the honing tool rotates, the arm expands radially and exerts the polishing pressure or radial force on the workpiece. This process produces a cross-hatched pattern which improves bearing ratio and useful for automobile parts. Schematic of honing process is shown in Fig.2.3.

A theoretical approach has been attempted for the dynamic modelling of the honing process. Forces and moments have been studied to gain better understanding for the material removal during honing process [17,18].

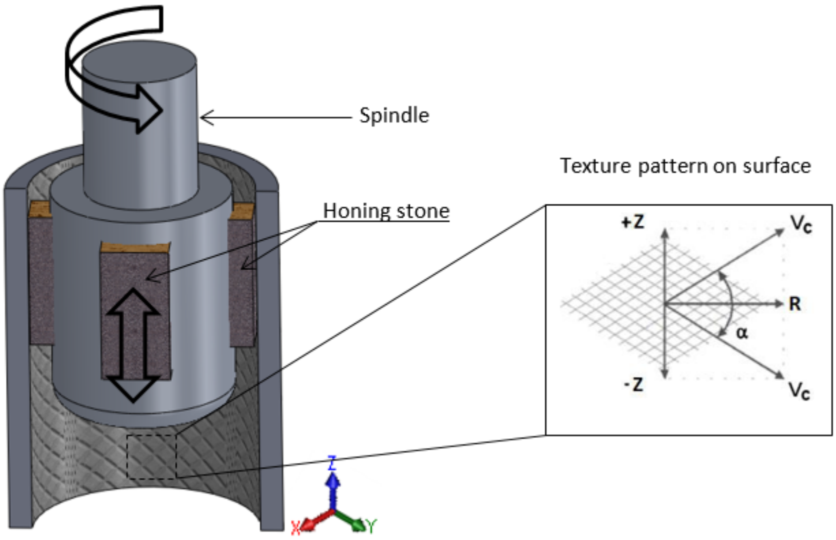

Fig.2.3: Schematic of honing process.

2.2.4 Summary of conventional finishing processes for surface finish quality

Table 2.1: Comparison and observations of various conventional finishing processes

Sr. No.	**Finishing process**	**Mechanism of Material removal**	**Surface quality**	**Remarks**
1	Grinding	Abrasion with permanently bonded abrasives, and the polishing pressure defined by the depth of cut.	-*Ra* ≈ 0.2-0.5 µm [12]. -Not suitable for mirror finish. -Finished surface consists defects such as scratches, cracks, lattice distortion and phase transformation.	Indentation force depends on abrasive size and their orientation. Whereas, the material removal depends on indentation force, sharpness of the abrasive particles and the grinding wheel loading.
2	Lapping	Abrasion with loosely floating abrasive particles and the polishing pressure comes from lapping pad.	-*Ra* ≈ 0.02-0.5 µm [19]. -Suitable for mirror finish. -Finished surface consists of defects such as scratches, digs, micro-cracks, lattice distortion and phase transformation.	Indentation force depends on abrasive size and the lapping pressure. The material removal mainly depends on indentation force, sharpness of the abrasive and orientation of the abrasive.
3	Honing	Abrasion with permanently bonded abrasives. Polishing pressure generates from centrifugal force on the honing stone and spring force.	-*Rt* ≈ 0.2-10 µm [19]. -Not suitable for mirror finish. -Finished surface consists defects such as scratches, cracks, lattice distortion and phase transformation.	Indentation force depends on abrasive size and rotational speed of honing tool and flexibility of the stretchable arm as well. Material removal on this process has similar interpretation.

Surface finish and the quality of finished surface depend on material removal rate and the type of degenerative layers associated with finishing process. Few aspects of conventional finishing processes are compared and summarised in the following Table 2.1.

In the conventional finishing process, the indentation force becomes more on bigger abrasive particle, as the polishing medium is mechanically hard and stiff [20]. *Thus, the material removal depends on abrasive size and its orientation, which are responsible for variation in material removal from one place to other on the finished workpiece. Hence, achieving nanofinished surface using conventional process is tedious and difficult.* There are a large number of advanced finishing processes in which indentation force is least prone to the abrasive particles size and their orientation by using flexible medium for polishing or by using abrasive free processes as discussed in the next section.

2.3 Advanced finishing processes (AFPs)

With the development of novel materials, difficult to machine materials, and complex geometrical shapes, the conventional finishing processes cannot achieve the desired surface finish to cater the requirements of the present high tech industries. The electronics industries are constantly in demand of high precision parts for miniaturisation of various types of memory devices with high data packing densities. This is possible when the device fabrication has been improved from macro and micro to nano-level of fabrication. The nano-fabrication cannot be realised unless surface finish in atomic scale and the form accuracy of the scale of few nanometers on large components are achieved. To finish surfaces in atomic scale (0.2-0.5 nm), material removal has to be controlled in the form of atoms or cluster of atoms. There are a few processes which give extremely low but controlled material removal rate (MRR) such as Elastic Emission Machining (EEM) and Ion Beam Machining (IBM).

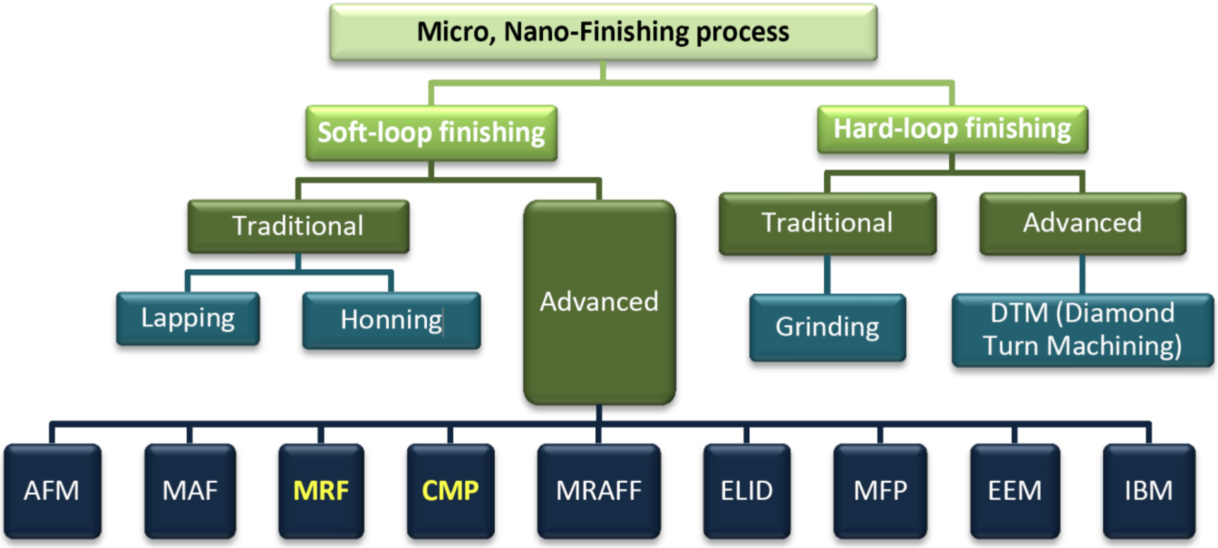

Fig.2.4: Classification of micro-nano finishing processes.

These processes remove material at atomic scale on the surface of workpiece to achieve surface finish in the range of 0.2-0.5 nm. However, these processes take enormously long finishing time due to extremely low MRR.

In the last 2-3 decades, some soft loop based finishing processes have been developed such as magnetic float polishing (MFP), magnetic abrasive finishing (MAF), magnetorheological finishing (MRF), and abrasive flow finishing (AFF). These processes are capable to generate surface roughness in the range of 10-100 nm on metals with flexible finishing medium and, therefore, these processes are also known as flexible nano-finishing processes. However, these flexible processes have few limitations, while finishing the engineering materials, such as surface defects, sub-surface damages and low finishing rate. Chemo-mechanical polishing (CMP) process is an example of an efficient finishing process, which is extensively used in IC (integrated circuit) industries to process metals and non-metals for generating nanometric and atomic level of surface roughness respectively. The CMP process has capability to process the materials at high polishing rate with extremely good surface finish, 0.2 to 0.3 nm in case of hard materials like semiconductors or ceramics. However, CMP is not capable of finishing geometries other than circular and flat wafers as it utilises polishing pad which is highly sensitive to working gap. In addition, a hard loop based finishing process was developed by using single crystal diamond tool in an ultra-precision lathe machine and this process is called as diamond turn machining (DTM). DTM has capability to generate shape and size accuracy of the order of few hundreds of nanometers, and surface finish of the order of few nanometers.

Fig. 2.4 shows a classification of most of the micro and nano-finishing processes from the field of traditional as well as advanced manufacturing. There are only few abrasive based AFPs such as AFM, MAF, CMP, MFP, EEM, MRF and MRAFF. Research carried out in some of these processes are discussed in the subsequent sections.

2.3.1 Abrasive Flow Machining (AFM) process

AFM process was introduced in 1960s for deburring and polishing of intricate inner surfaces or edges by reciprocating abrasive laden viscoelastic polymer under the applied hydrostatic pressure. Operation configuration of AFM is categorised in three different types such as one way AFM, two way AFM and orbital AFM. The two way AFM has become more popular because of its simplicity. In this process, two vertically opposed cylinders are used to flow the abrasive medium in a passage in which the workpiece is held firmly with tooling as shown in Fig.2.5. Literature of AFM process has been reviewed and discussed as follows.

Material removal is experimentally studied by Rhoades, and it is reported that the size, hardness and sharpness of abrasive particle and extrusion pressure play a vital role [21]. He has also reported that the medium viscosity is a critical parameter for the same. The medium viscosity temporarily rises when the medium is suddenly forced through a restrictive passage and causes high material removal. Hence, low viscosity medium was recommended for nanofinishing of narrow passages, and high viscosity medium for large passages.

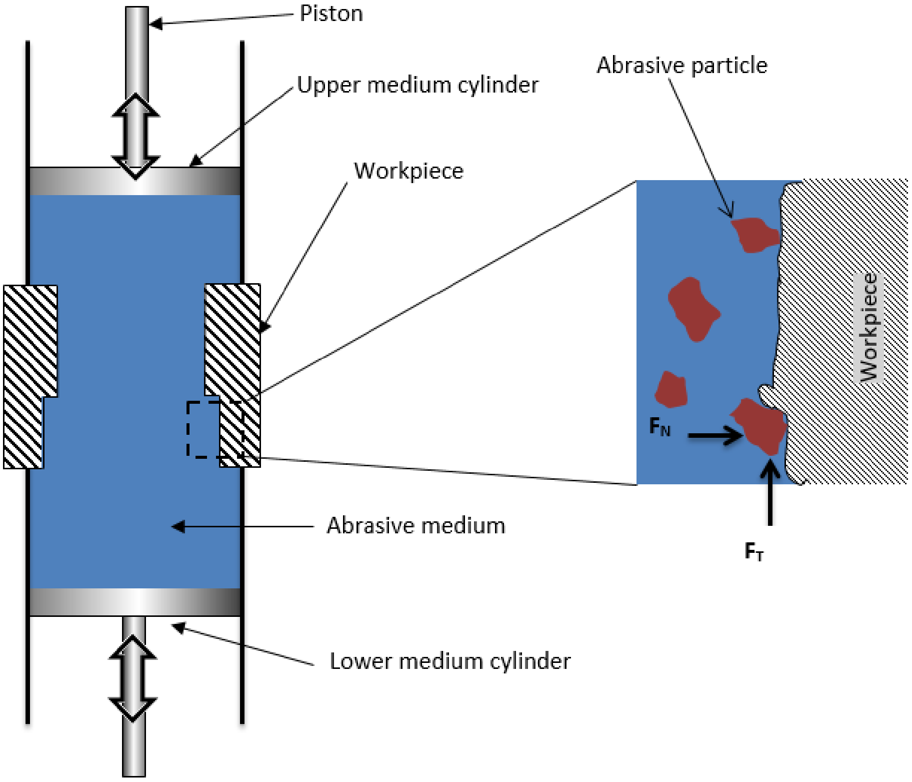

Fig.2.5: Schematic of abrasive flow machining process.

Williams and Rajurkar [22] have reported that the effect of medium's viscosity is more significant on material removal as compared to extrusion pressure.

Jain and Adsul [23] reported that the material removal depends on initial surface roughness and hardness of the workpiece. They have also reported that the material removal and reduction in surface roughness increases with increase in percentage concentration and size of abrasive particle as these parameters play significant role during AFM process.

Loveless et al. [24] have also reported that the initial surface roughness affects material removal during AFM process. The surface generated by WEDM is more suitable for AFM when compared to others.

Jain et al. [25] have carried out simulation of finished surface profile and material removed considering the interaction of abrasive particles with workpiece. In this work, a finite element based simulation has been carried out for the prediction of the stresses developed during AFM process. It is assumed that force on each abrasive particle is same and it results in the same depth of indentation for uniform material removal. Subsequently, a study [26] has reported on the effect of abrasive concentration and mesh size on medium viscosity at different temperature.

Rajeshwar et al. [27] have developed a mathematical model using constitutive equations of Maxwell model and carried out simulation to study the medium flow. It was reported that there is a linear relationship between MRR and shear stress acting on the worksurface. Gorana et. al. [28] studied the mechanism of AFM process by developing a theoretical model of forces acting on a single abrasive particle.

2.3.2 Magnetic Abrasive Finishing (MAF) process

Magnetic Abrasive Finishing (MAF) is a non-conventional superfinishing process in which magnetic abrasive particles experience finishing force under the influence of magnetic field in the finishing zone to remove material in the form of micro/nano chips towards generation of good quality of surface finish. Schematic of MAF process is shown in Fig. 2.6 (a-b). The MAF process was patented by Harry P. Coats in 1940 [29,30]. Afterward, a series of research work was carried out in the late 1950’s and 1960’s [31]. Literature of MAF process has been reviewed and discussed as follows.

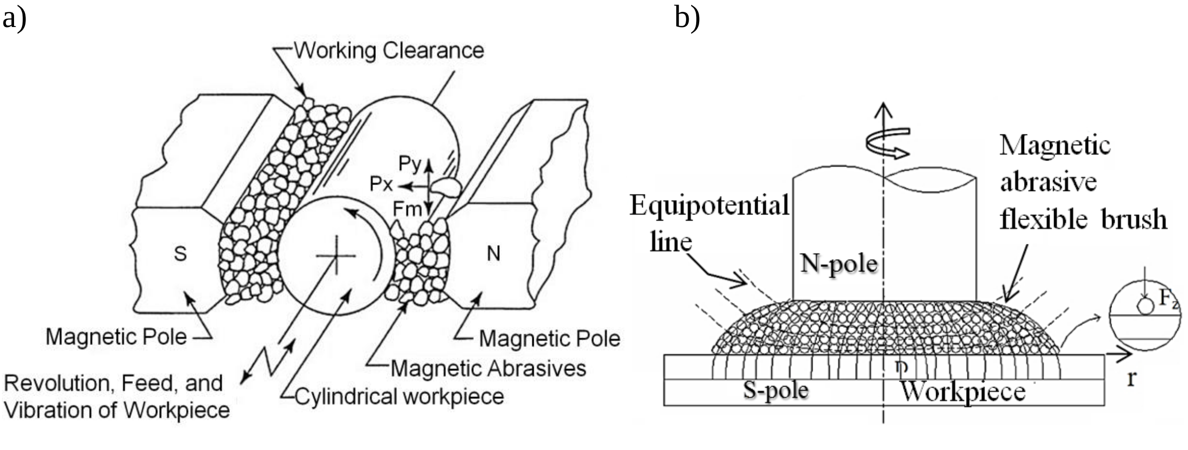

Fig. 2.6: Schematic of magnetic abrasive finishing. (a) for cylindrical workpiece [32]. (b) for flat workpiece [33].

Kremen et al. [29] have developed an empirical expression for estimation of machining time. Later they proposed that the material removal rate is large at the beginning of the process due to large unevenness on the surface of workpiece, and decreases with decrease in unevenness.

Kim and Choi [34] have developed a mathematical model to predict the surface finish with respect to the processing time. The simulation-results agree well with the experimental obseravtions.

Khairy [35] reported that the process has capability to produce extremely fine surface finish in the range of 10-50 nm. Mori et al. have [36] proposed a theory for explaining the formation of magnetic abrasive brush during MAF process. They have also calculated normal force which agrees well with experimental result.

Jayswal et al. [37,38] and Kwak [39] have developed a finite element model and carried out simulation to evaluate the distribution of magnetic forces associated during MAF process. The simulation results were verified with the experiments.

Hou and Komanduri, [40–42] have presented a thermal model with FEA based simulation. It was found that the flash temperature was the function of pressure, sliding speed and scratch length made by the abrasive during nanofinishing. Kumar and Yadav [43] have developed a model for the heat flux generated on workpiece surface, and they have carried out FEA based simulation. The effects of various process parameters including the temperature rise in the workpiece have been studied and reported.

Mishra et al. [44] have carried out FEA based simulation and studied the heat generated at the workpiece surface due to the rubbing action of magnetic abrasive particles on the work surface. They have estimated the temperature at the rubbing zone in the range of 34–51°C.

Shinmura and co-workers have extensively studied the MAF process on various materials from 1984 to 1995 [31,45]. They have studied the effects of various process parameters like magnetic flux density, working gap, types of abrasives, types of workpiece, and cutting speed on finishing characteristics.

Singh et al. [46] have studied the effect of electromagnet input voltage, working gap, rotational speed of electromagnet and mesh size of *SiC* abrasive particle on the surface finish and material removal. They found that high voltage, low working gap, high rotational speed and fine abrasive particles are desirable for improving the surface finish.

Singh et al. [47] have investigated the forces acting during MAF process by the experimental means, and a correlation between the surface finish and the forces was presented. They found that forces and improvement in the surface finish increase with the increase in magnetic flux density by increasing current to the electromagnet and decreasing in the working gap.

Ahmad et al. [48] have carried out an experimental optimization work and reported that the influence of the sintered magnetic abrasive particle on the machined surface with appropriate size of the particle, optimizes the surface finish.

Jain et al. [49] have experimental studied MAF on ferromagnetic and non–ferromagnetic materials. They reported that the magnetic flux density increases by three times on ferromagnetic material as compared to non–ferromagnetic workpiece. Final achieved surface finish was 20 nm and 60 nm in case of ferromagnetic and non–ferromagnetic stainless steel, respectively. In addition, normal magnetic force was much higher in case of ferromagnetic than non–ferromagnetic workpiece material but no significant change was found in tangential cutting force.

Heng et al. [50] have reviewed MAF process and they have also highlighted the limitations associated with this process such as a micro-scale workpiece material is not possible as fragility to MAF and negligible surface finishing on ferromagnetic materials (e.g. nickel and cobalt alloys).

The researchers have reported that there are many process parameters which affect the material removal and surface finish. However, magnetic field strength, abrasive particles size and working gap have been found to be most significant parameters to control surface finish as well as MRR. In addition, the surface finish significantly depends on the type of workpiece material used.

2.3.3 Magnetorheological Finishing (MRF)

MRF process was initially developed for nanofinishing of optics, ceramics and semiconductors and subsequently it was commercialised by QED Technologies Inc. [51–53].

Magnetorheological (MR) fluid has been used with abrasive particles for finishing in which finishing force on the abrasive particles is controlled by changing the flow properties of MR fluid enabled through the magnetic field. Additionally, the material removal mechanism was conceived using hydrodynamic lubrication theory of journal bearing, in which the material removal occurs due to shearing by magnetically stiffened MR fluid on the surface of work piece. Schematic of MRF process is presented in Fig. 2.7.

Kordonski and Golini [54] have reported the surface stresses and material removal during MRF process. The MRR was predicted using generalized Preston’s model.

Nano-alumina and nano-diamond abrasive particles mixed in MR-fluid were used as effective abrasive particles which are suitable for manufacturing of infrared optics [55].

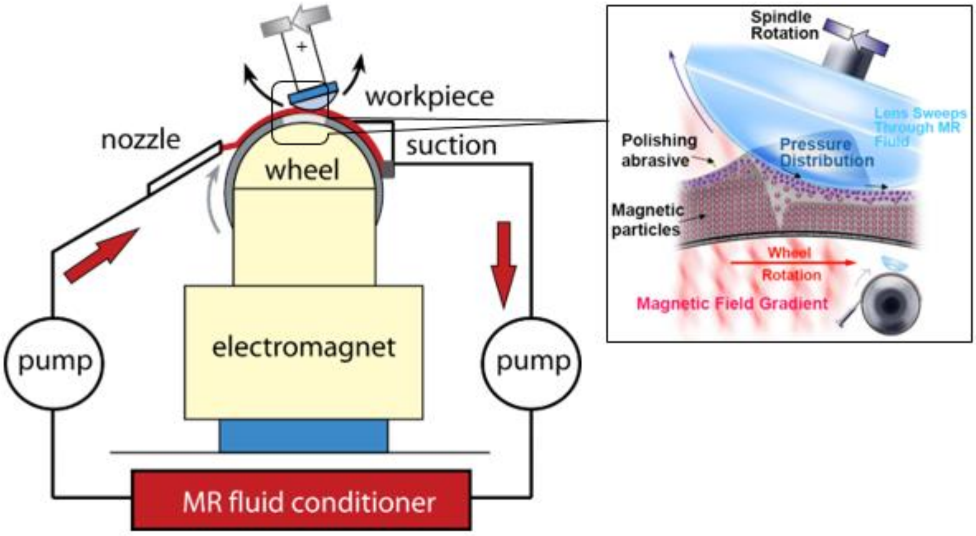

Fig. 2.7: Schematic of MRF process [53].

Finishing force along tangential and normal directions during magnetorheological finishing of freeform surface is carried out, and it is reported that the normal force is found to be more dominant compared to the tangential forces [56]. Furthermore, MRF process was used to obtain nanometric surface finish on free form surfaces of knee implant.

While comparing to AFM, MAF and MRF, the MRF process has better capability in terms of final surface finish achieved as discussed in Table 2.2. This capability is possible because of the MR fluid medium which provides better cushioning to abrasive particles and it has better control for indentation when abrasive sizes are varied.

Thus, MRF process is capable to generate uniform MRR hence uniform scratch formation. This leads to generate *Ra* value from 1- 10 nm as the finishing force can be controlled precisely.

On the other hand, MRF also results in some micro/nano scratches because of which getting *Ra* value less than one nanometer is challenging. Hence, to achieve surface finish less than one nanometer, there is a need to incorporate chemical to mitigate the scratch formation.

Table 2.2: Comparison of AFM, MAF and MRF processes.

Parameters	**AFM**	**MAF**	**MRF**	**Remarks**
Finishing properties of medium	Medium properties cannot be controlled precisely.	It can be controlled by changing magnetic field or working gap	It can be controlled by changing magnetic field or working gap	MAF and MRF have better control over the finishing force (indentation and cutting force)
Effect of particle size distribution	Effect of particle size variation would result in variation of finishing force due to the variation in the viscosity of the medium.	Effect of particle size variation would result in small extent of variation of finishing force due to change in the magnetic properties of the medium/ mixture. However, the magnetic brush exhibits some amount of stiffness.	Effect of particle size variation would result in small variation of finishing force as the magnetic ribbon of MR fluid exhibits some amount of stiffness as well as damping characteristic but the magnetic properties of the medium would change which is responsible for change in the force.	MRF has capability to shows less immune to the size variation of the abrasive particle size distribution.

2.3.4. Chemical Mechanical polishing (CMP)

Main constituent of CMP process is polishing pad adhered over a flat platen which rotates under a specified polishing pressure against workpiece in the presence of polishing slurry. Whereas, a carrier is used to hold the workpiece. The polishing pressure and relative velocity between workpiece and pad results material removal and it gets enhanced due to the chemicals of polishing slurry in CMP process towards attaining atomic level of surface finish [57,58]. Schematic of CMP process is shown in Fig. 2.8.

CMP process has been extensively used for surface finishing of the order of a few angstrom and flatness in range of few hundreds of nanometers. In CMP, polishing slurry contains chemical which converts top layer of the surface of workpiece into soft passivation layer and helps to remove the material by mechanical means. This technique helps to achieve surface finish in the range of 0.2-0.4 nm with comparatively large material removal rate.

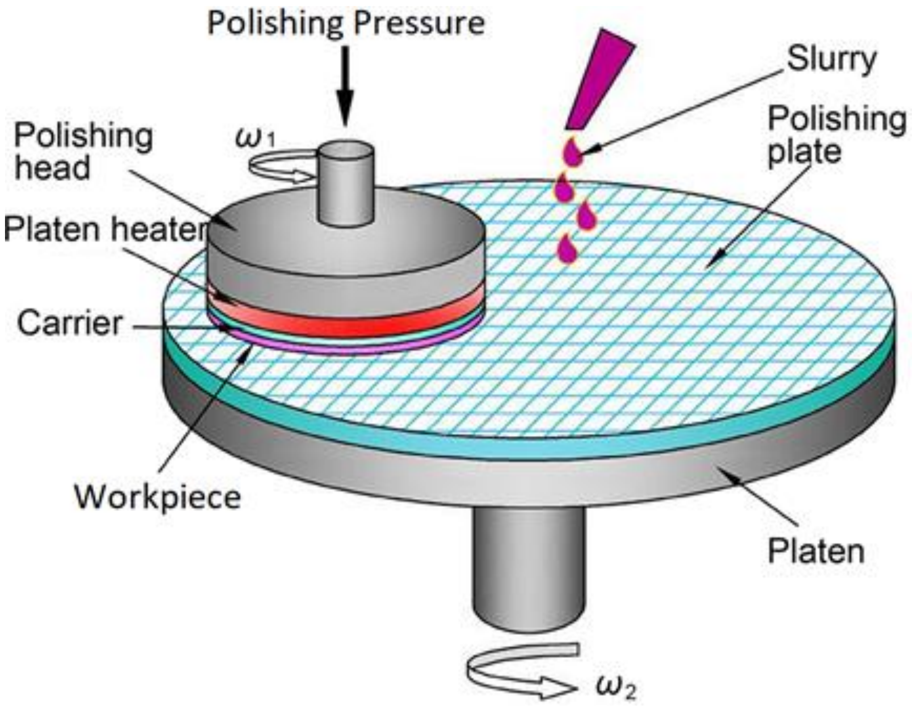

Fig.2.8: Schematic of CMP process [59].

This process has many parameters to control the process like pH value, size of abrasive particles, concentration of abrasive particles, quality of micro-texture of polishing pad, relative rotation speed, polishing pressure, temperature, etc. [57].

2.4 Chemo mechanical magnetorheological finishing (CMMRF)

Chemo mechanical magnetorheological finishing (CMMRF) has been developed in the recent past by combining the constructive aspects of CMP and MRF, and overcoming some of their undesirable effects during nanofinishing operation. CMMRF is one of the most important emerging nano-finishing processes, which is capable to generate surface roughness of the order of nanometer using a magnetic field based flexible polishing pad. This process was initially developed and experimental study was carried out on mono-crystalline silicon substrate [7]. Comparison between CMP, MRF and CMMRF processes has been presented in Table 2.3.

MR fluid is a main part of CMMRF process, which is used to form a flexible polishing pad under the influence of magnetic field using permanent magnet.

Table 2.3: comparison between CMP, MRF and CMMRF

Sr. No.	Basis for comparison	CMP	MRF	CMMRF	Suitability
1	Finishing rate	≈10nm/ min	≈1nm/ min	≈10nm/ min	CMP & CMMRF
2	Final surface finish (*Ra*) on metal & alloys	<1.0nm	≈10nm	<1.0nm	CMP & CMMRF
3	Final surface finish (*Ra*) on semiconductor & ceramics	≈0.2-0.4nm	≈1.0nm	≈0.4-0.5nm	CMP & CMMRF
4	Surface complexity (2D & 3D)	Flat-circular wafers (2D)	2-D as well as 3-D surfaces	2-D as well as 3-D surfaces	MRF & CMMRF
5	Type of materials to process	Suitable for brittle materials but not for ductile materials because of scratch formation in large number.	Not suitable for malleable & ductile materials	All materials	CMP & CMMRF
6	Surface defects or scratch-dig value	10-5 on brittle materials only.	40-20	10-5	CMP & CMMRF
7	Residual stress	Negligible	Significant	Negligible	CMP & CMMRF
8	Tactful finishing on fragile materials	Not suitable	Suitable	Suitable	MRF & CMMRF
9	Life of polishing pad	Limited	High	High	MRF & CMMRF

2.4.1. MR fluid

MR fluid is a smart fluid, whose rheological properties can be controlled under varying magnetic field. This fluid comprises abrasive particles and carbonyl iron particles (CIPs) in a carrier medium [60]. The fluid behaves like a Newtonian fluid without magnetic field and it behaves as a Bingham plastic fluid under the influence of magnetic field. The transformation of MR fluid behaviour from Newtonian to Bingham plastic occurs by inducing magnetic force in MR fluid due to magnetic field [61] under specific value of time which is known as response time. In general, the response time is few milliseconds to create a chain of CIPs, and few seconds to form thick layers of MR fluid [62]. The abrasive particles acquire magnetic force from CIPs to abrade superficial layer of workpiece precisely. In general, the magnitude of magnetic force on MR fluid depends on the intensity of magnetic field. The carrier medium belongs to either hydrocarbon oil based fluid or water based fluid. In CMMRF process, water based MR fluid is used as water dissolves all types of the polar chemicals which are necessary to maintain chemical assisted material removal on the work piece.

In general, applications of MR fluid are classified into four major classes. These classes are expressed on the basis of operation like, shear mode, valve mode, squeeze mode and combination of them [63]. Amongst all these modes of operation, squeeze mode exhibits highest pressure in the working zone and the shear mode is responsible for better shearing stress. It was also reported that the polishing pressure plays a vital role for material removal in CMP process [57]. It means, there is a need to achieve pressure more than a threshold value towards material removal during nanofinishing. Hence, squeeze mode in combination of the shear mode is suitable for CMMRF based nanofinishing process.

2.4.2. Summary of literature survey of finishing processes

Chronological order of technological development in the field of CMP, MRF and CMMRF is summarised as follows.

- MR fluid was invented by Rabinow in late 1940s [64].
- CMP process was conceptualised and developed by Bob Walsh, in 1961 [57].
- MRF process was developed by Kordonski and Jacobs in1996 [51].
- MR Polishing fluid for hard metal in MRAFF is investigated by Jha and Jain, in 2006 [65].
- Sedimentation study of MR fluid by agglomeration of CIPs is carried out by Kciuk, et. al in 2009 [66].

- An experimental investigation was carried out using CMMRF process on silicon [7].
- An integrated simulated study using FEA has been carried out on the MR fluid under shearing force by Parlak et. al, in 2012 [67].
- Modelling, experimental and characterisation of hydrocarbon oil based MR fluid for nanofinishing were reported by Jain, Jha, Das and Sidpara at IITK during 2004-2014 [56,68–73].
- CMP process was investigated for steel by Hu, et al., in 2012 [74], and Jiang, et al., in 2015 [75].
- Experimental investigation into Ball end –MRF of silicon is investigated by Saraswathamma, et al., in 2015 [76].
- Abrasive-free and ultra-low abrasive CMP is reviewed by Penta in 2016 [77].
- A theoretical study on swirl assisted MR finishing for tubular component is carried out by Kheradmand et al., in 2016 [78].
- Dual-rotation MR finishing is developed for better *Ra* value by Wang et al., in 2016 [79].
- MD simulation for CMP process for silicon was carried out by Wen et al., in 2017 [80].
- Modelling and simulation of Ball End MRF process is carried out by Alam and Jha, in 2017 [81].

The literature survey shows that CMMRF process has many advantages and few gap areas which are discussed in the following section.

2.5 Modelling and simulation tool for micro and nano-finishing process

Modelling and simulation of any mechanical process needs an understating about the suitable modelling tools. These tools are classified on the basis of size scale and time scale as presented in Fig.2.9.

Quantum Chemical (QC) modelling is also known as first-principle-based molecular dynamics which does the computational work on various chemicals to find out behaviour of the molecules by solving the time-independent Schrodinger wave equation [82]. To solve this equation, there are few approximation techniques as follows.

1. Hartree-Fock theory works on basis of an approach of wavefunction which relies on the mean-field approximation [83,84].
2. Density Functional Theory obtains the energy from the electron density rather than the more complicated wavefunction [85].
3. Combination of multiple techniques.

QC methods are, in general, applicable to all types of chemical systems. However, this modelling work is computationally intensive which makes them inapplicable for large systems, e.g. more than 100 atoms. Hence, QC modelling has become a primarily applicable for single point or local energy minimization.

Molecular Dynamics Simulation (MDS): In general, MDS does the computational work by employing a suitable potential function under an environment of statistical ensemble to the system by using the verlet (velocity-verlet and displacement- verlet) algorithm to compute the time dependent positions of all atoms of the system [86].

This tool has been categorised in two branches. One is reactive-MDS which utilises reactive force field potential function and describes the relationship between energy and geometry with a set of relatively simple potential functions. Their simplicity of the potential function allows to be applied to much larger systems than QC systems (thousands of atoms on single processors; millions of atoms on multiprocessors). The parameters used in the potential functions are developed by fitting them against a large set of data, which is generated from the QC simulation. In general, this potential function includes various functions of energy as a set of parameters such as bond energy, atom energy, lone-pair energy, molecule energy, valence angle energy, double-bond valence angle penalty, valence angle conjugation energy, hydrogen bond energy, torsion energy, conjugation energy, van der Waals energy, Coulomb energy, electric field energy, and charge equilibration energy [87]. Hence, this technique is suitable to reveal chemical as well as physical phenomena of a system.

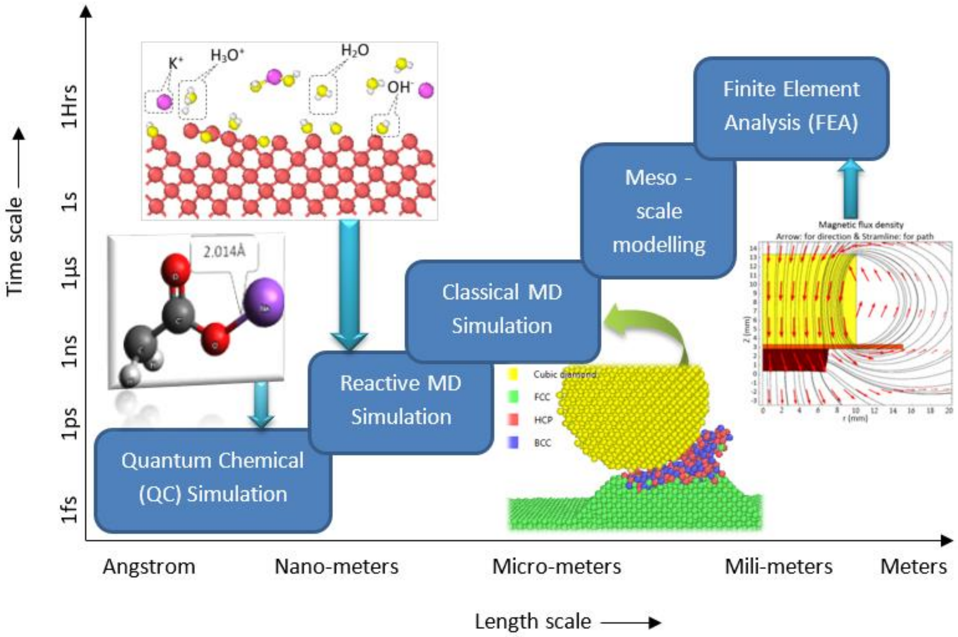

Fig.2.9: Hierarchy of process modelling at various scales

There is another form of MDS which utilises much simple potential functions like, Morse potential, Lennard Jones potential, embedded atom method (EAM), Tersoff potential, etc. This method is also known as classical MDS in which the potential function deals with bond energy and the bond length which makes it much simpler in the field of molecular dynamics simulation [88].

There are few techniques to simulate the system in meso-scale such as dislocation dynamics simulation [89], Brownian dynamics simulation [90] and kinetic Monte-Carlo simulation [91]. Dislocation dynamics simulation is suitable for structural mechanics and micro/nano finishing process. Dislocation dynamics is used to study about the crystal plasticity, in which the motion of dislocation lines and their interactions with themselves are simulated by discretizing them followed by adaptive re-meshing within the crystal (or within a grain or sub-grain). Thus the mechanical properties of the crystal in plastic zone of deformation can be investigated at meso-scale.

The Finite Element Analysis (FEA) is a numerical method which solves the problems of engineering and mathematical physics [92]. FEA can solve the problems in case of complicated geometry, loading and the material properties efficiently by dividing the geometry in small sub-domains which are known as mesh. In each subdomain, the governing equations are applied and a set of elemental matrix is calculated (which correlate force and displacement vector), thereafter, all elemental matrices are combined to form a global matrix which is further used to solve the relationship between force vector and displacement vector using given boundary and initial conditions. To analyse the results, post processing step is used. In the computational work, the geometry gets meshed using meshing technique followed by further processing by using a suitable solver to solve the problems under given environment of governing equations, boundary conditions and initial conditions. At the end, the post processing module is used to analyse the results for extracting the required information.

2.6 Gap areas

Based on the literature survey, it is concluded that there are some gap areas in the nanofinishing techniques which needs further work as listed as follow.

I. Analytical model and behaviour of MR fluid have not been explored for finishing pressure.
II. Process optimization for higher MRR in CMMRF has not been done.
III. MRF process modelling for surface modification at atomic scale has not been explored.

IV. MD simulation of CMP for finishing of some commonly used industrial materials such as stainless steel, aluminium, inconel, titanium etc., has not been carried out.

V. CMMRF mechanism of material removal on ductile and brittle material is not available.

VI. CMMRF process-models (empirical and mathematical both) and combined effects of mechanical abrasion and chemical reactions are not available.

VII. Multi-scale modelling for material removal in CMMRF is not carried out.

These gap areas show that there is a need for in-depth scientific understanding and detailed investigations in the field of CMMRF process. Hence, research areas have been identified which need to be investigated for enhancing the process performance in terms of material removal rate, percentage of improvement in Ra value, finishing rate, final Ra value etc. In view of this, specific plan for this research activity is listed as follows.

1) Experimental study supports process capability. However, there is a need to understand science behind the process for better utilisation of the process. Therefore, MR fluid behaviour for the formation of polishing pad is an important area to implement it for CMMRF process. This area needs to characterise the <u>CMMRF polishing pad</u>, and behaviour of MR fluid in micro and nano-scale.
2) <u>Material removal mechanism</u> of any finishing (or machining) process is an important area. In CMMRF, the material removal is at nanometric scale. Thus, material removal at nanometric scale is one of the significant areas. In this area, material removal mechanism for ductile and brittle materials need to be investigated.
3) <u>Mathematical modelling</u> is another area which is useful to understand the process behaviour by using mathematical relation, and it is also useful to predict the process outcome.

Based on the research gap areas, scope of the present work has been derived and presented in the following section.

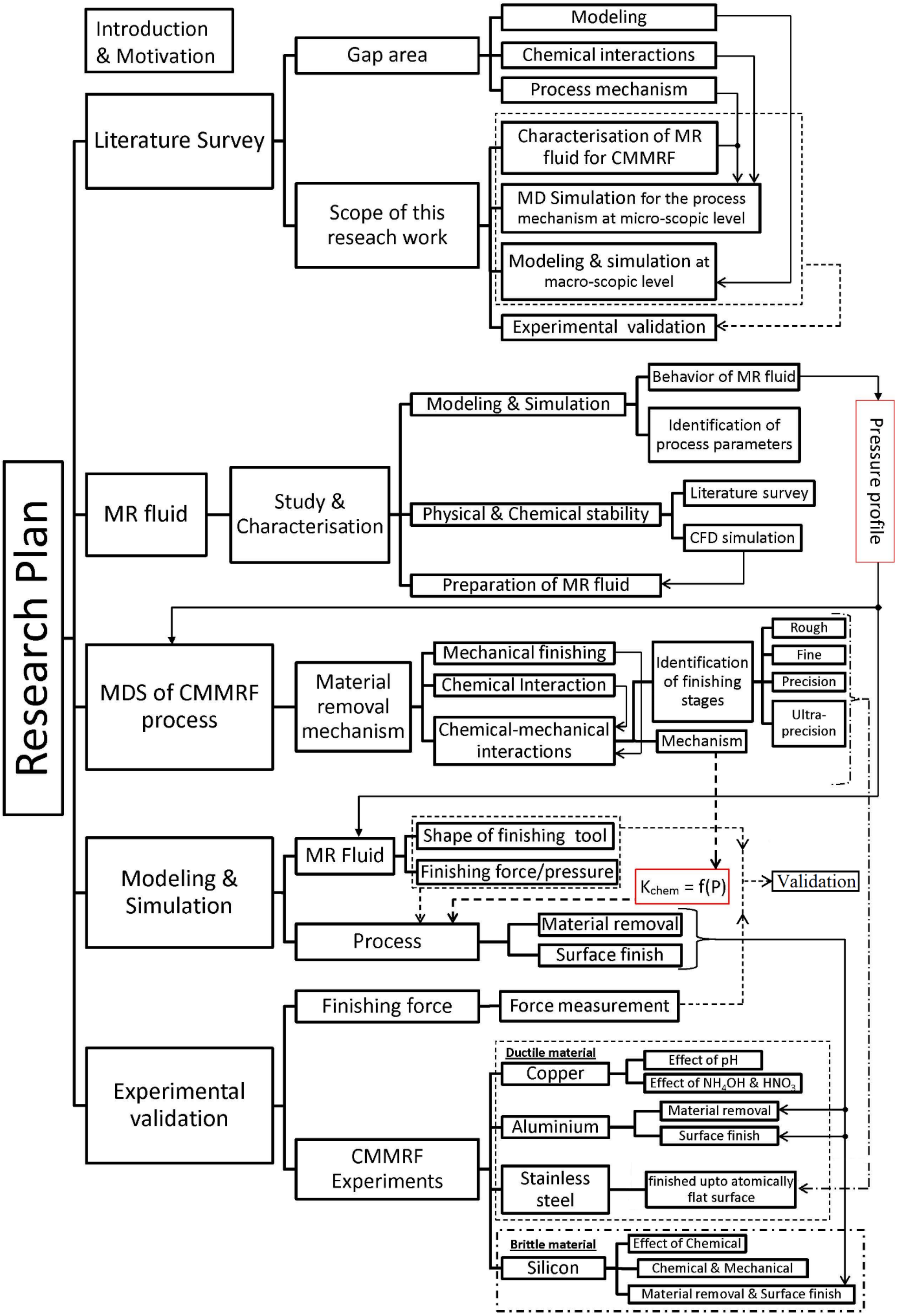

Fig.2.10: Research plan

2.7 Scope of research work

In general, a clean and scientifically sound understanding about process mechanism helps for commercialisation and deployment at mass scale. Hence, it is essential to understand and model the process behaviour at various-scale (atomic, micro, and macro-scale) under the influence of various process parameters.

To gain complete and intensive understanding of CMMRF process, there is a need to study on water based MR fluid, chemical interactions involved in CMMRF and material removal mechanism. In view of this, following areas of research activities have been identified as a scope for this research work.

I. Modelling, simulation, and synthesis of MR fluid for CMMRF process.
II. Study the mechanism of material removal at atomic scale for CMMRF process.
III. Modelling and simulation of CMMRF process at macroscopic scale.
IV. Experimental validation and demonstration of process capability to generate surface at nanometric scale in ductile as well as brittle materials.

These research works need to carry out various activities, and these activities have been mentioned as per the research work plan of this Ph.D. thesis as shown in Fig.2.10.

-------------X-------------

Chapter-3

ANALYSIS OF MAGNETORHEOLOGICAL FLUID FOR CMMRF PROCESS

3.1. Introduction

Water based MR fluid is one of the main constituents of CMMRF process and it forms polishing pad under the influence of magnetic field due to a permanent magnet. This fluid works with the combination of squeeze and shear mode to generate and apply the required polishing pressure for material removal by adjusting the working gap. After carrying out the literature survey, following gap areas are identified to study and analyse the magnetorheological fluid for CMMRF process.

- Formation of polishing pad: FEA and CFD integrated simulations are carried out to study the formation of polishing pad due to magnetic field.
- Mechanism to generate polishing pressure: Mathematical modelling, simulation and experiments are carried out to understand this mechanism.
- Sedimentation behaviour of MR fluid: This study is carried out using CFD simulation for different types of water based MR fluid.
- Synthesis of MR fluid: To synthesize water based MR fluid, suitable chemical reactions are studied and analysed using QC modelling to get physically and chemically stable fluid.

In view of this, MR fluid is analysed to characterise the polishing pad, to understand flow behaviour with and without magnetic field, and to study the chemical reactions involved within the MR fluid. These studies will be beneficial towards CMMRF process modelling and optimisation.

3.2. Formation of polishing pad

MR fluid behaves as Newtonian fluid without magnetic field and hence it does not form the necessary tool for nano-finishing. On the other hand, MR fluid forms a flexible polishing pad under the influence of magnetic field. In this section, FEA-CFD integrated simulation is carried out to understand the formation of polishing pad for CMMRF process.

3.2.1. Modelling and simulation of magnetism in MR fluid: FEA and CFD simulation

To study the effect of magnetic field, different portions of polishing pad are modelled such as, magnetic field in magnet, air, polymethyl methacrylate (PMMA) plate and MR fluid as shown in Fig. 3.1 (a). In this section, magnetic field is used to compute magnetic force towards flow of MR fluid.

3.2.1.1. Boundary conditions for FEA simulation

The magnetic potential of the side faces of the permanent magnet are set to zero, as magnetic lines flow along the direction of magnetisation within the magnet. Dimension for extreme portion of ambient air is obtained by ensuring the magnetic field less than 0.01 Tesla, and hence the extreme portion of the ambient air is also set to zero potential to represent infinitely large space for the magnetic field.

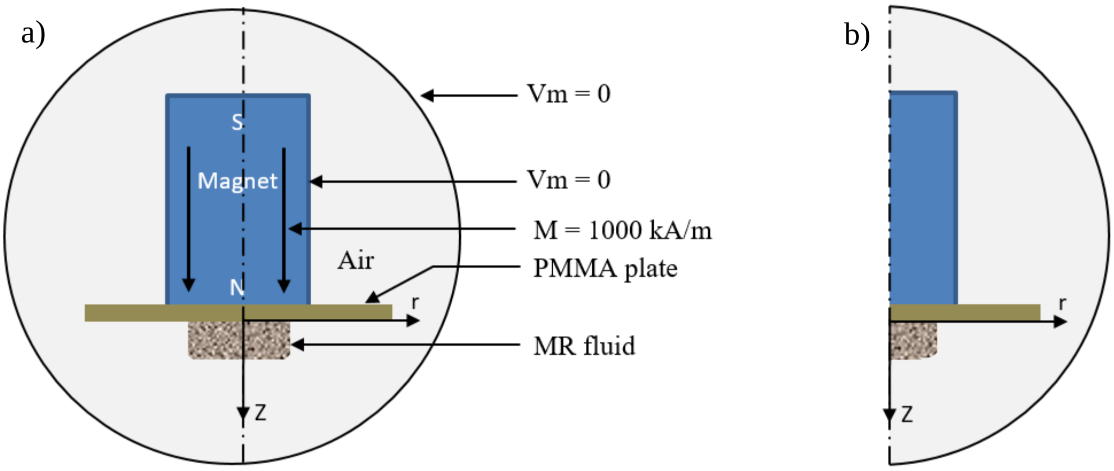

Fig.3.1: Schematic for the boundary condition of permanent magnet for FEA simulation. (a) Full model. (b) Half model, i.e. axisymmetric model.

Magnetization of the magnet was obtained from experiment to match with 0.6 Tesla of magnetic field as shown in the schematic, Fig.3.1 (a). Since, boundary condition and geometry are symmetric about z-axis, half model is presented in Fig. 3.1 (b) which is further used during simulation.

3.2.1.2. Boundary conditions for CFD simulation

CFD modelling is applied only on MR fluid and air. Velocity for the extreme portion of air, i.e. outer boundary of model, is set to zero. Normal velocity of fluid on the surface of magnet and on the surface of PMMA plate are set to zero. Pressure on the outer boundary of air is set to 1bar.

3.2.1.3. Initial conditions for FEA-CFD simulation

Initial value of magnetic field is set to zero except the magnetization of the magnet. Moreover, initial values for velocity and pressure are also set to zero and 1 bar respectively.

3.2.1.4. Modelling for Magnetic field

Magnetic field is computed by solving Gauss's law and constitutive relation of magnetism [93] as described in the following Eqs. (3.1-3.3).

$$\nabla . B = 0 \tag{3.1}$$

$$B=\mu_o(H+M) \tag{3.2}$$

$$M=\chi_v B; \text{ and } H=\nabla .(Vm) \tag{3.3}$$

Where, 'B' is the magnetic flux density which is also defined as gradient of the magnetic potential (Vm), 'H' is an external magnetic flux density, 'M' is the magnetisation of magnetic material, 'χ_v' is the volume magnetic susceptibility, 'μ_o' is the magnetic permeability in vacuum which is equal to $4\pi\times10^{-7}$ V·s/(A·m).

3.2.1.5. Modelling for magnetic force

The magnetic flux inside MR fluid magnetises carbonyl iron particles (CIPs) of MR fluid, and results in alignment of these CIPs due to the induced magnetic forces which are stored in the form of magnetic energy. The magnetic energy per unit volume (ξ) is expressed and written as per Eq. 3.4.

$$\xi = \frac{B.H}{2} = \frac{B.B}{2\mu_o\mu_r} = \frac{|B|^2}{2\mu_o\mu_r} = \mu_o\mu_r\frac{|H|^2}{2} \tag{3.4}$$

Where, ξ is the magnetic energy per unit volume stored in MR fluid.

According to the principle of the conservative force [94], the magnetic force can be written as gradient of the magnetically stored energy due to externally applied magnetic field from a magnet. Hence, magnetic force density (F) is expressed in Eq.3.5 which is the magnetic force per unit volume and unit of magnetic force density is ‘N/m^3’.

$$F = \nabla(\xi) \tag{3.5}$$

Magnetic force density is further simplified in terms of the magnetic potential and expressed as per Eqs. 3.6 and 3.7 for Cartesian and cylindrical coordinate system, respectively. These equations are useful to simulate MR fluid for flow due to magnetic field.

$$F = 0.5\mu_o\mu_r\nabla\left\{\left(\frac{\partial Vm}{\partial x}\right)^2 + \left(\frac{\partial Vm}{\partial y}\right)^2 + \left(\frac{\partial Vm}{\partial z}\right)^2\right\} = F_x\hat{\imath} + F_y\hat{\jmath} + F_z\hat{k} \tag{3.6}$$

$$F = 0.5\mu_o\mu_r\nabla\left\{\left(\frac{\partial Vm}{\partial r}\right)^2 + \left(\frac{\partial Vm}{\partial z}\right)^2\right\} = F_r\hat{\imath} + F_z\hat{k} \tag{3.7}$$

Where,

$$F_x = \mu_r\mu_o\left(\frac{\partial V_m}{\partial x}\frac{\partial^2 V_m}{\partial x^2} + \frac{\partial V_m}{\partial y}\frac{\partial^2 V_m}{\partial x\partial y} + \frac{\partial V_m}{\partial z}\frac{\partial^2 V_m}{\partial x\partial z}\right)$$

$$F_y = \mu_r \mu_o \left(\frac{\partial V_m}{\partial x} \frac{\partial^2 V_m}{\partial y \partial x} + \frac{\partial V_m}{\partial y} \frac{\partial^2 V_m}{\partial y^2} + \frac{\partial V_m}{\partial z} \frac{\partial^2 V_m}{\partial y \partial z} \right)$$

$$F_z = \mu_r \mu_o \left(\frac{\partial V_m}{\partial x} \frac{\partial^2 V_m}{\partial z \partial x} + \frac{\partial V_m}{\partial y} \frac{\partial^2 V_m}{\partial z \partial y} + \frac{\partial V_m}{\partial z} \frac{\partial^2 V_m}{\partial z^2} \right)$$

$$F_r = \mu_r \mu_o \left(\frac{\partial V_m}{\partial r} \frac{\partial^2 V_m}{\partial r^2} + \frac{\partial V_m}{\partial z} \frac{\partial^2 V_m}{\partial r \partial z} \right) \quad \text{and} \quad F_z = \mu_r \mu_o \left(\frac{\partial V_m}{\partial r} \frac{\partial^2 V_m}{\partial z \partial r} + \frac{\partial V_m}{\partial z} \frac{\partial^2 V_m}{\partial z^2} \right)$$

3.2.1.6. Modelling for flow of MR fluid

MR fluid flows and it takes specific shape due to the magnetic force by which the polishing pad forms. The flow behaviour of MR fluid obeys Navier-Stokes equation as shown in Eq.3.8 (a-b) [95]. Where, Eq.3.8 (a) shows the conservation of linear momentum, and Eq.3.8 (b) shows the continuity equation which is derived by considering the conservation of mass.

$$\frac{\partial(\rho u)}{\partial t} + (u.\nabla)(\rho u) = -\nabla p + \nabla.\left[\mu(\nabla u + (\nabla u)^T) - \frac{2}{3}\mu(\nabla.u)I\right] + F \tag{3.8a}$$

$$\frac{\partial \rho}{\partial t} + \nabla.(\rho u) = 0 \tag{3.8b}$$

Where 'u' is the fluid velocity, 'p' is pressure, 'ρ' is the mass density, 'I' is the unit matrix, 'μ' is the dynamic viscosity, and 'F' is the magnetic force density [95].

3.2.1.7. Simulation

In the present work, COMSOL4.3a multi-physics software has been used by coupling of few aspects such as magnetism and fluid flow using an algorithm of Arbitrary Lagrangian-Eulerian (ALE) method to apply moving mesh technique.

While simulating the magnetism, Gauss's law of magnetism of Maxwell equation and constitutive relation are solved to compute the magnetic force density. In addition, the Navier-Stokes equation is solved to simulate the flow behaviour of MR fluid. Thereafter, suitable post processing tools have been used to analyse the simulated results. Few assumptions are also made for the present simulation as presented in Table 3.1. Composition of MR fluid in volume is as follow, 30% CIPs, 2.5% alumina particle, 2.5% silica particle, 3% glycine, 2% glycerol and 60%water.

Table 3.1: List of assumptions which are used to simulate CMMRF polishing pad behaviour.

S.N.	**Assumptions for**	**Remarks**
1	MR fluid	It is similar to the magnetic fluid except viscosity, and the viscosity is equal to [5919 + 10191log$B$ + 6111(log$B$)^2 + 1223(log$B$)^3 Pa-s] which is taken from Das et al., 2008 [96].
2	Relative permeability of MR fluid	μ_r=10 (This value is computed from B-H curve) [97].
3	Friction between MR fluid and solid surface	0.2 [98].
4	Magnetic force density	Positive gradient of magnetic energy. It is taken from principle of conservative force [94].
5	Magnetization of the permanent magnet	Magnetisation equal to 1000 kA/m, was derived from experimental data to match magnetic flux density with experimental data, i.e. 0.6 Tesla on magnet-surface.
6	Workpiece	Incompressible solid body and non-magnetic with μ_r=1.
7	Negligible effect of minor electric field	In this work, the effect of electric field (variable or constant with respect to time) is not studied as the electric field less than 1 kV/mm will neither polarise the MR fluid nor generate magnetic field more than 4 mT. Hence, its effect is insignificant to CMMRF process.

3.2.2. Results and discussion

3.2.2.1. Magnetic field

A finite element analysis is carried out to study about the distribution of magnetic field as per the schematic of Fig.3.1 (b) by solving Gauss's law and constitutive relation of magnetism, and the result is shown in Fig.3.2.

It is observed that the magnetic lines of force flow uniformly within the specified medium and the flow of magnetic lines changes significantly when the medium changes. For better understanding, the magnetic flux density is analysed, and presented in Figs.3.3 (a-b). This result shows that the magnetic flux density increases by introducing MR fluid as shown in Figs. 3.3 (a-b).

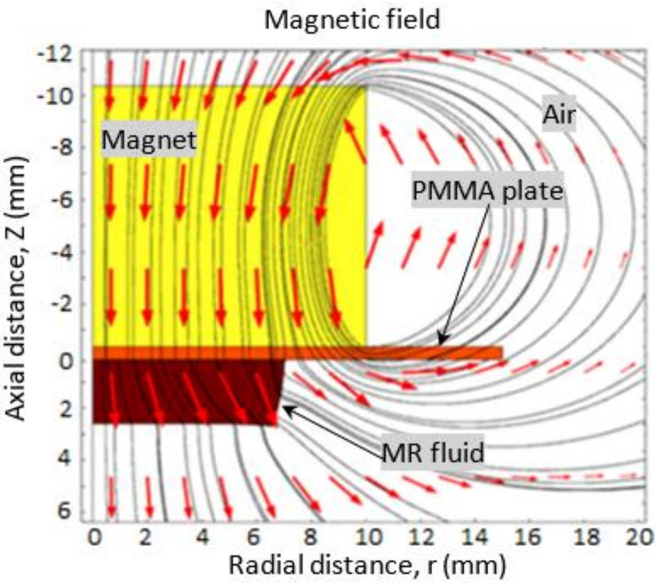

Fig. 3.2: Lines of magnetic flux distribution in which arrows show the direction.

The magnetic flux density increases on the edge of the magnet with respect to the central portion as shown in Fig. 3.3 (a). Fig. 3.3 (b) shows two spikes in which one spike comes from the boundary of MR fluid and other spike comes from the edge of magnet. Further, the magnetic flux density in different cases has been computed and plot as shown in Fig. 3.4.

Fig. 3.4 plots the distribution of magnetic flux density along radial direction at different condition such as, on the surface of PMMA (z=0) plate without MR fluid, on the plate with MR fluid (z=0), within MR fluid at z= 1.5 mm, and on the bottom surface of MR fluid at z=2.5 mm as labelled on Figs. 3.1 and 3.2.

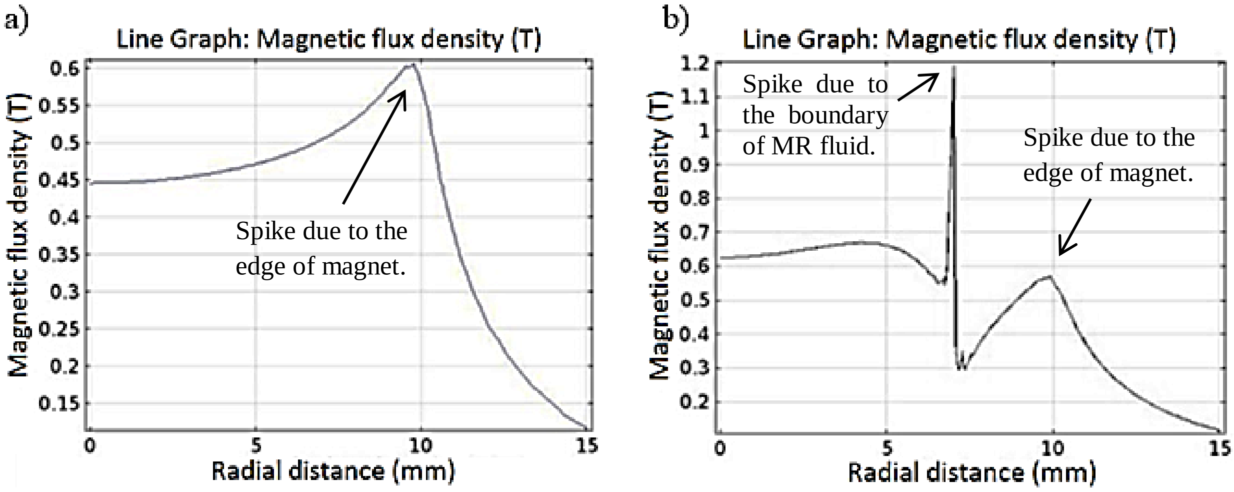

Fig. 3.3: (a) Plot of the magnetic flux density on the surface of PMMA plate (z=0) without MR fluid, (b) Plot of the magnetic flux density on the PMMA surface (z=0) with MR fluid.

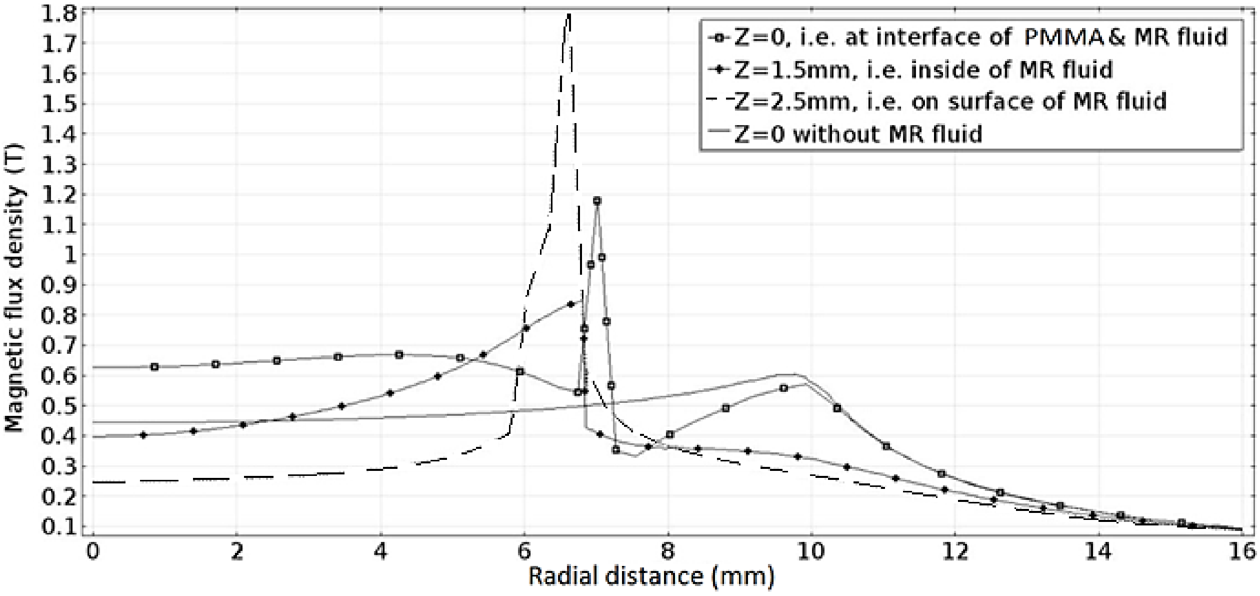

Fig. 3.4: Plot of magnetic flux density at various places of MR fluid.

The magnetic field magnetises MR fluid which further results in inducing the magnetic forces to store the magnetic energy. The magnetic force and the magnetic energy are analysed and discussed as follows.

3.2.2.2. Magnetic force

The distribution of magnetic forces is computed on MR fluid and presented in Fig. 3.5.

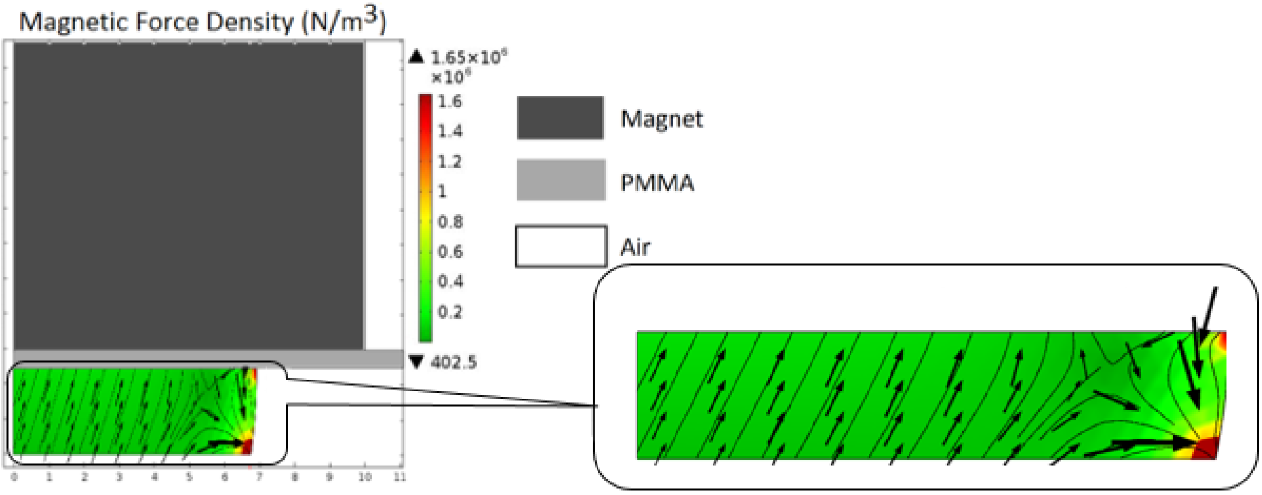

Fig. 3.5: Distribution of magnetic force density in the MR fluid after applying magnetic field at time, *t*=0s. Arrows show the direction of the forces and contour lines indicate their intensity.

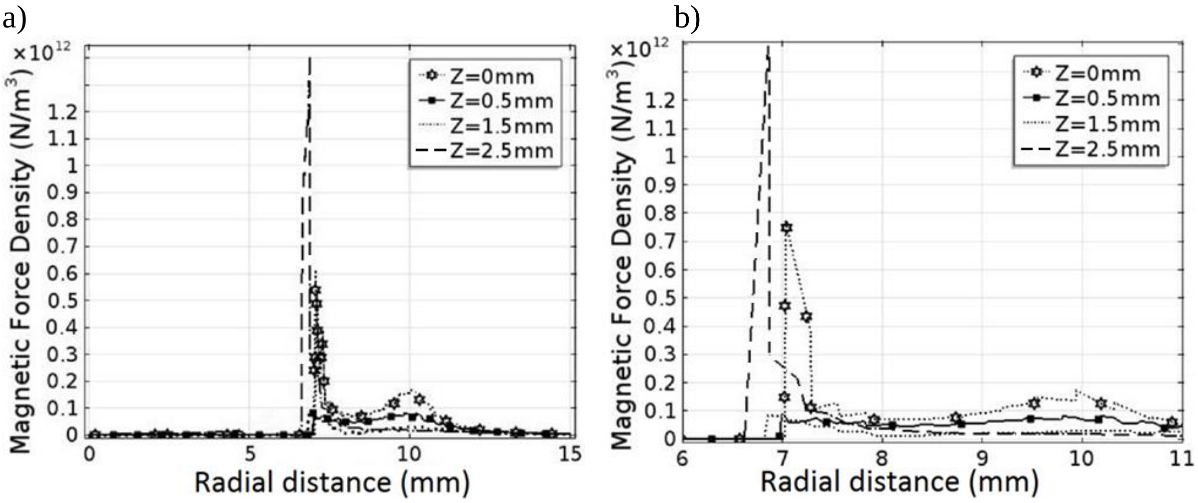

Fig. 3.6: (a) Magnetic force density at the interface of magnet and MR fluid (z=0), surface of MR fluid (z=2.5 mm), inside of MR fluid (z=0.5 &1.5 mm), (b) Zoomed view for the radial distance from 6 to 11 mm.

Force density has been computed and plotted at different z-sections of MR fluid as presented in Figs. 3.6 (a-b). This result shows that the magnetic force density is relatively low except at radial location from 6 mm to 11 mm. It is noticed that the magnetic force is more near the radial location of 7 mm which is an interface of MR fluid and ambient air. At the surface of MR fluid, the magnetic lines of flux come out with greatest degree of divergence which increases the value of magnetic field and its gradient. It causes increased value of magnetic force density at the surface of MR fluid irrespective of ‘z’ as shown in Fig. 3.6 (b). It is also observed that the magnetic force density is comparatively high at the interface of MR fluid and PMMA plate (i.e. z=0) near the edge of magnet as shown in Fig. 3.6 (b), and the magnetic force is comparatively less inside the MR fluid, because of the uniform magnetic flux density which is unable to bring significant value of the gradient in magnetic field.

3.2.2.3. Flow of MR fluid and formation of polishing pad

The magnetic force density as shown in Fig. 3.6 (a) tries to deform the shape of MR fluid, and the deformed MR fluid changes distribution of the magnetic flux which causes further change in the magnetic force density as shown in Figs. 3.7 (a-c).

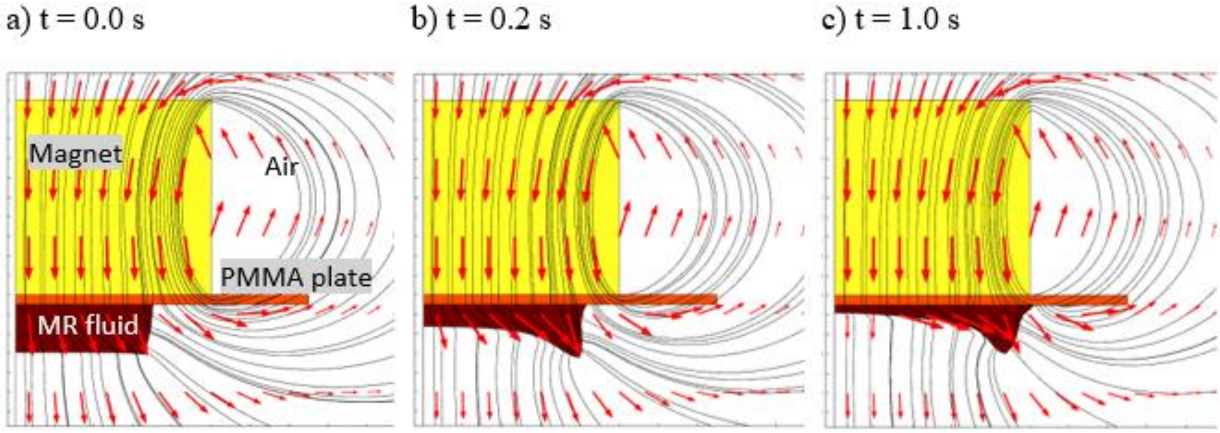

Fig. 3.7: (a) Magnetic flux with direction after applying magnetic field, *t* =0s; (b) Magnetic flux at *t* =0.2s; (c) Magnetic flux at *t* =1.0s, i.e. stable shape of the MR fluid.

When MR fluid deforms by the magnetic force as shown in Figs. 3.7 (b-c), the magnetically stored energy of the MR fluid reduces towards realization of final shape and formation of polishing pad of CMMRF process. To analyse this mechanism, the magnetically stored energy of MR fluid is computed and plotted in Fig. 3.8. It is observed that the MR fluid gets stiffened and forms the pad after some time, as the magnetic energy of MR fluid stabilises within 0.4 second, Fig. 3.8. During this process, the reduction in magnetic energy causes movement of magnetic particle (CIP) which further gets dissipated through frictional or damping energy because of the relative movement between CIPs.

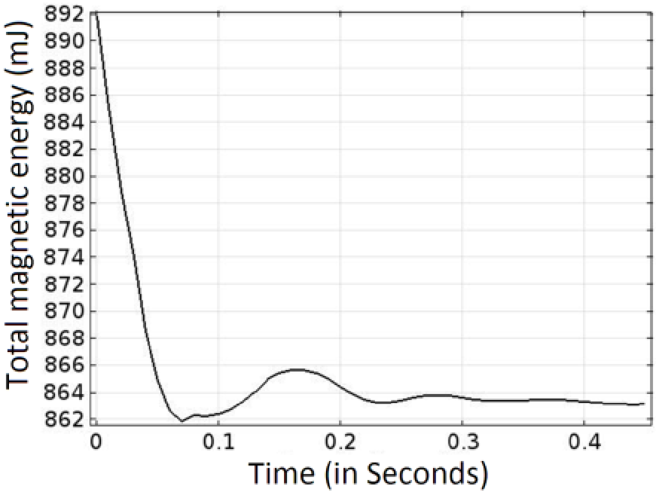

Fig. 3.8: Energy optimization of MR fluid in the range of 0.2-0.4s after introducing magnetic field using a permanent magnet.

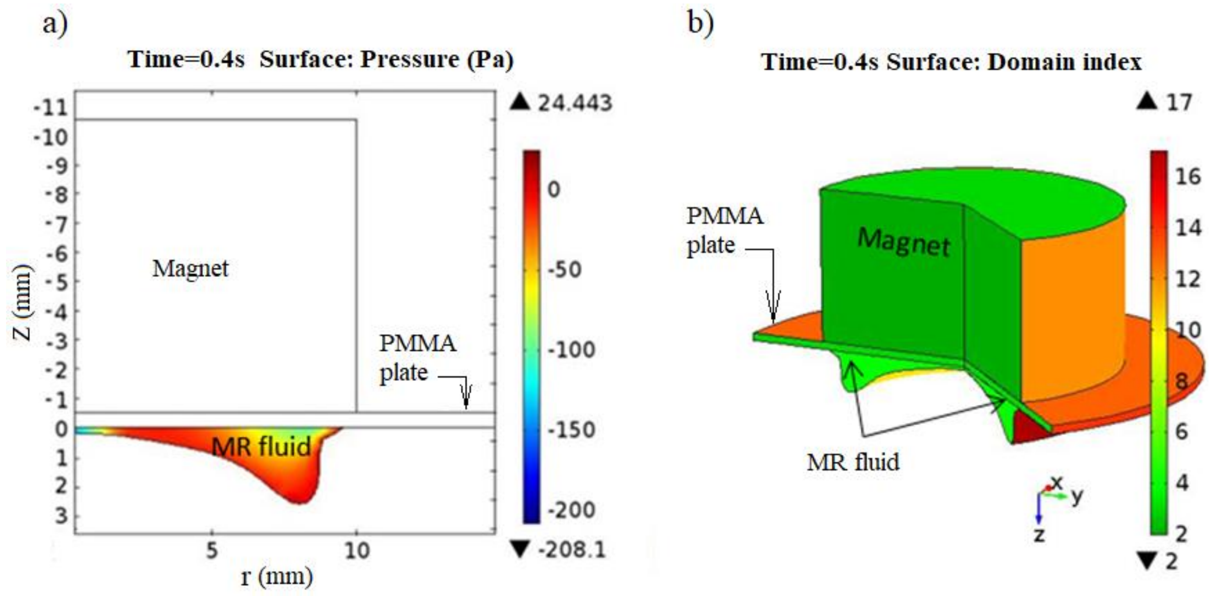

Fig. 3.9: (a) Final shape of MR fluid (in half of 2D model) due to magnetic force after *t* =0.4s, (b) shape of the MR fluid in 3-D.

The final shape of polishing pad is presented in Figs. 3.9 (a-b) which is obtained from FEA-CFD simulation. It shows that the size of polishing pad is comparable with magnet's cross-sectional size, as the magnetic particles of the MR fluid try to align along the region of high magnetic force density which is along the boundaries of magnet.

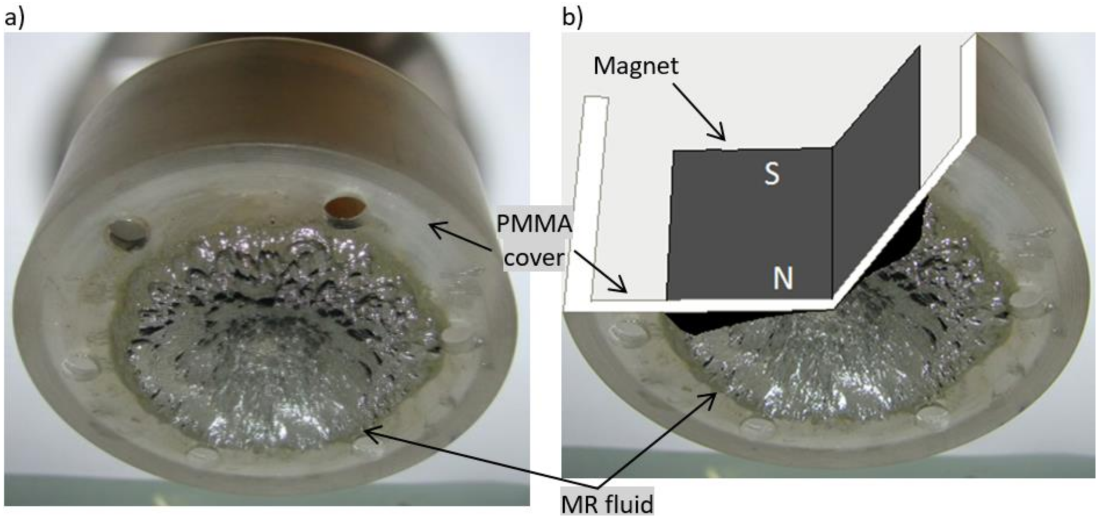

Fig.3.10: (a) Experimentally formed polishing pad of the MR fluid using a permanent magnet, (b) cut section view of the experimentally formed pad to realize shape of the MR fluid under magnetic field.

To validate the simulation in this section, a polishing pad of MR fluid was constructed experimentally and analysed as shown in Figs. 3.10 (a-b) which seems almost similar to the shape of simulated pad. It also shows that the magnetic particles are piling up near the edge of magnet and the polishing pad size is comparable with cross-section of magnet, as shown in the Fig. 3.10 (b). Next step is to analyse the extent of polishing pressure generated by the MR fluid.

3.3. Mechanism to generate polishing pressure

Before attempting the mathematical model formulation, it is necessary to understand mechanism of CMMRF process. Therefore, various aspects of MR fluid for CMMRF process are presented towards development of the mathematical model and schematic for the same is presented in Fig. 3.11. Magnetic field is generated by a permanent magnet and it helps to magnetise CIPs of MR fluid. It subsequently results in the formation of a polishing pad for CMMRF process. Since size of CIPs is of the order of few microns, they form micro-textures on the surface of the polishing pad which is similar to CMP pad [99,100].

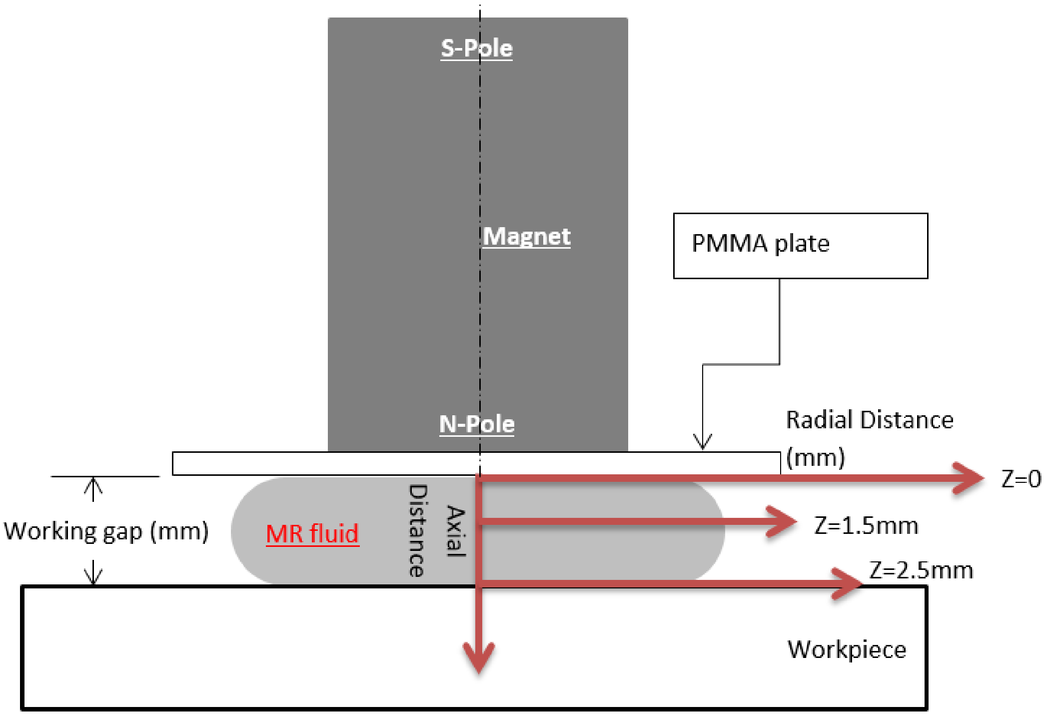

Fig.3.11: Schematic of CMMRF for modelling and simulation of MR fluid.

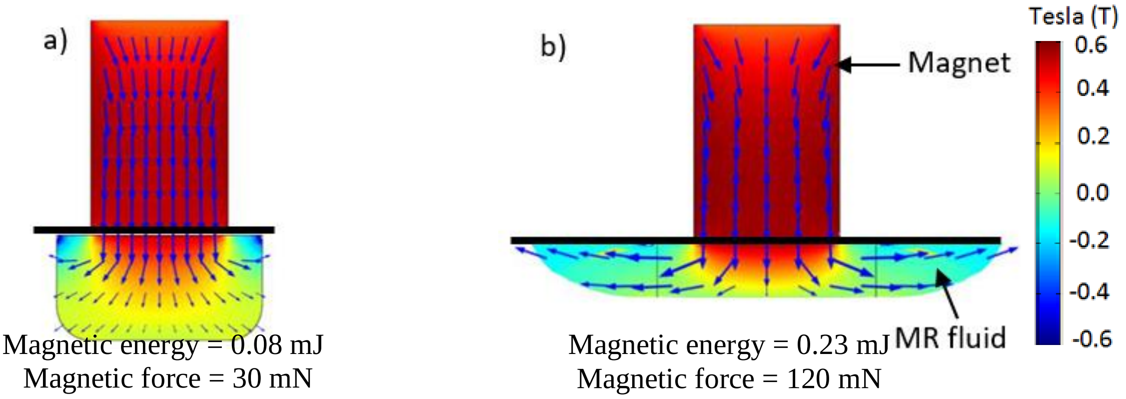

Magnetic energy = 0.08 mJ
Magnetic force = 30 mN

Magnetic energy = 0.23 mJ
Magnetic force = 120 mN

Fig. 3.12: Finite element analysis to understand magnetic field, magnetic force and magnetic energy with varying working gap. (a) Distribution of magnetic field at 15mm of working gap. (b) Distribution of magnetic field at 08mm of working gap.

These micro-textures are used to hold abrasive particles during nanofinishing operation. The abrasive particles acquire force from the magnetic forces of CIPs to abrade ‘chemically passivated layer’ precisely. In general, magnetic force on MR fluid depends on magnetic flux density and its gradient [101]. The magnetic force provides stiffness to the magnetically formed polishing pad.

In view of this, FEA based simulation is carried out to understand magnetic force on the MR fluid by solving Eqs. (3.4-3.5), and the results are presented in Figs.3.12 (a-b). These results show the magnetic force and energy at different working gaps. It has been observed that the magnetic energy increases as the working gap decreases provided the magnetic strength of magnet and volume of MR fluid are unchanged. The reason is that the larger working gap provides more space to stabilise the CIPs magnetically, towards optimal placement of the CIPs and it results in less magnetic energy.

Thus, following phenomena have been identified towards the mathematical modelling.

- The CIPs form chains under the influence of magnetic field because of magnetic lines of force [102] and due to this the magnetic energy gets stored because of the externally applied magnetic field on magnetically susceptible CIPs of the MR fluid [103].

- The stored magnetic energy changes in the MR fluid due to the movement of CIPs chains in the z-direction while squeezing the polishing pad against the work surface. Change in the stored magnetic energy is responsible to develop polishing pressure on the work surface during CMMRF operation.

3.3.1. Mathematical modelling and simulation

Magnetic force gets induced by the magnetic field of a permanent magnet, which is responsible to provide a specific shape to MR fluid as shown in Fig.3.13 (a). This shape is created due to grouping of CIPs along denser magnetic lines of forces [102]. Grouping and alignment of the CIPs towards higher magnetic flux density lead to minimise the magnetic energy, and it forms a magnetically stable pad of MR fluid as shown in Fig. 3.9. When this pad of MR fluid gets squeezed to maintain the working gap as shown in Fig.3.13 (b), the magnetically stored energy of MR fluid increases. Increase in magnetic energy of the MR fluid builds polishing pressure by deforming the shape of magnetically stiffened fluid from Fig.3.13 (a) to Fig.3.13 (b). This polishing pressure has also been measured at different working gap by using a force dynamometer during CMMRF finishing process as shown in Fig.3.14.

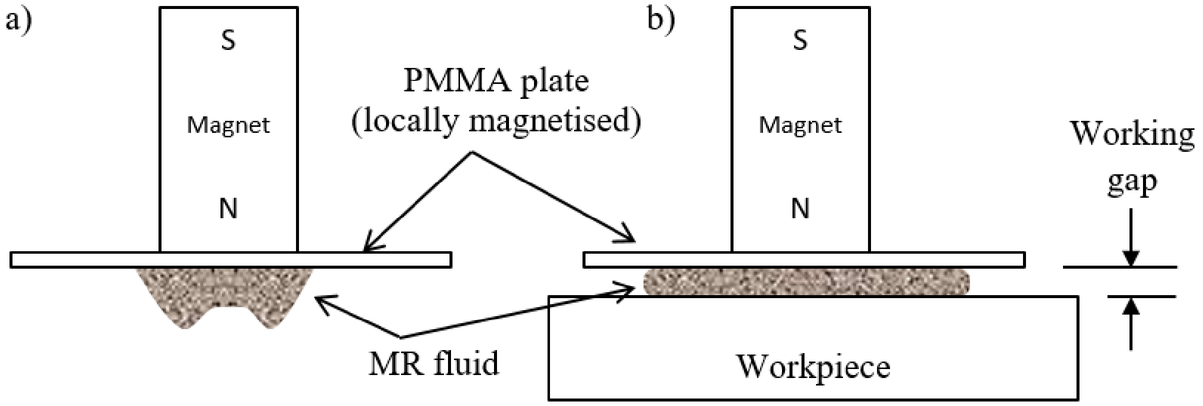

Fig. 3.13: (a) Formation of pad of MR fluid under free condition and (b) formation of pad of MR fluid during working condition at a specified working gap.

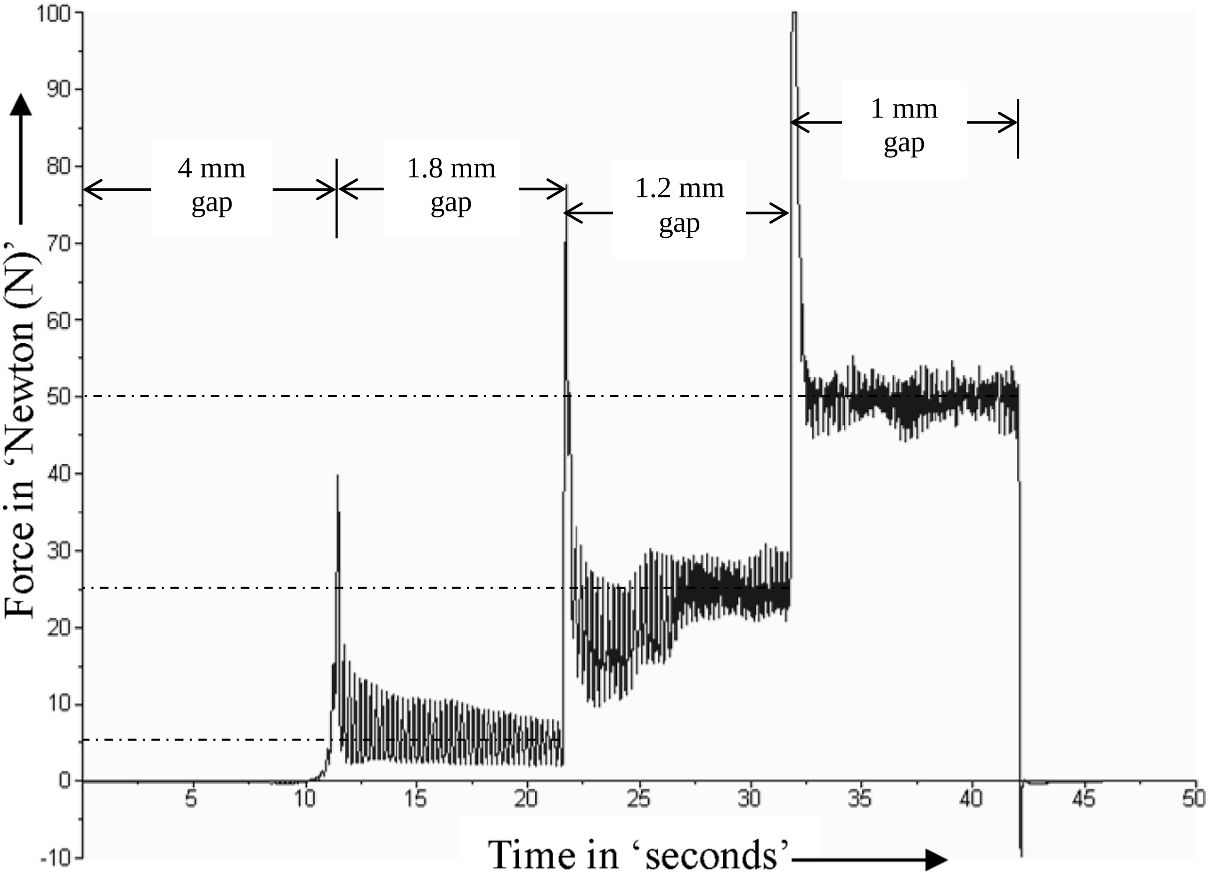

Fig. 3.14: Force due to 0.8 ml of MR fluid at different working gaps.

The working gaps are 4.0 mm for 0–10 s which shows almost zero polishing force, 1.8 mm for 10–22 s which shows 5 N of average polishing force, 1.2 mm for 22–32 s which shows 25N of average polishing force, 1.0 mm for 32–42 s which shows 50N of average polishing force and the process is unloaded after 42 s which shows zero force afterwards.

It is assumed that there is a work-done on MR fluid to squeeze it, which is '*W*', and the stored magnetic energy on the MR fluid is equal to 'ξ'. According to the first law of thermodynamics, heat input can be expressed as algebraic sum of work done and change in internal energy of the system [104] which is considered as MR fluid in the present case. Hence, energy balance equation for MR fluid is expressed as Eq.3.9.

$$\Delta Q = W + \Delta U = W + (C_v \Delta T + \Delta \xi) \tag{3.9}$$

When the working gap decreases, temperature of MR fluid becomes unchanged because of water as a main ingredient of MR fluid. Thus, ΔT = 0 and ΔQ = 0, as no source is added for heat input. Hence, Eq.3.9 is modified as shown in Eq.3.10.

$$0 = W + (0 + \Delta\xi) \implies W = -\Delta\xi \tag{3.10}$$

'W' is further simplified using following equations to compute magnetic polishing pressure (Ps) of MR fluid.

$$\begin{aligned} P_s V = constant \Rightarrow P_s dV + V dP_s = 0 \implies dW + V dP_s = 0 \implies W = -\int_0^{P_s} V dP_s \\ = -V P_s \end{aligned} \tag{3.11}$$

Where, V is the volume of MR fluid with is kept constant by considering MR fluid as an incompressible fluid.

By using Eqs. 3.10 and 3.11, 'Ps' is derived and expressed in Eq. 3.12.

$$P_s = \Delta\xi / V \tag{3.12}$$

Increase in the magnetic energy ($\Delta\xi$) is computed by subtraction of magnetic energy at a specified working gap with respect to the initial equilibrium state of MR fluid. The magnetic energy of MR fluid under the influence of an externally applied magnetic field 'B' is defined and expressed [65,103] as per Eq.3.13.

$$\xi = -M.B = \sum \rho V_{CIP} \chi_m B^2 / \mu_o \tag{3.13}$$

Where, ρ is mass density of MR fluid, V_{CIP} is volume of the magnetic particle, χ_m is the mass susceptibility of the magnetic particle.

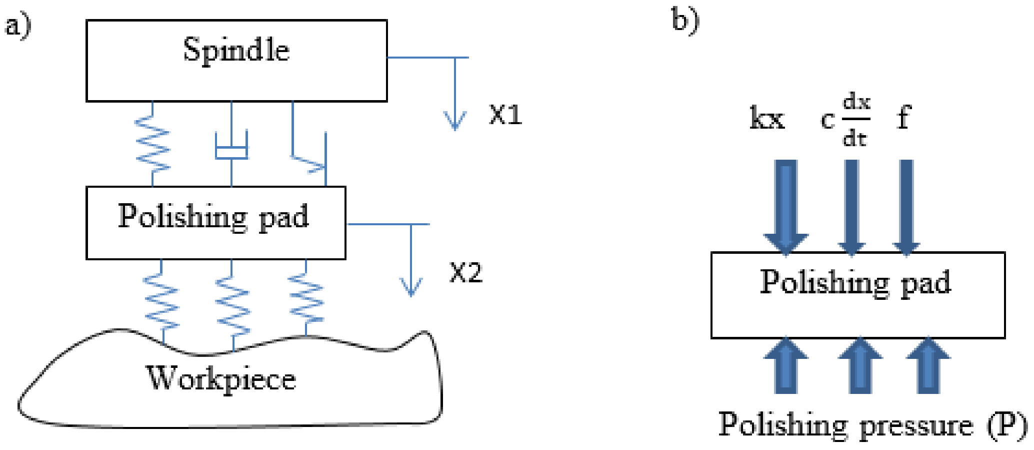

Fig 3.15: a) Model of CMMRF and b) Free body diagram of polishing pad.

Moreover, there are some more forces such as friction force and damping force which are incorporated in the model. For further formulation of polishing pressure to incorporate all forces, a simplified model is presented in Figs.3.15 (a-b).

This model of CMMRF describes that the MR fluid generates pressure by combination of frictional force, damping force and magnetically stored energy. In Fig. 3.15 (a), the displacement *X2* is a linear movement of MR fluid during squeezing it. The value of '*X2*' would be '*X1*' at the top of the polishing pad and it would be 'zero' at the lower region (it is interface of polishing pad and work surface) of the polishing pad. It is assumed that the polishing pad is a flexible element. Thus the following formulation is obtained by using free body diagram of Fig. 3.15 (b).

Using Newton's second law of motion for the polishing pad, Eq.3.14 can be derived.

$$m\frac{d^2x}{dt^2} = PA - kx - c\frac{dx}{dt} - f\ ; Where, \qquad x = X1 - X2 \tag{3.14}$$

After freezing the working gap, acceleration and velocity of the spindle along the axis of rotation would be zero, therefore the Eq.3.14 is modified and expressed as Eq.3.15.

$$0 = PA - kx - 0 - f \Rightarrow P = (kx + f)/A$$

$$\Rightarrow P = Ps + P_f \tag{3.15}$$

Where, Ps is pressure developed due to the magnetic energy which can also be called as spring pressure.

Thus, $Ps = \Delta\xi/V$. Besides, pressure due to friction (P_f) is evaluated by computing the friction force density (f/V) using Kelvin force [105] in Eqs.3.16-3.17.

$$f/V_{CIP} = \frac{\mu\,\rho\,V_{CIP}\chi_m}{\mu_o}\sqrt{\left[\left(B\frac{\partial B}{\partial x}\right)^2 + \left(B\frac{\partial B}{\partial y}\right)^2 + \left(B\frac{\partial B}{\partial z}\right)^2\right]} \tag{3.16}$$

$$P_f = \frac{4\mu\,\rho\,V_{CIP}\chi_m}{\mu_o\,\pi d^2}\sqrt{\left[\left(B\frac{\partial B}{\partial x}\right)^2 + \left(B\frac{\partial B}{\partial y}\right)^2 + \left(B\frac{\partial B}{\partial z}\right)^2\right]} \tag{3.17}$$

Where, μ is the co-efficient of friction between two CIPs, and ‘d’ is the diameter of CIPs.

The mathematical model of polishing pressure is further simulated as per the flow chart of Fig.3.16.

Depth of material removal under a given processing time depends on polishing pressure and shearing force which are key factors for better polishing rate and percentage of change in surface finish ($\%\Delta Ra$). The polishing pressure is continuously monitored and controlled for better surface finish and material removal during the CMP process [58].

Hence, it is essential to identify the key parameters which affect the polishing pressure significantly in CMMRF process. In view of this, the mathematical model (as shown in Eq. 3.15) is simulated as per the flow chart in Fig. 3.16 to investigate the effect of controlling parameters on the polishing pressure. It is found that the two parameters viz. working gap and volume of MR fluid have impact on the polishing pressure significantly as shown in Fig. 3.17.

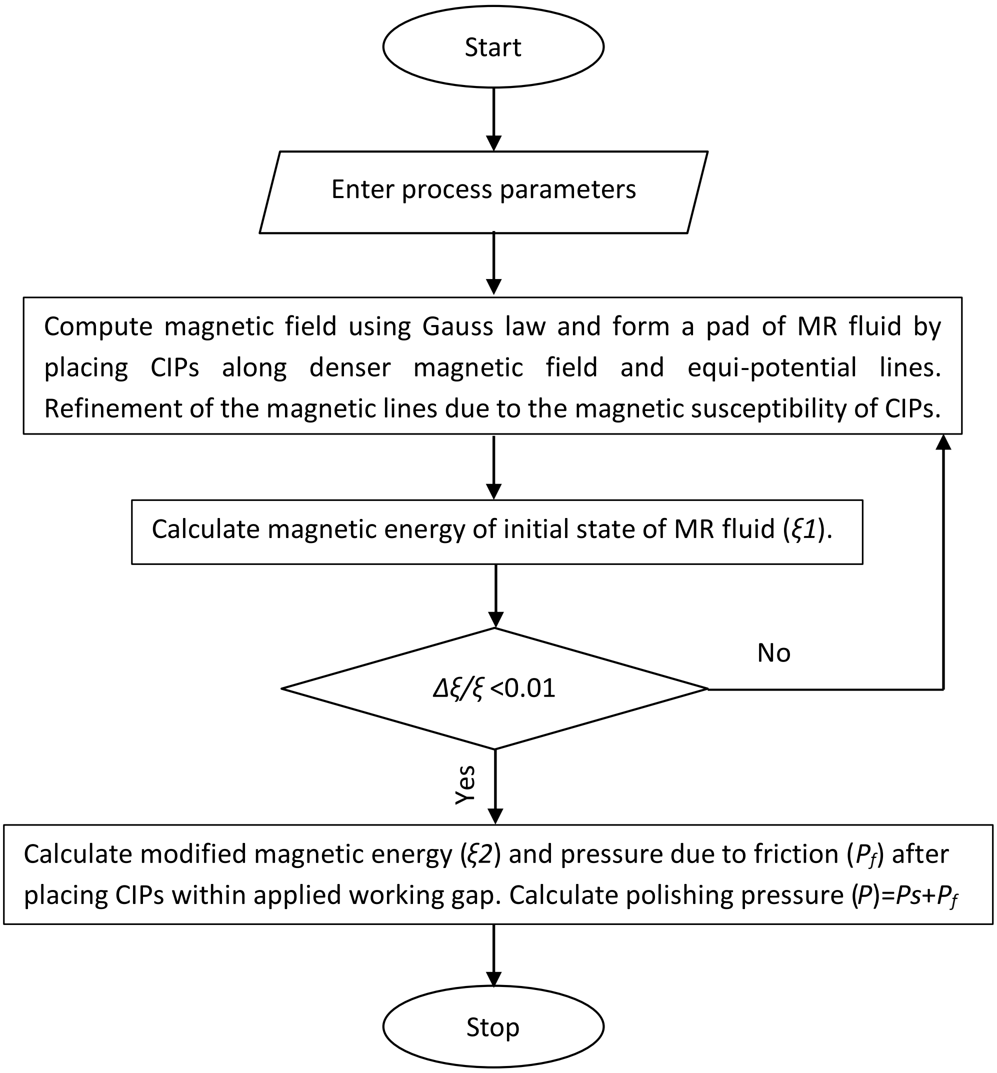

Fig. 3.16: Flow chart for simulation of the polishing pressure.

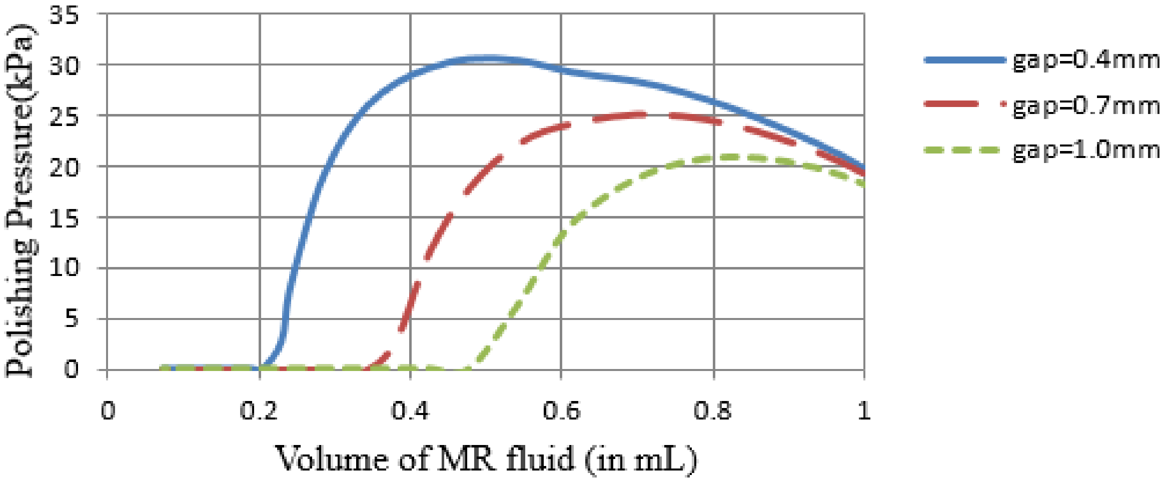

Fig. 3.17: Simulated results on polishing pressure due to the effect of volume of MR fluid at three levels of working gap.

It shows that pressure starts from zero at different value of volume when working gap is varied from 0.4 to 1 mm. The reason is that the lesser value of MR fluid does not fill the gap between PMMA plate and work piece, and due to this pressure does not build unless minimum required volume of MR fluid is applied.

3.3.2. Experimentations

The experimental set-up encompasses 3-axis computer numerical control (CNC)machine, finishing head with magnets, and workpiece as shown schematic in Fig.3.11.

Table 3.2: parameters of polishing pad of CMMRF process

Sr.No.	**Parameters**	**Value**	**Remarks**
1	Diameter of magnetic particles	1-5 µm	Composition (vol/vol): 30% CIPs +5% abrasive + 3% glycine + 2% glycerol + 60%water
2	Diameter of abrasive particles	1-5 µm	
3	Additives to maintain properties of MR fluid	Glycerol and glycine in Deionized water	
4	Rotational speed of magnet	250 rpm	
5	Working gap	0.2-4.5 mm, i.e. 0.28, 0.3, 0.33, 0.35, 0.4, 0.5, 0.8, 1, 1.5, 2, 3, 4, 4.5 mm.	
6	Permanent magnet	Nd-B-Fe, N50	Maximum magnetic flux density = 0.6 Tesla.
7	Volume of MR fluid	0.2-1 ml	
8	Time for CMMRF	15 minutes	

During the experiments, force dynamometer (KISTLER make; Model no. 5070) is used to record axial force (to correlate with polishing pressure). Finishing head consists the magnets (N50 grade) with PMMA plate as per the schematic of Fig.3.1, which is mounted on the spindle of the CNC machine. Parameters for the experiments are listed in Table 3.2. Force obtained during experiments at various working gaps are reported in Table 3.3.

Table 3.3: Axial force (thrust force) recorded with varying ‘working gap’.

Gap (mm)	5		4	3	2	1.5	1	0.8	0.5	0.4	0.35	0.33	0.3	0.28
Force(N)	0		0	2	4	12	50	125	135	210	238	263	275	288

In order to investigate the effect of working gap (or polishing pressure) on nanofinishing of hard brittle materials like silicon carbide (*SiC*) and ductile material like aluminium, a set of preliminary experiments are conducted and results are presented in Table 3.4

Table 3.4: Results of CMMRF for finishing of *SiC* and *Al* with different working gap

Sr. No.	Working gap (mm)	Initial *Ra* (nm)		Final *Ra* (nm)		Improvement of *Ra* (%)	
		SiC	*Al*	*SiC*	*Al*	*SiC*	*Al*
1	0.28	85	120	3	94	96.5	21.7
2	0.3	87	110	4	87	95.4	20.9
3	0.33	84	122	6	96	93.0	21.3
4	0.35	86	117	10	88	88.4	24.8
5	0.4	83	113	30	83	64.0	26.5
6	0.5	85	124	65	72	23.5	41.9
7	0.8	86	108	80	12	7.0	88.9
8	1	84	107	83	6	1.2	94.4
9	1.5	87	113	86	4	1.1	96.5

3.3.3. Results and discussion

To compute pressure, thrust force is measured using the force dynamometer and it is divided by contact area using following expression, pressure = (force x working gap)/volume of MR fluid. The experimental results of Fig. 3.18 show that the trends of the relationship between working gap and pressure are similar to the simulated results shown in Fig. 3.17.

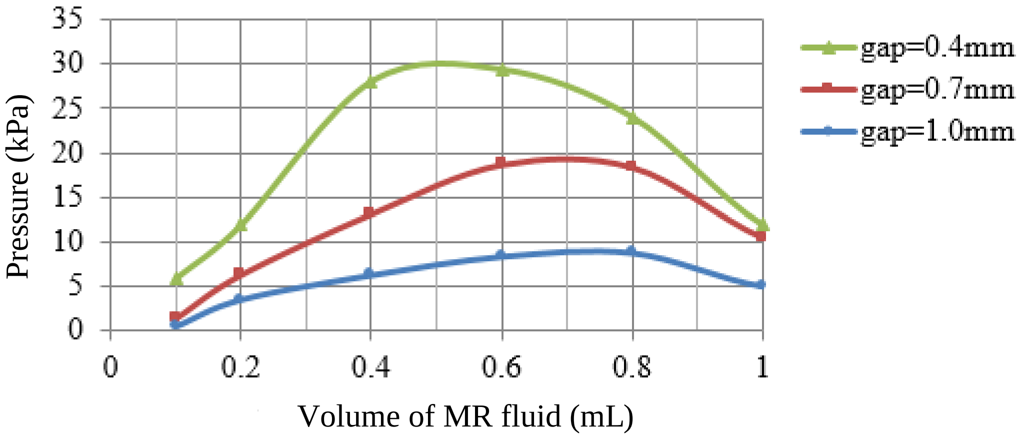

Fig. 3.18: Experimental plot of pressure with respect to the volume of MR fluid at varying working gap, and other finishing parameters are taken from Table 3.2.

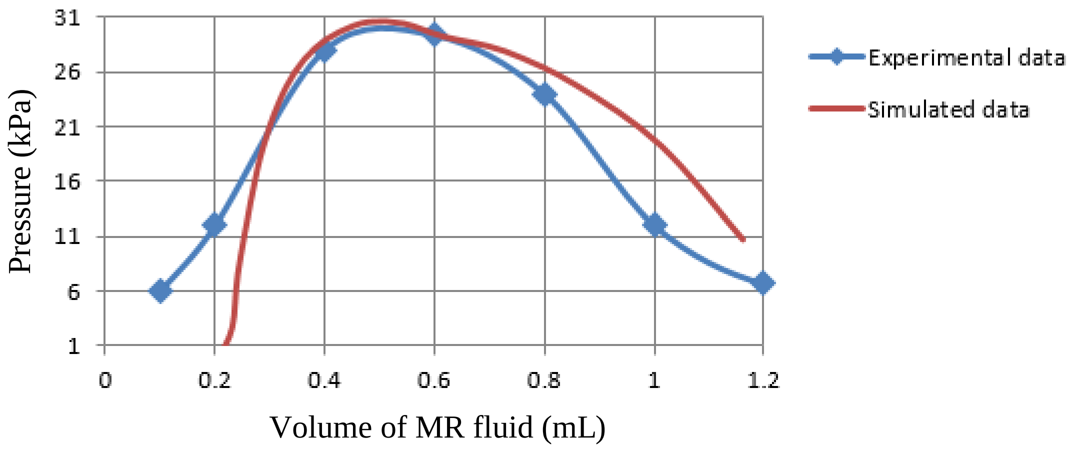

Fig. 3.19: Comparison between simulated and experimental results at working gap =0.4 mm.

3.3.3.1. Effect of volume of MR fluid

Fig. 3.18 shows that higher working gap reduces polishing pressure provided volume of MR fluid is unchanged. Simulated results for the effect of volume of MR fluid are validated at working gap equal to 0.4 mm as shown in Fig. 3.19. As the volume of MR fluid increases, pressure increases upto some extent, thereafter it starts decreasing when the working gap is unchanged. Fig. 3.19 shows that the polishing pressure increases from zero to an optimal pressure which is 30 kPa at a fixed working gap of 0.4 mm and 0.5 ml of MR fluid. Beyond the optimal value, pressure decreases gradually. Building of polishing pressure due to increase in volume of MR fluid happens because of the following two different phenomena.

- 1st phenomenon: When volume of MR fluid increases from zero to the optimal value, MR fluid gets magnetized which induces additional magnetic field as it has 10 times higher permeability compared to ambient air. Magnetisation of MR fluid helps to channelize and concentrate the magnetic flux coming out from magnet and due to this MR fluid experiences more magnetic force by increasing magnetic flux density as shown in Figs. 3.3 (a-b). When volume of MR fluid increases, it tries to cover the whole diameter of magnet at z=0 and it becomes less on the work-surface which forms conical shape of MR fluid. This conical shape acts as a magnetic horn to intensify magnetic flux density as well as magnetic force. At higher volume of MR fluid, the MR fluid turns down into magnetic horn shape and it channelizes maximum magnetic flux towards the surface of workpiece. Due to this, the polishing pressure increases upto a certain value of volume of MR fluid (or, optimum volume of MR fluid).

- 2nd phenomenon: When volume of MR fluid increases beyond the optimal value, shape of MR fluid changes from conical to cylindrical and diameter of the cylinder at the interface with the surface of workpiece increases. This increase in diameter channelizes magnetic flux in large area at the work-surface, which reduces the magnetic flux density by definition such as “magnetic flux density = (flux of magnet)x(working gap)/(volume of MR fluid)”. Thus, higher volume of MR fluid results in the reduction of polishing pressure (Fig. 3.19, beyond 0.5 mL volume of MR fluid).

In general, polishing pressure starts increasing with when volume of MR fluid increases from zero to the optimal value due to the 1st phenomenon, and when the volume increases beyond the optimal value, 2nd phenomenon dominates over 1st phenomenon which results in the reduction of polishing pressure. Hence, it is recommended to use volume of MR fluid near the optimal volume of the MR fluid for higher finishing rate (or higher material removal rate).

There are deviations between simulated and experimental results when Fig. 3.17, Fig. 3.18 and Fig. 3.19 are compared, because of the assumptions made while modelling the process to make it simple and solvable.

3.3.3.2. Effect of working gap

Simulations are carried out to understand the effect of working gap on polishing pressure, and the results are presented in Fig. 3.20. Fig. 3.20 (a) shows that the pressure on the MR fluid occurs by confining it under the influence of magnetic field. The pressure at the interface of

MR fluid and workpiece is called as polishing pressure, and its variation is plotted with respect to radial distance, Fig. 3.20 (b). It shows that there is a peak value near the edge of magnet as the magnetic force density becomes higher at this place.

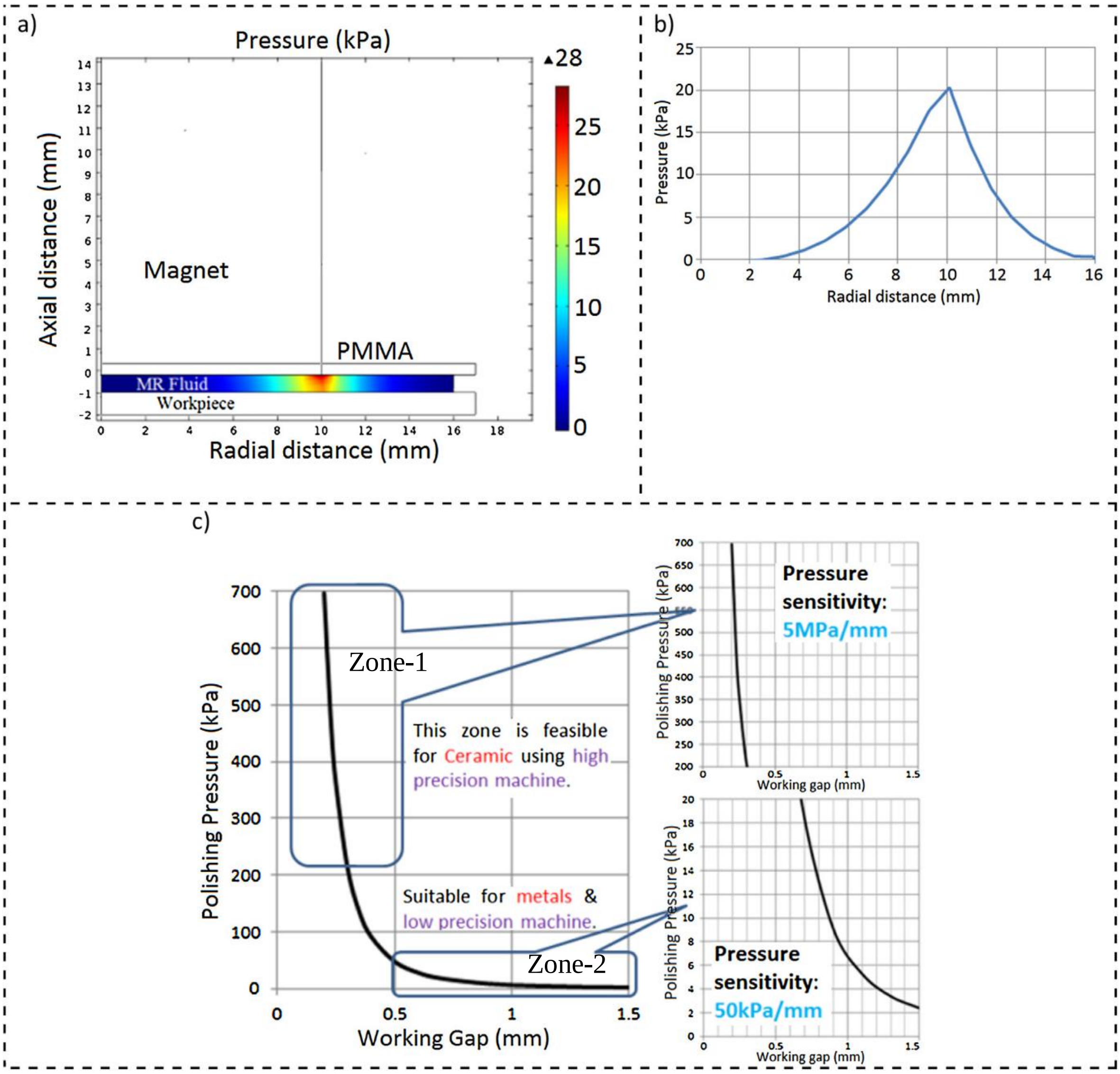

Fig. 3.20: (a) Pressure distribution on MR fluid, (b) Plot for the pressure along radial direction on the work surface at working gap = 0.7 mm, and volume =0.56 ml (c) Characteristic plots of polishing pressure on work surface with varying working gap.

The polishing pressure is also plotted with respect to varying gap as shown in Fig. 3.20 (c) in which two zones are observed to process a wide range of engineering materials through CMMRF process. The 1st zone occurs when working gap is less than 0.5 mm, in which polishing pressure is very high (≈ few hundreds of kPa) and high sensitive to the working gap i.e. of the order of 5MPa/mm. Hence, the 1st zone needs mechanism to maintain the working gap precisely so that the unwanted impact pressure and generation of defects (dig or scratch) on work surface can be avoided. The 2nd zone is when the working gap is more than 0.5 mm, typically 0.5–1.5 mm. Pressure in this zone is less sensitive to the working gap, which is of the order of 50 kPa/mm. The polishing pressure in this zone is one order lesser than the 1st zone. Hence, the 2nd zone can be used with a machine having lesser precision on working gap adjustment mechanism, without any noticeable damage on the surface. The advantages and disadvantages of these zones are presented in Table 3.5.

The polishing pressure varies along radial direction as shown in Fig. 3.20 (b). The simulated polishing pressure is converted into axial force by integrating the pressure on the surface of workpiece. This force is validated with the experimentally measured force (as shown in Table 3.3) as shown in Fig. 3.21, and it shows good agreement.

Table3.5: Characteristics of Zone-1 and Zone-2

Sr. No	**Zone-1**	**Zone-2**
1	Working gap=0.2 to 0.5mm.	Working gap=0.5 to 1.5mm.
2	Polishing pressure=50 to 700 kPa which is suitable to polish hard materials such as ceramics, SiC, Si, SiO_2, Al_2O_3, Glass, etc. [106,107].	Polishing pressure=2 to 50 kPa which is suitable to polish soft & ductile materials such as Cu, Al, Brass, Steel, etc. [106,108–110].
3	Gap sensitivity = 5 MPa/mm. Thus, the control of working gap needs to be precisely maintained, i.e. less than 0.02 mm.	Gap sensitivity = 0.05 MPa/mm. Thus, the control of working gap is not so critical, and it can be maintained upto 0.1 mm or less.

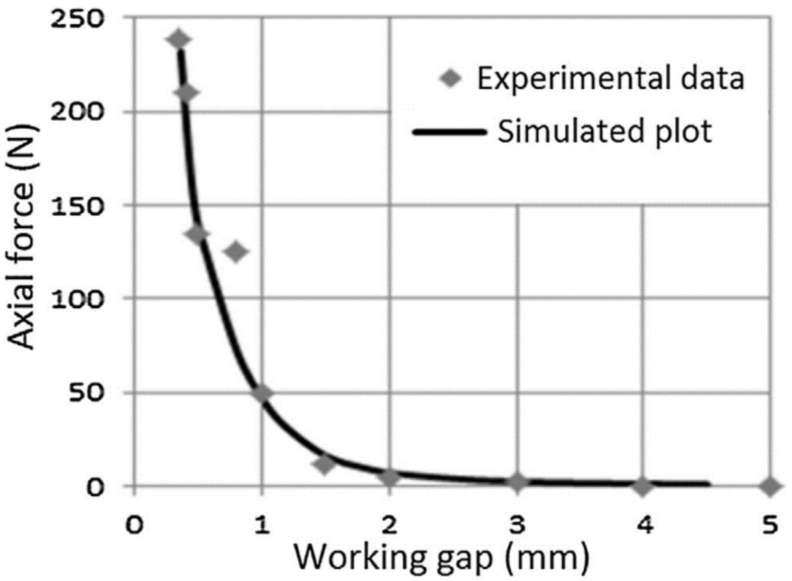

Fig. 3.21: Experimental validation of simulation on MR fluid (Note: simulated pressure in converted into force).

3.3.3.3. Effect of zone-1&2 on surface finish

Table 3.5 reports the effect of working gap into zone-1 and zone-2. In view of this, experimental investigation is carried out on brittle (*SiC*) and ductile (*Al*) materials as results are presented in Fig. 3.22 by plotting the results of Table 3.4. It is found that the zone-1 results better surface finish for *SiC*, and zone-2 for aluminium. While nano-finishing of *SiC* in zone-1, MR fluid applies more polishing pressure which is enough to remove all micro-peaks and valleys on the work-surface. When working gap increases, MRR of workpiece reduces which results in poor surface finish in the given time period as the low polishing pressure requires more time to remove the initial lay pattern of work-surface.

Further increase in working gap brings the nanofinishing process at the zone-2 in which low pressure generates which is unable to remove material from hard and brittle materials like *SiC*. Thus, zone-2 for *SiC* shows low improvement in surface finish, and zero when working gap is more than 1 mm as 1 mm gap builds only 6 kPa of polishing pressure which is insufficient to abrade *SiC*.

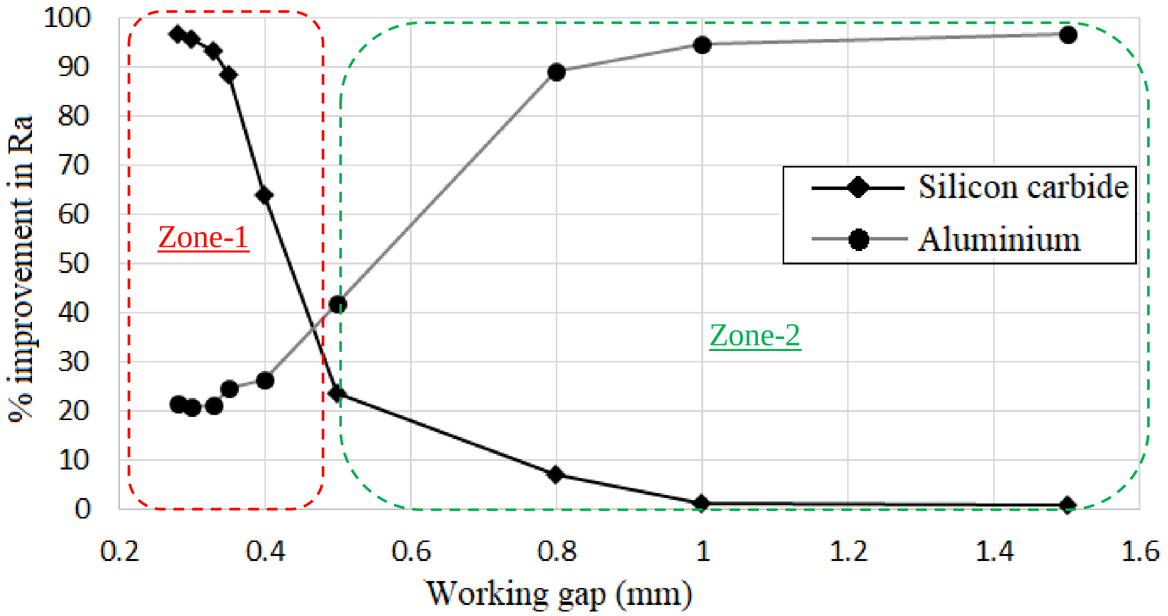

Fig. 3.22: Experimental results for surface finish (*Ra*) on *SiC* and *Al* at different working gap, and other parameters are used from Table 3.2.

In case of aluminium workpiece, zone-1 generates very high polishing pressure which creates deep scratches and results in more roughness. As the working gap reduces from 0.28 to 0.4 mm, scratching of surface does not reduce, and due to this, surface finish does not improve. When, the working gap comes to zone-2 then the extent of surface scratching reduces, and improvement in *Ra* value takes place significantly as shown in zone-2 of Fig. 3.22.

In this result, it is clearly observed that the zone-1 and zone-2 are suitable for the improvement in surface finish on *SiC* and aluminium workpiece, respectively, and thus CMMRF is recommended to use zone-1 for hard or brittle materials and zone-2 for soft or ductile materials.

3.4. Sedimentation behaviour of MR fluid

CMMRF process utilises water based MR fluid with solid particles and chemicals. Density of solid particles is higher (3 to 8 times usually) as compared to the liquid medium and this results in sedimentation under the gravitational force. The sedimentation of MR fluid is another important parameter, which affects the process quality in terms of 'lack of repeatability' during mass production. Hence, it is necessary to identify sedimentation behaviour of the MR fluid under given environmental conditions.

3.4.1. CFD simulation of MR fluid for sedimentation

To investigate the sedimentation phenomenon, CFD based simulation is carried out. Schematic for this simulation is shown in Fig. 3.23. CFD simulation is carried out on three different compositions of fluids as shown in Table 3.6.

Dynamic viscosity of the MR fluid gets affected due to the presence of solid particles, and dynamic viscosity increases with increasing concentration of solid particles [111]. The viscosities of these MR fluids shown in Table 3.6, are calculated and their values are as follows.

- Viscosity of Fluid-1=0.00264 Pa.s,
- Viscosity of Fluid-2=0.0014 Pa.s,
- Viscosity of Fluid-3=0.0009 Pa.s.

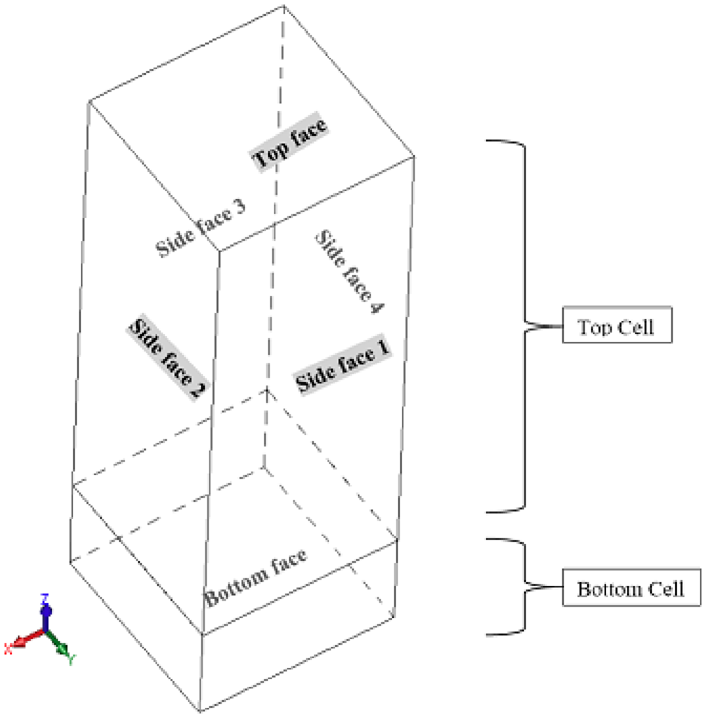

Fig. 3.23: Simulation cell for sedimentation study in MR fluid

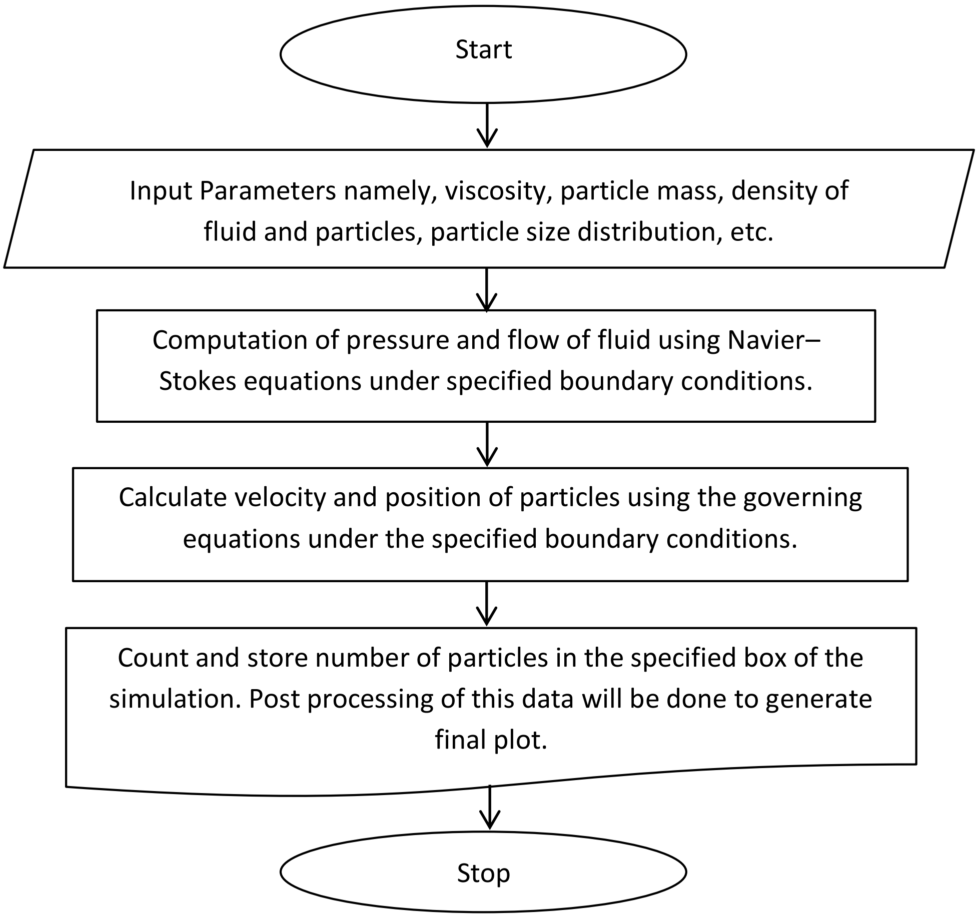

Fig. 3.24: Flow chart for CFD simulation to study about the sedimentation phenomenon in MR fluid.

Table 3.6: Composition (volume/volume) of MR fluid for CFD simulation.

Chemical	**Composition volume/volume**		
	Fluid-1	**Fluid-2**	**Fluid-3**
De-ionised (DI) water	48 %	64 %	72 %
Glycerol	12 %	16 %	18 %
Carbonyl iron particles (CIPs)	40 %	20 %	10 %

3.4.1.1. Governing equation

CFD simulation is carried out for the liquid medium of MR fluid using the Navier–Stokes equations. The solid particles are allowed to move under the influence of various forces which are listed as follow.

1) Gravitational force (Fg)=$m.g$
2) Buoyancy force (Fb) =(ρ_f/ρ_s)$m.g$
3) Drag force due to viscosity (Fvf)=$3\pi\eta d(v\text{-}v_f)$
4) Inertia force (ma)=$m(\partial v/\partial t)$ =$m.g\text{-}(\rho_f/\rho_s)m.g\text{-}3\pi\eta.d(v\text{-}v_f)$ =$(\rho_s\text{ -}\rho_f)g/\rho_s\text{-}3\pi\eta.d(v\text{-}v_f)/m$

Boundary conditions are listed as below.

- All faces namely, face1, face2, face3, face4 & Bottom face have zero velocity along the normal to the face.
- Interaction between particles and side faces (side face 1-4): bounce condition is applied. In the bounce boundary conditions, velocity of the particles after striking the faces becomes equal but opposite in nature along the normal direction as discussed later. Velocity after strike, $V= Vi - 2\,(n.Vi)n$, where, 'Vi' is incidence velocity of the particle and 'n' is normal vector of the face.
- On top face, atmospheric pressure is maintained.
- On bottom face, particles velocity is set to zero.
- For particle-particle interaction, interaction force is set as per Lennard-Jones formulation.

3.4.1.2. Initial conditions for the simulation are listed as follows.

- Fluid velocity =0 and pressure=1atmospheric pressure.
- Particles velocity=0.
- Particle distribution: For the present study, BASF make carbonyl iron particles (CIPs) of HQ grade are selected whose size ranges from 1 to 5 µm. Hence, random distribution of the particles diameter has been set on the scale of 1-5 µm.

CFD simulation to investigate the sedimentation of MR fluid, has been carried out and presented in a flow chart of Fig. 3.24.

3.4.2. Experiments for sedimentation study of MR fluid

In this work, a set of experiments are conducted on different types of MR fluids in which composition of the MR fluids is varied as shown in Table 3.6. These MR fluids are prepared by mixing their ingredients with the help of ball milling operation for 30 minutes as shown in Table 3.6. Thereafter, these fluids are poured in a test tube having a scale of least count of 0.2 mm.

The depth of sedimentation is monitored and measured with time under LASER light by visual means as shown in Fig.3.25. During the sedimentation study, a demarcation line is observed by two different phases in which one phase becomes denser and it becomes optically opaque, but the second phase becomes light and optically transparent. Thus, the demarcation line can be clearly monitored and quantified under the influence of LASER light, as shown in schematic of Fig.3.25.

From the analysis point of view, percentage of sedimentation is calculated which is the change in position of the demarcation with respect to the total change in the demarcation line after 10hrs. Whereas, the initial position of the demarcation line is taken at the top layer of fluid as shown in Fig. 3.25 (a). Fig. 3.25 (b) is a photograph taken on the actual setup of test tube without laser light, and it is difficult to identify layers of demarcation lines. Although, the demarcation lines are clearly visible in case of the effect of LASER light, as shown in Fig. 3.25 (c) of actual test set-up. Results of the sedimentation are presented with varying time as shown in Table A1 of Appendix.

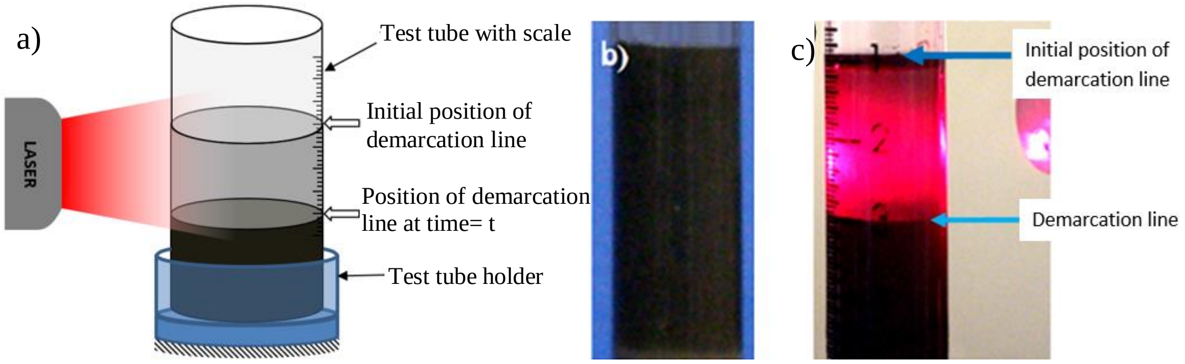

Fig. 3.25: (a) Schematic for measurement of sedimentation depth under 650 nm and 5 mW laser. (b) Snap-shot of the test tube without laser light. (c) Actual photograph of test tube under laser light.

3.4.3. Results and discussion for the sedimentation of MR fluid

CFD simulation and experimentation are conducted to study the sedimentation behaviour on different types of MR fluid such as fluid-1, 2, and 3 of Table 3.6.

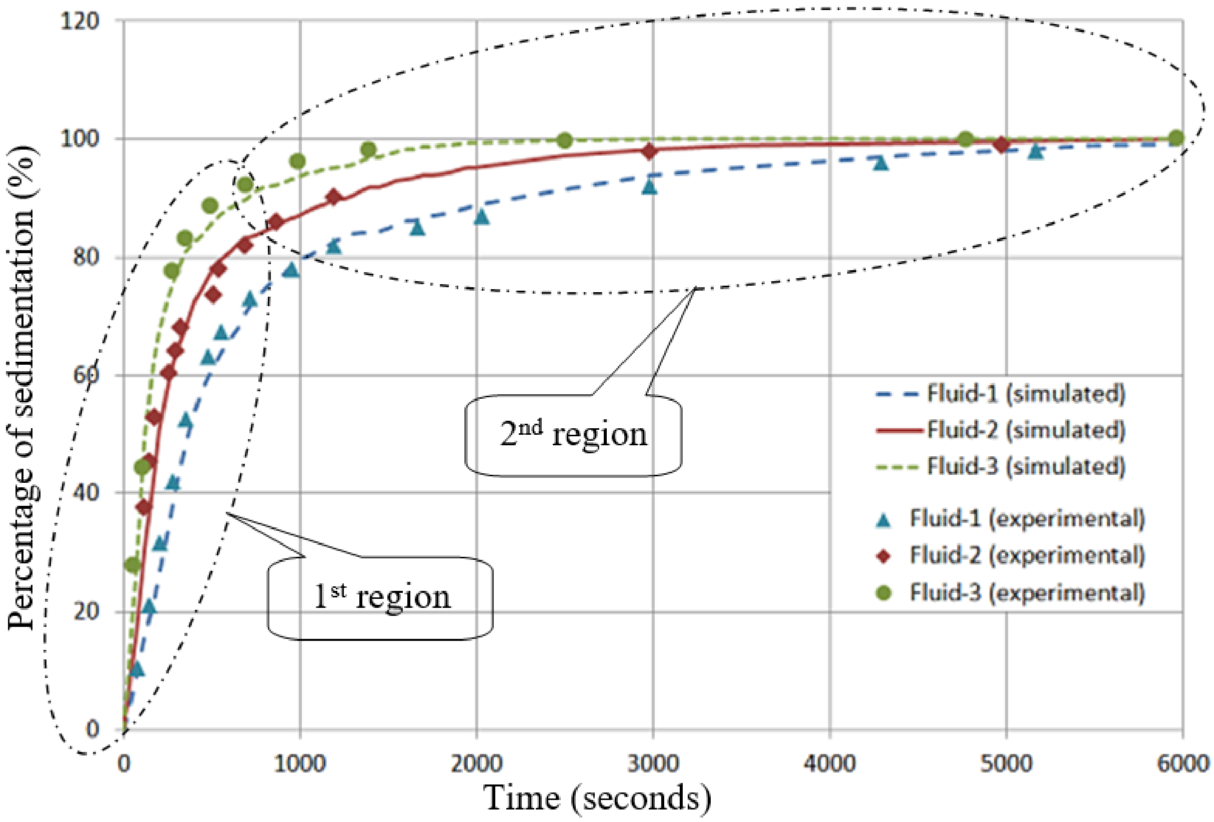

Fig. 3.26: Plot of CFD simulated results for the percentage of sedimentation with respect to time for MR fluid-1, 2, and 3, and also compared with experimental data.

Results of Table A1 are plotted in Fig. 3.26 which shows the sedimentation behaviour of solid particles such as micron size iron particles in the liquid medium (mixture of water and glycerine). In this figure, the simulated results are compared with experimental data points plotted together for the sake of validation.

It is seen that the sedimentation is faster in case of fluid-3 which contains least quantity of solid particles (10% of iron particles as shown in Table 2) as compared to fluid-1 and 2. When the percentage of iron particles increases by changing the MR fluid from the fluid-3 to fluid-1, the percentage of sedimentation reduces. Behaviour of the change in sedimentation occurs due to a change in dynamic viscosity by altering the concentration of solid particles in the mixture as per 'Frankel-Acrivos' equation [111]. After initial sedimentation time (which is 1000 s in present case), the particles concentration increases at the bottom and leads to an increase in dynamic viscosity as per the Frankel-Acrivos equation. Hence, the 2nd region indicates slow sedimentation as shown in Fig. 3.25, and the behaviour of sedimentation is categorised in two regions.

In the 1st region (time from 0 to 1000 s as shown in Fig. 3.26), particles settled down fast. Whereas, the particles sediment comparatively slows down in the 2nd region (time beyond 1st region or more than 1000 s), which is varying almost linearly with time.

Figs. 3.27 (a-c) show the particles sedimentation with varying time, t=0s, 500s and 1500s. The trajectories of the particles are shown in Fig. 3.27 (d) in which it is clearly seen that the smaller particles (1μm diameter which is represented by black colour) travel less distance compared to other particles. Hence, it can be stated that the sedimentation occurs mainly due to the gravitational force on the solid particles and opposed by viscous force which depends on surface area.

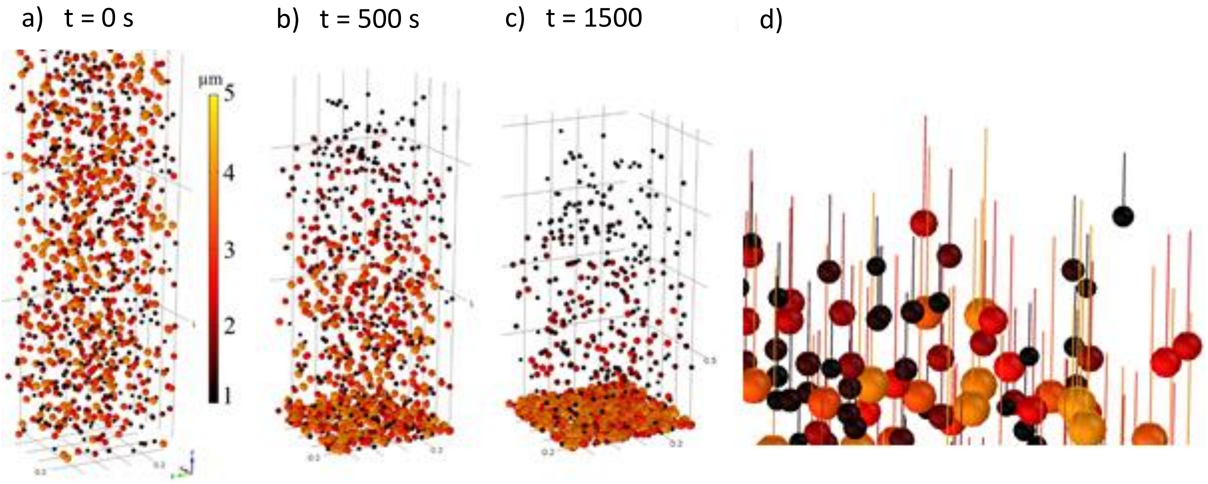

Fig. 3.27: (a-c) Particles sedimentation with varying time generated by CFD simulation. (d) Trajectories of particles tracing.

Few different types of forces are perceived to affect the behaviour of sedimentation, which are gravitational force (F_g), buoyancy force (F_b), inter-atomic force between solid and liquid phase (F_{IAF}) and viscous force within the liquid phase (F_{VF}). Here, F_g assists for sedimentation, and remaining forces oppose the sedimentation.

The buoyancy force depends on density of liquid medium and volume of the solid particles and it is 1 to 2 orders smaller with respect to the gravitational force, as density of solid particles becomes 1 to 2 order higher than the liquid phase in the MR fluid. This drastic change in density is responsible for the particles agglomeration and sedimentation.

The inter-atomic force is used to link the surface of solid phase and helps to maintain continuity against the density variation, which can be either ionic force or secondary force. This force helps to transfer the gravitational force to neighbouring molecules of liquid, and the viscous force gets induced as per viscosity force of Stokes's law. The viscous force becomes inversely proportional to the square of size of the particle ($1/r^2$) as compared to the gravitational force. Therefore, the viscous force dominates over the gravitational force when the size of the particles reduces, and the sedimentation rate becomes negligible in case of nano-particles suspended fluid [112].

3.5. Synthesis of MR fluid

To synthesize water based MR fluid, suitable chemical reactions are studied and analysed using QC modelling for physically and chemically stable fluid.

3.5.1. Quantum chemical (QC) modelling and simulation of MR fluid

In CMMRF process, volume of magnetic particles becomes almost six times higher with respect to abrasive particles [113] in the mixture of solid particles. Mass density of abrasive particles including alumina and silica particles are approximately half of iron particles. Thus, the weight contribution of abrasive particles is approximately 6-10 % which is very small. Hence, the present modelling work is simplified, and it is assumed that the main content of solid particles is CIPs which are responsible for the quality (in terms of physical stability) of MR fluid. Surfactants is another important ingredient of the liquid medium which improves agglomeration and sedimentation of the particles. In view of this, density functional theory (DFT) based quantum-chemical modelling and simulation is carried out to investigate the chemical reaction towards synthesis of chemically and physically stable water-based MR fluid for CMMRF application.

QC modelling has been carried out with the help of orbital method of density functional theory (DFT) using ORCA 3.0.3 program [114].

The density functional theory is derived from 'Z' particles Schrödinger equation (as shown in Eq.3.18) and it is entirely expressed in terms of the density distribution of the ground state $\rho_{GS}(r)$ and the single particle wave function φ_j.

$$H\psi = E\psi \tag{3.18}$$
$$\text{where, } \psi = \phi_1(\overrightarrow{r_1})\phi_2(\overrightarrow{r_2}) \ldots\ldots \phi_Z(\overrightarrow{r_Z})$$

Where, 'H' is Hamiltonian operator, 'ψ' is the wave function, and 'E' is energy Eigen value or proportionality constant.

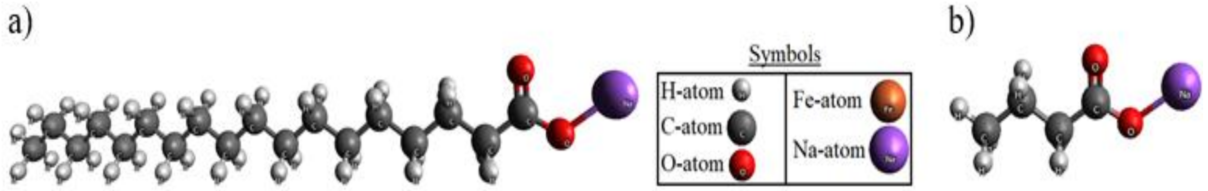

Fig.3.28: (a) Atomic model of sodium stearate; (b) Small cut-portion of sodium stearate to study the quantum chemical calculation.

Time-independent Schrödinger equation: The Schrödinger equation is known as a fundamental equation to describe quantum mechanical behaviour of atoms/molecules. In this formulation, kinetic and potential energies are transformed into a Hamiltonian operator (H) which acts as a wave-function to generate the evolution of the wave function, as shown in Eq.3.18.

Simulation: Unrestricted 'Becke, three-parameters, Lee-Yang-Parr' (B3LYP) functional, optimized with basis sets: SVP def2 and auxiliary basis sets: SVP/J level to understand chemical interaction between *Fe*-atom (from CIPs) and 'sodium stearate' as a surfactant of the MR fluid. Orbit of each electron is optimised in the field of all other electrons through a self-consistent field (SCF) technique.

The molecule structure for the present calculation is constructed using Avogardo software [116], which is obtained after geometry optimization under universal force field (UFF) [115] using algorithm of 'steepest descent'. To reduce computation effort, sodium stearate chain is reduced, as shown in Fig.3.28 (b). Although, Fig.3.28 (a) shows the complete chain.

During the QC simulation, distance between *Fe*-atom and *O*-atom of sodium stearate is varied by scanning it from 5.0 Å to 1.7 Å. Results are analysed with suitable post processing and discussed in the section of 'results and discussion'.

3.5.2. Results and discussion

In the present case of MR fluid, micro-particles are used in which size of the particles is distributed in the range of 1 to 5 μm for better magnetic susceptibility of the fluid. The interatomic force (F_{IAF}) between solid particles and liquid phase can be increased by applying nano-coating over the solid particles with low density materials towards mitigation of the drastic variation in the mass density [117,118]. Moreover, nano-coated solid particles can be inter-linked through a long hydrocarbon chain so that the change in density from liquid phase to solid phase can be varied gradually, and particles sedimentation can be avoided. To apply nano-coating and linking of solid particles, sodium stearate compound has been used, and the mechanism of nano-coating over the CIP surface is analysed using a density functional theory (DFT).

For DFT calculations, distance between *Fe*-atom and *O*-atom of sodium stearate is scanned from 5.0 Å to 1.7 Å to compute interaction energy by optimising molecular geometry, and plotted as shown in Fig. 3.29.

Fig. 3.29 shows that the interaction energy varies as sodium stearate comes near to iron hydroxide. Chemical interactions during this process happen because of some phenomenon as follows;

1) Formation of hydrogen bond (*H*-bond): When *Fe-O* interatomic distance between Fe-atom of iron hydroxide and *O*-atom of sodium stearate decrease from 5.0 Å to 4.0 Å, *H*-bond gets formed as shown by yellow dotted line in Fig.3.29, and energy reduces by 0.6 eV. Likewise, structure of these two molecules becomes more stable with the *H*-bond as the *Fe-O* distance changes from 4.0 Å to 3.5 Å, as energy reduces further by 0.25eV. Hence, sodium stearate is suitable to build *H*-bond when it is mixed with iron particle and water, and the mixture gets stabilised as energy reduces by 0.85 eV (0.6+0.25 eV) without any noticeable extent of the required activation energy.
2) Bond breaking: *Na-O* bond of sodium stearate breaks when the *Fe-O* bond length decreases from 3.5 Å to 2.8 Å. In this process, the *Na-O* bond dissociation requires an

activation energy equal to 0.2 eV. This activation energy can be achieved by applying warm water for chemical dissociation as the warm water carries 0.22 eV energy at 80 ^{O}C (0.1907 eV for *H*-bond + 0.0304 eV equivalent for 80 ^{O}C temperature = 0.22 eV) [119].

3) New ionic bond formation: After gaining the required activation energy, a new chemical reaction occurs in which *Fe*-atom gets bonded with *O*-atom of the sodium stearate. During this activity, the molecules energy reduces by 1.1eV as shown in Fig. 3.29 and the interatomic distance reduces from 2.8 Å to 2 Å, which causes stable chemical bond formation between *Fe*-surface and carboxylate ion. At this stable condition, the equilibrium length of *Fe-O* bond is equal to 2.05 Å.
4) Repulsive interaction of *Fe-O* bond: Once a stable chemical bond establishes between *Fe*-atom of the iron hydroxide and *O*-atom of sodium stearate, further reduction in the interatomic bond of *Fe-O* results a repulsive force because of 'Pauli Exclusion Principle' as shown in Fig. 3.29.

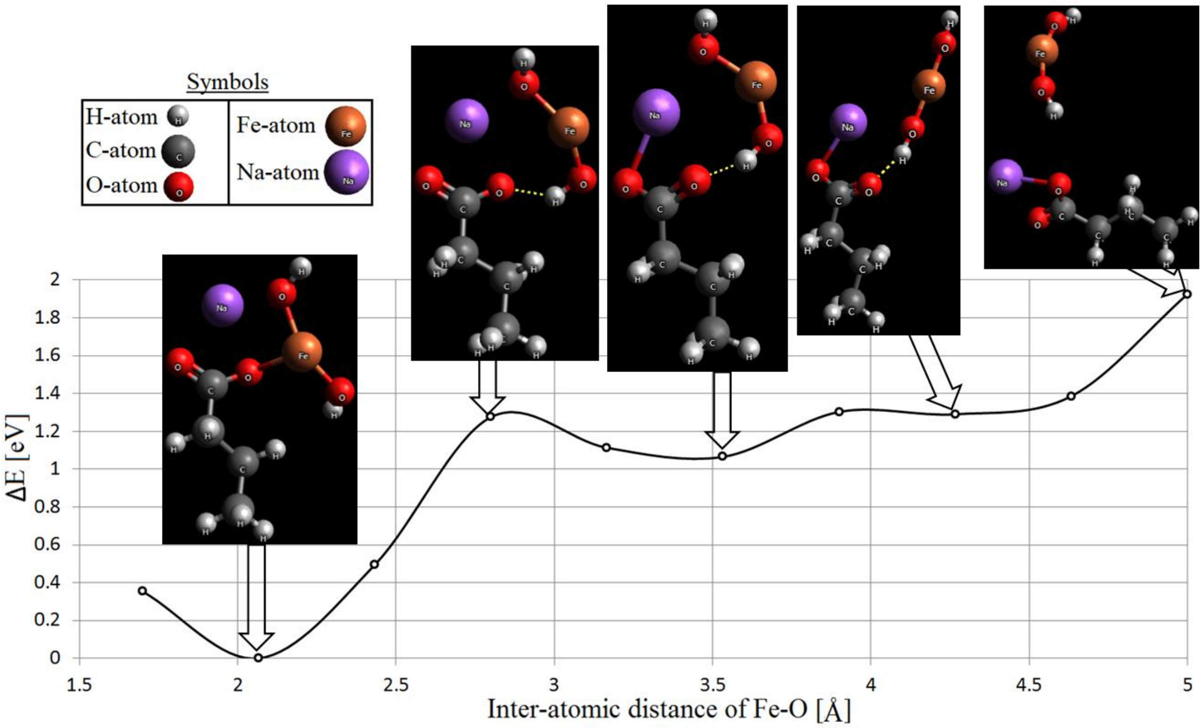

Fig.3.29: Variation in the change of interaction energy with respect to the inter-atomic distance between *Fe*-atom of CIP and *O*-atom of sodium stearate.

Based on these quantum chemical investigations, chemical reaction between sodium stearate and CIPs has been derived and discussed as follows.

When sodium stearate gets dissolved in water, carboxylate anions and sodium cations are produced as shown in Eq. 3.19.

$$CH_3(CH_2)_{16}COO^-Na^+ + H_2O \rightarrow CH_3(CH_2)_{16}COO^-(\mathrm{aq}) + Na^+(\mathrm{aq}) \tag{3.19}$$

Fe-atoms from CIPs also have tendency to form Fe^{2+} species when it comes in contact of water. The metal ions like Na^+ or Fe^{2+} form iron-stearate, when they come near to carboxylate anions, because, iron-stearate compound is more stable than sodium stearate as discussed previously. Hence, the sodium stearate will get transformed into iron stearate on the surface of carbonyl iron particles under the presence of warm water as shown in Eq. 3.20 and 3.21.

$$2CH_3(CH_2)_{16}COO^-Na^+ + 2H_2O + Fe^{2+} \rightarrow [CH_3(CH_2)_{16}COO^-]_2Fe^{2+} + 2H_2O + 2Na^+ \tag{3.20}$$

$$[CH_3(CH_2)_{16}COO^-]_2Fe^{2+} + 4H_2O + 2Na^+ \rightarrow [CH_3(CH_2)_{16}COO\text{-}]_2Fe^{2+} + 2H_3O^+ + 2NaOH \tag{3.21}$$

These chemical reactions help for the nano-coating over the iron micro-particles using carboxylate anions, and it is described in a simple schematic in Fig. 3.30. In general, length of the carboxylate becomes 2.44 nm (this is obtained by the geometry optimization using an universal force field (UFF) algorithm [115]) which is responsible for the nano-coating over the micro particle of CIPs as shown in Fig. 3.30.

Moreover, glycerol is also added in this slurry to link the nano-coated layer with base liquid medium using hydrogen bonds by connecting free carboxylate ion with nano-coated CIPs. This phenomenon results in multiple layering of carboxylate ions by using hydrogen bond which is weaker as compared to Fe- carboxylate ionic bond.

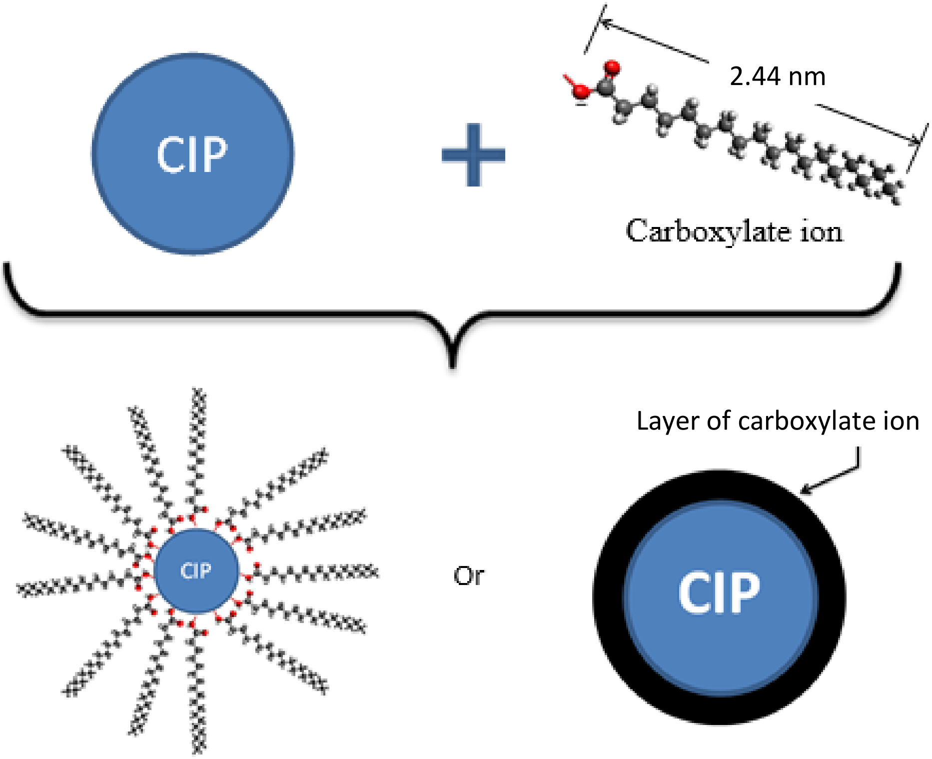

Fig. 3.30: Chemical interaction between CIPs and sodium stearate in water medium.

Hence, a model of CIPs has been made and presented in Fig. 3.31 (a-b). This model shows a single layer and multi-layers of nano-coating over CIPs, which reduces the packing factor of CIPs towards mitigation of particles agglomeration as well as particles sedimentation.

The MR fluid-4 is now prepared by stirring sodium stearate (8%) with water (80%), glycerol (2%) and iron particles (10%) at temperature equal to 80 ^{O}C till 30 minutes for homogeneous mixing. Subsequently, the synthesised MR fluid is cooled down upto room temperature in ambient air.

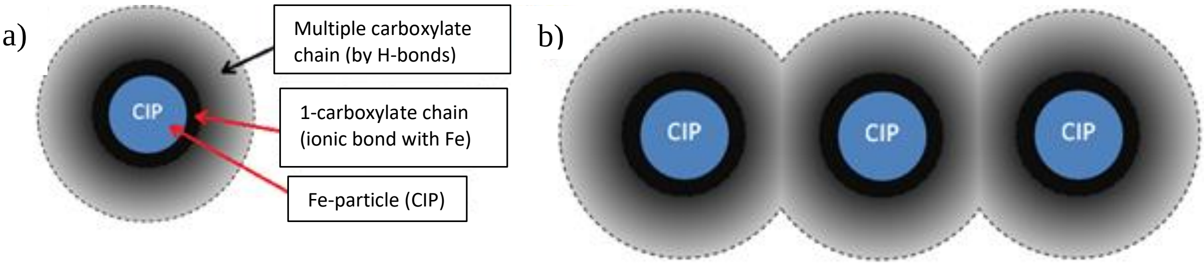

Fig. 3.31: (a) Model of iron particle with sodium stearate. (b) Model to link multiple iron particles using sodium stearate and *H*-bond.

The fluid-4 is placed on test tube for the sedimentation study, and continuously monitored upto 10 hrs under laser light, in which the demarcation line of sedimentation was not detected. Thus, it is identified that the fluid-4 shows extremely low sedimentation, as sodium stearate improves physical stability of the MR fluid against sedimentation. Hence, water based MR fluid for CMMRF and other applications can be synthesised by using sodium stearate and glycerol at warm condition (80 ^{O}C).

3.6. Summary

In this chapter, few different types of modelling and simulation techniques have been carried out to gain better understanding of polishing pad for CMMRF process. Significant outcomes of this chapter are summarised as follows.

- Lines of magnetic field and its gradient apply magnetic force on MR fluid which helps to store magnetic energy in the MR fluid. Magnetic force depends on magnetic properties of MR fluid, magnetic field strength, and gradient of magnetic field strength. Magnetic force creates chains of CIPs and provide a new shape to MR fluid.
- In fraction of a second (<1 s), the magnetic energy gets saturated and builds a characteristic shape to the MR fluid, by re-arrangement of CIPs chain governed by the magnetic force towards formation of polishing pad. Size of polishing pad depends on the physical spread of boundaries or corners of permanent magnet.
- During CMMRF operation, MR fluid applies polishing pressure on the work surface. At fixed working gap, polishing pressure increases with volume of MR fluid till optimal polishing pressure, and thereafter, the polishing pressure starts decreasing. Hence, the polishing pressure cannot be achieved beyond the optimal pressure at a specific working gap.

- Working gap is more sensitive parameter for the polishing pressure as the polishing pressure decreases exponentially when working gap increases.
- CMMRF process has two zones of operation as far as polishing pressure is concerned. These two zones have been identified to process a wide range of engineering materials. Wherein, hard and brittle materials are suitable to process in zone1 which needs high precision machine to maintain consistent working gap with the tolerance level of the order of ±20 μm or better. Zone 2 is identified to process ductile and malleable materials in which machine accuracy and precision are not so critical, in which working gap need to be maintained within ±0.1 mm of the tolerance level.
- Rate of sedimentation is another parameter of MR fluid, which is inversely proportional to the concentration of solid phase in MR fluid. Sedimentation shows two regions, in the 1st region, the solid particles settle down fast during initial phase of sedimentation. The 2nd region shows very slow sedimentation.
- DFT based simulation shows that sodium stearate reacts chemically over the *Fe*-atoms of CIPs to form a layer of few nano-meters. In addition, hydrogen bonds are used for multi-layer nano-coating over the CIPs by incorporating sodium stearate with glycerol at warm temperature of water to mitigates sedimentation of the MR fluid. Based on this result, MR fluid is synthesised and used for further experiments.

-----------x-----------

Chapter-4

MOLECULAR DYNAMICS SIMULATION OF CMMRF PROCESS

4.1. Introduction

CMMRF is an abrasive based nano-finishing process for ductile as well as brittle materials, in which material removal takes place under the ductile mode for precisely controlled abrasion. Such abrasion yields material removal rate (MRR) of the order of a few nanometres per 'stroke of abrasion' for the improvement in surface finish at nanometric level. Such an abrasion is known as nano-abrasion and it can be classified into two major types. The 1st type is called mechanical finishing and the 2nd type is known as chemical assisted mechanical finishing at atomic scale. A schematic of a typical nano-abrasion is presented in Fig. 4.1 for the ductile mode of machining by maintaining –ve rake angle and the un-cut chip thickness of few nanometres. This type of nano-abrasion needs to be investigated for the interaction between workpiece and abrasive particles, leading to material removal at nanometric scale. At molecular level, the interaction between abrasive particle and workpiece is very difficult to study by experimental techniques. Experimental results are often not useful to reveal the science of the material removal process due to the complexity of the process dynamics.

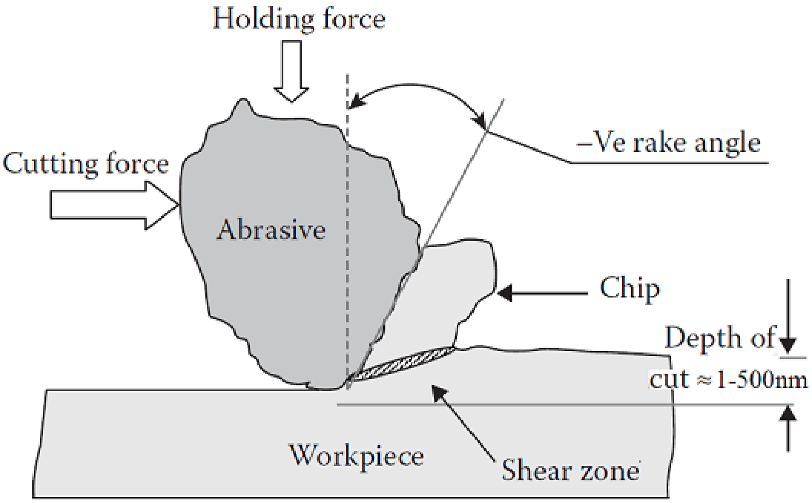

Fig. 4.1: Schematic diagram of nano-abrasion.

Molecular dynamics (MD) simulation [120] is a theoretical method which offers high temporal and spatial resolution. The MD simulation is almost an ideal approach to investigate and analyse about a process at atomic scale [121,122], and therefore it has become a significant tool for such studies.

In this chapter, MD simulation is extensively carried out to investigate CMMRF process at nanometric scale on three different materials, namely aluminium, silicon and stainless steel. MD simulation work is divided into three sections to study the effect of mechanical finishing, chemical reaction, and chemical assisted mechanical finishing. In the chemical assisted mechanical finishing, chemical reaction is studied on two possible routes, i.e. chemical reaction from the chemical species of the finishing medium and from the chemically active abrasive particles. Forces for the MD simulation are obtained from the polishing pressure which is discussed in chapter 3. At the end of the chapter, mechanism of material removal to generate defect free surface at nanometric scale during CMMRF process for ductile as well as brittle materials is also discussed.

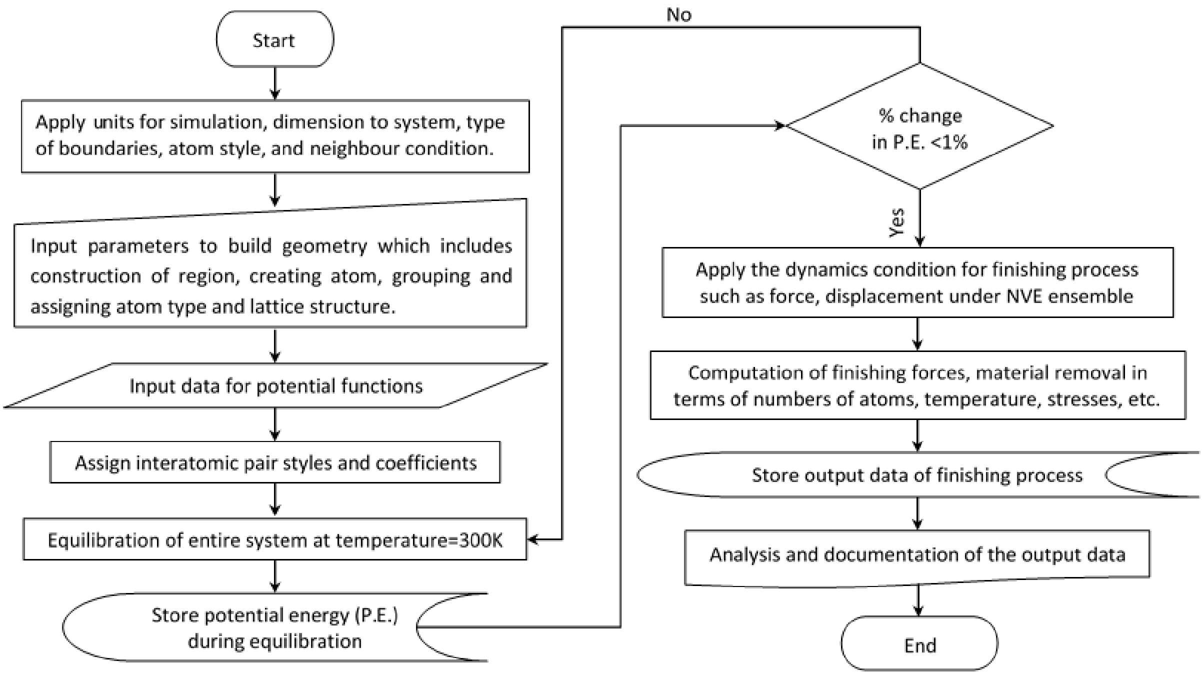

Fig. 4.2: Flow chart for MD simulation to study mechanical finishing, chemical reaction and chemically assisted mechanical finishing.

In brief, MD simulation is carried out on ductile and brittle materials, as per the flow chart shown in Fig. 4.2 to analyse the following critical attributes of CMMRF process.

- Classical MD simulation to analyse the effect of mechanical abrasion at nanometric scale during nanofinishing process of silicon as brittle material, and aluminium and stainless steel as ductile materials.
- Chemical reactions using reactive MD simulation on aluminium and silicon.
- Chemical assisted mechanical abrasion using reactive MD simulation on aluminium and silicon.
- Study of material removal behaviour on ductile as well as brittle materials for mechanical finishing and chemical assisted mechanical finishing.
- Chemical assisted mechanical abrasion using classical MD simulation on stainless steel of *SS304L* grade with atomic composition equal to 10% nickel, 20% chromium and 70% iron.
- Parametric quantification at nano-scale towards modelling and simulation of CMMRF at macroscale.

4.2. MD simulation for mechanical finishing

MD simulations (MDS) are carried out with usage of the large-scale atomic/molecular massively parallel simulator (LAMMPS) [123]. Furthermore, software package OVITO [124] is applied for visualization and analysis of the simulation results. This simulation is carried out for the analysis of nano-finishing on two different types of materials, namely aluminium and stainless steel as ductile materials, and silicon as brittle material. Here, aluminium belongs to the class of ductile material, silicon belongs to brittle material, and stainless steel of *SS304L* as another ductile material with a number of multiple alloying elements (mixture of *Fe*, *Cr*, *Ni*, etc.). To study about the chemical reaction and chemically assisted mechanical finishing, reactive MDS is used on aluminium and silicon workpiece. In case of stainless steel, classical MDS is used to simulate the effect of chemically active abrasive particle instead of chemically active slurry, as the reactive force field data set is not built for stainless steel which limits the implementation of reactive MDS on stainless steel.

4.2.1. MD simulation Methodology

Fig. 4.3 shows a schematic model of mechanical finishing using a spherical abrasive particle on workpiece of aluminium, silicon and stainless steel. The workpiece has a shape of rectangular slab with an asperity which represents surface roughness or surface un-evenness. The workpiece is composed of three layers viz. Newtonian layer, thermostat layer and boundary layer, whereas the abrasive particle is composed of Newtonian atoms. The boundary layer is used to restrain movement of workpiece in which atoms movement or vibration is seized.

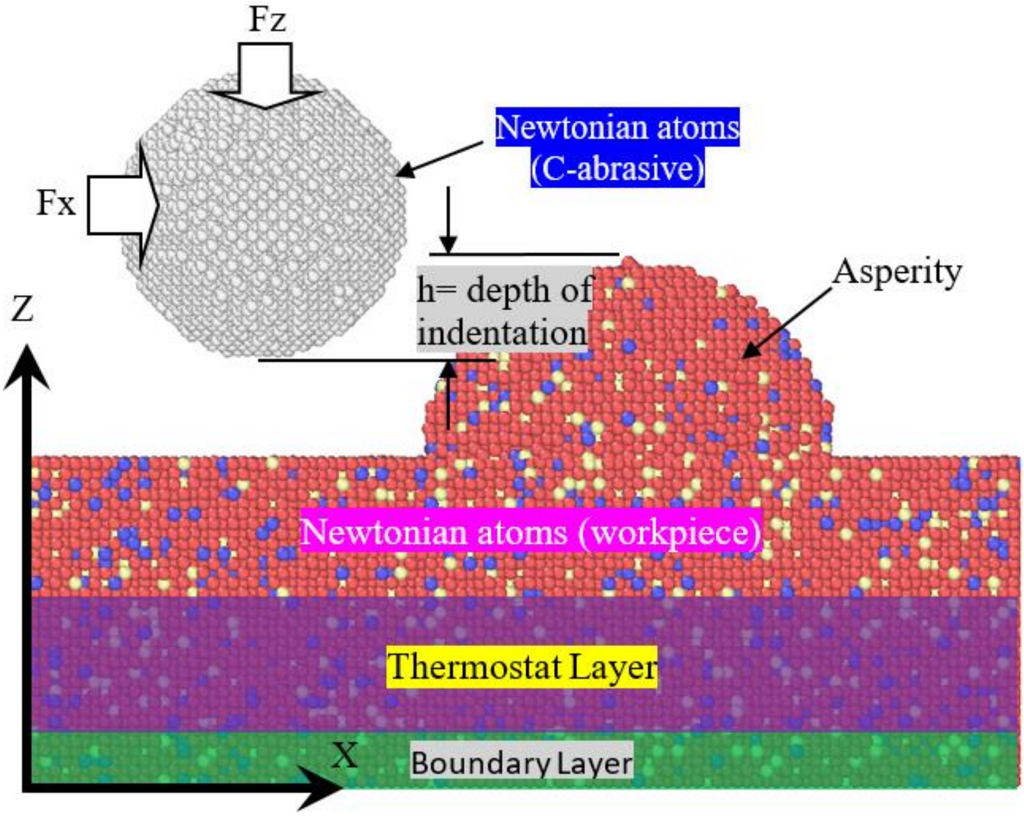

Fig. 4.3: Schematic model of mechanical finishing.

Atoms of the thermostat layer are maintained at constant temperature (i.e. 300 K by rescaling of atoms velocity) which helps in dissipating the heat generated during finishing process in the form of heat conduction in the bulk material of workpiece itself. This layer is used to separate Newtonian atoms and boundary layer. Newtonian atoms are used for material deformation and other analysis in which the positions and velocities of atoms are calculated based on Newton's second law of motion. Periodic boundary condition (PBC) has been imposed along X and Y-axis to minimize the size effects and realize the conditions for bulk material with reasonable computation effort. The parameters used in the classical MD simulation for mechanical finishing are presented in Table 4.1. In general practice of chemo-mechanical polishing (CMP), colloidal silica (SiO_2), is used for nano-finishing of silicon and quartz (SiO_2). In this case, workpiece does not deform as the hardness of abrasive particle and workpiece are same, and material removal takes place as shown in Figs. 4.4 (a-b). Fig. 4.4 (a) shows chemical bonding when abrasive particle makes proximity with workpiece, thereafter, few atoms of workpiece get removed by moving the abrasive particle as shown in Fig.4.4 (b).

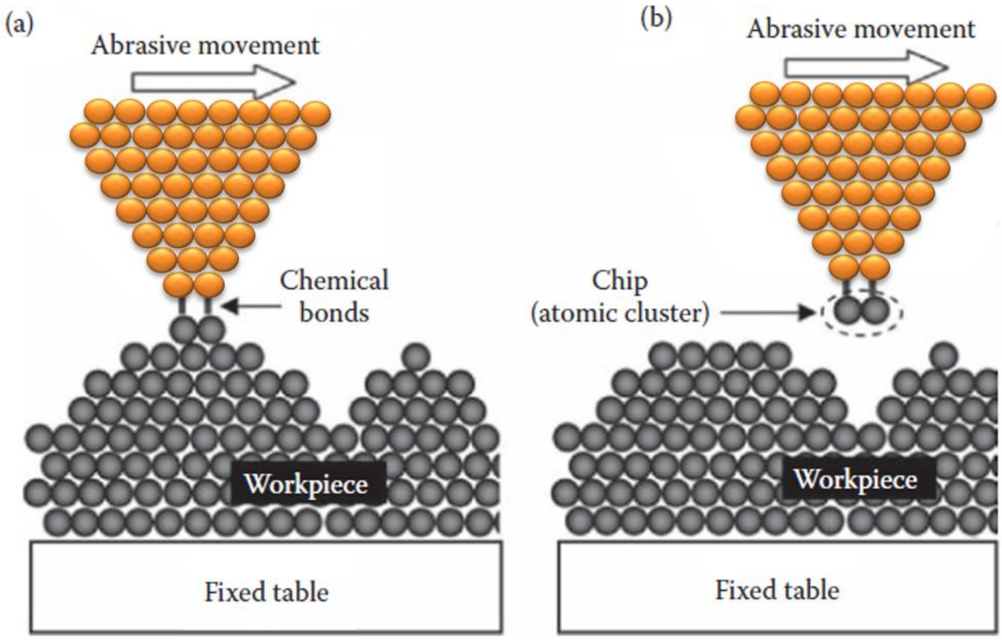

Fig. 4.4: (a) Chemical bonding between abrasive particle and workpiece after attaining sufficient proximity. (b) Removal of material with the help of relative movement between abrasive particles and workpiece.

In the present work, iron particle is used for material removal from aluminium workpiece and silicon as abrasive particle is used for material removal from stainless steel as well as silicon workpiece so that the material removal can be reduced to mitigate the severe surface damages.

Table 4.1: Parameters of the MD simulation used for mechanical finishing.

Sr. No.	**Parameters**	**Value/description**
1	Workpiece materials	Aluminium as ductile material, silicon as brittle material and *SS304L* as alloyed material.
2	Abrasive particles	Iron abrasive for aluminium workpiece, and silicon abrasive for silicon and stainless steel workpiece.
3	Depth of abrasion for material removal	0 nm, 0.5 nm, 1.5 nm, and 2.0 nm.
4	Inter-atomic potentials	EAM for *Al-Al*, *Al-Fe*, *Fe-Fe* and *SS304L*. TERSOFF for *Si-Si*. BHM for *Si-Fe* and *Si-Cr*. MEAM for *Si-Ni*.
5	Boundaries	Shrink along Z-axis, and periodic boundary condition along other directions.
6	Atoms grouping	Fixed layers of atoms (bottom) are set to be rigid. Thermostat layer in which temperature is fixed at 300 K to dissipate heat generated during finishing process. Remaining atoms are allowed to move as per Newtonian atoms.
7	Statistical ensembles	Constant number of atoms, volume and energy (NVE) is also known as the micro-canonical ensemble.
8	Ambient temperature	300 K, as water is used at room temperature in MR fluid.
9	Time step	One femto-second (1 fs)

4.2.2. Interatomic potentials for simulation

Movement of atoms affects the behaviour of material in view of metallurgical, mechanical, chemical, etc. Hence, accurate movement of atoms is the key of successful MD simulation to get correct output, which is mainly governed by interatomic potential. Interatomic potential is the potential energy required to escape an atom from the influence of another atom.

This interatomic potential is also helpful in extracting the required output parameters. Since abrasive particle and workpiece material are different by their chemical elements and lattice structure, suitable pair potential needs to be implemented.

4.2.2.1. Interatomic pair potential for workpiece of Aluminium

Interaction between aluminium to aluminium is well described by EAM [125] type to simulate atomic interaction and the same is used in aluminium workpiece for the present work.

4.2.2.2. Interatomic pair potential for workpiece of Silicon

To simulate the lattice structure like cubic diamond (DC) of silicon, Tersoff potential is used on ABOP (analytic bond-order potential) derived interaction on *Si*-*Si* [126]. Tersoff potential has capability for 3-body interaction with attractive Morse potential, short range repulsive potential, bond-order, and bond angle information.

4.2.2.3. Interatomic pair potential for workpiece of Stainless steel

Major alloying elements of any stainless steel have *Fe, Cr* and *Ni* atoms. Interaction between these atoms is well described by an embedded atom method (EAM) type interatomic potential for the ternary *FeNiCr* system [127]. The potential for *Fe-Cr-Ni* is extensively benchmarked against density functional theory, and, is validated with the consistent experimental values [127].

4.2.2.4. Interatomic pair potential for abrasive particle

To model and simulate two different type of abrasive atoms, different types of pair potential functions are chosen. For example, BCC structured Iron is simulated using EAM type [125] and DC structure silicon is simulated using Tersoff type [126].

4.2.2.5. Interatomic pair potential for the interaction between workpiece and abrasive particle

To build inter-atomic potential between abrasive particle and workpiece, following interatomic potential functions are implemented.

For the interactions between stainless steel (mixture of *Fe*, *Cr* & *Ni*) and silicon (*Si*)	⇨	BMH potential for *Fe*-*Si* [128] BMH potential for *Cr*-*Si* [128] MEAM potential for *Ni*-*Si* [129]
For Aluminium (*Al*) as workpiece and Iron (*Fe*) as abrasive	⇨	EAM potential for *Al*-*Fe* [125]
For abrasion on silicon (*Si*) with silicon (*Si*)	⇨	Tersoff potential for *Si*-*Si* [126]

4.2.3. Equilibration of MD simulation

Before introducing dynamics of nano-finishing process during MD simulation on a constructed model, it is essential to equilibrate the model for rearranging atoms placement on workpiece as well as on abrasive particle. This technique is used to place all atoms in a well-defined equilibrium positions, and by this technique, cohesive energy (or potential energy per atom) of materials gets stabilized. For example, equilibration result of *SS304L* workpiece and *Si* abrasive particle are presented in Figs.4.5 (a-b) which show that the cohesive energy stabilises with time.

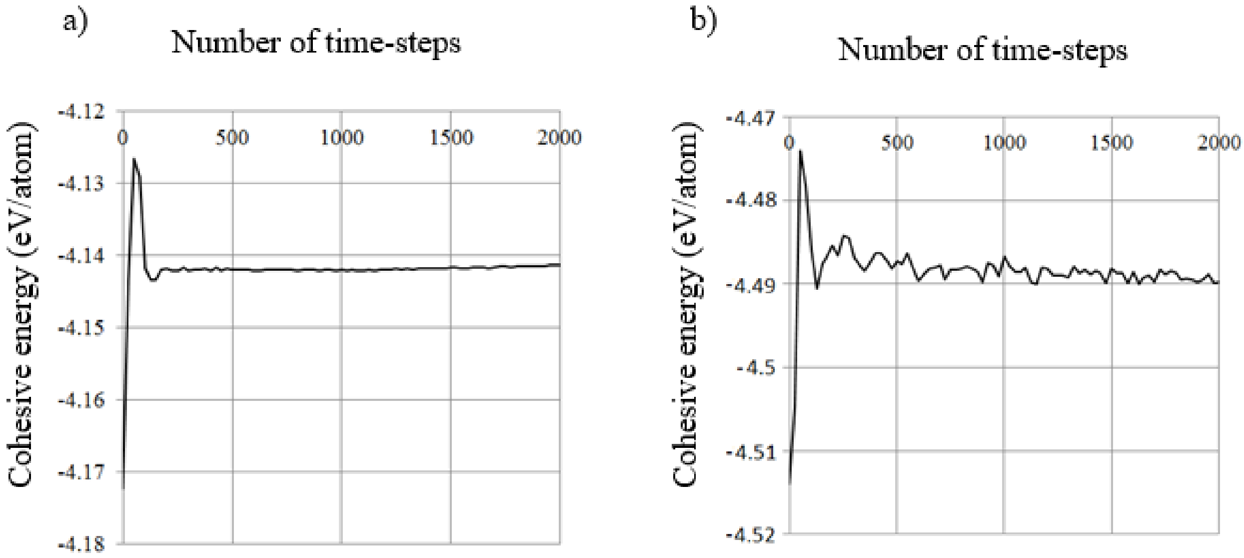

Fig.4.5: Variation of cohesive energy with time step during equilibration for (a) workpiece of *SS304L*, (b) abrasive particle of *Si*.

Here, potential energy at any state of a system is described as an energy required to move away all atoms in such a way so that the interatomic distance between atoms of the system are located more than the cut-off distance which is responsible to nullify the interaction due to neighbouring atom. After a certain time-step, the cohesive energy becomes saturated, and fluctuates about a constant value which indicates that the equilibrium condition has been achieved. The equilibrated conditions are further used to implement for actual parameters of nanofinishing process for material removal.

4.2.4. Analysis Techniques

4.2.4.1. Common neighbour analysis (CNA)

Structure analysis is an essential part of post processing for MD simulation to characterize arrangement of atoms, which helps in discriminating between several structures. Common neighbour analysis is an efficient algorithm to characterize local structural changes in the simulated system.

For example, two atoms can be stated as bonded in a known structure (like FCC, BCC, HCP, DC, etc.) provided their separation (or interatomic distance) has been maintained within a specified cutoff distance (r_c). Common neighbor analysis is also being used to filter the atoms in crystalline systems according to its relevance with phases and defects. Adaptive common neighbor analysis method available in OVITO [124] is used in this study to analyze the structural changes during nanofinishing process.

4.2.4.2. Forces between abrasive particles and workpiece

The interaction force between abrasive particles and workpiece has been computed by taking negative derivative of the inter-atomic potentials between them, as expressed in Eqs.4.1 & 4.2.

$$F_{ij} = -\frac{\partial V(r_{ij})}{\partial r_{ij}}; \qquad (4.1)$$

$$\vec{F_i} = \sum_{j=1}^{n} F_{ij}; \quad F_x = \sum_{i=1}^{m} \vec{F_i}.x_i; \quad F_y = \sum_{i=1}^{m} \vec{F_i}.y_i; \quad F_z = \sum_{i=1}^{m} \vec{F_i}.z_i; \qquad (4.2)$$

Where, F_{ij} is the force on i^{th} atom of workpiece by j^{th} atom of abrasive particle, and F_i is the total force on the i^{th} atom of workpiece by all atoms of abrasive particle. x_i, y_i, and z_i are unit vectors along x, y & z axis. 'm' and 'n' are number of atoms on workpiece and abrasive particle, respectively.

4.2.4.3. Atomistic stress

During nanofinishing process, atoms of abrasive particle and workpiece interact and lead to the development of stresses for material deforming followed by material removal in the form of tiny chips as shown in Fig.4.1. In general, virial stress [130] is used to compute stress on individual atoms. From the analysis point of view, von-Mises stress [131] has been computed which tells about the equivalent stress on a specific atom instead of having a set of stress matrix.

4.2.4.4. Centro-symmetry parameter (CSP)

The centro-symmetry parameter is an important technique to distinguish lattices of a structure by using various types of crystal defects. Kelchner et al. [132] have developed CSP to quantify the local loss of centro-symmetry at an atomic site, which represents the crystal defects. CSP is a powerful tool to analyse the deformation and defects evolution in the materials. The CSP of an atom, with 'N' number of neighbor atoms, is expressed as in Eq.4.3.

$$CSP = \sum_{i=1}^{N/2} \left| \vec{R_i} + \overrightarrow{R_{i+\frac{N}{2}}} \right|^2 \qquad (4.3)$$

Where, 'N' is the nearest neighbor and it is 12 for FCC lattice structure, and 8 for BCC lattice structure. For a defect free FCC material, CSP is zero. The CSP becomes positive in case of defects such as cavity, dislocations and dangling bonds.

4.2.4.5. Temperature

During abrasive based nanofinishing process, material removal zone is quite small and it is experimentally difficult to measure temperature in the nano-finishing zone. The temperature building has its subsequent effect on material removal at nanometric scale. Hence, molecular dynamics simulation is used to calculate kinetic energy of the workpiece atoms for mapping the temperature at every time-step as per Eq.4.4.

$$\frac{3}{2}nK_BT = \frac{1}{2}\sum_{i=1}^{n} m_i v_i^2 \tag{4.4}$$

Where ‘n’ is the number of atoms, ‘v_i’ and ‘m_i’ denote the velocity and mass of i^{th} atom, ‘K_B’ is the Boltzmann constant and T is the average temperature.

Above discussed analysis techniques are applied on ductile and brittle materials. Aluminium and silicon are modelled as pure bulk material, which are not suitable to study the defect generation within the bulk material. Multiple alloyed materials are responsible to create various types of defects/ dislocations. Hence, stainless steel was used as alloyed material, which consists three different elements namely, iron (Fe), nickel (Ni), and chromium (Cr).

4.2.5. Analysis of mechanical finishing on ductile material (aluminium)

In this section, mechanical finishing of aluminium workpiece is analysed and presented to understand the mechanism of this process for material removal and surface modification.

4.2.5.1. Structure analysis on Aluminium

Lattice structure of MD simulated results is analysed by CNA technique and presented in Figs. 4.6 (a-c). Fig. 4.6 (a) shows lattice structure of workpiece and abrasive particle before interaction between them, in which aluminium workpiece shows a lattice structure of FCC and iron abrasive shows another lattice structure of BCC.

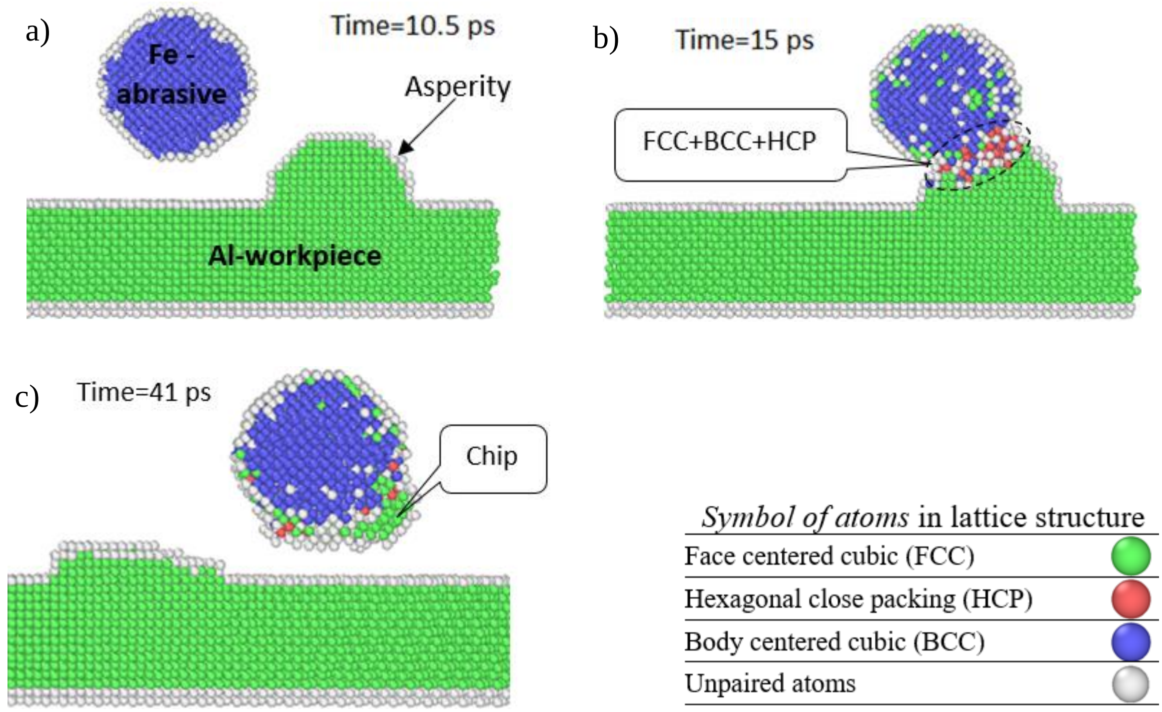

Fig. 4.6: Structural variation in aluminium with different levels of finishing time at indentation depth equal to 1 nm. (a) before interaction between abrasive and workpiece. (b) During abrasion of workpiece. (c) After abrasion.

When abrasive particle approaches workpiece, material of workpiece deforms by changing the parent lattice structure in a mixture of FCC, BCC and HCP lattices as shown in Fig. 4.6 (b). After passing away of abrasive particle from the zone of abrasion, removed chip (it occurs when the interatomic distance (R) increases beyond the cut-off length (R_c) as described in the interatomic function) from the workpiece recovers its own lattice structure of FCC as shown in Fig. 4.6 (c). This structure recovery phenomenon also happens with the workpiece material.

4.2.5.2. Finishing forces and potential energy of Aluminium

Finishing forces during mechanical finishing are computed along cutting (i.e. x-axis) as well as indentation (z-axis) directions with different levels of indentation depth as shown in Figs. 4.7 and 4.8 respectively. When proximity between abrasive particle and asperity builds, an attractive force of the range of 2-3 nN is generated as shown in Fig. 4.7. This attractive force occurs due to the free electron clouds available on metals to create metallic bonds.

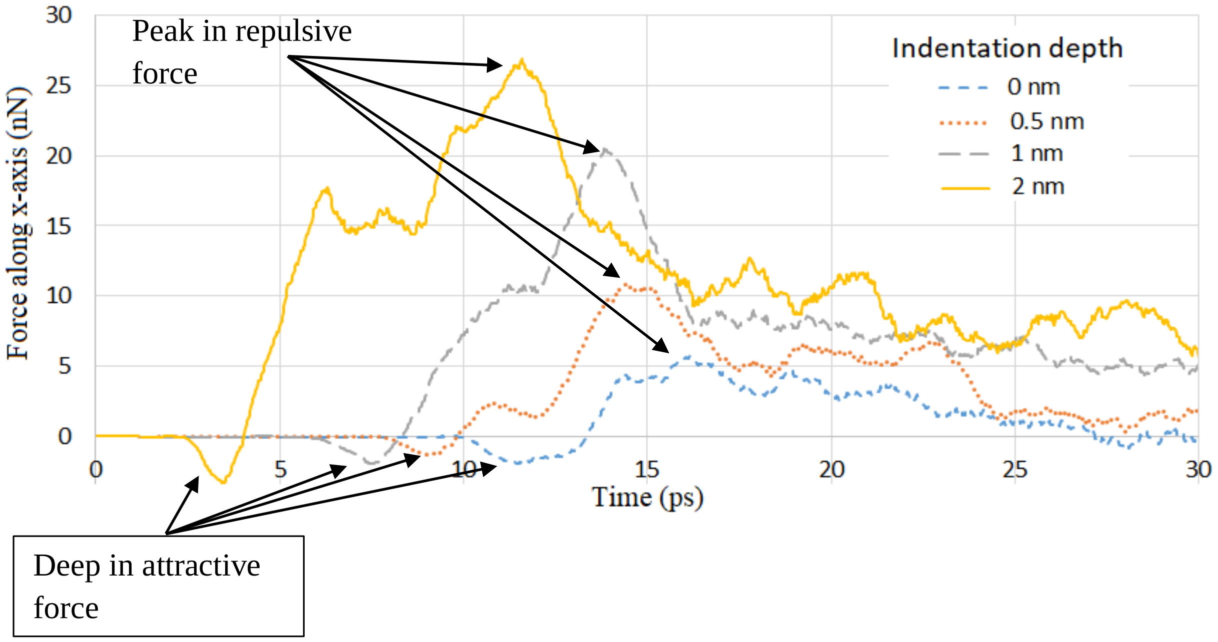

Fig. 4.7: Finishing force on *Al* along cutting direction or x-axis.

Subsequently, repulsive force dominates while passing the abrasive particle over the asperity with the maximum value of 27, 20, 11 and 6 nN for the indentation depth equal to 2, 1, 0.5 and 0 nm respectively. When the indentation depth increases, surface of abrasive particle makes more proximity with the asperity, as Fig. 4.7 shows a shift in time for the peak repulsive force as well as the deep attractive force with different levels of indentation depth. After completion of material removal from workpiece, force reduces.

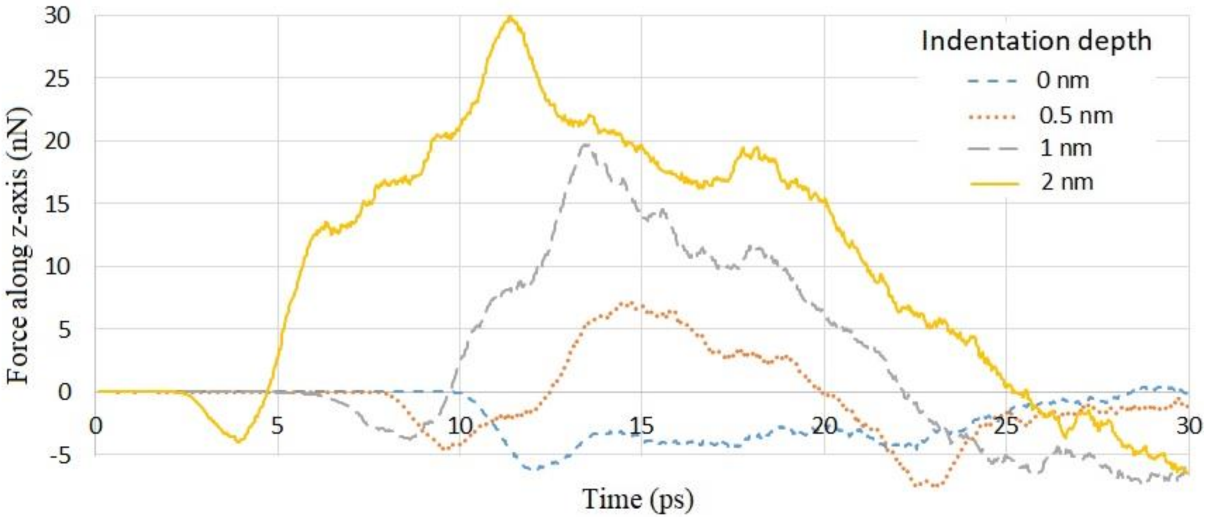

Fig. 4.8: Indentation force along normal to *Al* work-surface or z-axis.

Force along z-axis is presented in Fig. 4.8 which also shows similar behaviour as shown in Fig. 4.7. But the force along z-axis becomes less than zero after abrading the asperity, and this happens as the chip attached to abrasive particle gets attracted toward the surface of workpiece.

Maximum repulsive forces along x-axis and z-axis indicate the required stiffness of MR fluid during CMMRF operation under a specified set of process parameters. These parameters are capable to calculate the indentation force along z-axis by using polishing pressure of MR fluid.

Mechanical finishing of aluminium workpiece shows that the repulsive force (positive value) between workpiece and abrasive particle dominates along both x and z axes, which deforms workpiece and causes chemical instability by increasing the potential energy. After completion of the abrasion, the deformed material tries to relax which reduces the potential energy up to some extent. This potential energy increases with the time of finishing upto some value, thereafter, it reduces and saturates as shown in Fig. 4.9. An increase in potential energy from initial surface to final surface brings the chemical instability due to mechanical finishing as indicated in Fig. 4.9 which shows a jump in the potential energy by 4eV (app.) as compared to the equilibrated sample of workpiece.

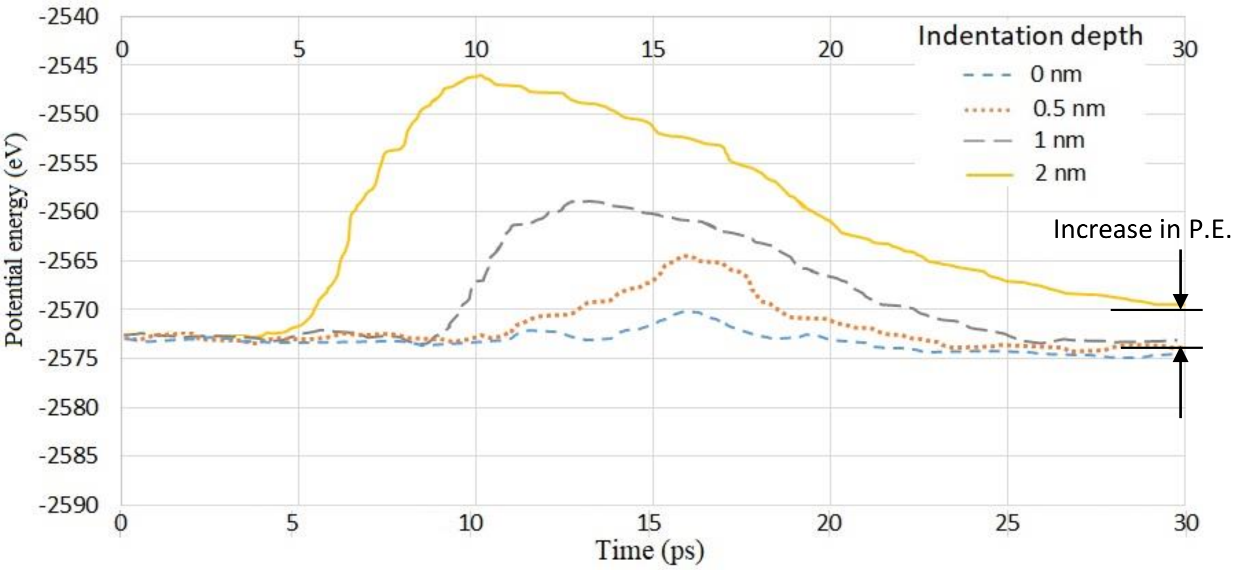

Fig.4.9: Potential energy on the asperity of *Al* workpiece.

A jump in the potential energy leads to increase in the surface reactivity by reducing the required activation energy as described by Arrhenius equation [133], and due to this, the finished surface with higher potential energy brings chemical instability.

4.2.5.3. von-Mises stress in Aluminium

MDS results are further analysed to understand the extent of mechanical stresses developed on the finishing zone at nanometric scale and presented in Figs. 4.10 (a-c) with different times of finishing process.

This result shows that the surface of workpiece contains atoms with nominally higher stress value as compared to the atoms at the core of workpiece as shown in Fig. 4.10 (a). When the abrasion starts, the contact zone between abrasive particle and workpiece shows more stress which is very near to the theoretical value of shear strength, i.e. $G/2\pi$ which is equal to 10 GPa approximately in case of aluminium, as shown in Figs.4.10(b-c). But, stress level inside the workpiece is still small in magnitude.

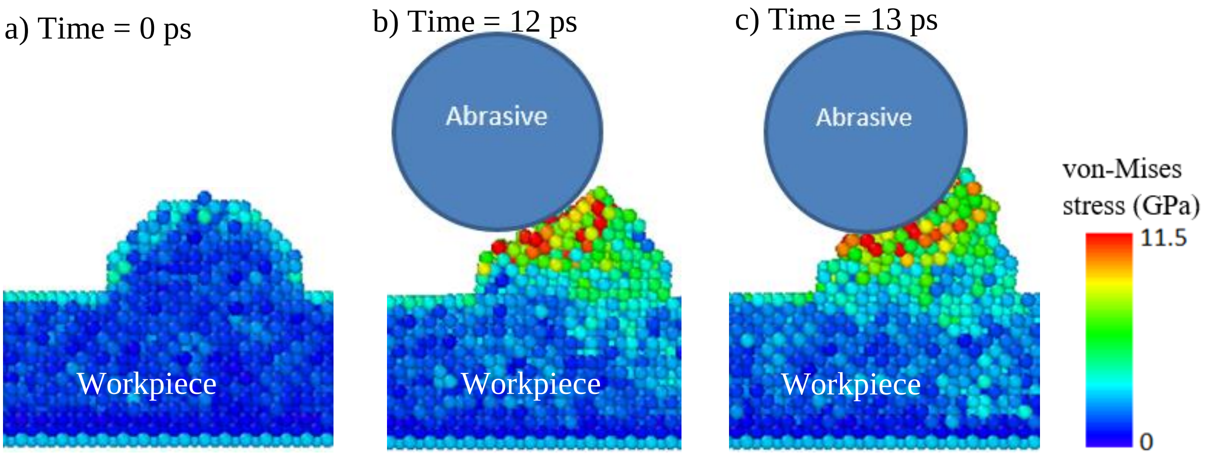

Fig.4.10: Distribution of von-Mises stress in *Al* during mechanical finishing at indentation depth equal to 1 nm. (a) stress distribution before abrasion. (b-c) stress distribution at two different times of abrasion.

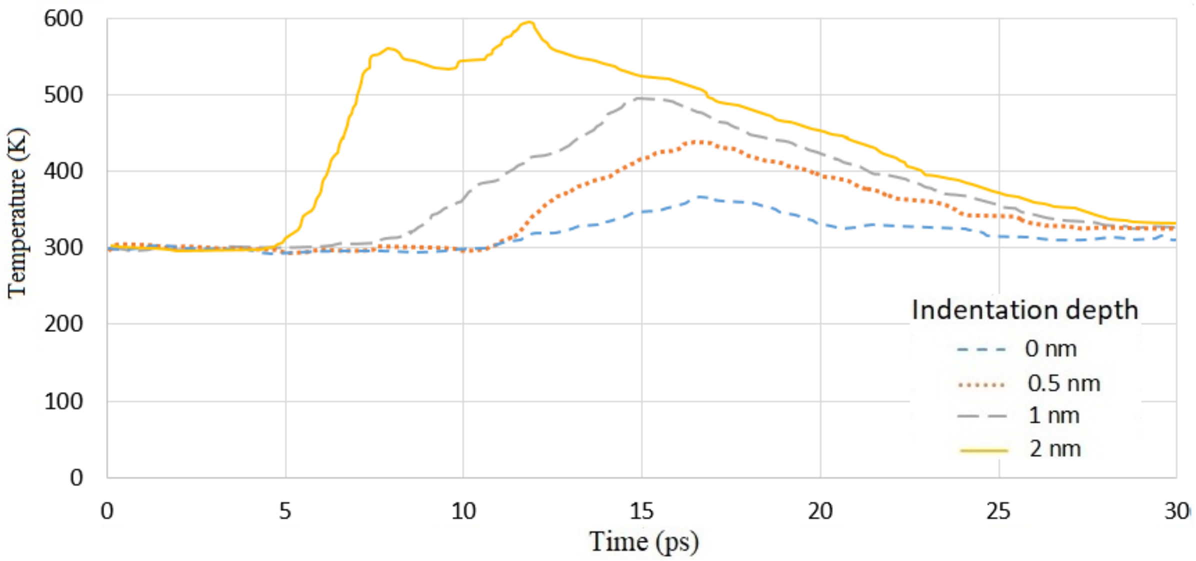

Fig.4.11: Temperature variation during mechanical finishing of aluminium.

4.2.5.4. Temperature rise in Aluminium

Average temperature near the finishing zone has been computed and plotted as shown in Fig.4.11. This temperature goes upto 600, 500, 440 and 360 K at indentation depth equal to 2, 1, 0.5 and 0 nm respectively. At these temperatures, FCC is the only stable lattice structure for aluminium workpiece. Hence, phase recovery happens after mechanical finishing as discussed during CNA analysis. Fig. 4.11 also shows a small rise in temperature, and it happens because of an attractive force between abrasive particle and workpiece as seen in Fig. 4.8. This small amount of attractive force perturbs the surface atoms of workpiece which results in addition in energy and rise in temperature.

4.2.6. Mechanical finishing of brittle material (silicon)

4.2.6.1. Structure analysis on Silicon

Figs. 4.12 (a-d) show lattice structure of silicon during the mechanical finishing process. When abrasive particle approaches asperity of workpiece, the interface between them undergoes phase alteration in the form of non-crystalline or amorphous phase as shown in Fig. 4.12 (c).

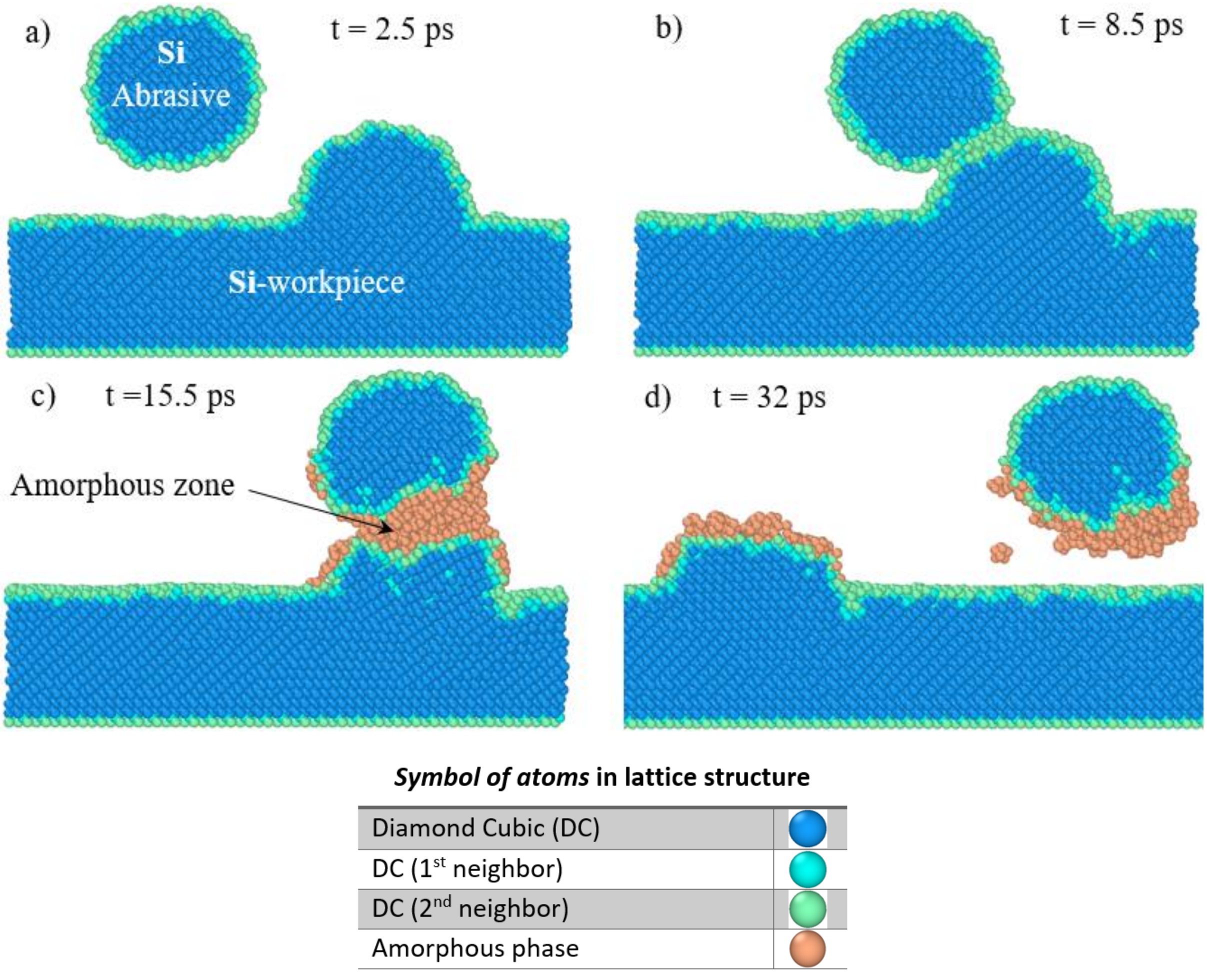

Symbol of atoms **in lattice structure**

Diamond Cubic (DC)	●
DC (1st neighbor)	●
DC (2nd neighbor)	●
Amorphous phase	●

Fig. 4.12: (a-d) Structural variation at different time intervals of mechanical finishing of silicon at indentation depth equal to 1 nm.

During this process, it is also observed that the abrasive and workpiece are getting deformed near the interface as shown in Figs. 4.12 (b-c). Fig. 4.12 (d) shows the debris or chip formation in the form of amorphous phase (non-crystalline structured lattice). Moreover, the finished surface also shows amorphous phase of the order of few atomic layers as shown in Fig. 4.12 (d). This amorphous phase remains permanent, and it does not vanish after the finishing process.

4.2.6.2. Finishing force and potential energy of silicon

Results of finishing forces along x-axis and z-axis are calculated and presented in Figs. 4.13 - 4.14, respectively. The finishing forces are higher in case of silicon as compared to aluminium workpiece.

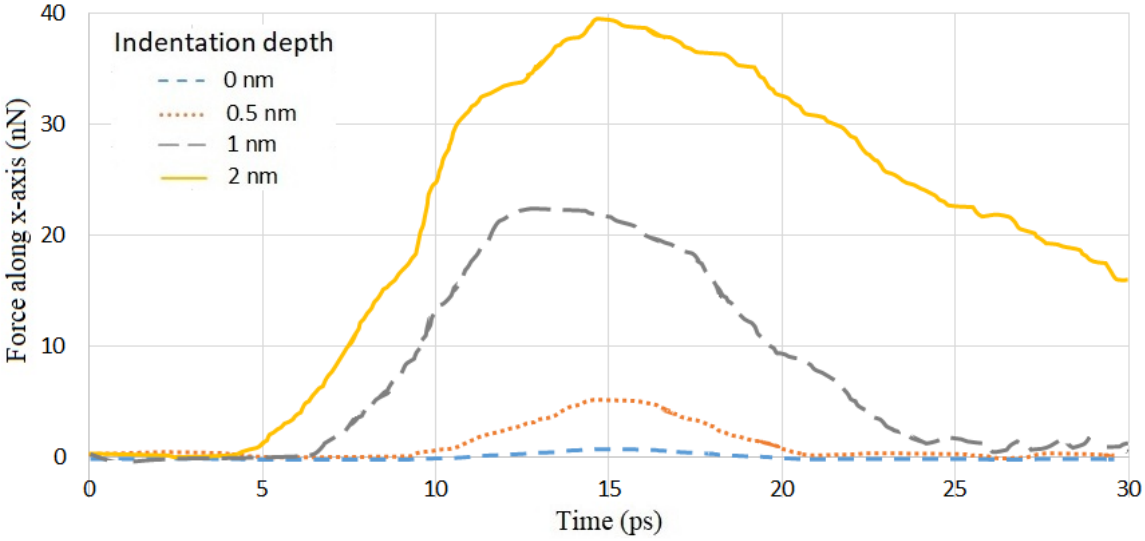

Fig.4.13: Finishing force on *Si* workpiece along cutting direction at different values of indentation depth.

During initial contact of finishing of silicon, it does not show the attractive force as compared to aluminium. Silicon always shows the repulsive force as it has covalent bonds and no free electron clouds with respect to aluminium. It is also observed that there is a small amount of repulsive force at zero depth of indentation in which atoms of abrasive particle tries to move apex atoms of workpiece due to the Pauli-repulsion. *Thus, it can be stated that adhesion between abrasive particle and workpiece during finishing is possible by building an ionic bond between them which is helpful for material removal in soft and ductile materials.*

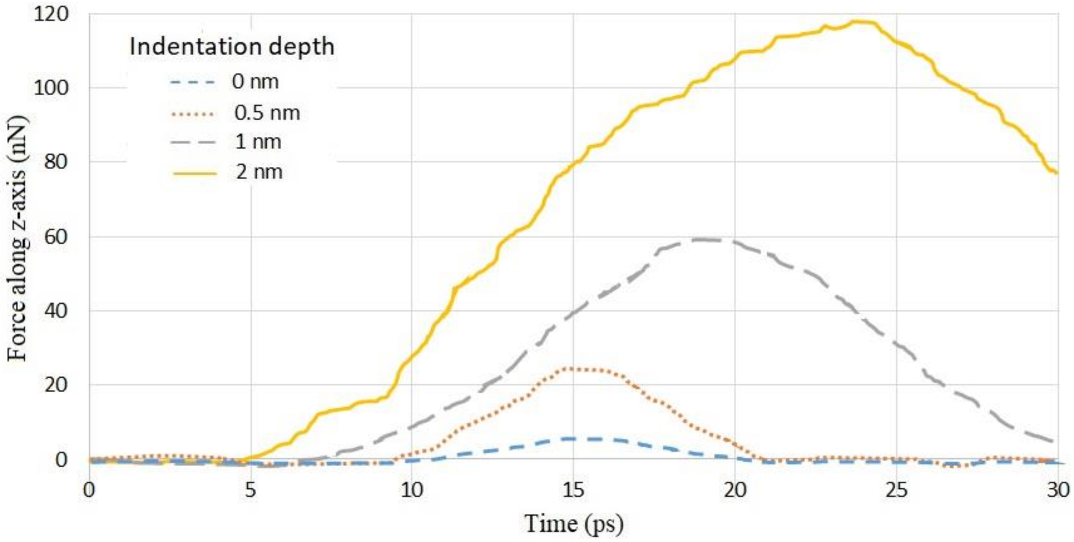

Fig. 4.14: Indentation force along normal to *Si* work-surface or Z-axis.

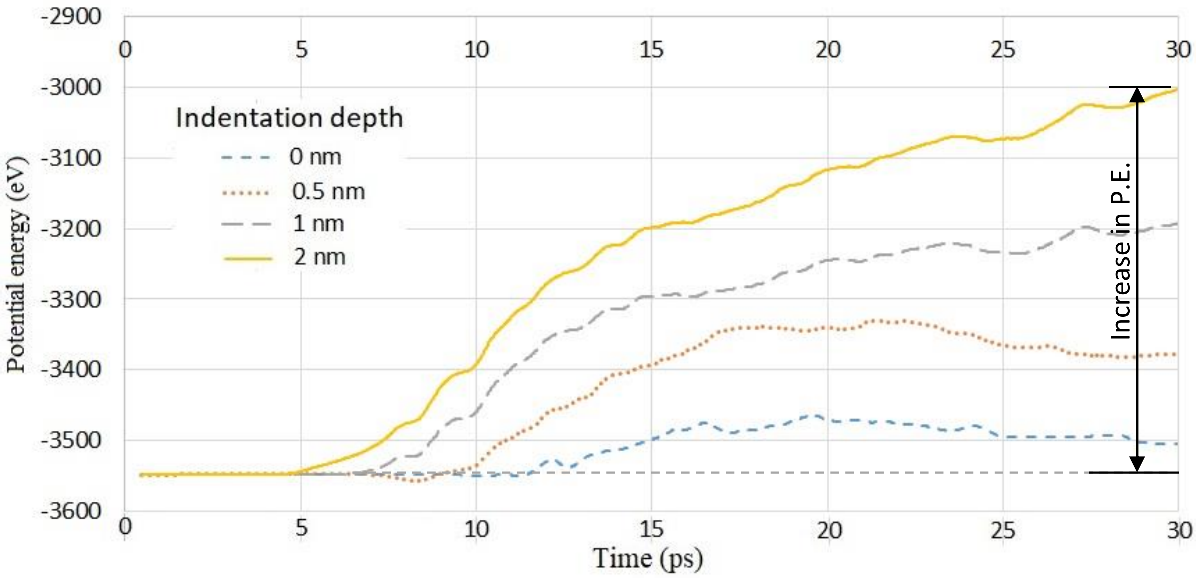

Fig. 4.15: Potential energy on the asperity of workpiece during mechanical finishing of silicon at different values of indentation depth.

Fig. 4.15 shows the variation in potential energy with finishing time, which is almost similar to the aluminium workpiece. After finishing, there is an increase in potential energy of workpiece by 550 eV which is two orders of magnitude higher as compared to aluminium. Hence, the mechanically finished silicon surface is much more unstable (chemically) as compared to aluminium, and due to this the deformed atoms do not recover to its own original lattice structure. Hence, brittle materials are strongly recommended to be machined or finished by using some softening means (chemical passivation or thermal softening).

4.2.6.3. von-Mises stress in silicon

Figs. 4.16 (a-d) show von-Mises stress in silicon workpiece at different time intervals of mechanical finishing. This result shows that the Mises stress of workpiece atoms are near to zero and homogeneous as shown in Fig. 4.16 (a). When the abrasion starts, maximum stress reaches near to the theoretical value of shear strength, i.e. $G/2\pi$ which is equal to 35 GPa approximately in case of silicon, as shown in Figs.4.16 (b-c). But, stress level inside the workpiece is still small in magnitude. After completion of finishing, abraded surface and chip of workpiece show some residual stress with respect to zero as shown in Fig. 4.16 (d).

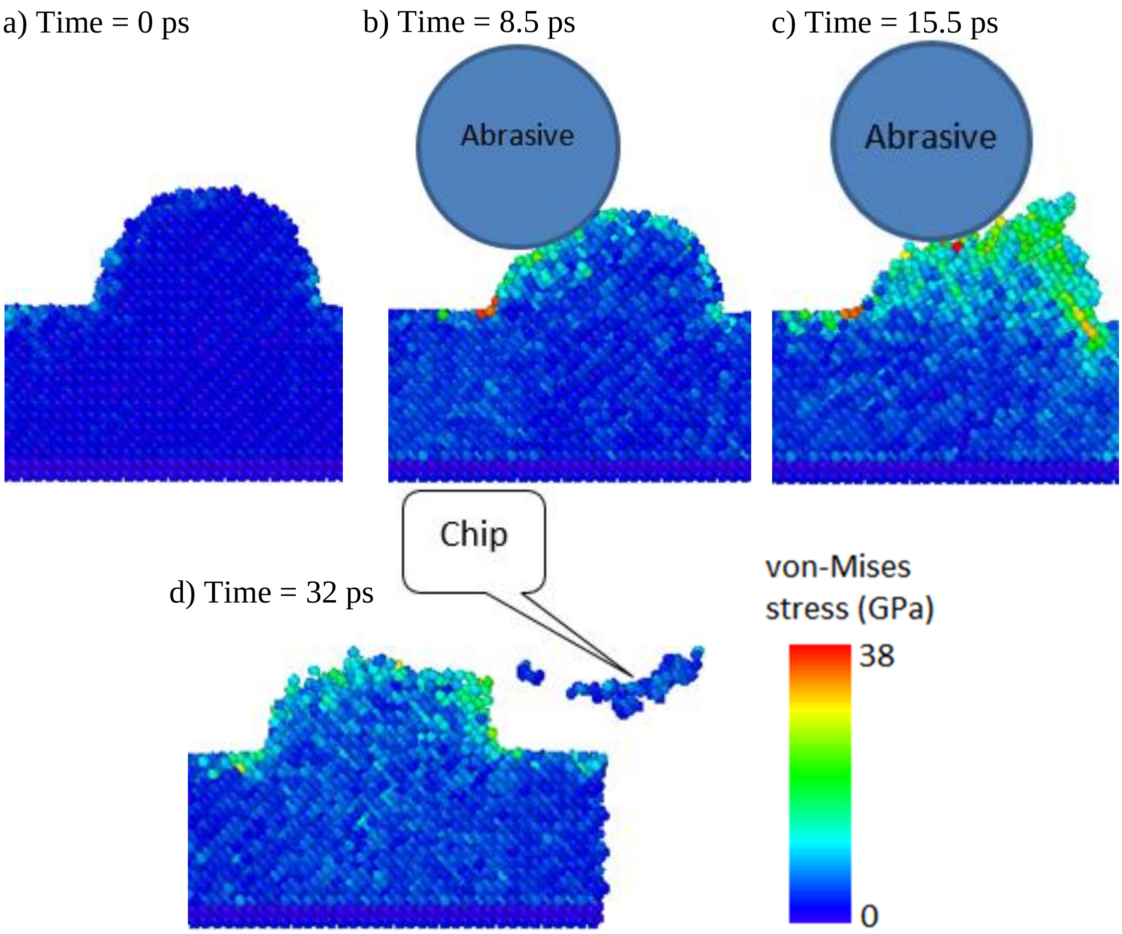

Fig. 4.16: von-Mises stress on silicon workpiece during different time of mechanical finishing at indentation depth equal to 1 nm.

4.2.6.4. Temperature rise in silicon

Average temperature near the polishing zone has been computed and plotted as shown in Fig. 4.17. This temperature goes upto 1500, 1300 and 1200 K for indentation depth equal to 2, 1 and 0.5 nm. So high temperatures are enough to soften the workpiece material for deformation followed by material removal. However, this temperature is less than the melting temperature (1700 K). In general, mono-crystalline silicon gets softened when temperature increases beyond 800 K, and due to this the workpiece deforms before material removal takes place during mechanical finishing.

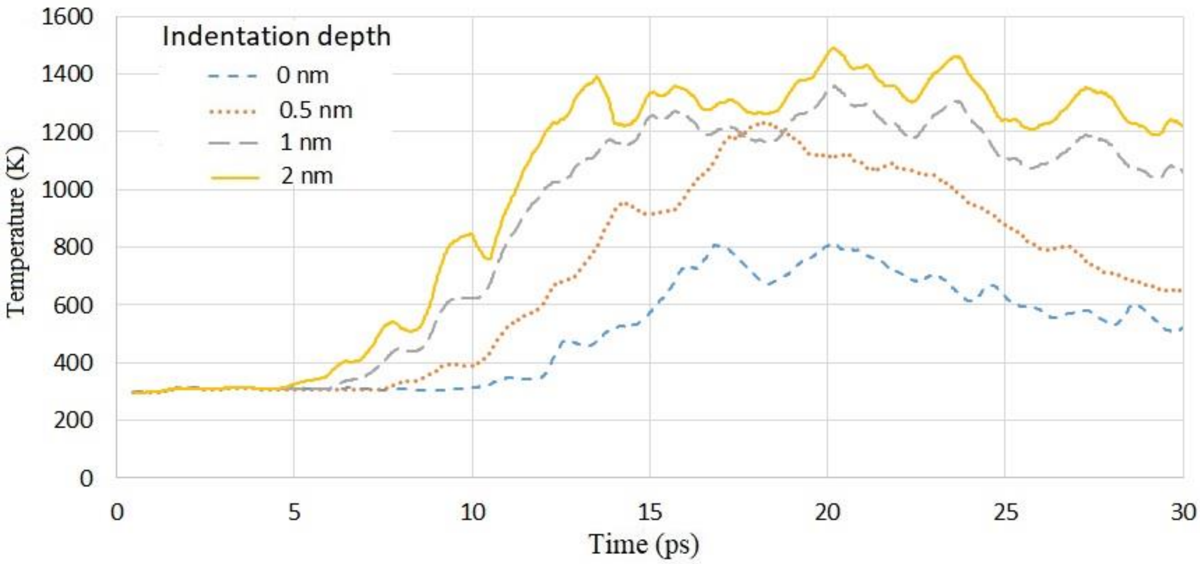

Fig. 4.17: Variation in average temperature of the asperity of the silicon workpiece with varying time and different values of indentation depth during mechanical finishing.

MD simulation on aluminium and silicon are presented as highly ductile and brittle materials respectively. These materials of MD modelling do not include any alloying elements which is almost an ideal case to investigate material removal and surface modification phenomenon.

In general, materials for industrial applications are not in pure form, as they contain some amount of impurity and alloying elements. For example, stainless steel is most popular material for industrial applications, which contains *Ni*, *Cr* and *Fe* as the major alloying elements. Hence, a set of MD simulation is also carried out on stainless steel and the same is presented in the subsequent section.

4.2.7. Mechanical finishing of stainless steel (SS 304L)

4.2.7.1. Structure analysis on stainless steel

Figs. 4.18 (a-b) show lattice structure during the material removal from the spherical asperity of stainless steel using purely mechanical abrasion, in which the material deformation occurs in the form of a chip by changing the lattice structure from FCC to a mixture of BCC and HCP. The material removal at nanometric scale happens when localised lattice transformation takes place in the abrasion zone, and this phenomenon is similar to aluminium workpiece as well.

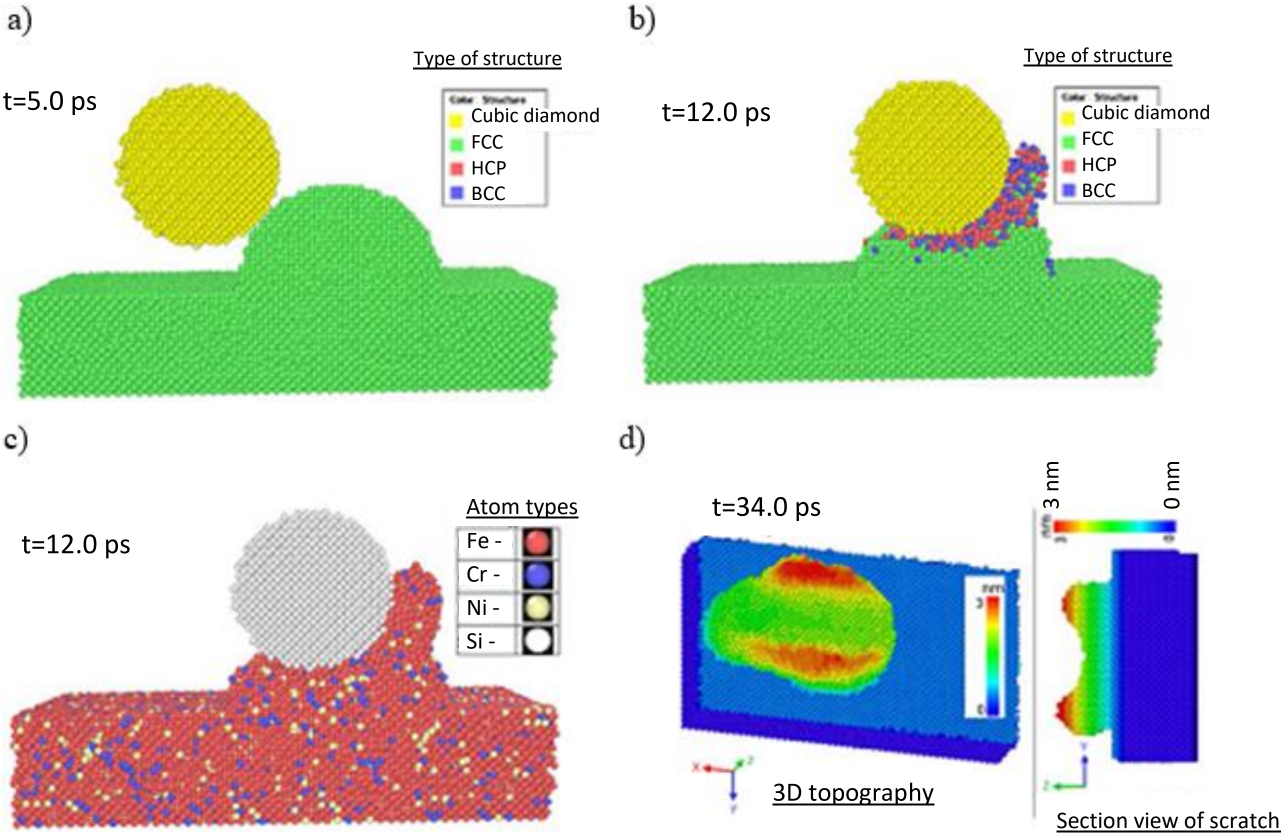

Fig. 4.18: Material deformation and chip formation at atomic scale during mechanical abrasion on stainless steel. (a-b) CNA on material removal at different time of abrasion, which shows information about the transformation of lattice structure. (c) Types of atoms involved as alloying elements. (d) Surface morphology after mechanical finishing process.

Fig. 4.18 (c) shows types of atoms involved in this abrasion process, in which red indicates *Fe*-atom, blue indicates *Cr*-atom, golden indicates *Ni*-atom and white colour indicates *Si*-atom. Fig. 4.18 (d) illustrates topography of the workpiece after the mechanical abrasion process in 3-D as well as 2-D images.

4.2.7.2. Finishing force and potential energy on stainless steel

Finishing force on the workpiece is computed by pair interaction with respect to the abrasive particle. Figs. 4.19 - 4.20 show the finishing force along cutting and indentation directions for varying finishing time (5–25 ps). It was observed that the finishing force in both directions (X-axis and Z-axis) increases as the abrasive particle approaches and passes over the asperity. After attaining maxima, the force starts decreasing till it reaches to zero.

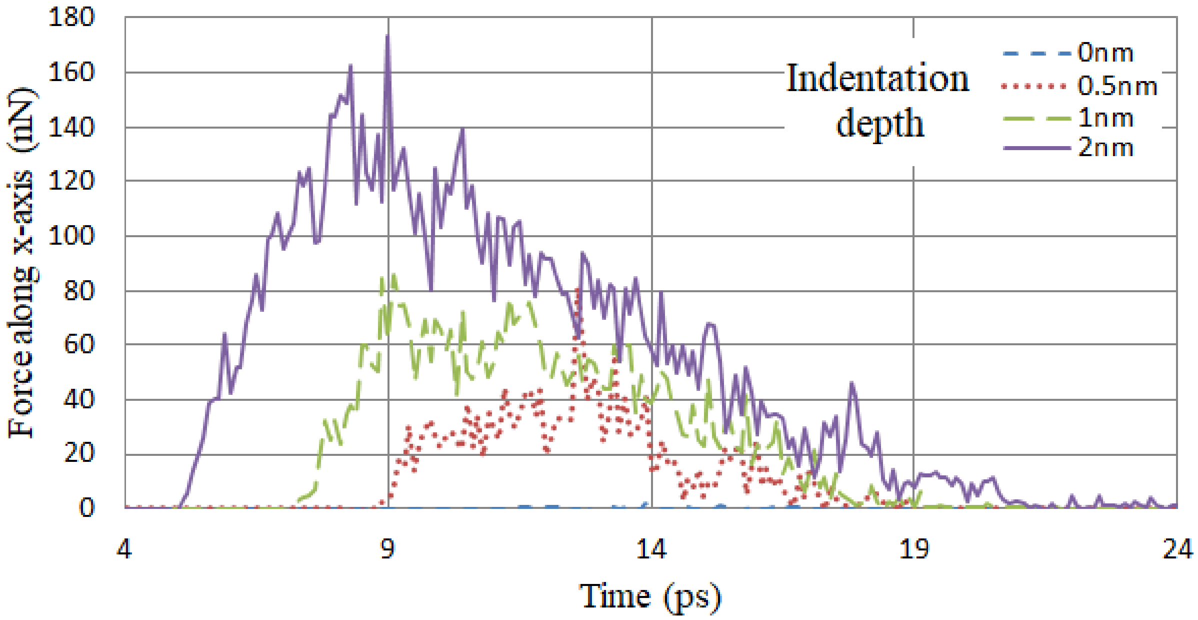

Fig. 4.19: Finishing force along cutting direction or x-axis on *SS304L*.

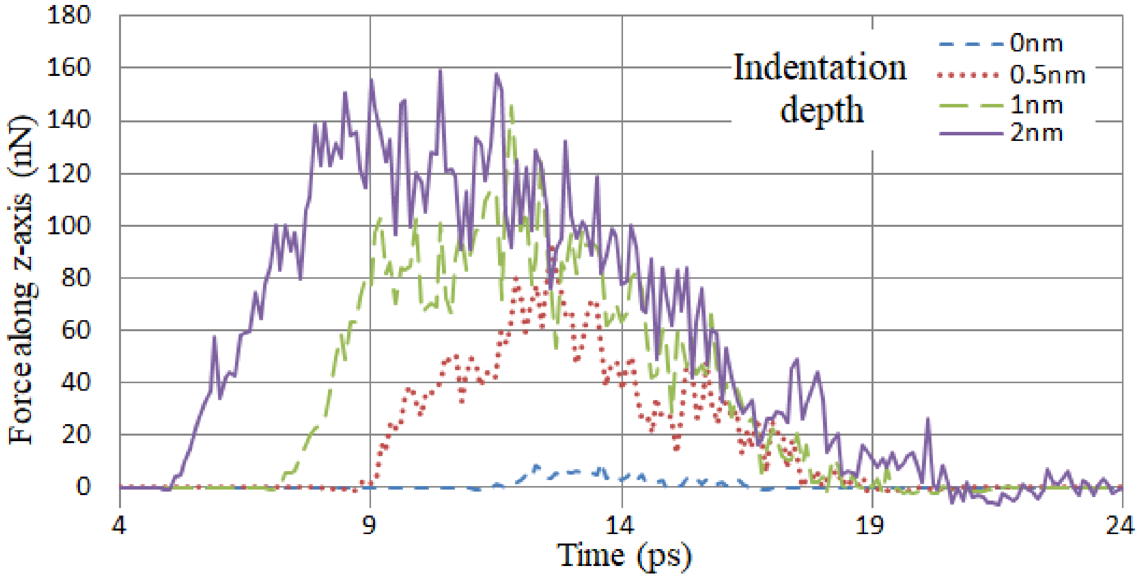

Fig.4.20: Finishing force normal to the surface of *SS304L* workpiece, or indentation force.

The finishing force also depends on the indentation depth. Higher the indentation depth, larger is the finishing force. The force along the cutting direction is somewhat similar in nature, but it is not same in magnitude, and the peak magnitude is maximum at different times as indentation depth increases. Similar trend is also noticed for z-axis. The reason for the shift in time due to indentation depth happens, as abrasive particle needs less time to approach the asperity by attaining reduced distance between them when indentation depth is increased. This shift in time can be conceived from the geometry of MDS model as higher indentation depth faces more materials to abrade and causes less time to make proximity with peaks of worksurface with respect to lower value of indentation depth.

Fig. 4.21 illustrates the variation in potential energy of the workpiece with varying time, and different levels of indentation depth during the abrasion process. Potential energy goes up till its maximum value (known as peak potential energy during the process) and then comes down before it saturates after the end of the abrasion process. Moreover, the potential energy of the abraded workpiece is always higher when compared to the initial workpiece, which also depends on the depth of indentation. As the depth of indentation increases, the peak potential energy and the final potential energy also increase which indicate that the workpiece material gets deformed mechanically which is not desirable for a nanofinishing process. Because, such type of abraded surface with high potential energy becomes unstable and, would interact with environment (chemical species and dust particles). This type of interaction would lead to impair the surface quality at atomic scale.

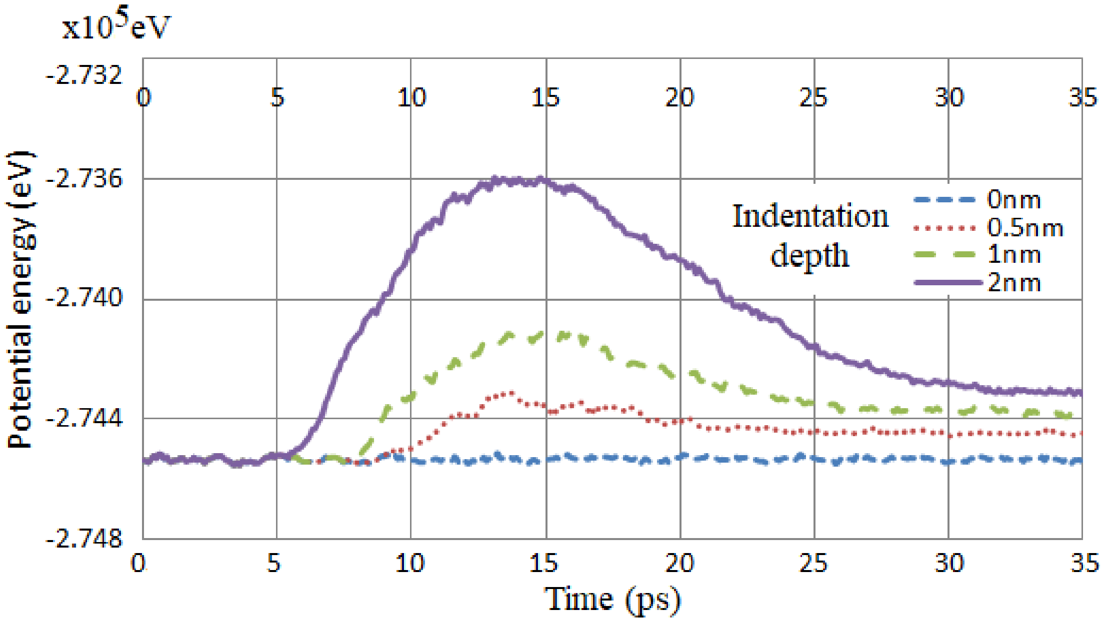

Fig. 4.21: Variation of potential energy of *SS304L* workpiece during mechanical abrasion

Thus, the nanofinished surface should not be subjected to ‘mechanical abrasion’/ ‘mechanical finishing’. Only, the surface with high roughness or sharp asperities is suitable for purely mechanical abrasion-based finishing process.

4.2.7.3. von-Mises stress in stainless steel

von-Mises equivalent stress at different times of polishing is presented in Figs. 4.22 (a-b) to understand severity of stress involved during this process. The stress gets generated at the interface or contact region of abrasive and workpiece, and it travels inside the workpiece material to assist material deformation as shown in Fig. 4.22 (b).

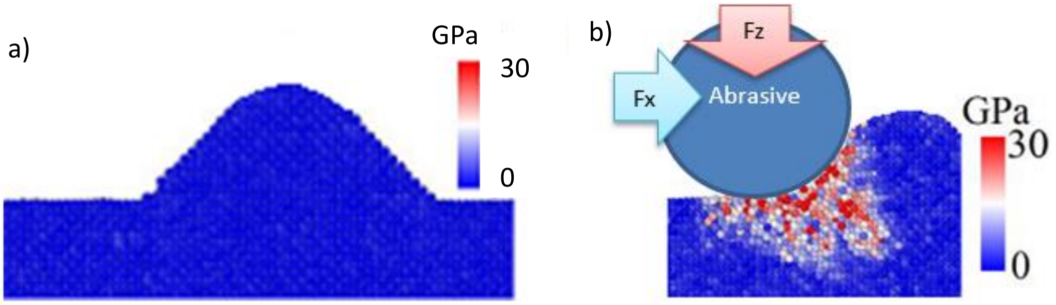

Fig. 4.22: (a) Atomic distribution of von-Mises stress before initial contact of finishing. (b) Atomic distribution of von-Mises stress during initial contact of polishing.

4.2.7.4. Centro-symmetry parameter (CSP) analysis in stainless steel

Stainless steel is a kind of alloyed metal in which types of defects or the phase transformation are not similar to aluminium and silicon. The types of defects/ dislocations are somewhat complicated to analyse in stainless steel. Hence, CSP analysis is carried out in this case. Figs. 4.23 (a-d) show various sub-surface defects generated during mechanical finishing with varying time. These defects are identified by using Centro-symmetry parameter (CSP) on the work-piece. To evaluate the defects, only selected atoms have been analysed whose CSP values are more than unity (or numeric value equal to 1).

As finishing process progresses, various defects occur underneath the top surface. These defects comprise stacking faults, “V-shaped” dislocation loop, point defects, and atomic cluster defects. The sub-surface defects are quantified and plotted with varying polishing time as shown in Fig. 4.23 (e). The number of defects increases suddenly as mechanical contact made between the abrasive particles and workpiece is established. After attaining the maxima of defects, the number of defects starts decreasing and becomes almost asymptotic, Fig. 4.23 (e). Initially, all types of defects are generated as shown in Figs. 4.23 (b-c). Thereafter, the dislocation loop gets mitigated and atomic clusters form as shown in Fig. 4.23 (d). Hence, the defects are nucleated at the top surface of finishing region (Fig. 4.23 (b)) of the workpiece, and migrate inside the workpiece. Movement of these defects to free surface of the workpiece annihilate themselves. However, some of the dislocation defects do not have sufficient energy to migrate to the free surface; and form atomic cluster defects.

Stacking fault is a type of defect which alters the periodic sequence of crystalline atomic layers. The stacking fault can also be stated as a wrong layer inserted into the periodic sequence, a change of the layer sequence or a different translation between two subsequent layers. When two stacking faults combine orthogonally, it forms “V” shaped dislocation, Fig. 4.23 (c).

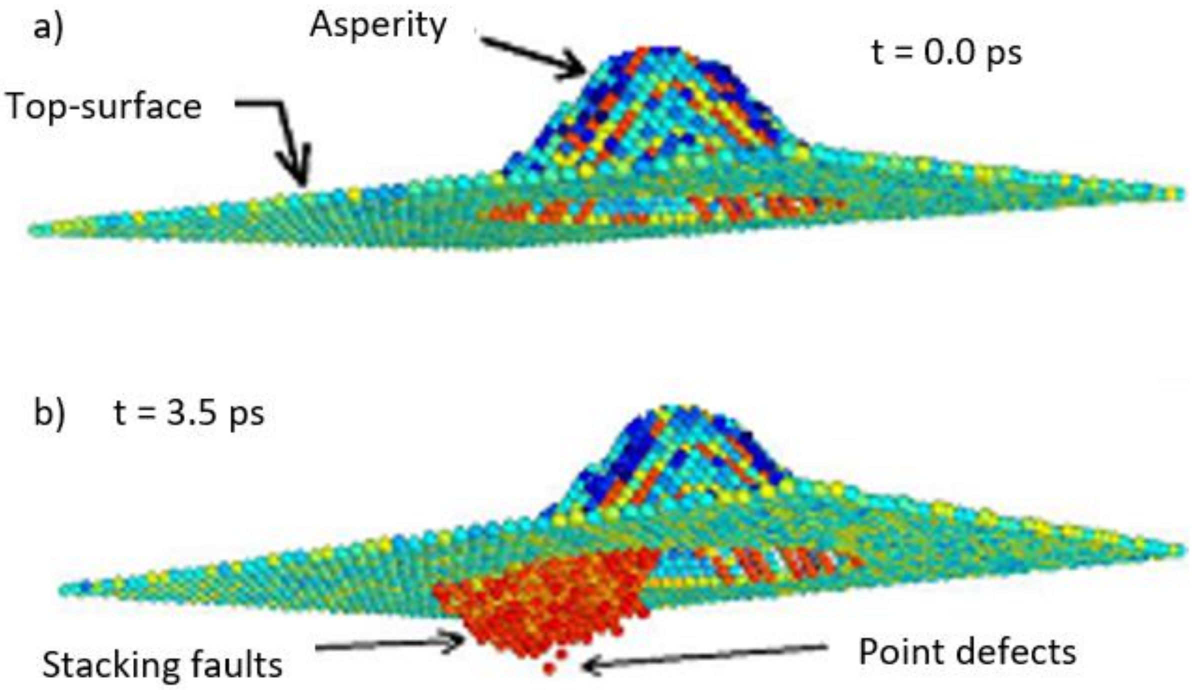

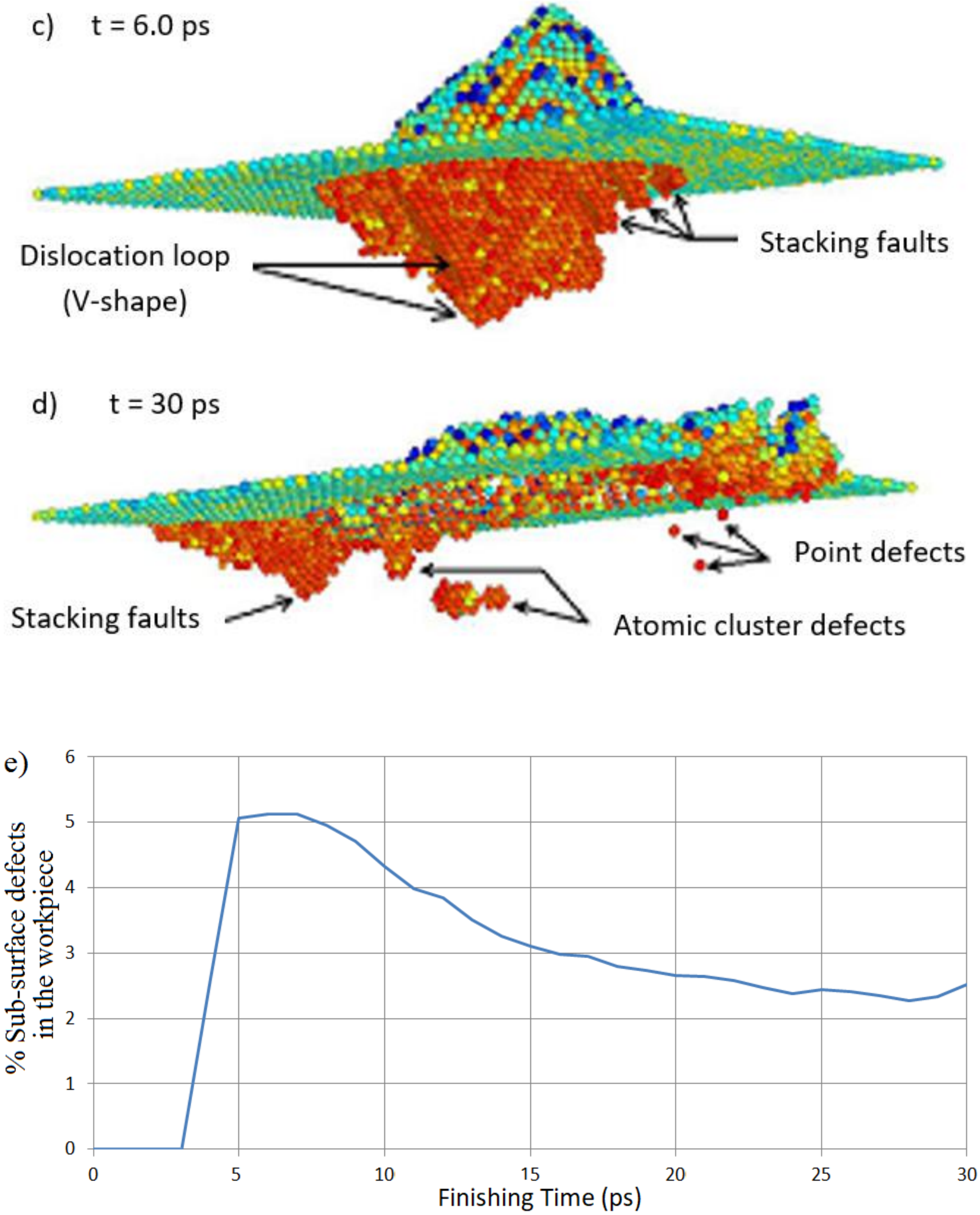

Fig. 4.23: Sub-surface defects during mechanical finishing on stainless steel at different levels of time steps (a-d). (e) Plot for generation of sub-surface defects in percentage and variation of the defects as the polishing process progresses.

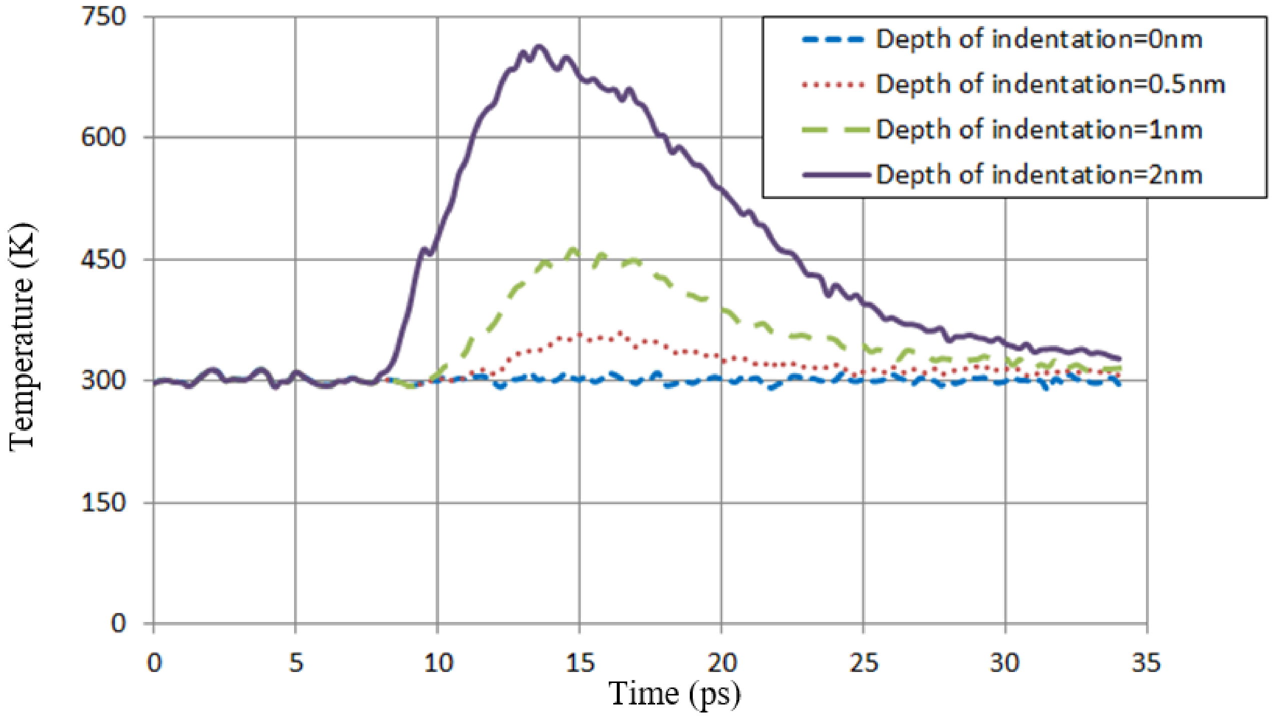

Fig.4.24: Temperature variation during the abrasion process with different depth of indentations as labelled on the plot on *SS304L*.

4.2.7.5. Temperature rise in stainless steel

Initial temperature of the entire system including the base of the workpiece becomes 300 K as the Newtonian atoms are equilibrated at 300 K and the thermostat atoms are set at 300 K.

When abrasion of a single stroke is applied with a known value of indentation depth (0, 0.5, 1 and 2 nm), the workpiece deforms by the abrasive particles resulting in chip formation and the temperature variation as shown in Fig. 4.24. This change in temperature occurs for a small contact time, and it gets stabilised to the ambient temperature as time progresses. In this case, the maximum temperature attained is around 700 K.

4.2.8. Correlation for material removal

Material removal and indentation depth significantly depend on the indentation force. Indentation force has relation with polishing pressure of CMMRF process, and MDS results are presented in Table 4.2 to develop a mathematical formulation to represent a relationship between the indentation force and material removal for three engineering materials. This results show indentation force (*Fz*) and cutting force (*Fx*) at different levels of material removal (in depth).

Table 4.2: MDS results on stainless steel, aluminium and silicon.

Depth of removal (nm)	Stainless steel		Aluminium		Silicon	
	Fz (nN)	*Fx* (nN)	*Fz* (nN)	*Fx* (nN)	*Fz* (nN)	*Fx* (nN)
0	0	0	0	0	0	0
0.5	24	16	6.4	4.8	104	32
1	48	35.2	12	9.6	200	72
2	104	88	25.6	22.4	240	56

A mathematical correlation is also expressed as follows.

Let, the cross-sectional area of the abrasive indented inside the workpiece $=A=\pi r^2$; and $r^2=R^2-(R-h)^2 \approx 2hR$. Thus, the average stress on workpiece $(\sigma)=Fz/A=F/2\pi hR$. This stress can be equated to the stress developed in the workpiece in the form of maximum stress level or theoretical tensile strength $(E/2\pi)$ of workpiece. Now, *Fz* is expressed in Eq. (4.5).

$$Fz= C\mathrm{x}(E/2\pi)\mathrm{x}2\pi hR \qquad (4.5)$$

Here, Fz=indentation force in nN, h=depth of indentation in nm, R=radius of abrasive particle in nm. From MDS results of Mises stress, it is seen that material removal happens at theoretical value but stress value changes from one atom to others as shown in Fig. 4.10 (c) and Fig. 4.17 (c). Thus, the average value of stress of the abrasion zone will be lower than the maximum stress, and it can be correlated by a factor '*C*' which will be a function of chips' size and shape as chip forms ahead of abrasive particle to resist the motion of abrasive particle. C=correlation factor which takes care to correlate theoretical strength to flow material in terms of average flow stress. It is found to be equal to 0.05 in present case. This correlation is validated with MDS results as shown in Fig. 4.25.

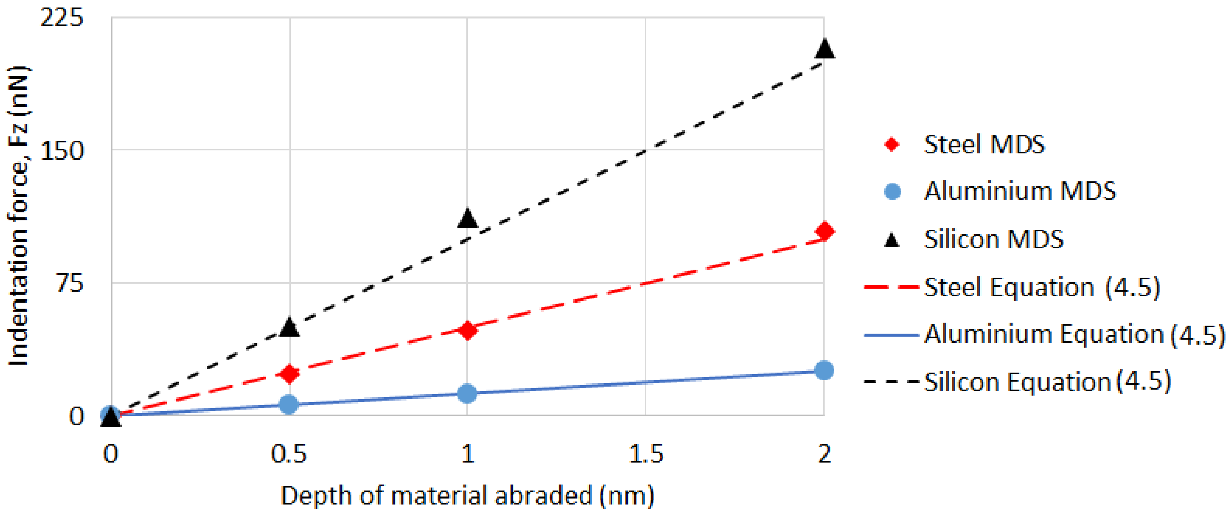

Fig.4.25: Correlation between indentation force and material removal along depth is made by using MDS results for aluminium, silicon and stainless steel.

Thus, there will be a correlation between indentation force and material removal, which is governed by the hardness of workpiece material as one of the significant property. However, behaviour of phase transformation and temperature building depend on other parameters also. For example, the phase transformation depends on the type of materials, such as ductile and brittle material. In case of silicon, the phase transformation is taking place from diamond cubic to amorphous phase. In other words, aluminium shows the phase transformation from FCC to the mixture of BCC and HCP.

4.2.9. Discussion on mechanical finishing

In case of ductile material, the material removal takes place by elasto-plastic deformation which occurs mainly due to the phase transformation of lattice structure. During abrasion, abrasive particle moves along [100] direction which is x-axis and as abrasion progresses, abrasive particle tries to push the asperity in all possible directions which depends on the normal to the surface of abrasive particle at the contact between them. However, FCC lattice has only three slip directions which are a line family of <1 -1 0>, BCC has another two sets of slip directions which are a line family of <1 -1 1> and HCP shows three slip directions which are <1 1 -2 0>. To facilitate material deformation and flow of chip along a defined direction made by abrasive particle, lattice transformation takes place so that the slip direction can match with the normal direction towards minimisation of the energy for the chip flow efficiently and due to this FCC phase is getting converted in to BCC and HCP as shown in Fig. 4.6 (b).

When abrasion takes place, the finishing force applies excessive stress (as shown in Fig. 4.10) on the workpiece to increase potential energy which induces strain energy of workpiece and it also gets transformed from the strain energy to the thermal energy. Moreover, the thermal energy also gets conducted and reduced due to the thermal conductivity of material. In present case, conductivity is modelled by applying a set of thermostat atoms as described in the section of MD simulation. Hence, abrasion increases temperature upto some value due to the strain induced thermal energy, thereafter, it reduces upto room temperature with the help of conduction, as shown in Fig. 4.12. This variation in temperature also assists for the phase transformation and phase recovery.

In case of brittle material, material deformation takes place in form of elastic deformation followed by rupture, and the elastic deformation causes distortion of lattice structure in the same phase. When finishing stress exceeds beyond the elastic limit, the interatomic distance between atoms becomes more than the cut-off length which results in undefined and random position of atoms. Thus, the phase of material gets transformed into amorphous phase. After this phenomenon when amorphised atoms come closer to each other, these atoms do not form any defined lattice as rearrangement of atoms in a well-defined structure of ‘diamond cubic’ needs excessive energy, and due to this, phase of workpiece after finishing process does not recover as shown in Figs. 4.12 (a-d). Potential energy of material also increases with the finishing force as the force does the bond breaking without allowing plastic deformation of parent lattices and increases Gibb’s free energy of the abraded atoms drastically. This jump in potential energy is approximately two orders of magnitude higher in case of silicon with respect to aluminium as aluminium consumes a good amount of energy through the plastic deformation as discussed earlier.

As far as abrasive particle is concerned, it degrades or damages due to the following reasons.

- Adhesion of chip on abrasive particle through strong bonds like ionic bond and metallic bonds.
- Wear of abrasive particle happens by phase transformation when workpiece hardness is comparable with abrasive particle.

These types of damages are temperature dependent also. When finishing force increases, local temperature increases which yields intensive damage to the abrasive particles. To avoid such problem, mechanical finishing at low temperature or under a cooling medium such as water should be used.

The outcome on the study of finishing process by mechanical abrasion is categorised as advantages and disadvantages of mechanical finishing.

4.2.9.1. Advantages of mechanical finishing

This process is useful for material removal and there are following parameters which help in higher MRR.

1. Temperature rise: Local temperature near the finishing zone depends on the indentation and abrasion force. Higher force induces more temperature and it can go upto the melting point of material. By getting higher temperature, workpiece material gets softened selectively and yields in easier material removal.
2. Phase transformation: The finishing force changes lattice structure and its orientation towards the plastic deformation followed by the chip formation.

3. Finishing force: Indentation and cutting force are responsible for material removal. It is observed that the material removal increases approximately linearly with increasing indentation and cutting force.

It is now observed that the mechanical finishing helps in material removal at nanometric scale by using two mechanisms (temperature rise and the phase transformation). However, there are some challenging aspects which deteriorate the surface quality. These aspects are listed and reported as disadvantages of mechanical finishing as follows.

4.2.9.2. Disadvantages of mechanical finishing

MD simulation reveals that mechanical finishing damages the surface quality and the same are discussed as follow.

1. Potential energy: potential energy of workpiece after mechanical finishing increases, which makes them chemically unstable and corrosive. From the potential energy graph, it is observed that the optically finished (or nanofinished) surface is not recommended for mechanical abrasion. This process damages surface quality at the atomic scale.
2. Lattice structure: lattice structure of workpiece gets altered after mechanical finishing. For example, FCC lattice of stainless steel or aluminium is changed to HCP and BCC. Diamond cubic (DC) lattice of silicon changes to amorphous phase.
3. Sub-surface damages: sub-surface damages are observed and it is found that the sub-surface defects increase as mechanical finishing progresses.
4. Surface morphology: In general, hard tool does material removal and generates its impression on comparatively softer workpiece. Thus mechanical finishing creates surface defects in the form of digs and scratches and the same effect is observed in MDS after morphological analysis. This effect seizes the process capability to generate atomically flat surface.

4.2.9.3. Details of mechanical finishing

To understand the phenomenon of mechanical finishing, a schematic has been made by considering some of the significant attributes and presented as shown in Fig. 4.26.

When force is of the order of few nano-newton, few atoms get removed and a little deformation of the lattices take place which recovers back after finishing and due to this there is a slight change in potential energy in 'ultra-precision zone' as shown in Fig. 4.26. As force increases beyond this zone, workpiece material gets permanently deformed and it also damages the lattices permanently which results in an increase of potential energy to make the surface chemically unstable.

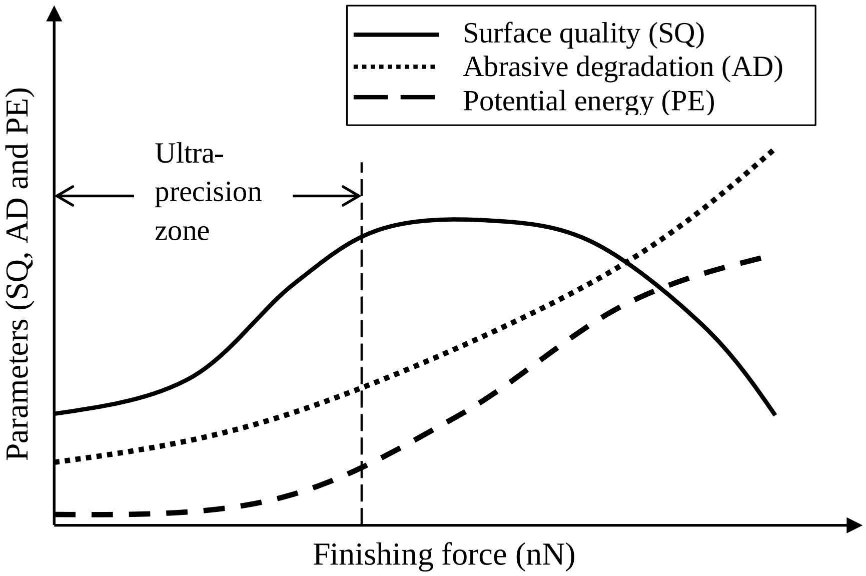

Fig. 4.26: Effect of finishing force on surface quality, abrasive particle degradation and potential energy due to mechanical finishing.

Surface quality is a parameter which indicates the surface quality in term of roughness which improves when finishing force increases from 0 nN to few nN or less. In this case, finishing force does smoothening of roughness without altering phase and potential energy of nano-peak when the force is within the ultra-precision zone. Maintaining of such small force need ultra-high precision machine tool or tactful tool so that the finishing force cannot go beyond the vertical dotted line (as shown in Fig. 4.26). When force becomes more than tens of nano-

Newtons, it creates scratches and digs in nanometric scale which increases surface roughness, and accordingly the surface finish quality starts deteriorating as shown in Fig. 4.26.

Finishing force leads to increase in temperature which assists material loading and the wear rate on the abrasive particle, and due to this the quality of abrasive particles degrades with finishing force as shown in Fig. 4.26.

In brief, the mechanical finishing is not capable to generate defect free and atomically flat surface. Therefore, it is required to mitigate the disadvantages of this process. In view of this, effect of chemical and chemical assisted mechanical finishing is studied and reported in the following sections.

4.3. MD simulation for chemical reactions

The potential energy of surface atoms varies from one place to another, and it results in different chemical reaction rate in different zones. Similar study was also carried out by French et.al [134] as shown in Fig. 4.27.

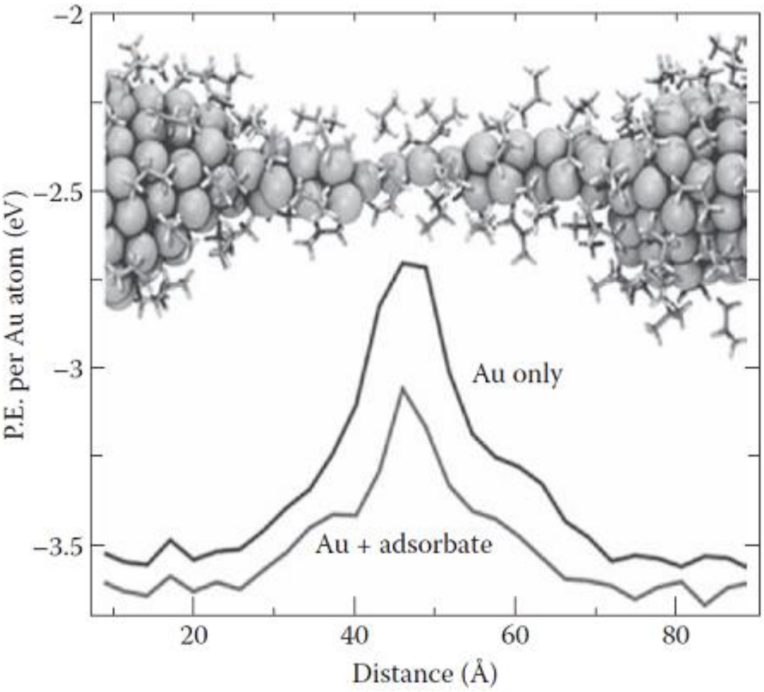

Fig. 4.27: Effect on potential energy per atom and adsorption due to variation of sharing atoms [134].

Moreover, the chemical reactions occur in the form of chemical etching or passivation. Chemical etching results in material removal and chemical passivation results in the formation of protective layer over the workpiece. These types of reactions are studied by using reactive molecular dynamics simulations as per flow chart shown in Fig. 4.2. Details for the MD simulation on chemical reactions are discussed as follows.

4.3.1. MD simulation for chemical reaction on Aluminium, Silicon and Stainless steel

To carry out MD simulation for chemical reactions, reactive force field (ReaxFF) potential functions [135] are used for aluminium and silicon materials. ReaxFF technique was developed by Duin and Kimberly [136] to bridge the gap between quantum chemical and classical MDS. In case of stainless steel, hybrid type of potential function is used which consists EAM, MEAM and MORSE. Details for the chemical reactions are given in Table 4.3.

Table 4.3: Selection of materials to study chemical reaction through MD simulation

Sr. No.	Workpiece materials	Chemical medium	Remark
1	Aluminium	Water, Aqueous KOH, Aqueous H_2O_2 and Aqueous HNO_3	Effect of alkaline, bleaching and acidic medium on Al.
2	Silicon	Water, Aqueous KOH and Aqueous H_2O_2	Effect of alkaline and bleaching medium on Si.
3	Stainless steel	Chemically active oxygen for the oxidising agent such as HNO_3, H_2O_2, etc.	Effect of oxidising agent on steel.

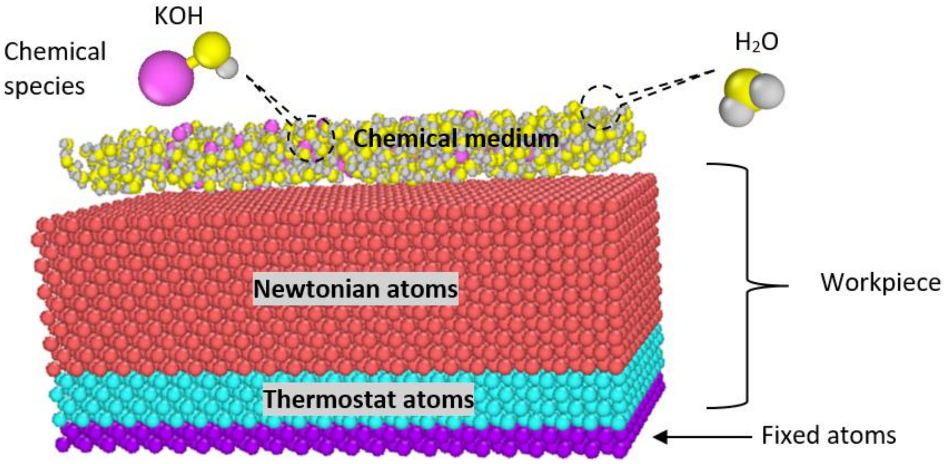

Fig. 4.28: Schematic of the model for reactive MD simulations to study chemical reactions.

Schematic for the MD simulation is presented in Fig. 4.28. In this study, possible chemical reactions are studied and their effects are also investigated on material removal, morphological changes and chemical contamination on workpiece.

Details about chemical building for MDS: Steps to build the data file for a specific chemical to simulate using LAMMPS, is reported in the section A2 of Appendix.

4.3.2. Chemical reaction

In this study, chemical environment is used to understand chemical reactions listed in Table 4.4.

Table 4.4: List of inter-atomic pair potential for chemical reaction.

Sr.No.	**Workpiece material**	**Chemicals**	**Inter-atomic pair potential for chemical reaction.**
1	Aluminium	H_2O, KOH, H_2O_2 & HNO_3	Reactive force field
2	Silicon	H_2O, KOH, H_2O_2 & HNO_3	Reactive force field
3	Stainless steel	Oxidiser	Hybrid of EAM, MEAM, Morse and Tersoff

4.3.3. Effect of chemical reaction on rough surface

In this study, a conical asperity is incorporated to represent surface roughness. It is found that the chemical reaction gets intensified on sharp and nano-peaks.

For example, results of stainless steel are presented. Figs. 4.29 (a-d) show the effect of chemical reactions on stainless steel due to oxidiser. Fig. 4.29 (a) shows lattice structure of workpiece before chemical reaction, in which all atoms belong to FCC lattice except on the top surface with one atomic layer. Fig. 4.29 (b) illustrates the phase transformation due to the chemical reaction which exhibits higher reaction rate at sharp apex as shown in Fig. 4.29 (c). After removing of the chemically affected layers, lattices of workpiece are mapped and presented in Fig. 4.29 (d) which show that the chemical reaction yields the smooth surface formation.

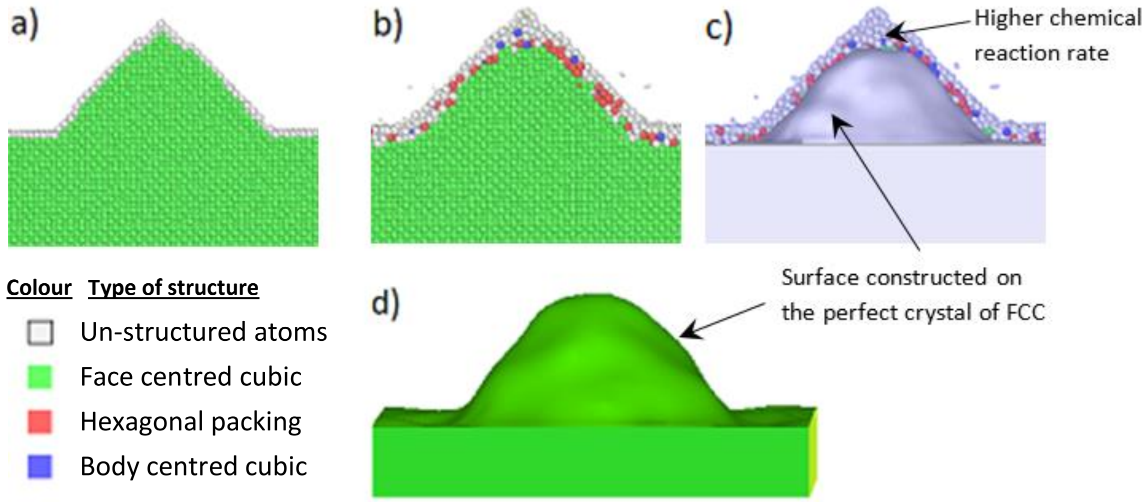

Fig. 4.29: Chemical reactions on stainless steel with oxidising agent. (a) Surface with sharp asperity without chemical. (b) Chemically reacted surface due to oxidisers. (c) Meshing of perfect FCC lattice after chemical reaction. (d) Mesh of surface after removal of chemically reacted layers.

From this it is understood that the chemical reaction gets intensified near the sharp edges (there will be high possibility for such sharp edges in rough surface) of workpiece. There is a need to understand the mechanism of chemical reaction using various types of chemical species such as alkaline medium, bleaching agent, and acidic medium. These reactions are carried out using reactive-MD simulation and reported in the following section.

4.3.4. Effect of chemicals on aluminium

Three different chemicals are used namely, aqueous KOH (alkaline medium), aqueous H_2O_2 (bleaching medium) and aqueous HNO_3 (acidic medium) to study their effects on aluminium workpiece. Workpiece contains 8505 numbers of atoms in which 467 atoms are exposed to the chemical media on the surface of workpiece.

4.3.4.1. Effect of alkaline medium on aluminium

Alkaline, or base media are chemicals which have pH value more than 7 when it is mixed with water. In general, it consists hydroxide ions (OH^-) such as potassium hydroxide (KOH), sodium hydroxide ($NaOH$), calcium hydroxide ($CaOH$), etc. Effect of the chemical reaction due to alkali medium such as aqueous *KOH* is studied on aluminium workpiece, and it is found that the aqueous *KOH* solution attacks *Al-Al* bonds and forms *Al-OH* as shown in Fig. 4.30. This bond breaking occurs when the interatomic bond (*R*) becomes more than the cut-off length (*Rc*) as described in the pair-potential function of atoms. During this reaction, *KOH* and H_2O also get adsorbed on the surface of bulk aluminium material.

In order to understand the chemical reaction, number of atoms is computed and plotted after their absorption in aluminium substrate as shown in Fig.4.31. In this plot, *K*-atoms are not interacting with aluminium. As, *O*-atoms and *H*-atoms interact from OH^- species, the number of *O*-atoms and *H*-atoms are in the same proportion from time duration of 0 to 0.8 ps. Thereafter, oxidation of aluminium starts and results in the formation and evaporation of *H*-atoms as H_2 gas. In the same time one more reaction starts, which is adsorption of water molecule as shown in Fig. 4.30.

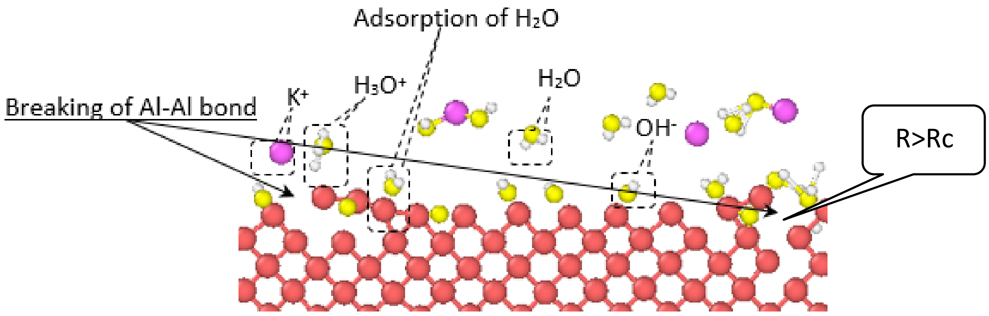

Fig. 4.30: Oxidation and removal of *Al*-atom under the presence of aqueous *KOH*.

After 1.4 ps, number of atoms for chemical reaction becomes constant which means that the surface of aluminium is completely covered by chemicals as aluminium oxide or hydroxide. As the atoms of workpiece surface is completely oxidised and prevents further reaction, is also known as passivation of the surface. Thus, alkaline medium causes the formation of metal hydroxide followed by oxidation and passivation of workpiece in which maximum of 110 numbers of oxygen atoms are absorbed.

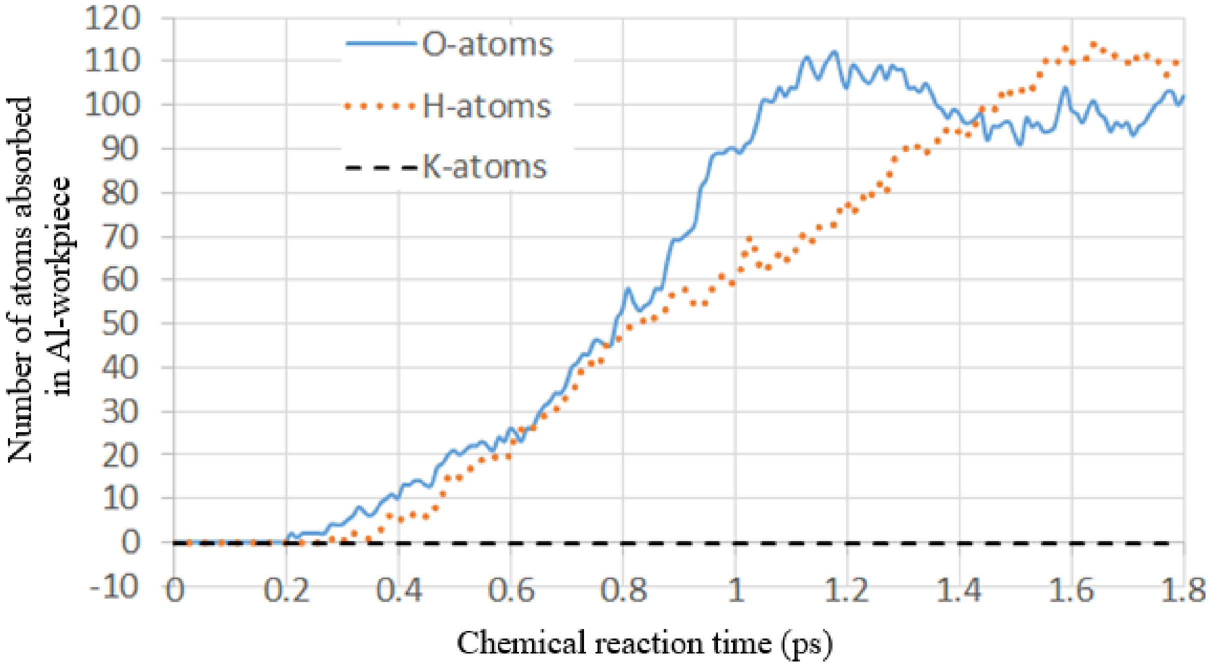

Fig. 4.31: Absorption of atoms from aqueous *KOH* into aluminium workpiece.

4.3.4.2. Effect of bleaching agent on aluminium

Bleaching agents mostly work as oxidizing agents, such as sodium hypochlorite (*NaOCl*) or hydrogen peroxide (H_2O_2), and these agents are generally used for the removal of stains. Figs. 4.32 (a-b) show chemical reaction of aluminium workpiece under the presence of aqueous H_2O_2 at time 0.1 ps and 0.3 ps respectively.

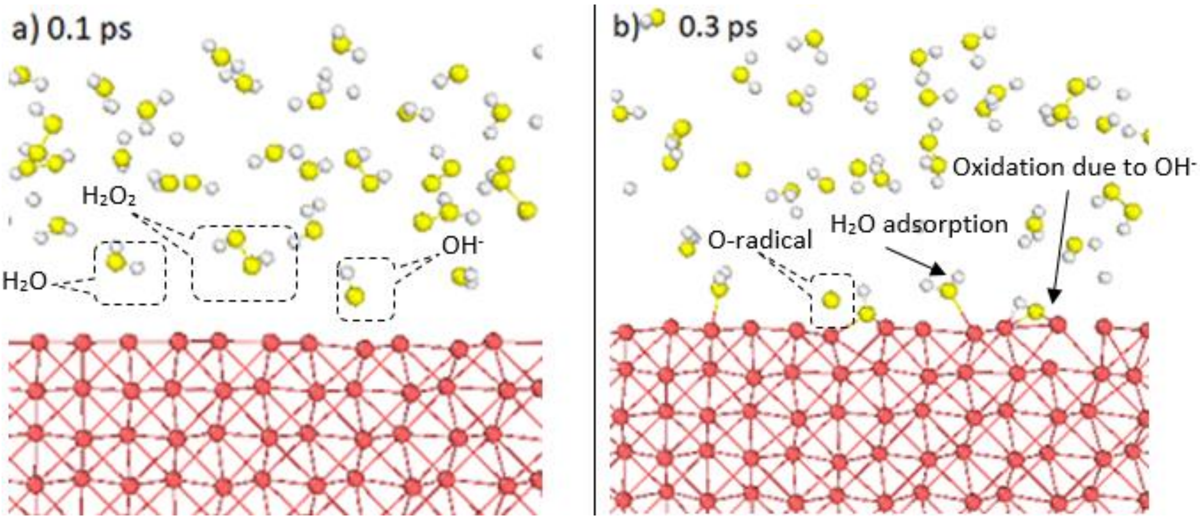

Fig. 4.32: Oxidation and removal of *Al*-atom under the presence of aqueous H_2O_2.

In this chemical reaction three phenomena are observed, the 1st phenomenon illustrates oxidation of aluminium due to hydroxyl anions. The 2nd phenomenon shows adsorption of water molecules. The last one is about formation of oxygen radicals from the hydrogen peroxide molecules, which further results in oxidation and material removal as well.

Fig. 4.33 shows adsorption and absorption of atoms from the chemical molecules on aluminium workpiece. It is observed that during initial stage of reaction (time ranging from 0.2 to 0.9 ps), effects of hydroxyl anions and oxygen radicals dominates and results in more number of oxygen transfer inside the aluminium substrate as shown in Fig. 4.33. In other words, the hydrogen peroxide rich layer depletes with time, which causes to domination of adsorption of water molecules and passivation of the surface of workpiece.

After 0.9 ps, number of *H*-atom increases with respect to *O*-atoms, and their quantity stabilises with time after 1.2 ps as the surface of the workpiece gets passivated with the maximum of 220 oxygen atoms.

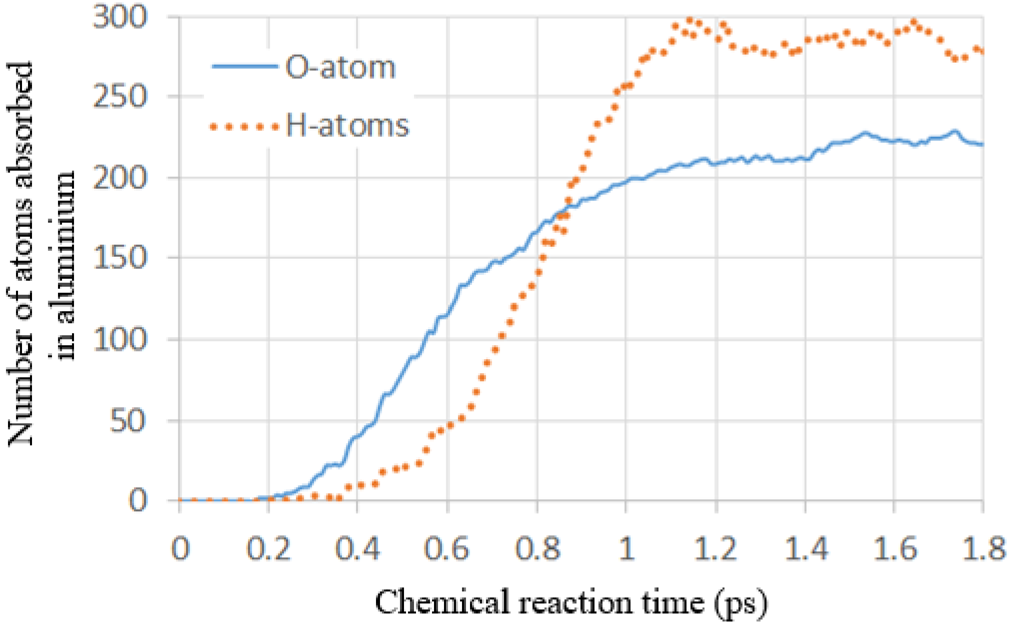

Fig. 4.33: Adsorption and absorption of atoms from aqueous H_2O_2 into aluminium workpiece.

4.3.4.3. Effect of acidic agent on aluminium

In the present case aqueous nitric acid is used for chemical reaction. Figs. 4.34 (a-b) show chemical reaction between aqueous HNO_3 and aluminium workpiece. It is seen that the chemical reaction produces aluminium oxides and nitrates on the surface of workpiece. In addition, H-atoms get absorbed in the aluminium substrate as shown in Fig. 4.34 (b).

Results of these chemical reactions are computed and plotted as shown in Fig. 4.35. It is observed that the oxidation process dominates initially, thereafter, adsorption of water and nitrate formation also starts. After some more time, the chemical reaction stops as the number of atoms does not change after 1.4 ps, which can be called as passivation, as shown in Fig. 4.35. At the time of 1.8 ps, aluminium absorbs 220 O-atoms which is similar to the chemical of aqueous H_2O_2 but two time more than aqueous KOH.

From the results of Fig. 4.35, it is observed that the chemical reaction starts on the workpiece and it stops after some time as the reaction (or transaction of atoms) saturates after a definite time of the chemical reaction.

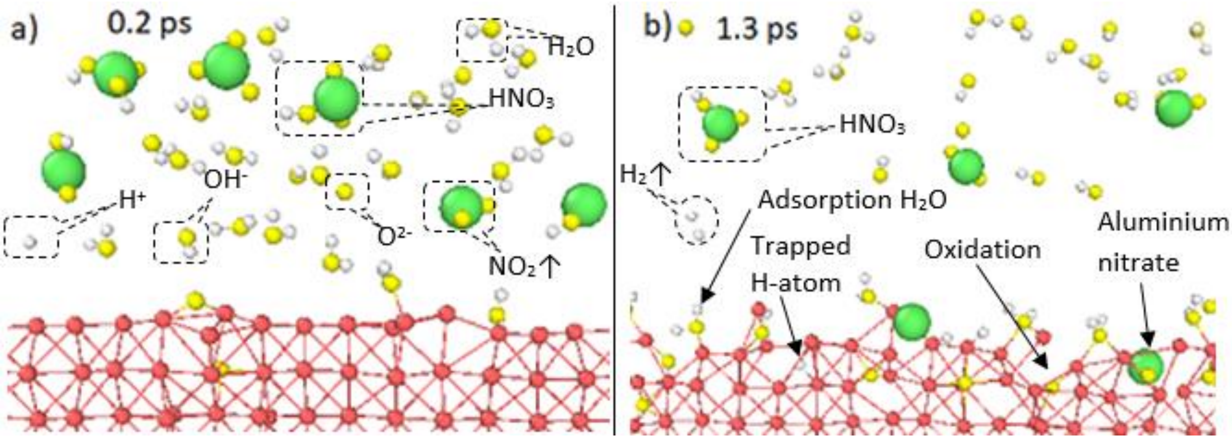

Fig. 4.34: Oxidation of Al-atom under presence of aqueous HNO_3. (a) Position of atoms at time =0.2 ps. (b) Chemical reaction at time=1.3 ps.

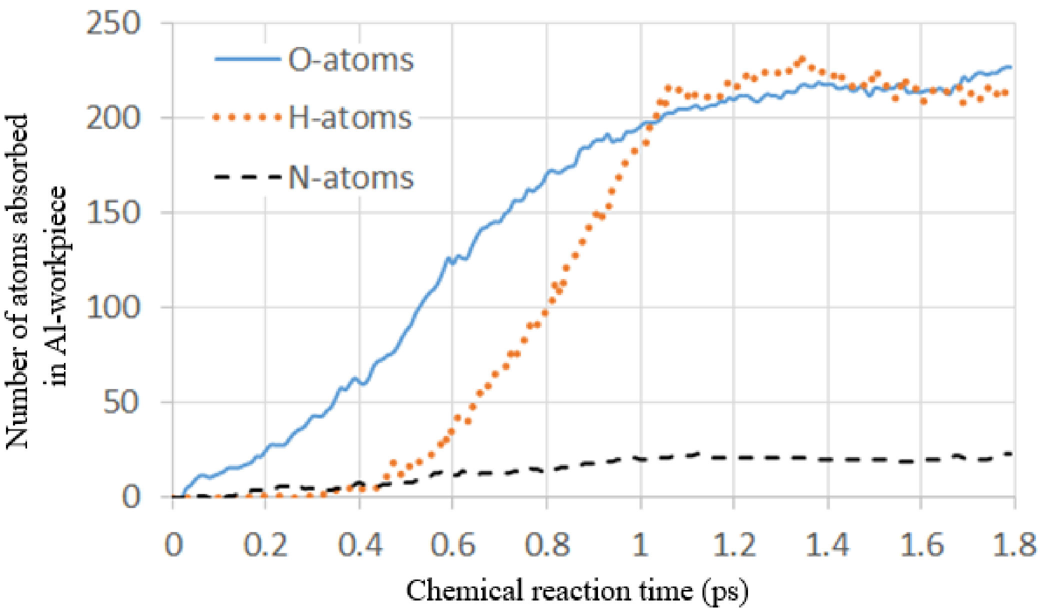

Fig. 4.35: Absorption of atoms from aqueous HNO_3 into aluminium workpiece.

4.3.5. Effect of chemicals on silicon

Three different chemicals are used namely, aqueous *KOH* (alkaline medium), aqueous H_2O_2 (bleaching medium) and aqueous HNO_3 (acidic medium) to study their effects on silicon workpiece.

4.3.5.1. Effect of alkaline medium on silicon

Potassium hydroxide (*KOH*) is used as an alkaline medium in this study. In order to understand the chemical reaction, number of atoms is computed and plotted after their absorption in silicon substrate as shown in Fig.4.36. This plot indicates that potassium atom does not interact with silicon, hydrogen atom interacts more and oxygen atom interacts moderately. After 1.5 ps of time, quantity of hydrogen and oxygen atoms become same, which indicates towards the formation of silicon hydroxide (*Si-OH*) compound on the surface of workpiece. For better understanding about the chemical reaction, positions of atoms are also captured at 1.6 ps and presented as shown in Fig. 4.37 which indicates about the hydride and oxide formation on surface.

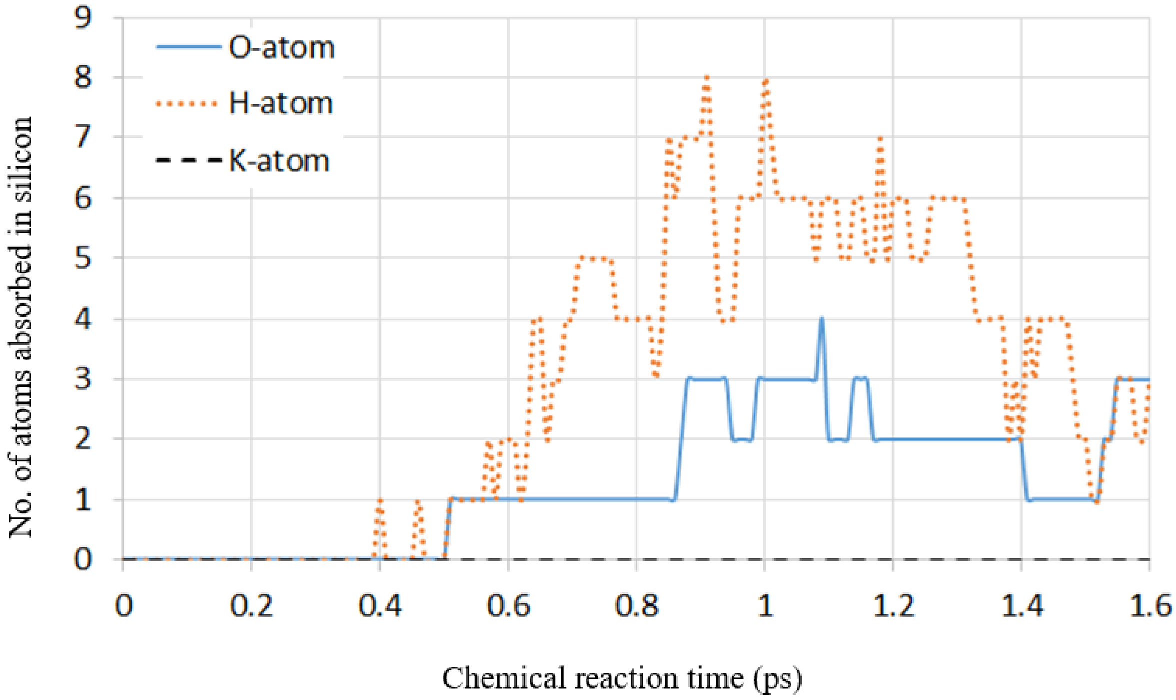

Fig. 4.36: Absorption of atoms from aqueous *KOH* into silicon workpiece.

Thus, alkaline medium causes the formation of oxide, and 3 numbers of oxygen atoms are absorbed in silicon at 1.6 ps.

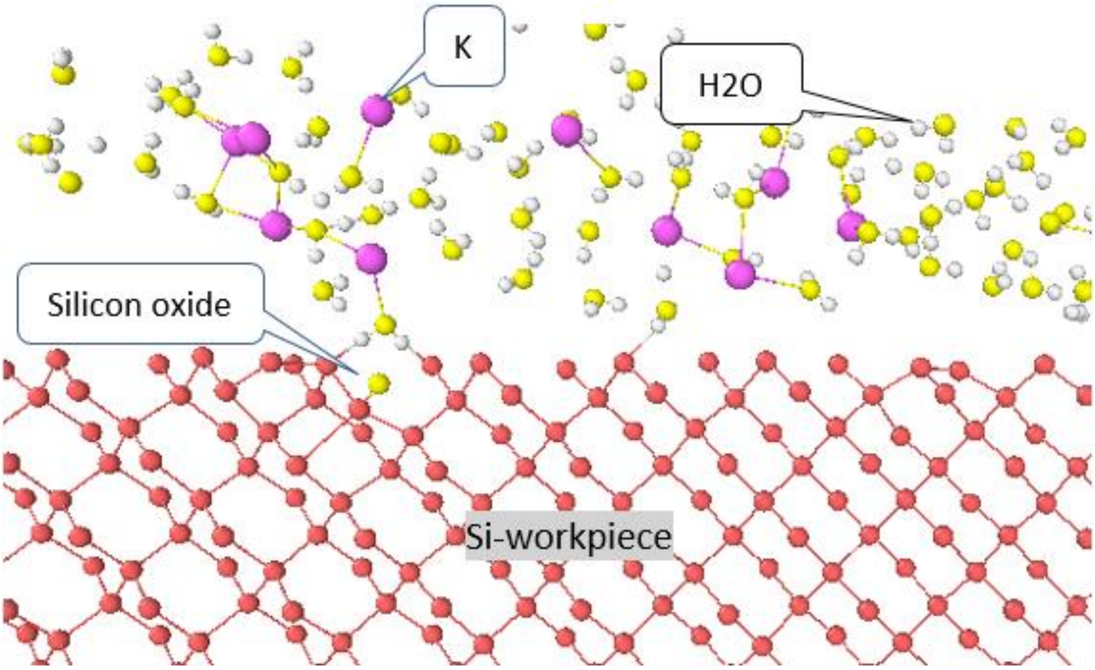

Fig. 4.37: Chemical reaction from aqueous *KOH* on silicon surface workpiece at 1.6 ps.

4.3.5.2. Effect of bleaching agent on silicon

Hydrogen peroxide (H_2O_2) is used as a bleaching agent in this study. In order to understand the chemical reaction, number of atoms is computed and plotted after their absorption in silicon substrate as shown in Fig.4.38. It is observed that there is an increase in *O*-atom and *H*-atom with time till 1 ps, and thereafter, it saturates which indicates passivation of Si-workpiece. Fig. 4.39 shows oxidation and absorption of water on surface. After 1.2 ps, the surface of the workpiece gets passivated with 12 oxygen atoms as shown in Fig. 4.38.

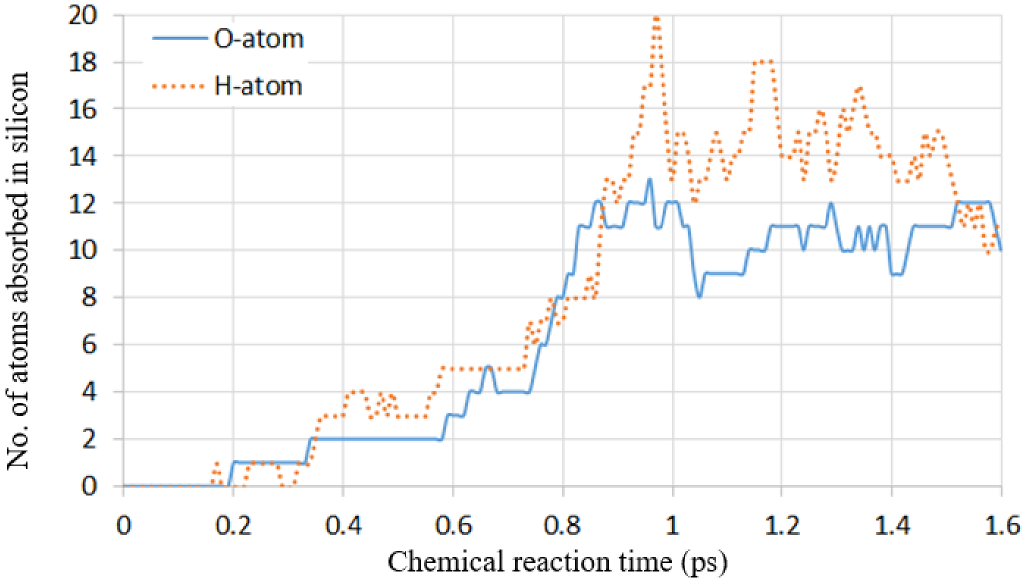

Fig. 4.38: Absorption of atoms from aqueous H_2O_2 into silicon workpiece.

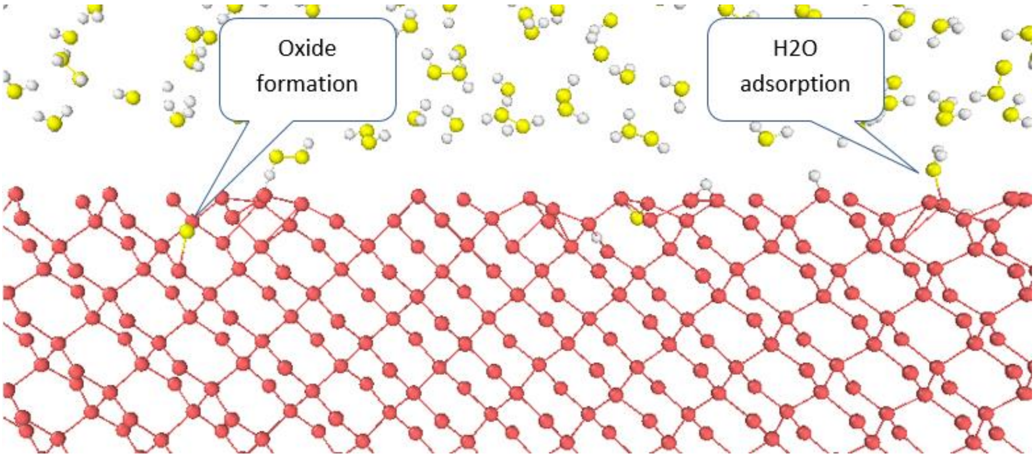

Fig. 4.39: Chemical reaction on surface of *Si* under presence of aqueous H_2O_2.

4.3.5.3. Effect of acidic agent on silicon

In the present case aqueous nitric acid is used for chemical reaction. Results of these chemical reactions are computed and plotted into silicon workpiece as shown in Fig. 4.40. From time 0 to 1 ps, absorption of all three atoms (*O*, *H* & *N*-atoms) increases, where, the absorption rate is more in case of oxygen, moderate in case of hydrogen and least in case of nitrogen atom.

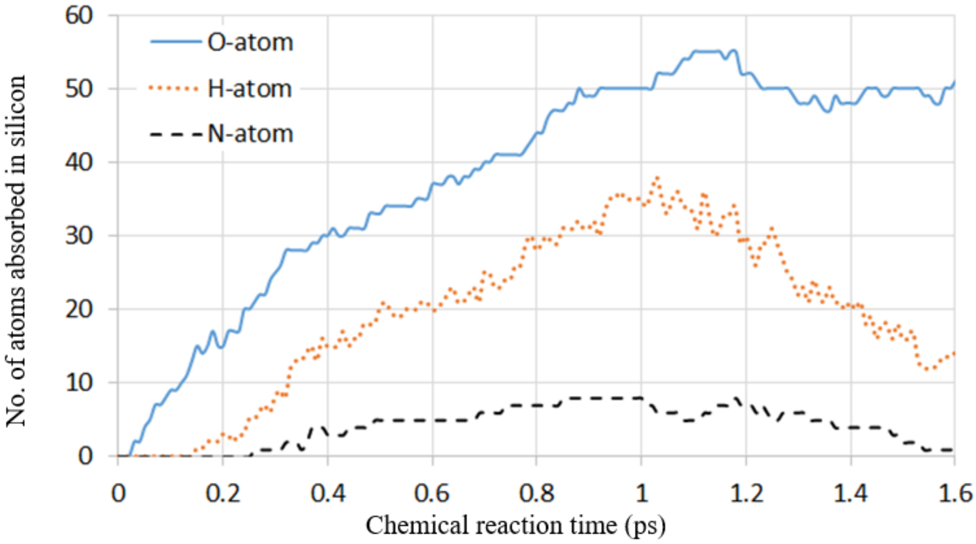

Fig. 4.40: Absorption of atoms from Nitric acid into silicon workpiece.

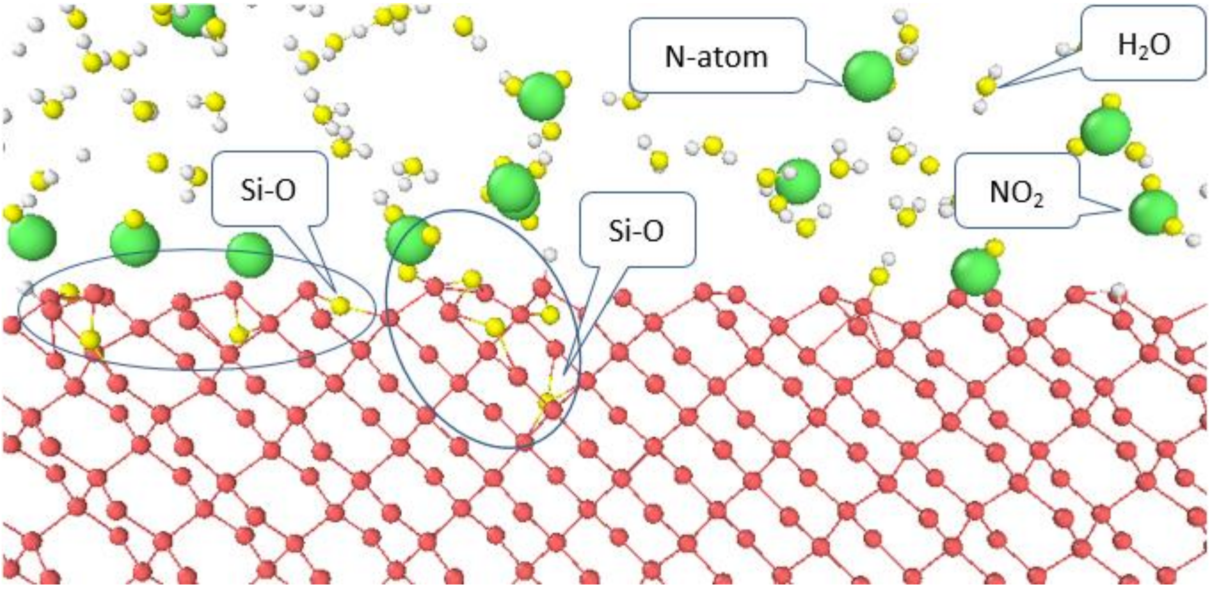

Fig. 4.41: Chemical reaction on surface of *Si* under presence of nitric acid

Since, nitric is a strong oxidising agent, it offers more oxidation and percolation inside of workpiece as shown in Fig. 4.41. After 2 ps, nitrogen atom starts reducing and it comes down near to zero. However, oxygen atom remains unchanged after 1.2 ps, which indicates silicon oxidation with passivation. This oxidation phenomenon is clearly seen on Fig.4.41. At the time of 1.6 ps, 50 *O*-atoms are absorbed in silicon workpiece which is much higher than *KOH* and H_2O_2. Workpiece contains 8505 numbers of atoms in which 467 atoms are exposed to the chemical media on the surface of workpiece.

4.3.6. Chemical reaction on SS304L

Since, reactive force field based interatomic parameters for chemical reactions on the alloying atoms of stainless steel (*Fe*/*Cr*/*Ni*) is not developed, reactive MDS is not possible in *SS304L*, and due to this the chemical reaction for analysis could not be performed on this material. Moreover, chemical reaction on the surface is possible by adding ‘Morse pair potential’. Thus, to study the effect of chemical on *SS304L*, chemically active oxygen is used to model oxidising agents like H_2O_2 and HNO_3. Results are presented in Figs. 4.42 (a-b).

A hybrid pair potential is used through classical MDS for chemically assisted mechanical finishing and the same is presented in the next section.

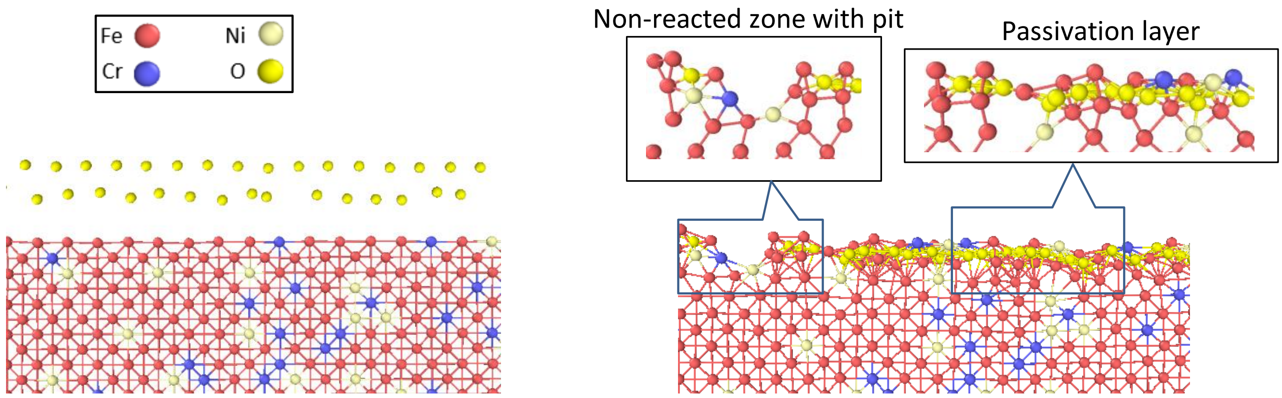

a) Time =0 ps

b) Time = 1.6 ps

Fig. 4.42: Chemical reaction on the surface of *SS304L*. (a) Atomic configuration at initial time, i.e. at t = 0 ps. (b) Atomic configuration after 1.6 ps of chemical reaction.

Fig. 4.42 (b) shows two aspects of chemical reaction, namely, non-reacted zone and passivated layer. Herein, non-reacted zone means the surface atoms which is not reacted by O-atoms and passivated layer means the layer formed with an intact layer of metal oxides which covers the parent atoms of workpiece to minimise further reaction, as shown in Fig. 4.42 (b). These two aspects ensure randomisation in chemical reaction by which some part of surface does not interact with chemicals and many places shows chemical reaction to form intact layer of metal oxides, i.e. passivation layer.

4.3.7. Comparison of chemical reactions

Chemical reaction of MDS study is compared in a Table 4.5.

Table 4.5: effect of chemical reaction on Al, Si and *SS304L*

Sr. No.	**Workpiece**	**Number of O-atoms absorbed in workpiece after 1.6 ps**			**Remark**
		KOH	**H_2O_2**	**HNO_3**	
1	Aluminium	110	220	220	KOH is suitable as it shows slow reaction rate and stable passivation.
2	Silicon	3	12	50	KOH is suitable as it shows slow reaction rate and stable passivation.
3	*SS304L*	-	-		Oxidisers damages surface in random manner.

From the above results, it is observed that the chemical reaction starts on the workpiece and it stops after some time as the reaction (or transaction of atoms) saturates after a definite time of the chemical reaction. Hence, there is a need to apply a mechanical drive to remove the chemically reacted layers so that the chemical reaction progresses with time. It is found that KOH has slow reaction rate and better control on passivation of workpiece as compared with other chemicals, which are essential for chemically assisted mechanical finishing. In case of *SS304L*, oxidiser shows surface damages and due to this chemically active abrasive is implemented to study chemically assisted mechanical finishing.

4.4. MD simulation of chemically assisted mechanical finishing (CAMF)

Chemical environment and chemically active abrasive particles are used for material removal during chemically assisted mechanical finishing. This mechanism deals with the chemically assisted mechanical abrasion, which is studied and analysed. In this study, few engineering materials are selected such as Aluminium, Silicon and Stainless Steel. Suitable abrasive particles are used under the presence of chemical medium as listed in Table 4.6. MD simulation is presented in two different directions. 1st type is CAMF due to the chemical mixed in MR fluid; and the 2nd type is CAMF due to the chemically active abrasive particle. This work is also used to demonstrate the mechanism of material removal and quantification of parameters for mathematical modelling. Hence, a correlation has been established to compute material removal under the specified parametric conditions for CMMRF process. As far as simulation is concerned, a flow chart of Fig. 4.2 is implemented.

Table 4.6: List of inter-atomic pair potential for chemical assisted mechanical finishing.

Sr. No.	Workpiece material	Chemicals	Abrasive particle	Inter-atomic pair potential
1	Aluminium	Aqueous *KOH* as chemically active slurry	Silicon	Reactive force field – *Reactive MDS*
2	Silicon	Aqueous *KOH* as chemically active slurry	Diamond	Reactive force field – *Reactive MDS*
3	Stainless steel	Water to control temperature	Silicon dioxide as chemically active abrasive particle	Hybrid of EAM, MEAM, Tersoff & Morse – *Classical MDS*

4.4.1. CAMF in the presence of chemically reactive slurry

In the previous results of chemical reactions, it was found that the behaviour of chemical reactions was almost similar on aluminium and silicon. After enough time of chemical reaction, workpiece becomes inert by attaining a chemically passivated layer on the top surface of workpiece.

4.4.1.1. Effect of chemical slurry (aqueous KOH) during CAMF of Aluminium

During this process, both mechanical abrasion and chemical reaction as discussed earlier, are combined. The 1st aspect is mechanical aspect which is almost similar to the mechanical finishing, where phase change due to mechanical pressure comes from abrasive particle as shown in Fig. 4.43. It is found that the parent phase of aluminium is transformed to BCC and HCP.

Moreover, the top surface of workpiece is subjected to chemical reaction and it causes phase alteration on the parent lattice of workpiece. The 2nd aspect of this process is chemical reaction and its effect on mechanical finishing. Hereafter, the 2nd aspect is studied extensively, in which few significant mechanisms like chemical assisted material removal, surface and sub-surface quality improvement and effect of chemicals on abrasive particles are analysed.

Fig. 4.44 shows the chemical reaction before the indentation, and it is found that the top surface of workpiece gets oxidised near the indentation zone.

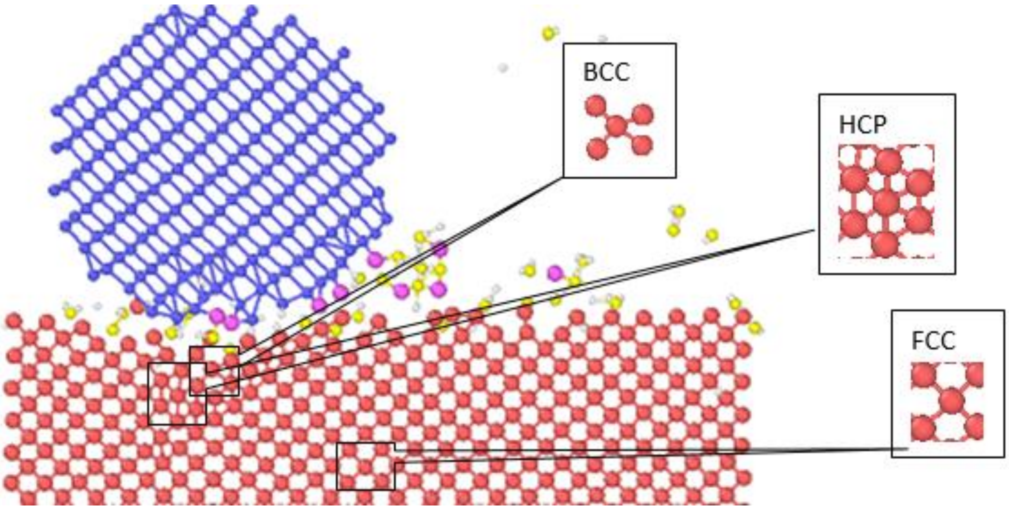

Fig. 4.43: Mechanical abrasion of aluminium due to silicon abrasive

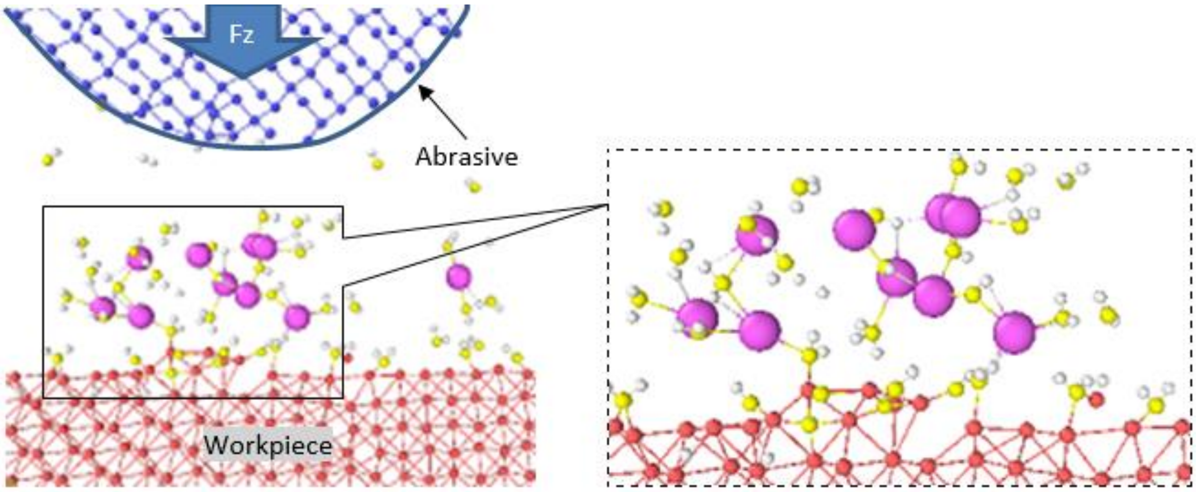

Fig. 4.44: Position of atoms before indentation of abrasive particle.

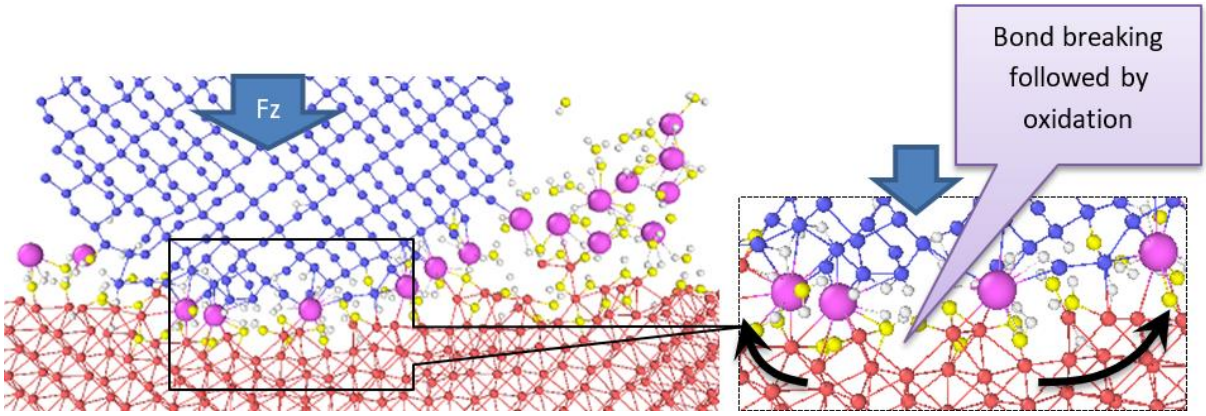

Fig. 4.45: Position of atoms/molecules at the time of indentation.

When an abrasive particle indents or abrades the workpiece, *KOH* and H_2O molecules get energized due the rise in local temperature (discussed in mechanical finishing) and cause bond breaking of parent material because of entrapped radicals of *H*-atoms as shown in Figs. 4.45-4.46. Fig. 4.45 illustrates that the concentration of *KOH* increases near the abrasion zone/direction as the mechanical deformation of workpiece increases its potential energy which further causes more oxidation.

Fig. 4.46 shows that the oxidised surface of workpiece which interacts with the abrasive particle having a strong bond. During the abrasion process, most of the oxidised atoms of workpiece gets removed. The material removal in this case occurs by stretching of oxidised layers which results in the parent bond breaking of workpiece with relatively less stable region or the rough surfaces. Hence, this is a method which is responsible to remove atoms from the rough surface significantly as compared with the smooth surface, and it results in atomically smooth surface.

Chemical oxidation to the workpiece material causes interaction of workpiece with abrasive particle, and the chemical reaction gets intensified when high indentation or pressure is applied. This phenomenon was studied by applying an impact with high indentation force with respect to the abrasion, as shown in Fig. 4.47. This figure illustrates that there is a formation of dig (shown by arrow which is caused by impact of the abrasive) during the impact load of indentation and it yields more material removal. In addition, the removal of material occurs in the form of oxides as discussed earlier.

In brief, chemical bonding between abrasive and workpiece occurs due to oxidation, and material removal from workpiece starts by breaking of weak metallic bonds compared to the newly formed oxides as shown in Figs. 4.46-4.49. Fig. 4.49 shows abrasive particle and workpiece after chemical assisted mechanical finishing. It indicates that the finished surface of the workpiece is free from the chemical contamination.

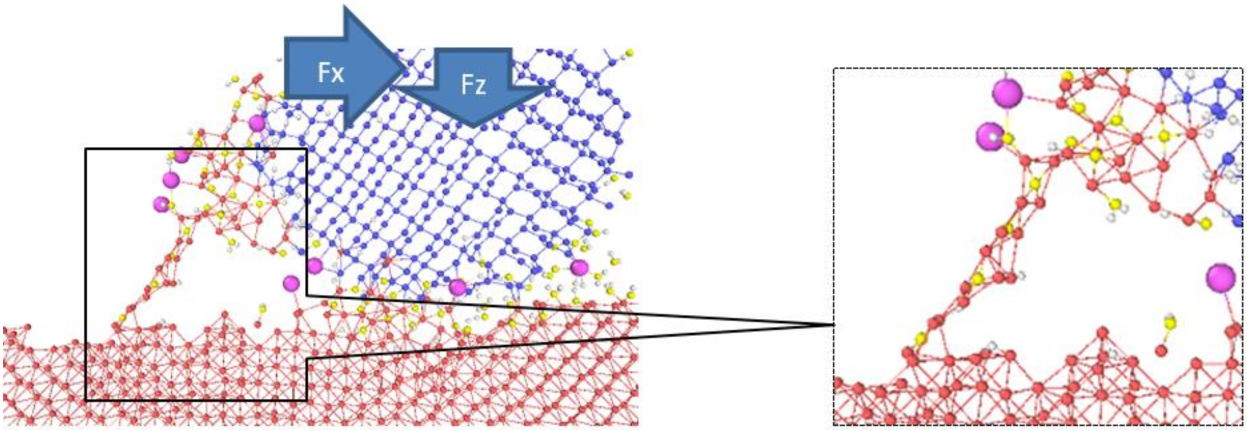

Fig. 4.46: Position of atoms/molecules and material removal during abrasion.

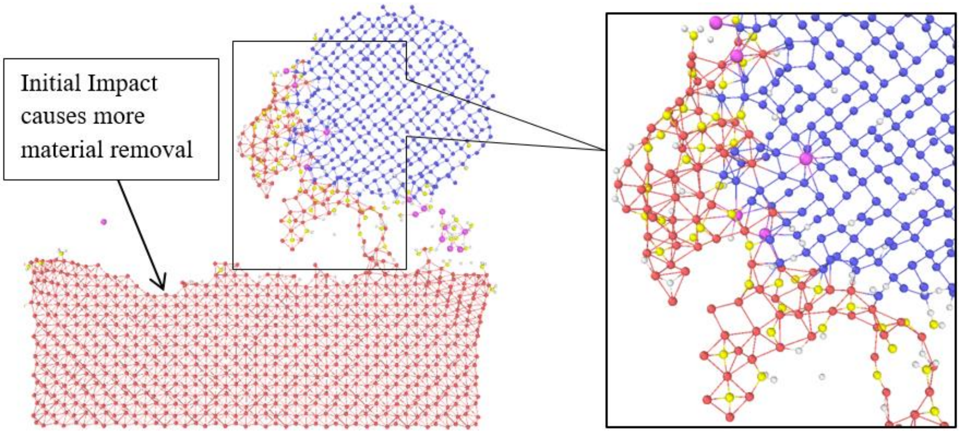

Fig. 4.47 Material removal after abrasion in case of higher impact during indentation.

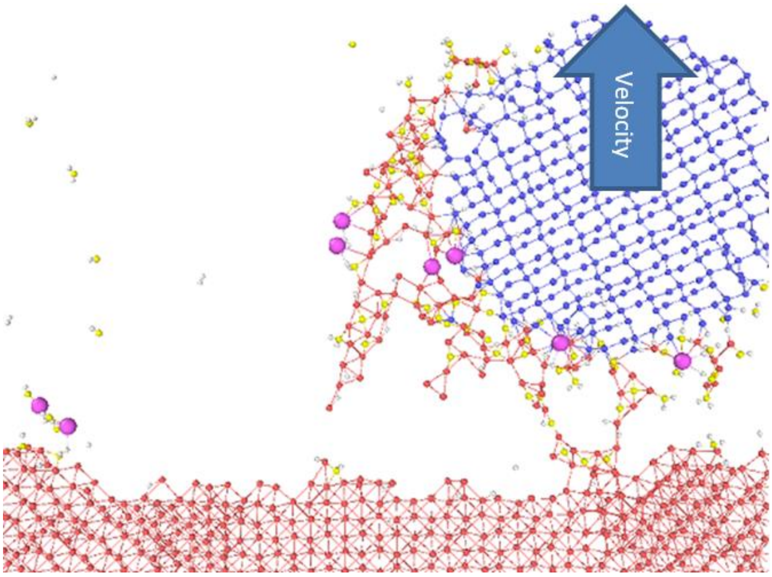

Fig. 4.48: Material removal during abrasion in the form of oxides/hydroxides.

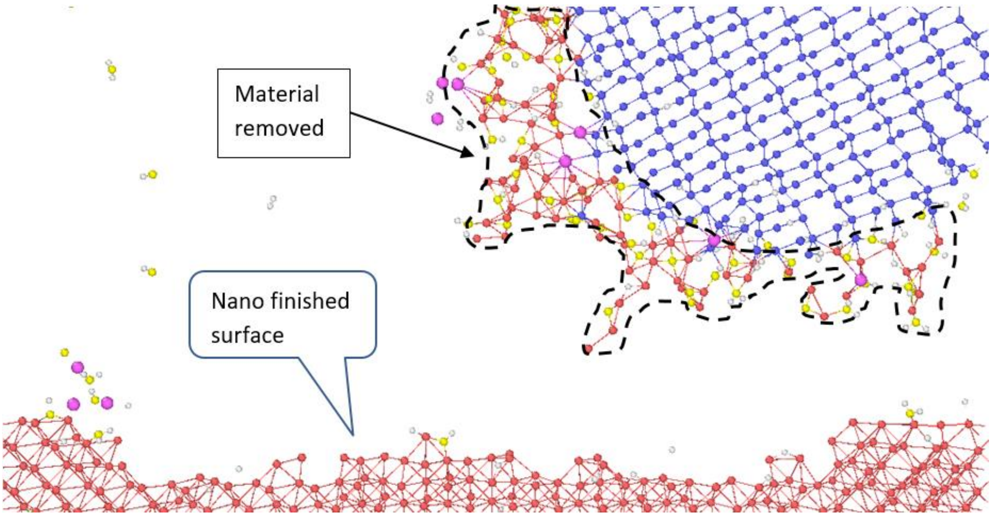

Fig. 4.49: Structure of workpiece and abrasive after finishing process. Abrasive particle is surrounded by alumina structure, and the finished workpiece is free from intensive oxidation.

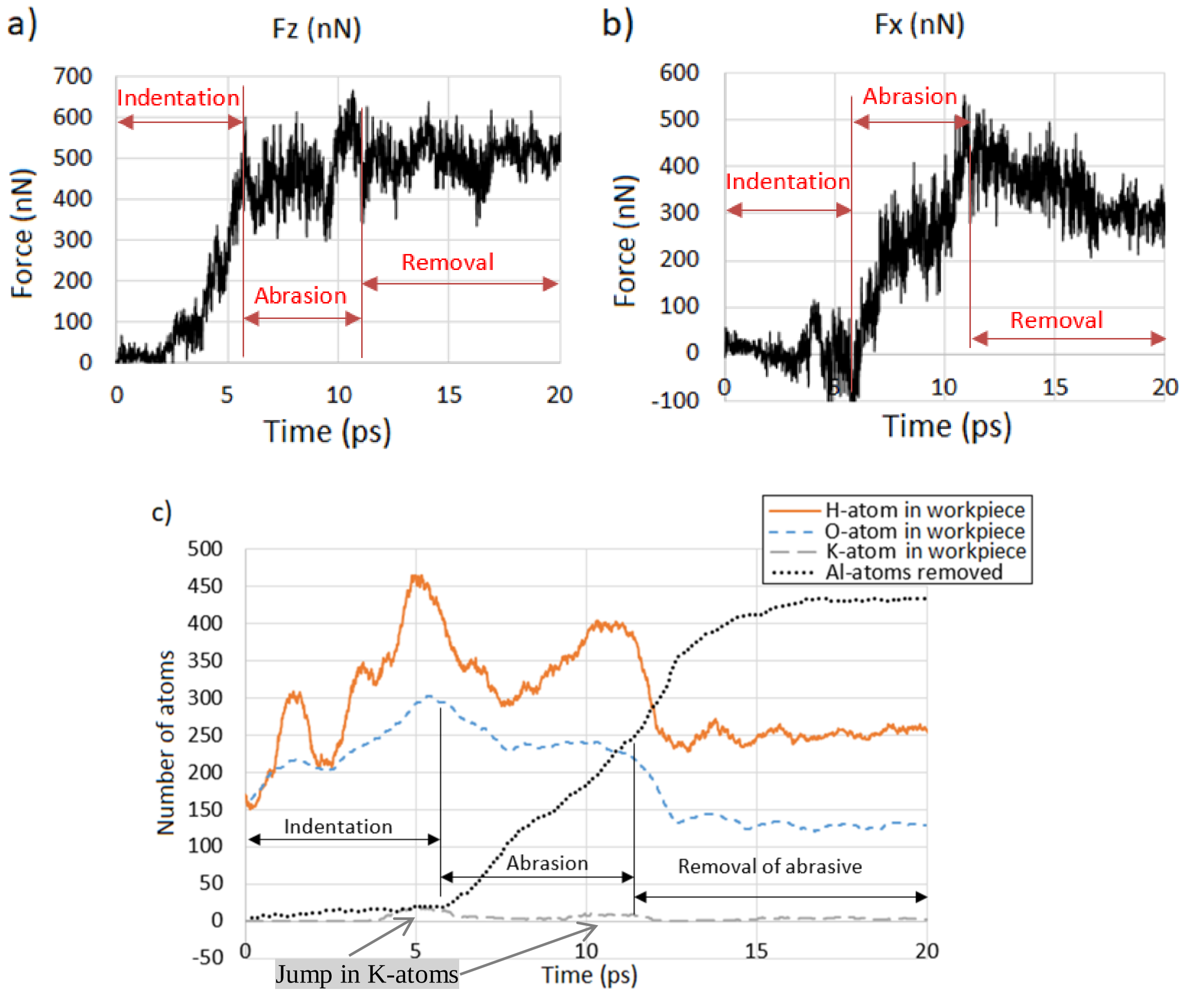

Fig. 4.50: (a) Normal force on workpiece, (b) abrasion force on workpiece, (c) chemical reaction and material removal from workpiece.

The MDS results are further quantified and plotted to understand the chemical reaction and chemo-mechanical abrasion in detail. These results are shown in Figs. 4.50 (a-c). As time for finishing progresses (i.e. after 4 ps), *O*, *H* and *K* atoms get pushed inside of aluminium workpiece which results in a jump of *K*-atoms as shown in Figs. 4.50 (c). Some atoms of *H* and *O* reside in aluminium even after completion of finishing and removal of abrasive particle. Whereas, *K*-atoms get completely removed after completion of finishing process, as shown in Fig. 4.50 (c). With time, material removal of workpiece is also shown as a black dotted line in Fig. 4.50 (c). Thus, these plots indicate that the chemicals get pushed by abrasive particle for more chemical reaction, and it leads for more MRR in terms of chemically assisted mechanical abrasion.

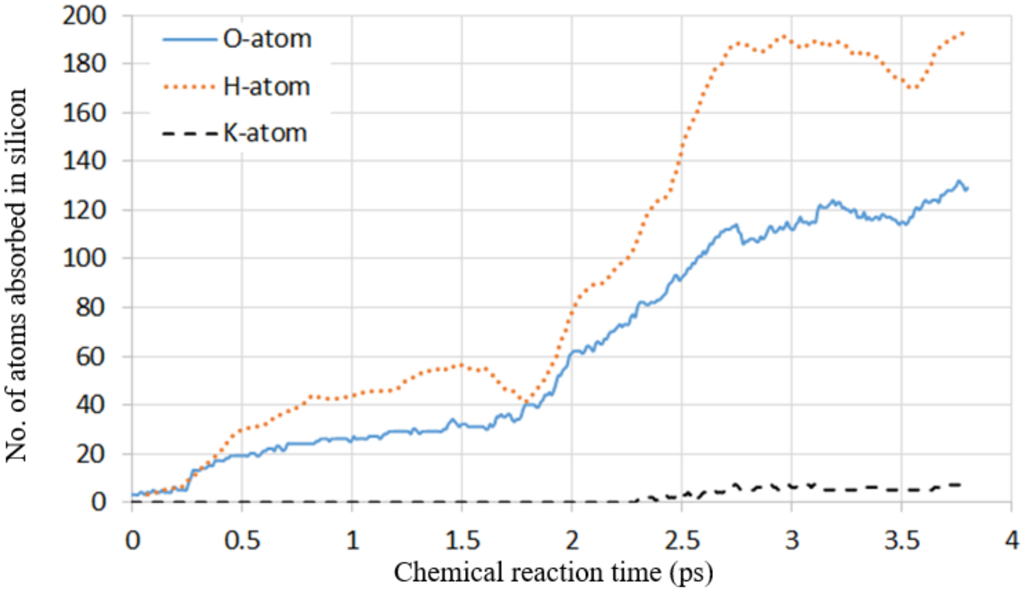

Fig. 4.51: Transfer of atoms from aqueous *KOH* into silicon workpiece during indentation of abrasive particle.

4.4.1.2. Effect of chemical slurry (aqueous KOH) during CAMF of Silicon

Fig.4.51 shows the chemical reaction on silicon workpiece with diamond abrasive particle during CAMF in aqueous *KOH*. From time 0 to 1.8 ps, molecules of aqueous *KOH* get squeezed between abrasive particle and workpiece due to constant velocity of abrasive particle, which increases oxidation. After 1.8 ps, abrasive particle makes physical contact with workpiece, and it leads to accelerate chemical reaction further. This plot also shows some part of potassium atoms entrapped after 2.5 ps due to the physical force of abrasive particle on *KOH* molecule.

Fig.4.52 shows position of atoms and chemical reaction in which chemical reaction increases as the abrasive particle indents physically over *Si*-workpiece. In this figure, reacted layers are propagated inside of workpiece, and marked as 'chemically reacted zone', whereas, other part of surface show oxidation on the surface only. Fig.4.52 supports the effect of mechanical force assisted chemical reaction as quantified and plotted in Fig. 4.51.

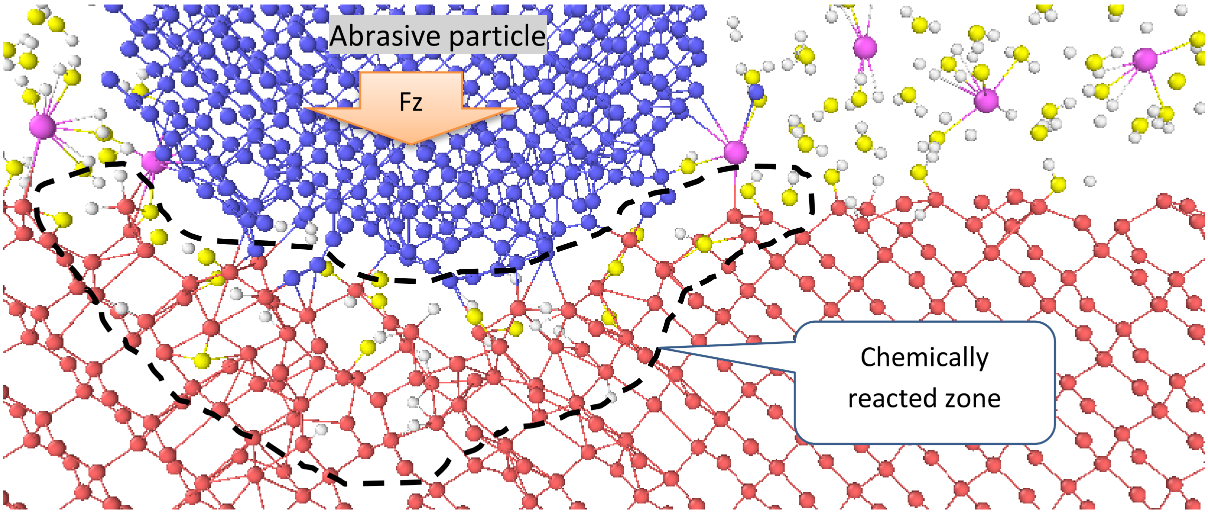

Fig. 4.52: Chemical reaction on surface under indentation force from abrasive particle.

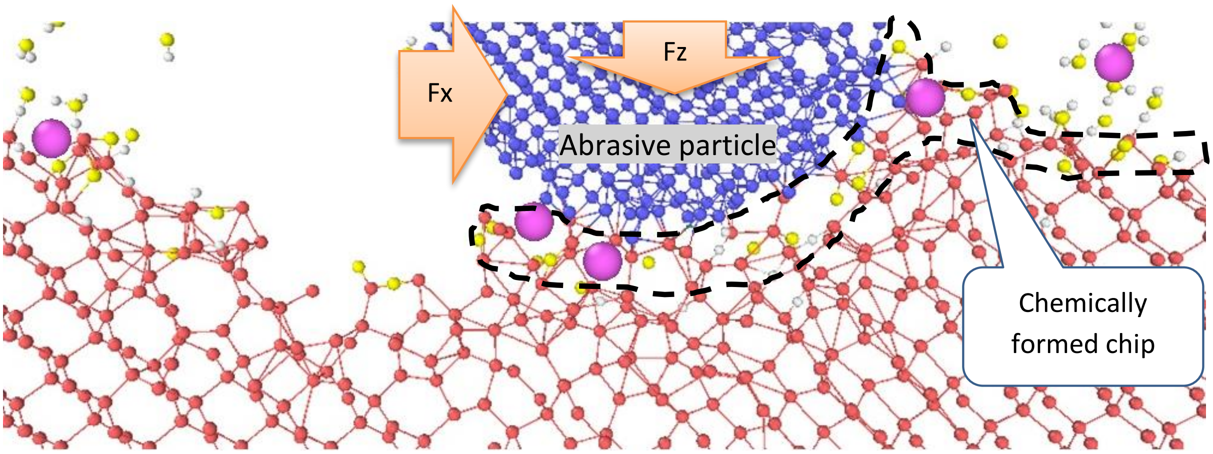

Fig. 4.53: Chemically assisted material removal and chip formation on silicon workpiece.

Fig. 4.53 shows the chip formation due to chemically assisted mechanical finishing of silicon under an alkaline medium of *KOH*. It is observed that the chemically reacted layers of workpiece get sheared off and pile up ahead of abrasive particle.

4.4.2. CAMF due to chemically active abrasive particles

There are few combinations of abrasive particles and workpiece which are responsible for this case. In the present work, silica abrasive particle is used on stainless steel as oxygen atom of silica has sufficient electronegativity to attract metallic atoms toward formation of ionic bond.

4.4.2.1. Material removal due to chemically active abrasive particle on SS304L

The abrasive particle plays the role of exerting indentation force as well as chemical interaction with work material. To study material removal mechanism due to chemically active abrasive particle, the MD simulation was performed using SiO_2 as abrasive particle, and presented in Fig. 4.54. Figs. 4.54 (a-f) show the mechanism of material removal due to the chemically active abrasive particle.

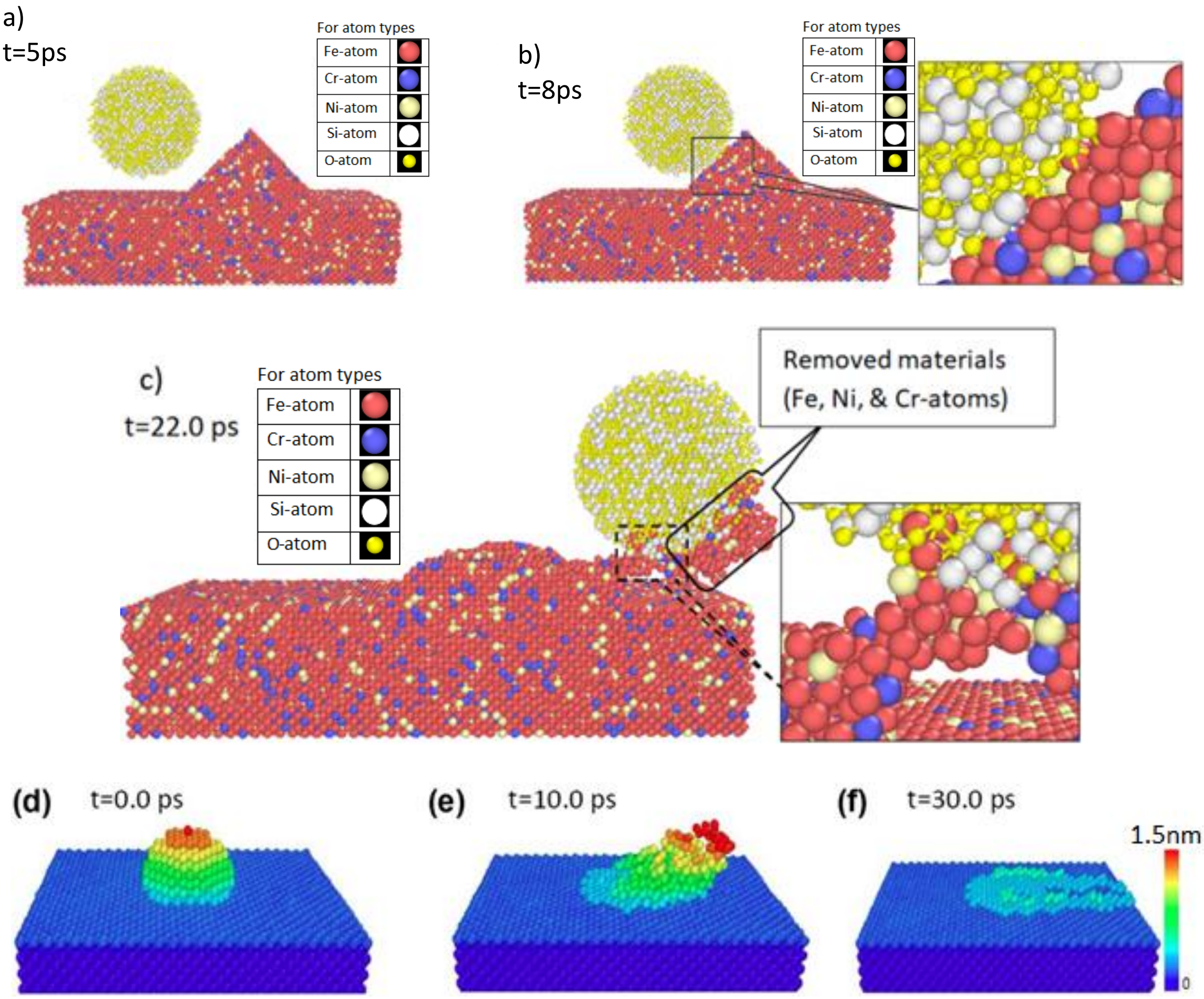

Fig. 4.54: Material deformation and chip formation at atomic scale.
(a) Atomic position for SiO_2 abrasive particle and *SS304L* workpiece before abrasion. (b) Atomic position during initial contact. (c) Atomic position during the finishing process. (d)–(f) Morphological study at varying time on material removal with a chemically active abrasive particle of diameter equal to 5.0 nm.

Figs. 4.54 (a-b) show the interaction between abrasive particle and workpiece, in which a new chemical bond between *O*-atom and *Fe*-atom is created as they come closer to each other. Fig. 4.54 (c) shows the material deformation (to form a chip) followed by further new bond formation on the deformed material. In this figure, material removal is shown from the asperity, in which the parent bond of the workpiece gets de-bonded as the newly formed bonds are stronger. This illustrates the mechanism of material removal and formation of a smooth surface.

Morphological study of the process is shown in Figs. 4.54 (d-f) with varying time (starting from left to right: before abrasion, during abrasion and at the end of abrasion) of the material removal on the spherical or smooth asperity. This study was carried out to investigate the smallest amount of material removal precisely, and the finished surface illustrates surface disorder in the range of 1–2 atomic layers as shown in Fig. 4.54 (f). In this study, it was found that the chemically active abrasive particle is suitable for precise level of material removal towards generating an atomically flat surface.

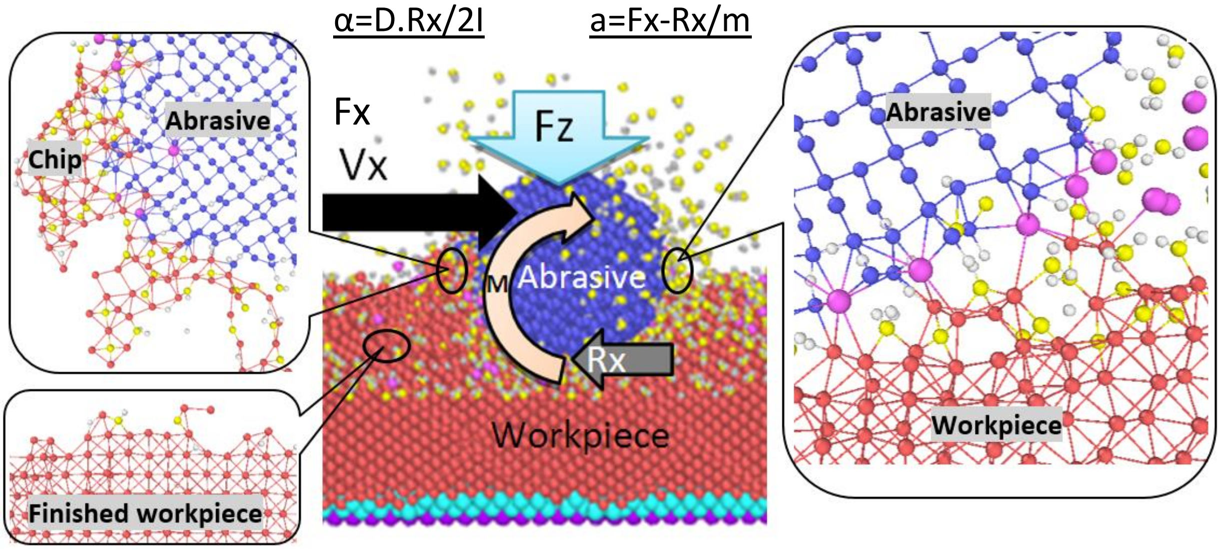

Fig. 4.55: Various attributes of CAMF under indentation force of *Fz* and velocity *Vx*. Where, *D*, *I* and *m* are diameter, moment of inertia and mass of abrasive particle.

4.4.3. Mechanism of material removal during CAMF

Various attributes of MDS result is combined and presented in Fig. 4.55. It shows that Fz force helps for chemical reaction and bonding between abrasive particle and workpiece because of higher temperature at the contact region. When velocity Vx is applied using external cutting force (Fx), a resistive force of Rx builds due to the strong bond between abrasive and workpiece, and it further results in rotation and translation of abrasive using angular acceleration (α) and linear acceleration (a) as shown in Fig. 4.55. The angular acceleration helps to remove material by de-bonding of parent bonds and results in nanometric smooth surface and it is suitable for ductile materials to process without creating defects. When Fx crosses the maximum value Rx (i.e. strength of the bonds between abrasive and workpiece), abrasive also translates to generate scratch. This result also reveals that the chemical reaction takes place and increase just ahead of abrasive particle which supports for material removal in brittle material by forming a soft passivation layer towards higher material removal rate.

Based on Fig. 4.55, a schematic model at macroscopic scale for material removal has been proposed as shown in Figs. 4.56 (a-c) for ductile and brittle material. Fig. 4.56 (a) shows the intensified chemical reaction due to the mechanical force.

In ductile material, chemical reaction does the formation of metal oxide which interacts with abrasive particles by means of attractive force and it forms strong bond with respect to the parent bonds of workpiece. The chemical bond between abrasive and workpiece resists linear movement of abrasive particle and forces it to rotate for material removal by piling up the chip through abrasive particle as shown in Fig. 4.56 (b). In case of brittle materials, chemical reaction does the formation of soft passivation layers which is comparatively less effective as compared with ductile materials, and due to this abrasive particle moves in form of rotation as well as translation.

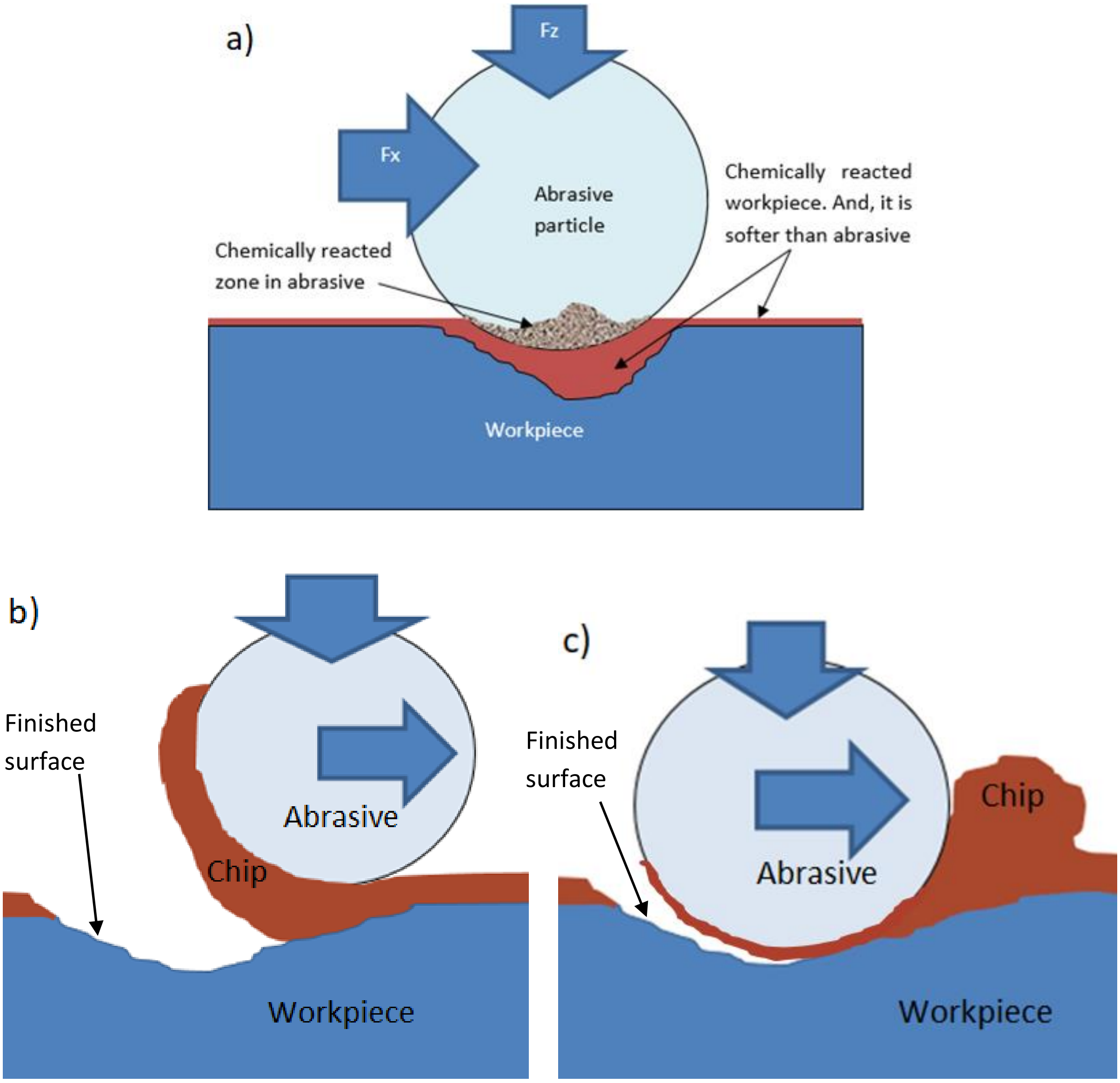

Fig. 4.56: Model for finishing zone of CAMF process. (a) Chemical reaction due to the indentation of abrasive particle. (b) Material removal on ductile material. (c) Material removal on brittle material.

Thus the material removal happens by pilling and partly shearing of passivation layer. For modelling, the material removal can be expressed in a function of mechanical stress and chemical concentration significantly, which is discussed and presented in the next chapter.

4.5. Discussions

From mechanical finishing, it is observed that low finishing force improves surface quality and the force beyond 10 nN damages surface but it yields in more MRR for higher finishing rate.

In mechanical finishing, material removal can be categorised in two types. The first type is ‘rough finishing’ using higher finishing force which is possible by implementing coarse abrasive particles as the force is multiplication of polishing pressure and surface area of abrasive particles. In the rough finishing process, MRR is more which reduces time to achieve certain value of surface finish. The second type of mechanical finishing is ‘fine finishing’ in which extremely low finishing force is required and this is possible only when abrasive size is extremely small or fine mesh size. Fine finishing process leads to further improvement of surface finish but it will not be free from scratch and digs.

To mitigate such defects, chemical reactions are studied so that the surface of workpiece can be protected during nano-finishing process. It is observed that the aqueous KOH controls passivation by creating a thin layer of oxides on both aluminium as well as silicon workpiece. The passivation layer helps to prevent the surface of workpiece for further chemical reaction, and it also assists material removal as studied during chemically assisted mechanical finishing (CAMF). In CAMF, it is found that the depth of passivation layer increases with abrasion action as local temperature of abrasion increases temperature selectively to accelerate the reaction rate. This chemical reaction forms a protective layer against abrasion and it also creates new chemical bonds to bridge the surface of workpiece and abrasive particle, and due to this abrasive particle starts rolling over workpiece instead of scratching. Hence, material removal occurs without damaging surface as observed during mechanical finishing. However, a size of abrasive particles is capable to apply force more than the value of ‘Rx’ to scratch workpiece when ‘$a > 0$’. In addition, abrasive particle rolls in case of ‘$\alpha >0$’, and abrasive particle mixture does scratching as well as rolling if a & $\alpha > 0$. CAMF is also categorised in two types, i.e. ‘precision finishing’ which utilises medium size of abrasive particles (size from 100 to 500 nm typically) and ultra-precision finishing in which abrasive particle should be less than 50 nm size so that translation of abrasive particle can be suppressed completely. Based on the type of surface quality, nano-finishing process is categorised into four stages as presented in Table. 4.7.

The present work is useful to understand and optimise an abrasive-based finishing process for the surface finish and the material removal rate.

Table 4.7: Steps in generating atomically flat surface from a rough surface

Sr. No.	Steps of finishing	Its importance
1	*Rough finishing*: Rough finishing using hard and coarse abrasive and magnetic particles.	To bring down the surface roughness value. It is useful to remove contamination or hard layer of the workpiece.
2	*Fine finishing*: Fine finishing with hard but small abrasive and magnetic particles.	To bring down the surface roughness by one order or more. In this step, the surface finish improves but it has many defects in the form of scratches.
3	*Precision finishing*: Finishing with chemically active abrasive particle with medium size.	It brings down the surface roughness by one more order. But the medium size of abrasive particle results in slight mechanical damage to the surface.
4	*Ultra-precision finishing*: Final finishing using ultra-fine and chemically active abrasive particles.	It gives an ideal surface finish.

Thus the present study reveals following capabilities.

- Atomic level of surface finish: It is possible by using CAMF by introducing low finishing force which helps to remove few atoms at a time, and this process repeatedly occurs on the nano-peaks to reduce its height upto atomically flat surface. The phenomenon can be expressed as CAMF does intensive chemical reaction on chemically unstable region (e.g. nano-peaks) and its removal in multiple cycles, which helps to equalise potential energy of all atoms on the surface towards formation of atomically flat surface. Thus, CAMF is capable for generating the surface finish of the order of atomic level.

- Defect free surface: In the field of nano-finishing, generating a defect free surface is always a challenge to researchers when the abrasive based finishing processes are being used for ductile materials. In CAMF, chemical reaction helps to roll abrasive particle over workpiece without allowing it to follow the motion of scratching, which helps to remove material without creating defects on the surface.

4.6. Summary

In this chapter, molecular dynamics simulation was carried out for mechanical abrasion, chemical reactions and chemically assisted mechanical finishing on three materials viz. aluminium, silicon and stainless steel. Important aspects of these works are summarised as follows.

- During mechanical finishing, material of workpiece deforms, and changes the parent lattice structure of workpiece which leads to increase in potential energy towards chemical instability of work surface. At lower finishing force, potential energy of workpiece recovers back after finishing. In case of higher finishing force, increase in potential energy becomes significant for silicon only, temperature of contact zone increases leads to generate sub-surface defects. Material removal occurs with the help of a phenomenon of adhesion-de-bonding in which the adhesion happens by an attractive (ionic) force while getting proximity between abrasive particle and workpiece and rupture of parent bonds of workpiece.
- The workpiece after mechanical finishing shows a permanent jump in potential energy which indicates that the mechanically abraded surface will be chemically less stable as compared to the equilibrated sample (which is an ideal condition) of workpiece by comparing the potential energy. The jump in potential energy at 1 nm of indentation depth for *Al*, *Si* and *SS304L* are 4, 550 and 250 eV respectively.

- When the mechanical finishing starts, in both ductile and brittle materials, the maximum stress of the contact zone becomes the theoretical value of shear strength, i.e. $G/2\pi$ irrespective of other properties of material. In addition, stress also propagates inside the workpiece but small in magnitude.
- During mechanical finishing of silicon, when abrasive particle approaches workpiece, the interface between them undergoes phase alteration in the form of non-crystalline or amorphous phase. This amorphous phase remains permanent on workpiece as well as chips.
- In brief, Mechanical finishing in ultra-precision zone (force ≈ few nano newton), is suitable for better surface finish. In case of higher finishing force, abrasive particle degrades and surface finish also degrades as shown in Fig. 4.26.
- In case of ductile materials like *Al* and *SS304L*, mechanical finishing does the phase alteration in the form of BCC and HCP. These new phases partly recover back.
- Based on the study about mechanical finishing, the nanofinished surface is strongly recommended not to be processed with any kind of mechanical abrasion. Only, the surface with high roughness is suitable for the mechanical abrasion-based finishing process.
- It is observed that the chemical reaction gets intensified on sharp peaks of surface and it leads to form a smooth surface. Chemical reaction is categorised in to three steps, i.e. adsorption, absorption due to chemical reaction and finally passivation to stop further reaction. These three mechanisms are similar in all kinds of materials for nano-finishing.
- In chemical assisted mechanical finishing, the chemical reaction enhances by increasing indentation force or by increasing mechanical force for finishing in addition of chemical concentration.

- MDS study shows that the chemically assisted mechanical finishing results in the surface finish at atomic scale.
- The material removal in the chemically assisted mechanical finishing process completely depends on chemical reaction on the workpiece as the removed material belongs to the product of chemical reaction.
- CAMF shows its capability to finish both ductile and brittle materials without defects, as CAMF assists material removal by rolling abrasive particle over work-surface instead of scratching.
- Chemical reaction during CAMF passivates the surface of workpiece by oxidisation which leads to form hard passivation layer and piling it up through newly formed bonds between abrasive and workpiece towards material removal.
- In case of brittle material, chemical reaction does softening, and abrasive particle abrades it which results in material removal of chemically reacted surface of workpiece.

-------x-------

Chapter-5

MATHEMATICAL MODELLING AND SIMULATION OF CMMRF PROCESS

5.1. Introduction

In the previous chapter, MD simulation is carried out for mechanical finishing of ductile as well as brittle materials, and their mechanism for the material removal was also discussed with some issues associated in achieving nano-finished surfaces and some of the issues related to phase transformation, surface defects, sub-surface defects, etc. MD simulation was also carried out for studying the role of chemical reactions towards surface smoothening. Finally, chemical assisted mechanical finishing for CMMRF was also studied through MD simulation. This study was carried out to understand the science behind material removal on CMMRF process and a list of possible finishing steps was developed as presented in Table 4.7. Furthermore, MD simulation is also carried out to compute coefficients for the mathematical model of CMMRF process as developed and discussed in this chapter.

This chapter aims to model and simulate the CMMRF process and the model is developed in two different stages viz. first modelling of mechanical abrasion due to polishing pressure and second with chemical assisted mechanical abrasion. From literature, it was found that the MRF based processes are comparatively more suitable for non-ferromagnetic materials. Hence, all theoretical and experimental work related to CMMRF process are investigated on non-ferromagnetic materials only [137]. In case of MDS, the material removal occurs at atomic scale, in which the chemical reaction is increased due to the indentation force and the material removal is directly proportional to the chemically reacted atoms of workpiece.

FEA based simulation tool is used for CMMRF process by solving the mathematical model. Necessary coefficients to solve the model at various levels of parameters are obtained through

MD simulation and the results are presented in Tables 5.1. Simulation results of this mathematical model are also discussed in this chapter.

5.2. Modelling of the CMMRF Process for Material Removal and Surface Roughness

The schematic of CMMRF process is illustrated in Figs. 5.1-5.2.

Fig. 5.1 shows schematic of CMMRF process in which CMMRF head (which consists a magnet to magnetise MR fluid) is mounted attached with a rotary spindle to apply finishing force on worksurface through magnetically stiffened MR fluid. During this process slurry circulatory system supplies chemical to the worksurface through a nozzle. Moreover, feed is also incorporated to drag the nano-finishing zone over the surface, and through this, entire portion of worksurface gets nanofinished as shown in Fig. 5.1.

Based on the theoretical study as reported in previous chapters, mechanism of material removal is presented for CMMRF process in Fig. 5.2. It shows that the chemical reaction alters the superficial layer of workpiece which is further removed by abrasion action and the magnetic forces (F_{mv} and F_{mh}) generated through magnetised CIPs of MR fluid.

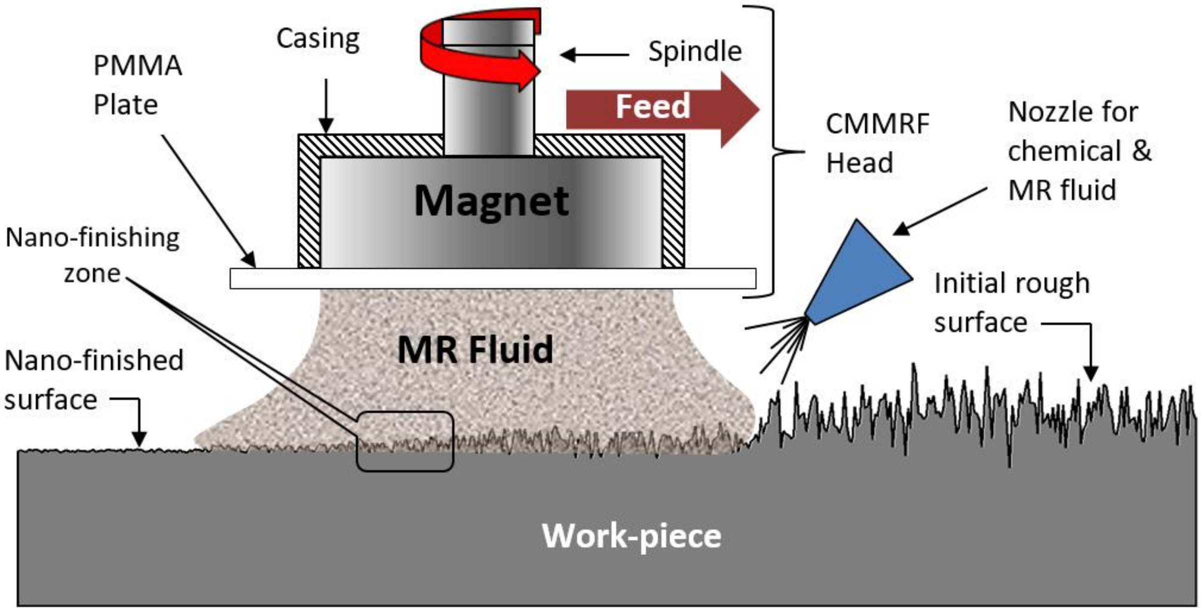

Fig.5.1: Schematic of CMMRF process

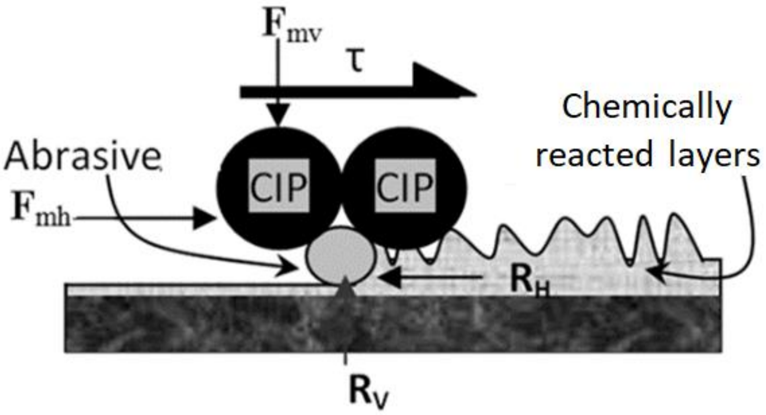

Fig.5.2: Material removal mechanism in the nano-finishing zone during CMMRF process.

In this section, model of CMMRF is discussed along with the mathematical formulation in segment wise. These segments are divided as follows.

- Modelling of Mechanical abrasion: In this segment, the shearing energy of MR fluid at the interface of MR fluid and workpiece, is used to convert the required energy to abrade the surface of workpiece. The material removal rate is formulated as a function of roughness parameter, friction co-efficient, polishing pressure, finishing speed and specific cutting energy of workpiece at nanometric scale. Here, the friction co-efficient and specific cutting energy are taken from the MD simulation (Table 5.1), and the pressure is computed using FEA simulation. This model is further expanded in the next stage to include chemically assisted material removal.
- Modelling of CMMRF process: As mentioned above, chemical reaction is introduced along with the mechanical abrasion in this model. The chemical reaction effect on material removal is added by applying a factor which is derived from MD simulation. Further, modelling of MRR and surface finish are carried out.

5.2.1. Modelling of material removal using mechanical abrasion

Model of MR fluid is simplified by assuming it as a Bingham plastic fluid when it comes under the influence of magnetic field (Fig. 5.3). This behaviour of Bingham plastic fluid shows a special behaviour of rheological property which can be expressed as per Eq. (5.1) [72]. In this behaviour of MR fluid, yield shear strength is mainly governed by magnetic means.

$$\tau = \tau_o + \mu(\dot{\gamma}) = \tau_o + \mu\left(\frac{V}{Wg}\right) \tag{5.1}$$

Where, $\dot{\gamma}$ = strain rate, Wg = working gap; τ = shear stress on the MR fluid at the finishing plane; τ_o = yield shear strength of the MR fluid at a given magnetic field; V= relative velocity between MR fluid and workpiece and μ = dynamic viscosity of the MR fluid.

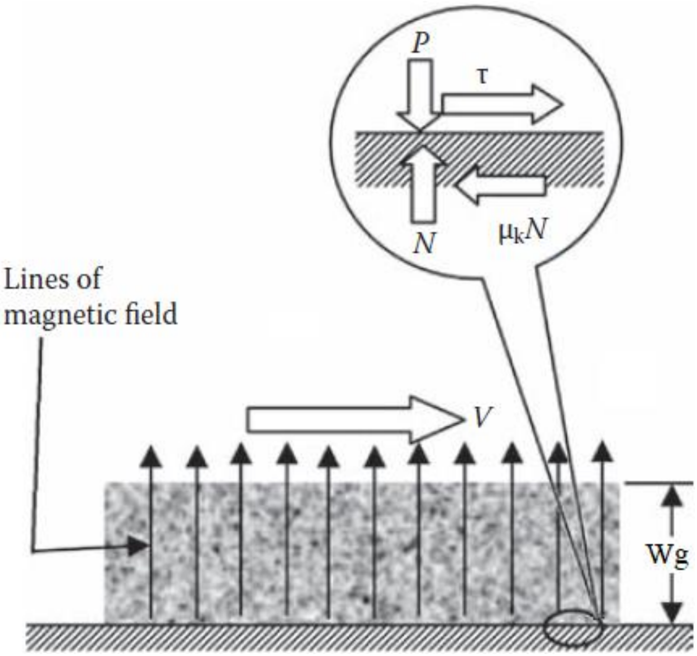

Fig.5.3: Schematic of MR fluid while in working condition.

In MR fluid, polishing pressure and shear stress can be correlated, as shown in Fig.5.3 and discussed as follows.

According to force equilibrium conditions along the direction of the fluid flow, $\tau = \mu_k N$, and along normal to the work surface, $N = P$, where μ_k is the friction factor between the work surface and the MR fluid. Thus, the shear stress on the workpiece can be expressed in term of polishing pressure, as $\tau = \mu_k P$. The polishing pressure 'P' is taken from Fig. 3.20 (c) which was obtained by simulation in chapter 3.

In CMMRF process, polishing pressure is used to apply indentation force on abrasive particle, and removal of material in the form of chips that happens due to the shearing stress. This shearing stress becomes equal to the material's resisting stress along cutting or finishing direction, which depends on the indentation depth of abrasive particles due to the polishing pressure. Hence, it can be stated that the energy due to the shearing stress of MR fluid helps to abrade the surface of workpiece.

Mechanical based material removal mechanism plays an important role for micro- and nano-finishing process such as magnetorheological finishing process in which MR fluid applies the abrading force through abrasive particles. Hence, it is assumed that the MR fluid acts as stiffened pad to abrade the workpeice, and the abraded volume of workpiece is directly proportional to the energy available on the MR fluid. To make the mathematical formulation, mechanism of such material removal is implemented as follows.

Let dV_t be an elemental volume (under dZ_t height) removed from the workpiece during time interval from 't' to 't+dt' as shown in Fig. 5.4. It is assumed that the required energy to remove dV_t volume of workpiece is taken from the energy of MR fluid at the interface of MR fluid and workpiece. Hence, the material removal phenomenon can be expressed as per Eq. (5.2).

$$\frac{\Upsilon_s}{\alpha} dV_t = \tau A \frac{\partial x}{\partial t} dt; \text{where}, \tau = \mu_k P \qquad (5.2)$$

Where, Υs=specific cutting energy of work surface, which can be correlated with shear strength of workpiece as discussed (Eq. 4.5) in chapter 4, τ & A =shear stress and contact area between MR fluid and workpiece respectively. $\partial x/\partial t$ =cutting speed (V) = ωr and r = radial position on the pad. μ_K is kinetic friction coefficient and P is pressure of MR fluid.

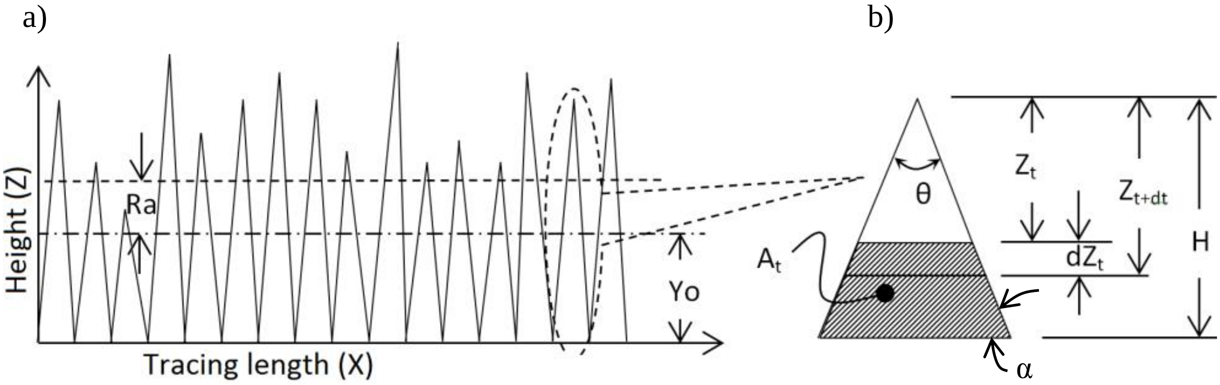

Fig. 5.4: Surface profile for modelling of CMMRF process. (a) Assumed surface roughness profile, (b) Zoomed view of a single peak of the profile.

From Fig.5.4 (b) another angle 'α' is calculated to calculate dV_t, which is described as below, Eq. (5.3).

$$\theta + 2\alpha = \pi \Rightarrow \alpha = \frac{\pi - \theta}{2} = \frac{\pi}{2} - \frac{\theta}{2}; \text{and } \alpha \ll 1, \text{as Z and X are in nm and μm, respectively.} \tag{5.3}$$

Projected area along the cutting direction (Ac) and removed volume (V_t) are expressed as per Eq. (5.4).

$$A = \frac{Z_t}{\alpha} l \text{ and } V_t = \frac{1}{2} Z_t A = \frac{{Z_t}^2}{2\alpha} l, \text{where}, l = \text{thickness of triangle of Fig. 5.4(b).} \tag{5.4}$$

After differentiation of V_t and simplifying Eq. (5.4), dV_t is expressed as per Eq. (5.5).

$$\mathrm{dV_t} = \frac{\mathrm{Z_t}}{\alpha} \mathrm{l.dZ_t} = \mathrm{AdZ_t} \tag{5.5}$$

Now, Eq. (5.2) and Eq. (5.5) are solved to derive material removal rate, and expressed in Eq. (5.6).

$$\frac{dZ_t}{dt} = \frac{\alpha \mu_k P}{\gamma_s} \frac{\partial x}{\partial t} \tag{5.6}$$

This Eq. (5.6) shows linear relationship between linear material removal rate and polishing pressure (this pressure is directly converted into indentation force), which is similar to the MDS result as shown in Fig. 4.26 of chapter 4. MDS results reveal that the finishing force is directly dependent on the depth of indentation and higher depth of indentation leads to larger finishing force. Thus this equation has similarity with MD simulation for mechanical abrasion as discussed in section 4.3.4 of chapter 4.

5.2.2. Modelling of CMMRF process

5.2.2.1Material removal rate

In CMMRF process, material removal phenomenon takes place due to chemically assisted mechanical abrasion. The mechanical stress in the finishing zone increases chemical reaction as shown in Fig. 4.56 (a) of the chapter 4. Thereafter, the material removal occurs in the form of the chemically reacted atoms of workpiece as shown in Figs. 4.45-4.48.

In view of these aspects, Eq. (5.6) is modified to incorporate stress assisted chemical reaction followed by material removal. Stress at a given height Z_t of Fig. 5.4 (b) can be written as follows;

$$\sigma_{Zt} = \sigma_o \left(\frac{H}{Z_t}\right); \text{where}, \sigma_o \text{ is stress at } Z_t = H \tag{5.7}$$

Now, using Eqs. (5.6 and 5.7), stress assisted linear material removal rate can be presented by Eq. (5.8).

$$\frac{dZ_t}{dt} = \frac{\alpha\mu_k P}{\gamma_s}\frac{\partial x}{\partial t}\left(\frac{\sigma_{Zt}}{\sigma_o}\right) = \frac{\alpha\mu_k P}{\gamma_s}\frac{\partial x}{\partial t}\left(\frac{H}{Z_t}\right) \tag{5.8}$$

Eq. (5.8) is further extended for the chemical assisted mechanical finishing by multiplying with a factor K_{chem} as shown in Eq. (5.9). It indicates a change in the amount of material removal rate due to chemical reaction.

$$\mathrm{MRR} = \frac{dZ_t}{dt} = K_{chem}\frac{\alpha\mu_k P}{\gamma_s}\frac{\partial x}{\partial t}\left(\frac{H}{Z_t}\right) \tag{5.9}$$

Material removal rate (MRR) of Eq. (5.9) depends on cutting speed ($\partial x/\partial t$) and pressure (P), and these parameters will not become same at a given coordinate of workpiece as the polishing tool rotates and also moves with linear feed. Thus, MRR will keep increasing and decreasing linearly in a cyclic function at a given point of workpiece with finishing time. The depth of material removal will be the time integration of MRR without any effect of the linear feed. Hence, average value of MRR is used to compute the depth of material removal, and after solving Eq. (5.9), depth of material removal can be expressed by Eq. (5.10),

$$Z_t = \left[\frac{K_{chem}}{\gamma_s}\alpha H\mu_k P\, V_{max}\, t\right]^{0.5} \tag{5.10}$$

Where, V_{max} is the maximum rotational speed of polishing tool.

The values of K_{chem}, Υ_S and μ_K, using MD simulation are computed as follows.

A set of MD simulations is carried out on aluminium and silicon to find out the values of 'K_{chem}, Υ_S and μ_K '. Value for Υ_S and μ_K are 11000 MPa and 0.6 for aluminium and 48000 MPa and 0.5 for silicon workpiece, respectively. In case of the value of 'K_{chem}', a list is presented for both aluminium and silicon workpieces as shown in Tables 5.1. Υ_S and μ_K are computed from the mechanical finishing of MD simulation. K_{chem} is computed by taking ratio of material removal under chemical environment and without chemical environment, as shown by Eq. (5.11).

$$K_{chem} = \frac{\text{Number of atoms removed under chemical assisted abrasion}}{\text{Number of atoms removed under mechanical abrasion}} \quad (5.11)$$

Here, 'number of atoms removed under the chemically assisted abrasion' means total number of atoms removed from workpiece at a known value of finishing force and percentage of KOH during 5 ps of CAMF time. On the other hand, 'number of atoms removed under mechanical abrasion' stands for the total number of atoms removed from workpiece in the same value of finishing force but without using any chemical medium.

During CMMRF process, indentation force and abrasion force of abrasive particle comes from CIP of MR fluid according to the magnetic force per CIP and it is also responsible to generate the polishing pressure. Hence, a correlation is made by using polishing pressure of a known working gap of CMMRF to compute maximum possible value of the indentation force for MD simulation. This correlation is expressed by Eq. (5.12).

$$\text{Force} = \text{Pressure} \times \frac{\pi d_{\text{CIP}}^2}{4} \quad (5.12)$$

Force from Eq. (5.12) is used for MD simulation, which is calculated from FEA simulation by computing the polishing pressure at a known value of working gap and a set of specified parameters of MR fluid.

Table 5.1: Values of parameters for *Al* and *Si* workpiece using MD simulation

Sr. No.	%*KOH*	Working gap (mm)	Polishing pressure (kPa)	Indentation force (nN)	K_{chem} of *Al*	K_{chem} of *Si*
1	0	0.5	50.5	1200	0.14	0.14
2	0	1.0	6.3	150	0.14	0.14
3	0	1.5	2.1	50	0.14	0.14
4	5	0.5	50.5	1200	0.07	0.28
5	5	1.0	6.3	150	0.08	0.238
6	5	1.5	2.1	50	0.148	0.168
7	10	0.5	50.5	1200	0.035	0.308
8	10	1.0	6.3	150	0.05	0.252
9	10	1.5	2.1	50	0.126	0.175

In the present work, zone-1 (gap =0.5 mm) and zone-2 (gap=1 & 1.5 mm) of Fig. 3.20 (c) are used to simulate CMMRF model on both Al and Si workpiece to understand the severity of their impact on brittle as well as ductile material. This study is also aimed to validate the investigation completed and reported in Table 3.5 of chapter 3.

5.2.2.2 Surface finish

One of the surface finish (quantification by calculating roughness) parameters is described by symbol '*Ra*' which is an arithmetic average of the absolute values of the profiles height deviations from the mean line. This parameter of surface roughness, *Ra* can be expressed from the Annexes of Japanese Industrial Standards (JIS) B 0031 (1994), as per Eq. (5.13).

$$R_a = \frac{1}{L}\int |Z_x|\, dx \tag{5.13}$$

Where, L=sample length, Z_X=height from the mean line at a known value of the tracing length (X).

In case of ideal surface roughness with identical peaks and triangular in shape, a mathematical model for surface roughness (*Ra*) can be expressed after modifying earlier developed formulation [138] based on roughness profile as expressed in Eq. (5.14).

$$R_a = \frac{(H - Z_t - Y_o)^2 + 2Z_t(H - Z_t - Y_o) + Y_o^2}{2H} \tag{5.14}$$

Where, $Y_o = (H^2 - Z_t^2)/(2H)$; H and Y_o are height of peak and centre line of profile as shown in Fig. 5.4 respectively.

Mathematical model for material removal as expressed in Eq. (5.9), is used to get the surface profile after CMMRF. Towards this direction, actual surface is measured using optical profile-meter (Make: Taylor Hobson & model: CCI) then it is processed as per the simulation procedure, shown in the flow chart in Fig. 5.6.

5.2.2.3 Modelling of critical surface finish to calculate theoretical roughness value

Any manufacturing process of micro/nano- finishing process improves surface finish by reducing the surface roughness value with processing time. After some time of finishing, the roughness value gets saturated and it is called as critical surface roughness [139]. Where the 'critical surface roughness' is a roughness value which indicates the process capability of a nano-finishing process, which also limits the final surface finish. For example, an atomically finished surface is represented in Figs.5.5 (a-b) which is obtained after equilibration of geometry during classical MD simulation. Fig. 5.5 (a) is a three dimensional view in which *X*, *Y* and *Z* axis show <100> line of the lattice orientation. Fig. 5.5 (b) is a cut sectional view of the three dimensional structure along with high packing factor. Here, *X1* axis shows [1 1 0] line orientation of the lattice.

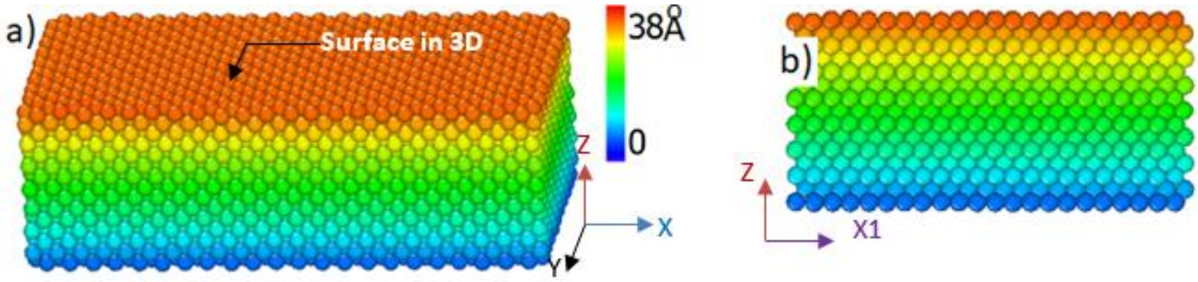

Fig.5.5: (a) 3-dimensuonal view of atomic arrangement in a face centred cubic (FCC) lattice structure. (b) 2-dimensional view of atomic arrangement along high packing plane.

The ideal surface can be defined as a surface in which atoms are linearly arranged as shown in Fig. 5.6.

For an atomically ideal surface, the average roughness (*Ra*) value can be derived as follow;

Let us assume that the area above the *Yc* or mean line within unit cell is 'A_{above}'. From Fig. 5.6 (a), the area below the mean line (A_{below}) within the unit cell is expressed as per Eq. (5.15). It is also assumed that the inter-atomic distance is equal to the 'diameter of atom (*D*)' [140].

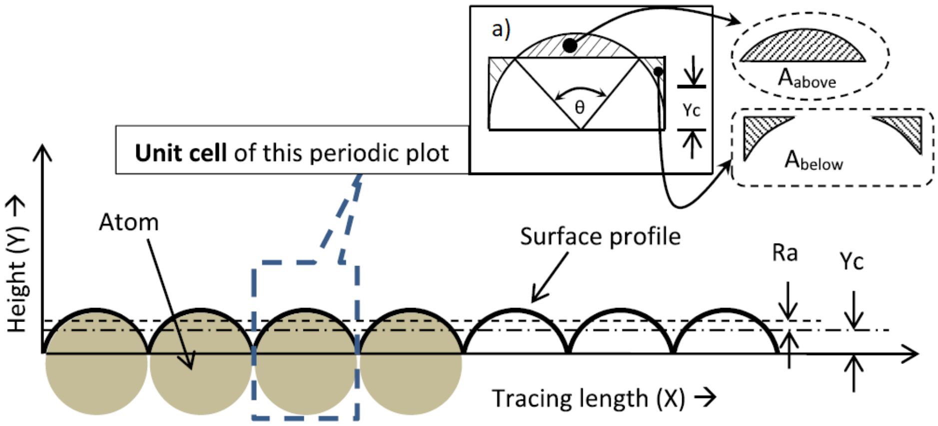

Fig.5.6: Schematic diagram of an ideal surface profile at atomic scale.

A_{below}= area of rectangle under mean line-{area of half circle - area above the mean line};

$$A_{below} = DY_c - \left(\pi \frac{D^2}{8} - A_{above}\right) \tag{5.15}$$

As per the definition of mean line, both areas, A_{above} and A_{below} need to be equal. Thus Yc is derived and presented in Eq. (5.16).

$$A_{below} = DY_c - \left(\pi \frac{D^2}{8} - A_{above}\right) \Rightarrow \cancel{A_{below}} = DY_c - \pi \frac{D^2}{8} + \cancel{A_{above}}$$

$$Y_c = \pi \frac{D}{8} \tag{5.16}$$

As per the definition of 'Ra', it is the ratio of total modulus of area and the tracing length. From Fig. 5.6 (a),

$$R_a = \frac{A_{above} + A_{below}}{D} = \frac{2A_{above}}{D} \tag{5.17}$$

After solving the geometry of the circle as shown in the unit cell of Fig. 5.6 (a), the value of 'A_{above}' is expressed as per Eq. (5.18).

$$A_{above} = \frac{D^2}{8} \left(\theta - \sin\theta\right); where\ \theta = 2\cos^{-1}\left(\frac{2Y_c}{D}\right) = 2\cos^{-1}\left(\frac{\pi}{4}\right) \tag{5.18}$$

After replacing the value of 'A_{above}' from Eq. (5.18) into Eq. (5.17), Ra value is expressed in Eq. (5.19). Hence, theoretical Ra would be 0.02-0.04nm as D becomes 0.2-0.4 nm.

$R_a \approx \frac{D}{11}$; Where, 'D' is the diameter of the atom. (5.19)

Moreover, an analytical Eq. (5.20) has also been used for studying the Ra value on a surface with complexity such as dissimilar atoms (i.e. in case of *SS304L*) or atomically non-ideal.

$$R_a = \frac{\int |Y - Y_c| dx}{\int dx}; \quad \text{Where, } Yc \text{ is the location of centre line, chosen such that the areas above and below the line are equal.} \qquad (5.20)$$

For example, *Ra* is computed using Eq. (5.20) for an ideal surface of *SS304L* to see the effect of dissimilar atoms such as *Fe*, *Cr* and *Ni* atoms with atomic diameter (taken from periodic table) equal to 3.12, 3.32 and 2.98 Å respectively. Here, number of atoms are randomly varied and it is found that the range for *Yc* and *Ra* value becomes 1.19 – 1.27 Å and 0.26 – 0.29 Å respectively. If there is an irregularity (as shown in Fig.4.49 of chapter 4) of the order of one atomic layer, then the *Ra* value becomes 0.105 – 0.110 nm. If the surface is composed by 50% as ideal surface and 50% with irregularity of one atomic layer, then *Ra* becomes 0.07 nm.

5.3. Simulation of CMMRF process

In CMMRF process, there are some critical areas which need to be studied for better understanding and prediction of the process behaviour. These areas are presented in Table 5.2.

Table 5.2: List of study area towards understanding of CMMRF process.

Sr. No.	**Area to study**	**Stipulation of the study as per CMP and MRF characteristics**
1	Formation of Polishing Pad.	To visualize shape and size of polishing pad towards finishing on a given surface area.
2	Polishing pressure or axial stiffness (axial force).	Indentation depth of abrasive particle on work-surface to study and quantify material removal (or polishing rate) as well as surface damages.
3	Improvement on surface roughness.	To predict the process performance using a set of operating parameters.

These areas of work, as mentioned in the Table 5.2, have been studied by implementing different types of modelling and simulations namely, MD simulation, mathematical modelling, and FEA-CFD simulation. These areas include the material behaviour under different scales of time and size, as described in Fig. 2.9 of the chapter 2. These modelling and simulation are carried out as per the work-plan in a schematic diagram of Fig. 5.7.

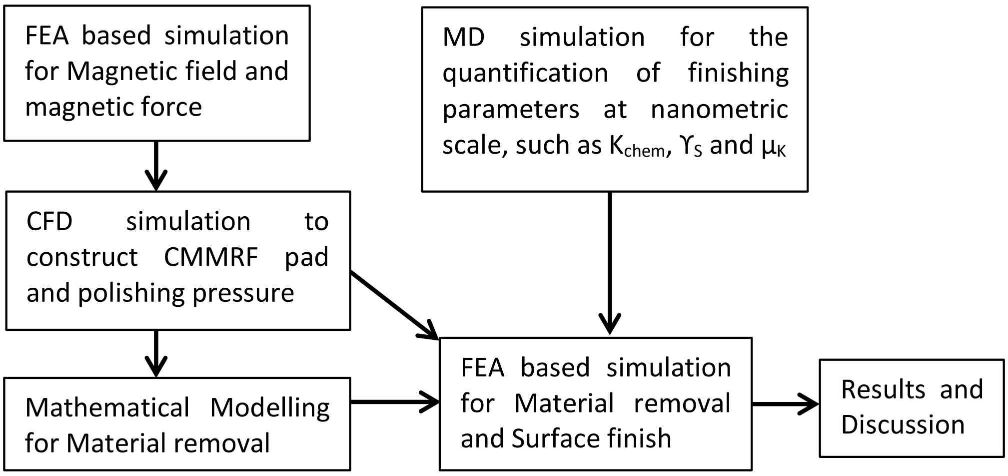

Fig. 5.7: Schematic diagram of work-plan for modelling and simulation of CMMRF process to predict material removal and surface finish.

FEA based simulation is carried out for magnetic force and CFD simulation used for the computation of polishing pressure. To understand science of material removal, MD simulation is carried out. MD simulation is also used to quantify some critical parameters and the outcome of these parameters are used in the mathematical model of material removal of CMMRF process. Then the model of CMMRF is simulated to predict material removal and surface finish.

5.3.1. Procedure of FEA based simulation for material removal and surface finish

Entire modelling and simulation work has been carried out as per the flow chart as shown in Fig. 5.8.

In this work, COMSOL4.3a multi-physics software has been extensively used for coupling of multiple physics such as Magnetism, Fluid flow and Arbitrary Lagrangian-Eulerian (ALE) method, and subsequently incorporated suitable post processing on the simulated data. Parameters for FEA based simulation are listed in Table 5.3.

Table 5.3: FEA parameters to simulate CMMRF process for material removal and surface roughness.

Sr. No.	Parameters	Description
1	Solver configuration	Coupling of magnetism, laminar flow, and ALE based moving mesh.
2	Solver type	MUMPS
3	Non-linear method	Constant (Newton)
4	Simulation type model	Time dependent
5	Geometry type	Axisymmetric
6	Relative permeability of MR fluid	10
7	Shape function for magnetic potential	Lagrange (Quadratic)
8	Shape function for laminar flow	Lagrange (Linear)
9	Shape function for solid mechanics	Lagrange (Quadratic)
10	Geometric shape order	Quadratic
11	Type of mesh	Triangular
12	Mesh smoothing type	Winslow

Simulation for the present work is carried out by using following steps of the flow chart as shown in Fig.5.8.

- Parametric values for simulation: Simulation of this work consists various aspects of physics such as magnetic force, rheological aspects of MR fluid, and nano-metric scale of abrasion. All these three vital areas need a set of parameters to solve the relevant governing equations under the fixed boundary conditions and initial conditions. These sets of parameters are obtained from the experimental values of magnetism and MR fluid rheology, abrasion force parameters from finite element (FE) simulation and nano-abrasion parameters from MD simulation. After compilation of all these parameters, they are imported in the FEA simulation software under the parameters library of pre-processing of simulation.

- Magnetic force computation: A set of equations for magnetic force density has been developed and discussed in chapter 3. These equations are used as governing equations for evaluating the induction force within the MR fluid which is a significant parameter to build the polishing pressure towards nano-abrasion.

- Rheological aspect: The governing equation for flow of MR fluid and pressure building within the MR fluid is taken as per the Navier-Stokes equations for momentum and mass equilibrium. Furthermore, to achieve consistent and accurate value of polishing pressure, ALE based moving mesh technique is used along with optimisation of magnetic energy of MR fluid.

- Material removal rate: Eq. (5.9) is used to compute material removal rate and the depth of removed material with the processing time. These results are further used for computation of surface roughness.

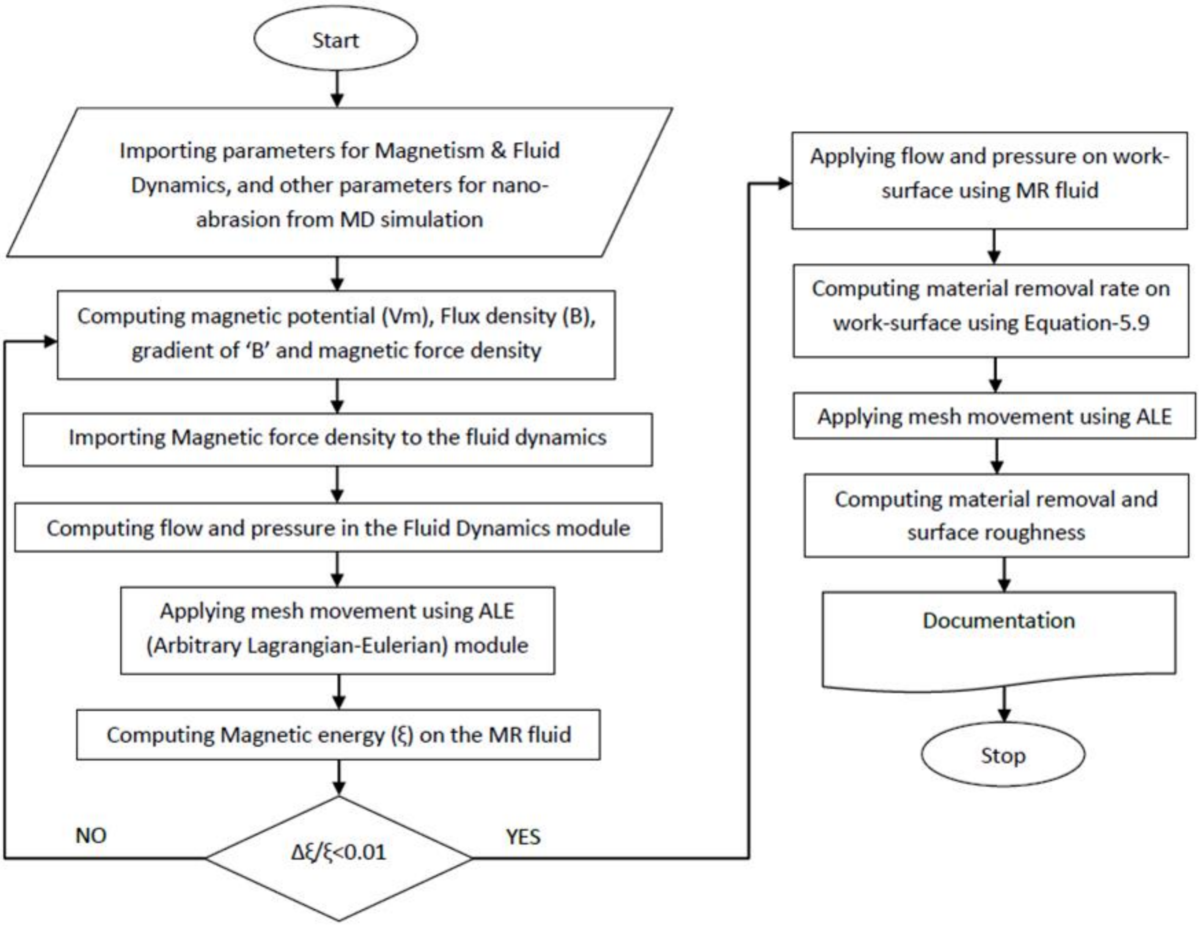

Fig.5.8: Flow chart for the present study of modelling and simulation of material removal and surface finish.

- Computation of surface roughness: Before implementing all previous steps, right from magnetic force to polishing pressure and material removal, a necessary pre-processing stage is implemented to measure surface roughness value. This surface roughness value is continuously computed and stored with all process parameters and processing time.
- Documentation: The computed value of material removal and surface roughness as discussed earlier are plotted and stored during post-processing of simulation results.

5.4. Results and discussion

5.4.1. Simulation results

Mathematical model for material removal is expressed in Eq. (5.9) and it is used to simulate it on the actual surface profile as shown in Figs. 5.9 (a-b). The simulation study of this chapter at macro-scale has been analysed to understand the effect of CMMRF process parameters on material removal with time and the time required to achieve the critical surface finish.

Fig.5.9 (a) shows the mesh construction on the imported data after measuring them in a coherent correlation interferometer (Make: Taylor Hobson, Model: CCI). The meshing is applied with varying size in triangular shape and Quadratic-Lagrange shape function. The mesh size is refined near sharp edges of the profile as shown in Fig. 5.9 (a). Fig. 5.9 (b) shows the initial surface profile which is plotted after pre-processing of raw data to show the mean line and *Ra* line, and this profile is further used as an initial surface profile to apply FEA based simulation of material removal.

Simulation for material removal is carried out on this profile. Figs.5.10 (a-b) show the modified mesh and surface profile after 10 minutes of CMMRF processing on initial surface, which shows the surface finish of *Ra* equal to 10 nanometers.

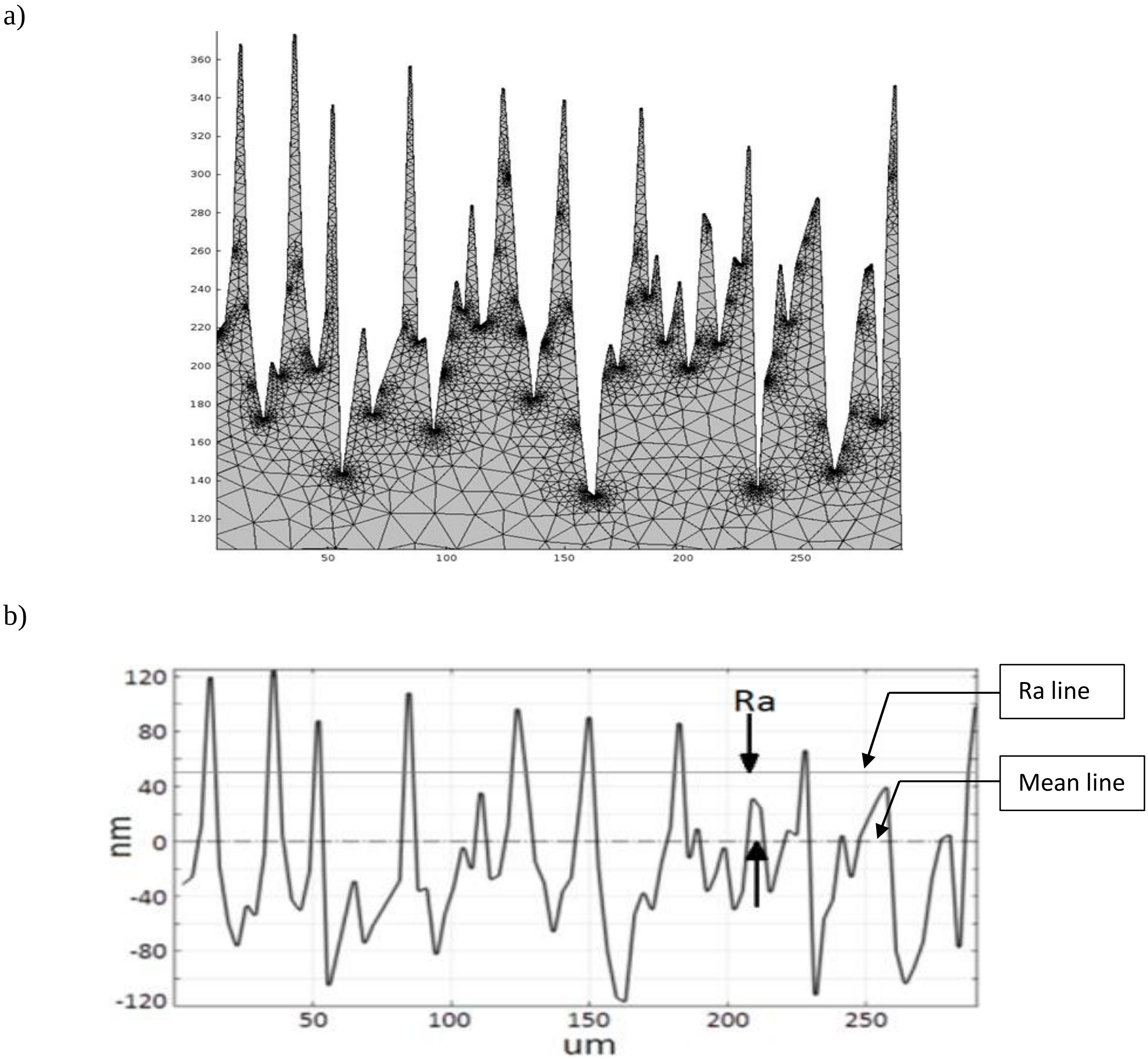

Fig.5.9: Initial surface profile data is imported from the experimentally measured profile from CCI instrument in the form of CSV format, *Ra*=50 nm. (a) Meshing on the imported surface, (b) Surface profile with pre-processing for computation of mean line and *Ra* line.

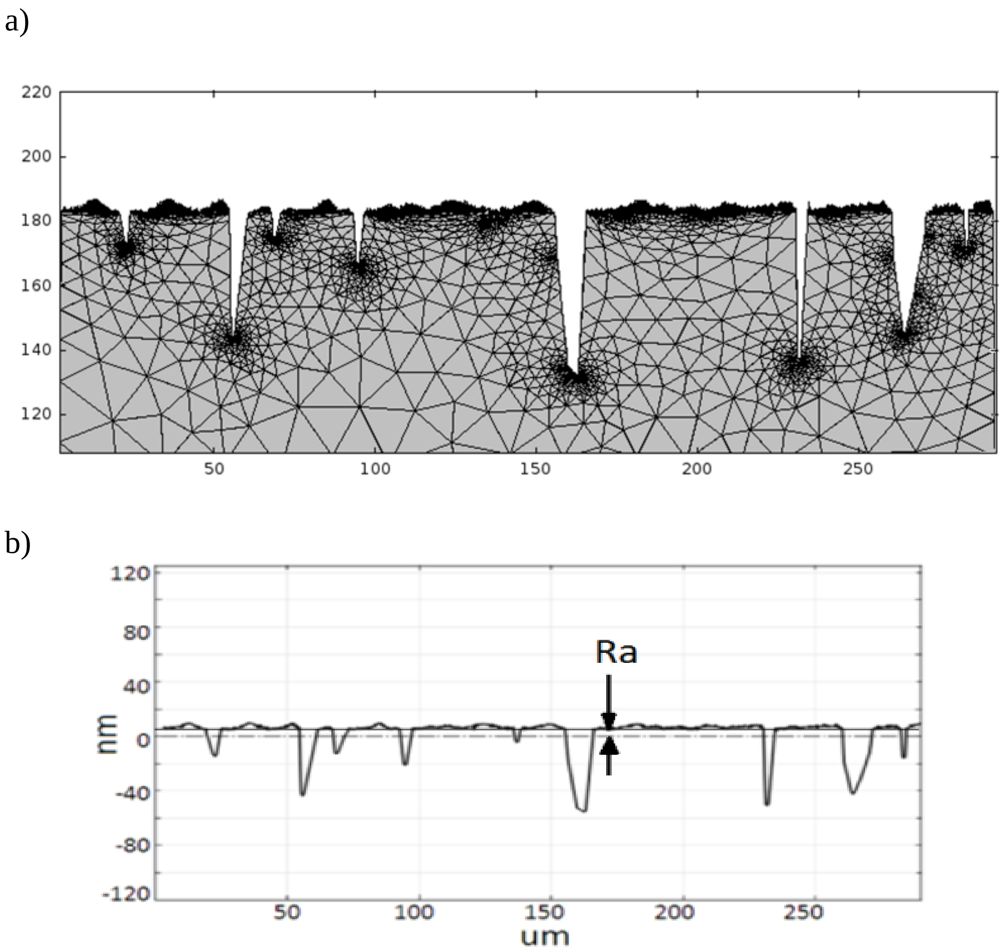

Fig.5.10: Simulated surface profile of aluminium after 10 minutes of CMMRF process, *Ra*=10 nm. (a) mesh of the profile after 10 minutes, (b) surface profile after 10 minutes.

The simulated results for the material removal for aluminium and silicon with different concentration of *KOH* chemical, processing time and working gap equal to 1 mm are presented in Figs. 5.11 (a-h). In this result it is clearly understood that the peaks of the surface profile reduce to make it flat and reduce the surface roughness (*Ra*) value as shown in the figures. Figs. 5.11 (a-d) show the material removal from aluminium workpiece at different levels of *KOH* and processing time. Figs. 5.11 (e-h) show material removal from silicon workpiece at different levels of *KOH* and processing time.

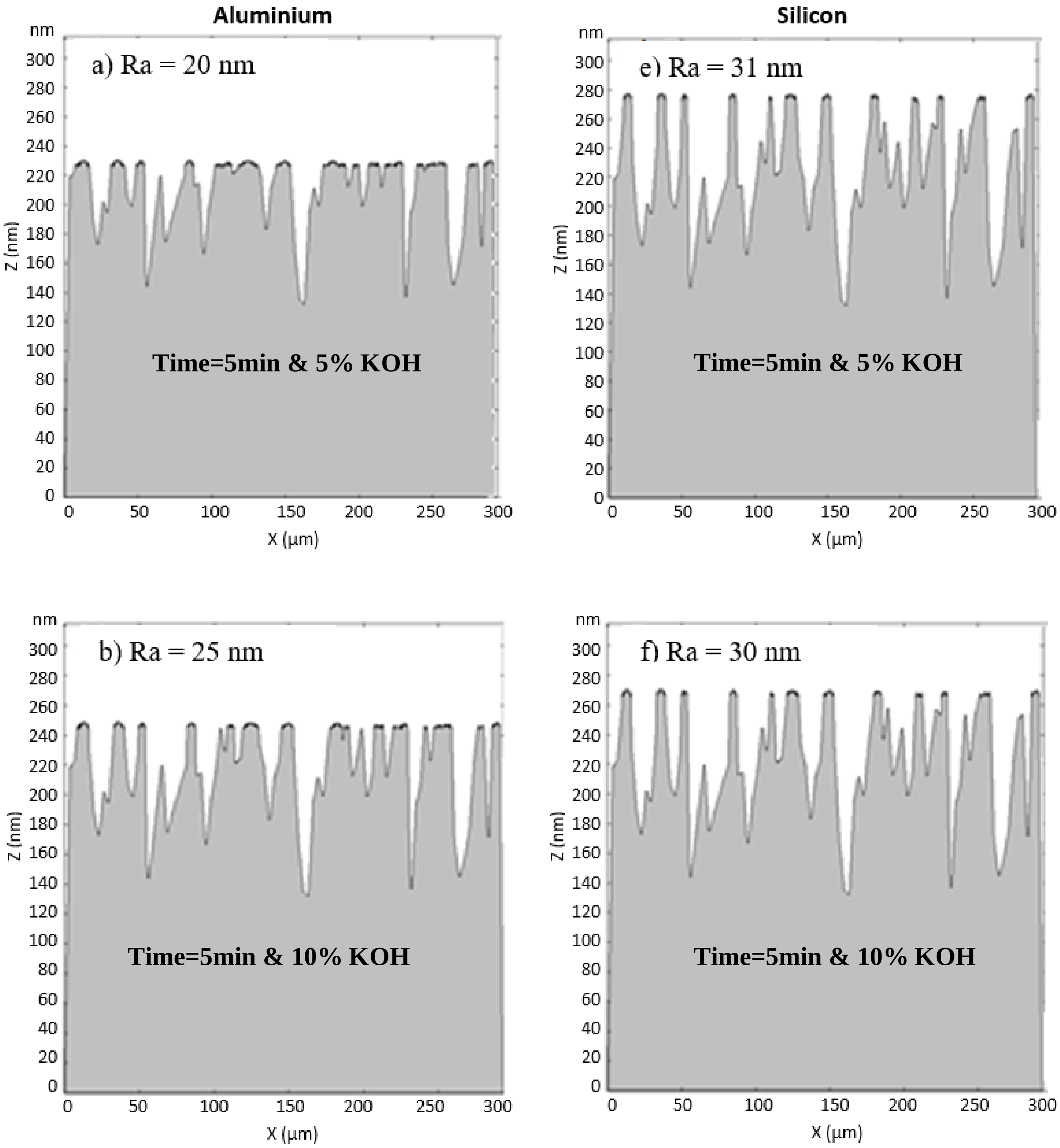
Aluminium
Silicon
a) Ra = 20 nm
Time=5min & 5% KOH
e) Ra = 31 nm
Time=5min & 5% KOH
b) Ra = 25 nm
Time=5min & 10% KOH
f) Ra = 30 nm
Time=5min & 10% KOH
nm
Z (nm)
0
20
40
60
80
100
120
140
160
180
200
220
240
260
280
300
X (μm)
0
50
100
150
200
250
300

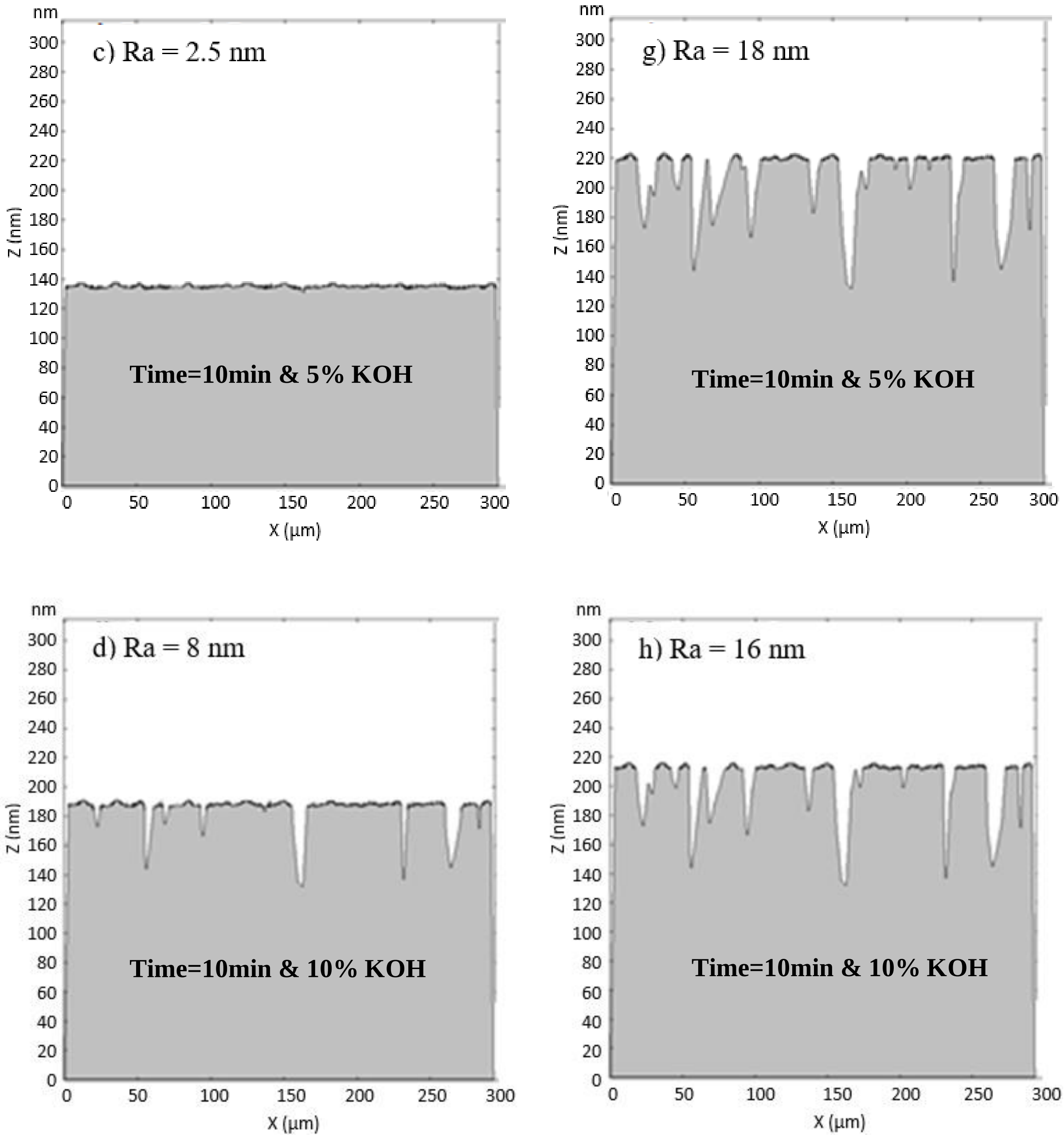

Fig. 5.11: Surface profile results obtained by simulation and presented on *Al* (a-d) and *Si* (e-h) due to different values of *KOH* and processing time.

The simulated results are plotted for the material removal in terms of thickness for aluminium workpiece and the same are shown in Figs. 5.12 (a-c). These plots illustrate variation in material removal value with finishing time under different levels of working gap and concentration of chemical.

a)

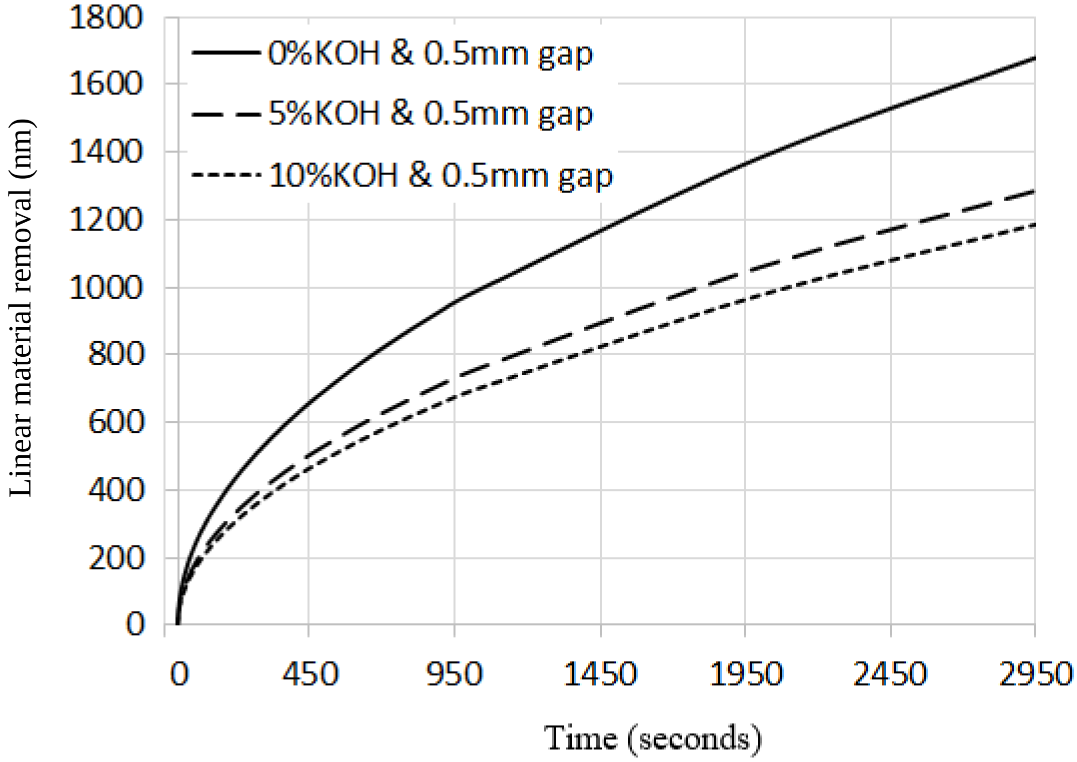

1800
1600
1400
1200
1000
800
600
400
200
0
Linear material removal (nm)
0%KOH & 0.5mm gap
5%KOH & 0.5mm gap
10%KOH & 0.5mm gap
0
450
950
1450
1950
2450
2950
Time (seconds)

b)

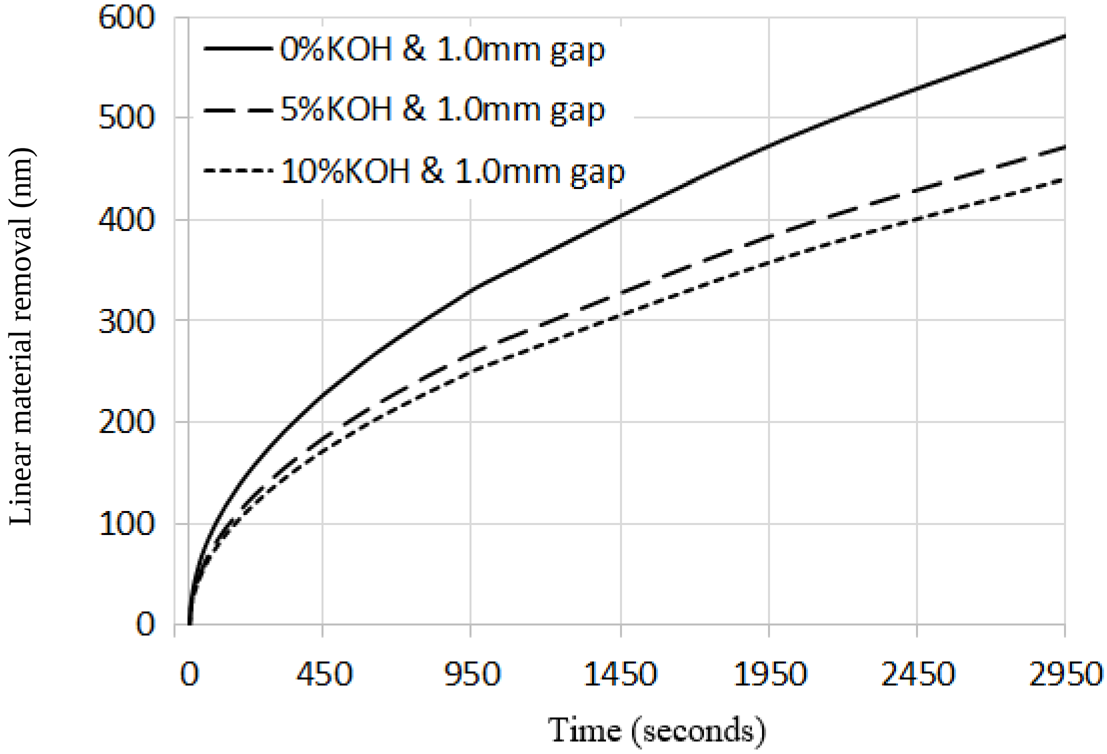

600
500
400
300
200
100
0
Linear material removal (nm)
0%KOH & 1.0mm gap
5%KOH & 1.0mm gap
10%KOH & 1.0mm gap
0
450
950
1450
1950
2450
2950
Time (seconds)

c)

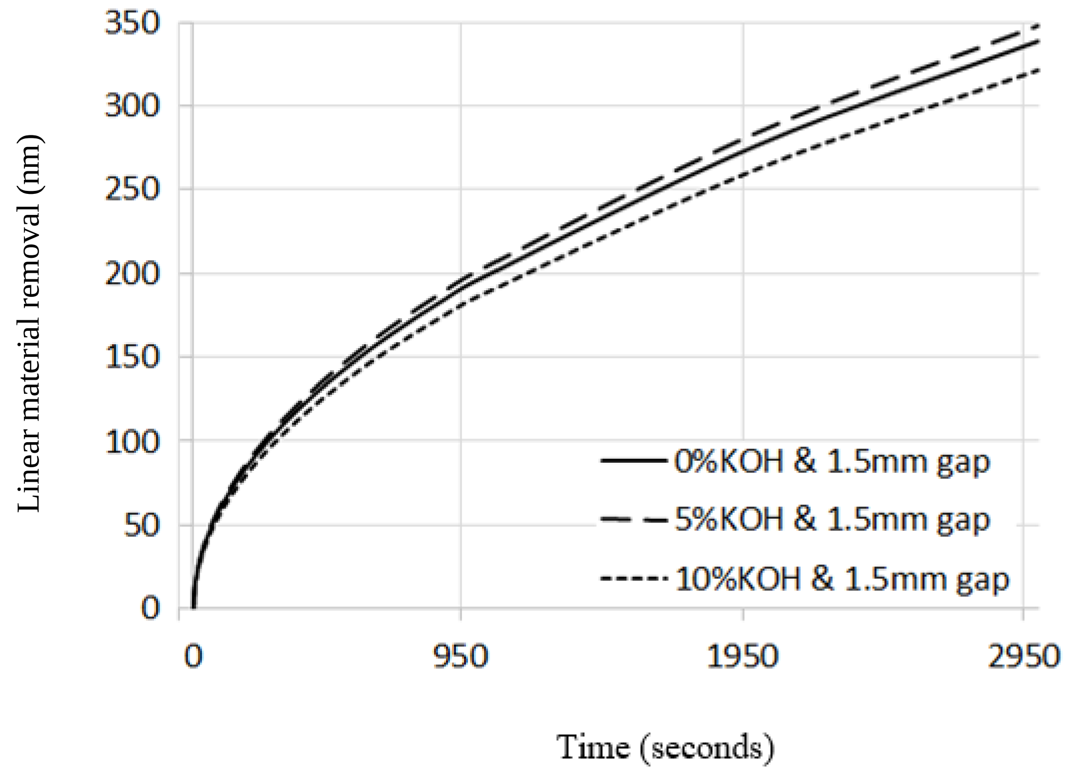

Fig.5.12: (a) Effect of chemical concentration on simulated material removal of aluminium with respect to time when working gap =0.5mm. (b) at the gap=1mm. (c) At the gap =1.5mm.

By comparing the Figs. 5.12 (a-c), it is found that the maximum material removed are 1700, 600 & 350 nm for the working gaps of 0.5, 1.0, 1.5 mm respectively.

Fig. 5.12 (a) shows material removal with respect to the finishing time, three different levels of *KOH* concentrations and the working gap equal to 0.5 mm which will exert more pressure than the required value of the ductile materials as shown in Table 3.5 and Fig. 3.20 (c) of chapter 3. During the initial 600 seconds (or 10 minutes) of finishing time, material removal increases non-linearly and it seems as parabolic, afterwards it becomes linear for the constant value of MRR (here, MRR is slope of the plot). The material removal reduces when *KOH* increases from 0% to 10%. For example, the maximum material removal (or penetration) at 0%, 5% and 10% of *KOH* yield 1700 nm, 1300 nm and 1200 nm, respectively. The reason for such reduction in the material removal is due to oxidation of workpiece by *KOH* as shown in

Fig. 4.44-4.45 of chapter 4. These oxides increase surface hardness and resist against abrasion, which further results in the reduction of material removal.

Fig. 5.12 (b) is plotted for the working gap equal to 1.0 mm and other parameters are same as that of Fig. 5.12 (a). When the working gap is increased from 0.5 to 1 mm, polishing pressure reduces and results in lower material removal with the same proportion.

Figs. 5.12 (a-b) show the effect of *KOH* concentration at two different levels of working gap, in which, the *KOH* concentration reduces material removal with working gap in a non-linear proportion. Whereas, Fig 5.12 (c) is plotted at the working gap of 1.5 mm, which shows very least variation on material removal when *KOH* concentration varies, because the polishing pressure reduces drastically when the working gap increases beyond 1 mm as shown in Fig. 3.20 (c). This sudden reduction in polishing pressure reduces the stress assisted chemical reaction (ability to push the chemical species in the workpiece) towards the formation of metal oxide. Due to this, the change in material removal is very less and all the three curves are closer to each other. The variation in material removal mainly occurs due to the stress assisted-oxide formation which is least significant at the working gap of 1.5mm.

Figs. 5.13 (a-c) are plotted for material removal on silicon workpiece. Fig. 5.13 (a) shows significant change in material removal when the percentage of *KOH* is varied in the aqueous *KOH* solution. It indicates that the material removal increases as *KOH* increases, because of the formation of soft layer of silica over the workpiece, which helps for the material removal. This effect is reduced when the working gap is increased from 0.5 mm to 1.0 mm as shown in Fig. 5.13 (b).

The effect of stress assisted chemical reaction, is least significant when the working gap is 1.5 mm, as the polishing pressure becomes 2 kPa (in Fig. 3.20 (c)). In this case the polishing pressure of MR fluid does not stratify the stress assisted chemical reaction in significant way towards higher material removal. Thus there is a marginal difference in material removal when *KOH* varies from 5% to 10%.

a)

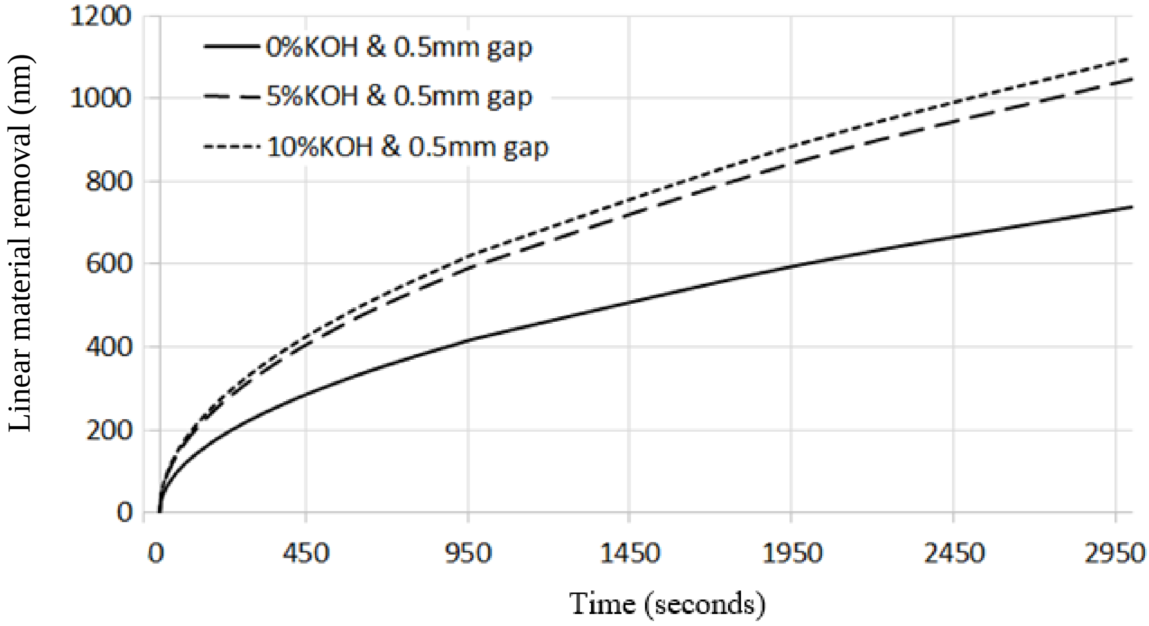

b)

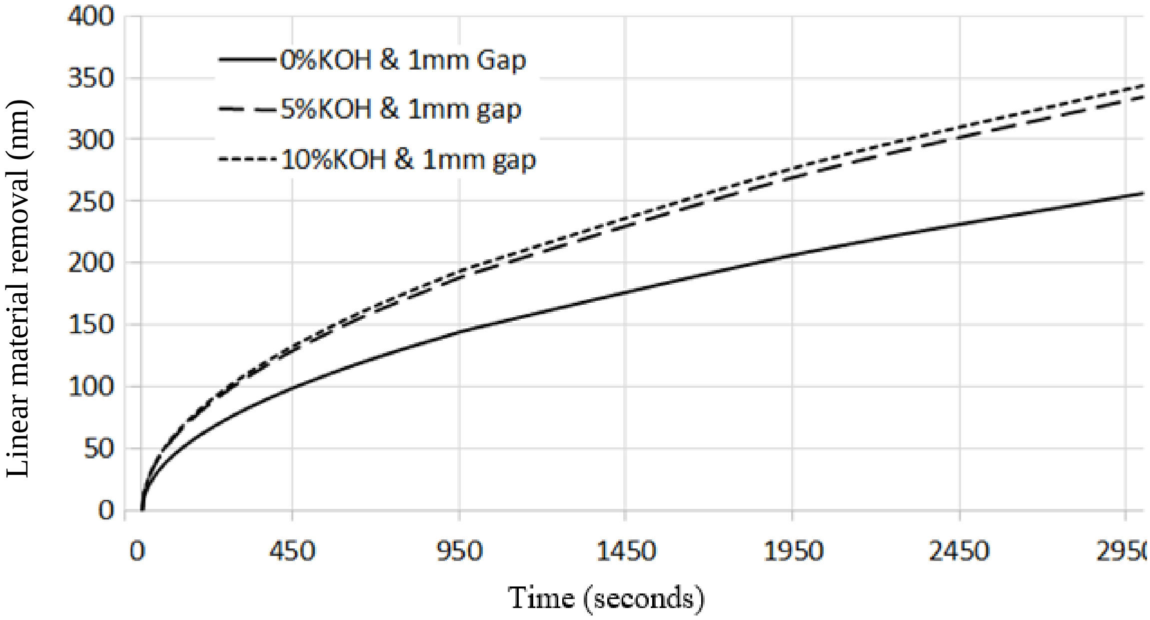

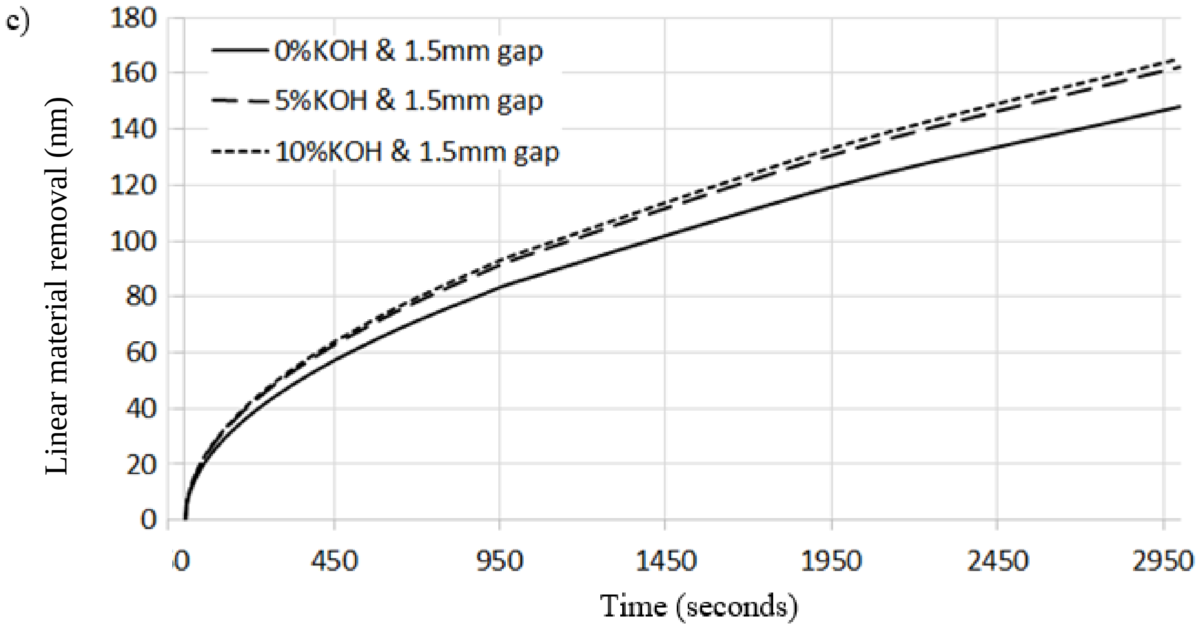

Fig.5.13: Effect of chemical concentration on simulated material removal from silicon with respect to time. (a) At the working gap =0.5 mm. (b) At the working gap =1.0 mm. (c) At the working gap =1.5 mm.

In both types of material, *KOH* chemical helps to protect the surface quality. For example, *KOH* makes the protective layer of alumina to protect base material of soft aluminium. *KOH* also helps in silicon workpiece by making the soft silica layer to reduce the required abrasion force for finishing.

5.4.2 Mechanism of material removal for CMMRF process

In the presence of an environment of aqueous *KOH* during CMMRF process of aluminium alloy as a ductile material, a hard layer forms to protect the aluminium workpiece against the indentation and scratching due to the abrasive particles. This is the reason which reduces material removal upto 30% (approximately in working gap of 0.5 mm).

In case of silicon workpiece as a brittle material under presence of aqueous *KOH*, a soft layer forms to assist material removal even by softer abrasive particles. This mechanism is responsible for high material removal rate with least defects which is inversely proportional to the hardness and size of abrasive particles.

Hence, the chemical reaction in the CMMRF process avoids the possibilities of surface damages due to mechanical abrasion in the following two categories.

1) In ductile material such as metals and alloys, the surface of workpiece gets hardened due to the oxidisation of the chemical reaction. Hence, the material removal gets reduced as compared with the mechanical abrasion, which leads toward better surface finish.
2) In brittle material like semiconductors or insulators, the surface of workpiece gets softened due to the chemical reaction. Hence, it becomes possible to remove the material with softer abrasive particles with respect to the workpiece material hardness. Finishing of such workpiece materials with soft abrasive particles leads to the production of defect free surface.

After presenting the material removal phenomenon as shown in Figs. 5.12 (a-c) and Figs. 5.13 (a-c), improvement in surface finish is also presented as follow.

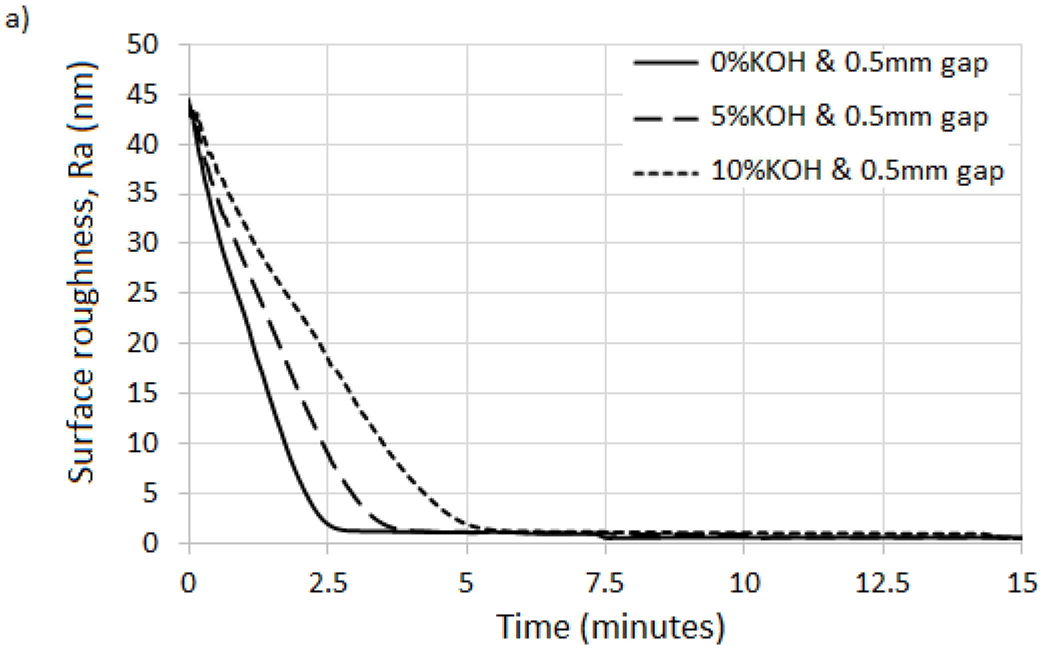

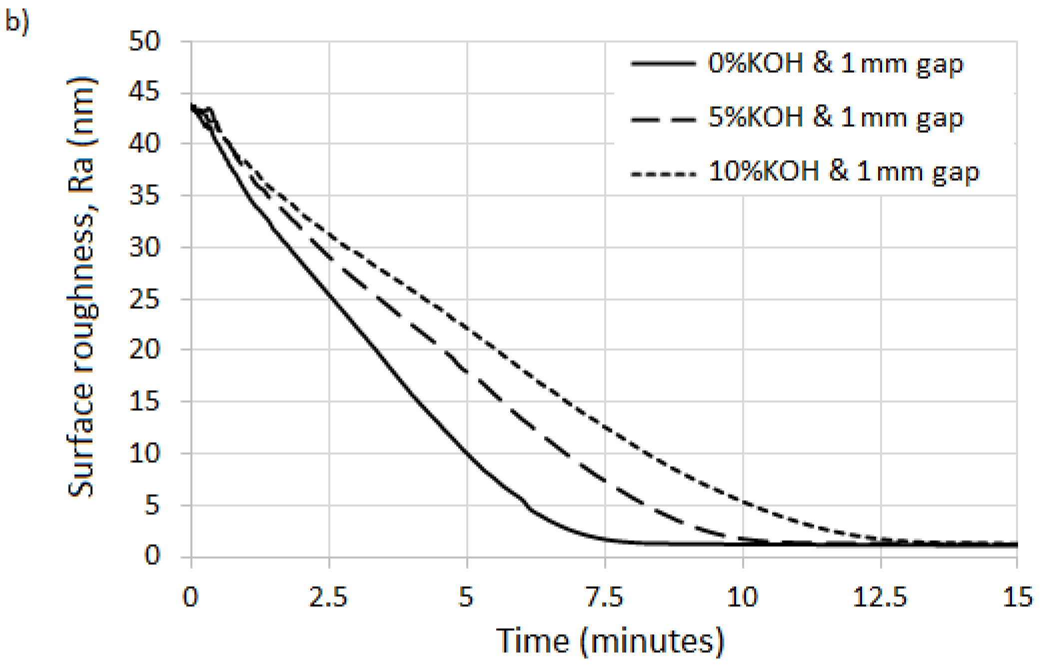

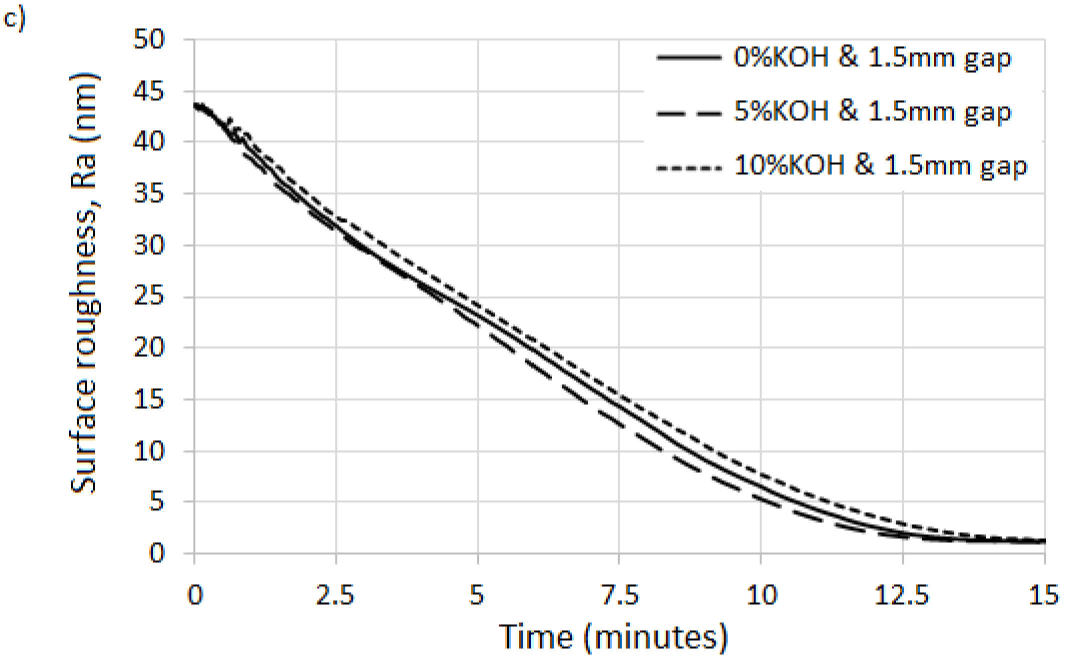

Fig. 5.14: Effect of chemical concentration on the simulated improvement in surface finish of aluminium workpiece, (a) at the working gap =0.5 mm, (b) at the working gap= 1.0 mm and (c) the working gap =1.5 mm.

To understand the surface finish improvement, the mathematical model is used to plot surface roughness with varying chemical environment and working gap for aluminium and silicon workpiece. The results are presented in Figs. 5.14 (a-c) and Figs. 5.15 (a-c).

Fig. 5.14 (a) shows the improvement in surface finish of aluminium workpiece at the working gap of 0.5 mm, and three different levels of *KOH* concentration. Surface roughness reduces with finishing time upto the critical surface roughness, thereafter, it becomes constant. The time required to achieve the critical surface roughness increases with the concentration of *KOH*.

Fig. 5.14 (b) shows the improvement in surface finish of aluminium workpiece at the working gap of 1.0 mm, and three different levels of *KOH* concentration. Trend of this plot shows similar behaviour as in Fig. 5.14 (a). Time required to achieve the critical roughness value increases approximately by 3 times higher with respect to the working gap of 0.5 mm.

Fig. 5.14 (c) is plotted with the working gap of 1.5 mm, which shows slow improvement in surface finish as compared to Figs. 5.14 (a-b). In this plot, the time to achieve critical surface roughness is almost same in all three levels of *KOH* values. In this study, it is clear that the time required to achieve the critical roughness value marginally increases by increasing *KOH* concentration and significantly by reducing the working gap. However, the effect of *KOH* becomes negligible when the working gap is equal to 1.5 mm.

To see the simulated effects of CMMRF process parameters during nanofinishing of brittle materials like silicon, the results are analysed and presented in Figs. 5.15 (a-c).

Fig. 5.15 (a) shows the surface finish improvement with CMMRF processing time, in which the surface finish improvement needs less time in case of higher concentration of *KOH*. It indicates that the oxide formation assists the material removal and reduces the time to achieve the critical surface finish. In addition, the final surface finish after 15 minutes shows the same value in all the three case, but, the presence of *KOH* yields the critical surface finish at the time of 6 minutes. Hence, the material removal and CMMRF process in this case, can be called as formation of soft passivation layer towards material removal.

Fig. 5.15 (b) shows the surface finish improvement with CMMRF processing time at the working gap of 1.0 mm, which shows similar trends as in Fig.5.15 (a) except the time required to achieve the critical roughness. In this case the surface gets critical roughness value after 35 minutes when *KOH* is not introduced, and this time reduces upto 20 minutes when *KOH* is introduced.

When the working gap is increased upto 1.5 mm, time required to achieve the critical roughness increase significantly as shown in Fig. 5.15 (c). The effect of *KOH* shows small improvement with respect to Figs. 5.15 (a-b).

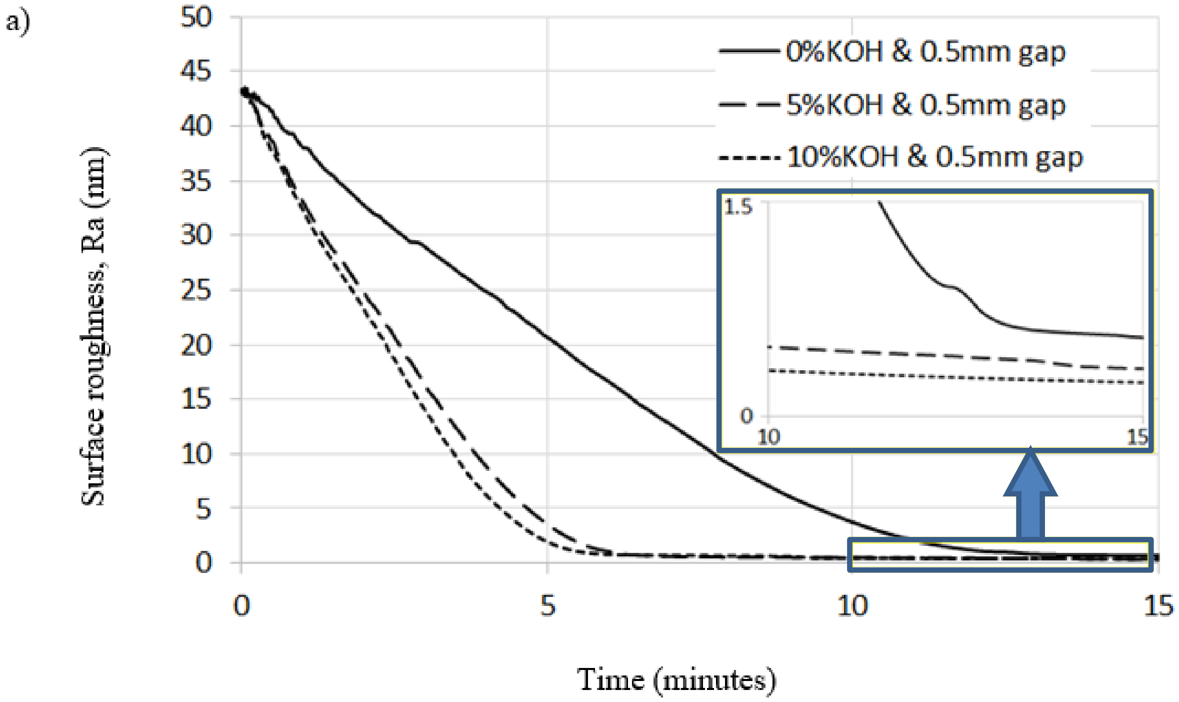

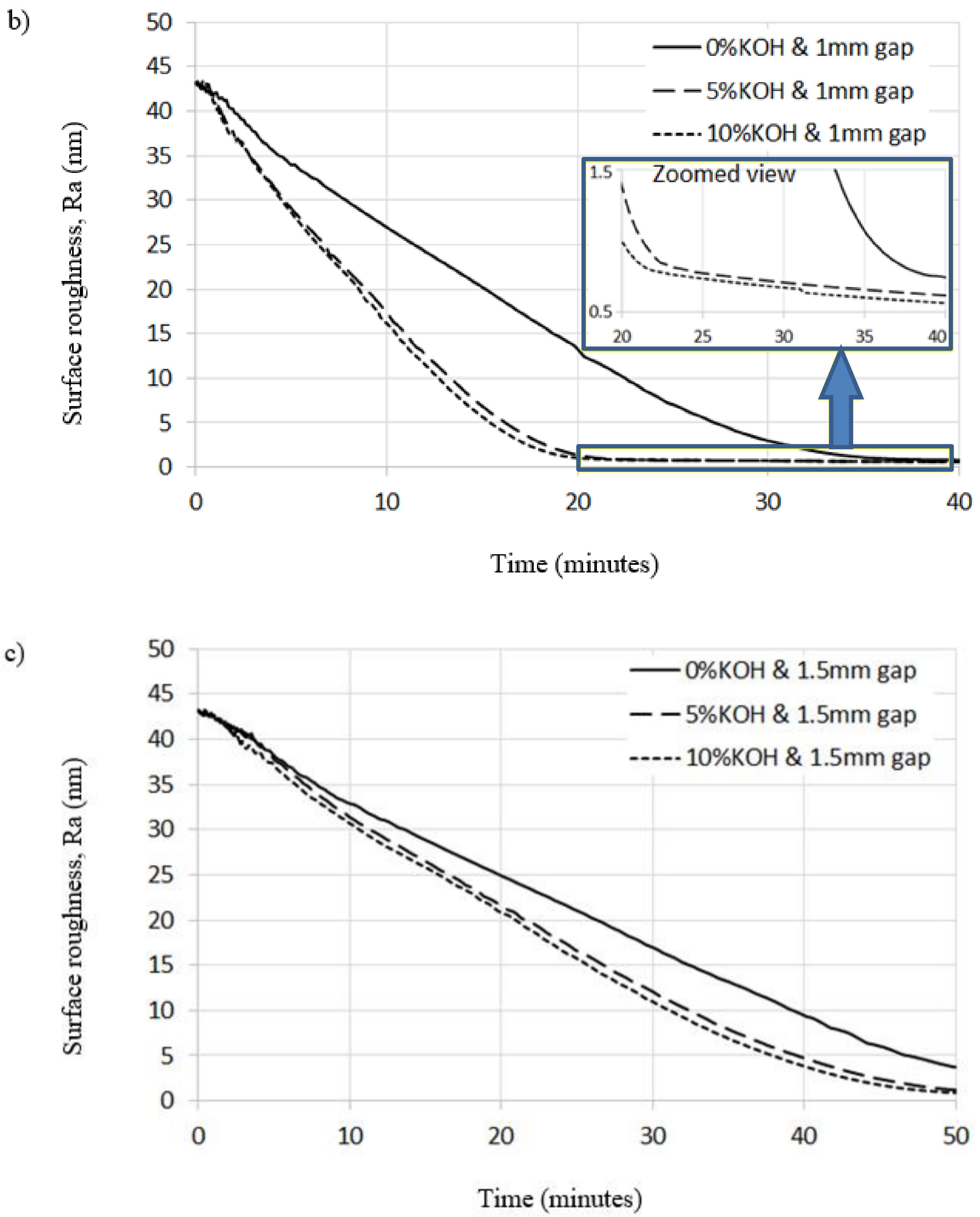

Fig. 5.15: Effect of chemical concentration on the simulated improvement in surface finish of silicon workpiece, (a) at the working gap =0.5 mm, (b) at the working gap= 1.0 mm and (c) at the working gap =1.5 mm.

Figs. 5.15 (a-b) also show zoomed view of the critically finished region in which slopes of all curves (0%, 5% & 10% *KOH*) are very small. Hence, after achieving the critical roughness value, improvement in the surface roughness becomes almost zero.

From the present study, it is observed that the surface roughness gets almost saturated after some time of the CMMRF processing. Final surface finish after that time yields the 'critical surface roughness' which is governed by parameters for mechanical and chemical finishing of the process. For example, the critical roughness in case of rough finishing, fine finishing, precision finishing and ultra-precision finishing of Table 4.5 are in order of 200 nm, 50 nm, 5 nm and less than 1 nm, respectively.

Simulated results of this chapter are further used for the next chapter toward experimental validation and investigation of the process capability.

5.5. Summary

In this chapter, mathematical modelling and FEA based simulation are carried out for chemically assisted mechanical abrasion of CMMRF process. In the present work, material removal and surface finish are studied by varying working gap, concentration of *KOH*, and finishing time. Important conclusion of this work are summarized as follows.

- Mathematical modelling of CMMRF process is carried out to predict material removal and surface finish at different sets of process parameters like chemical concentration, working gap, and finishing time.
- It was observed that material removal in case of aluminium under *KOH* chemical environment helps to protect surface of parent material against mechanical damage, and it also reduces material removal rate. Hence, CMMRF processing time increases in case of chemical. In addition, it is also observed that the effect of chemical does not affect

the material removal when the working gap is 1.5mm (or the abrasion force equal to 50 nN or less as shown in Table 5.1 & 5.2).

- In case of silicon workpiece, material removal increases with concentration of *KOH* which produces chemical environment. This effect enhances significantly when abrasion force increases by reducing working gap.
- The surface roughness reduces with high finishing rate during initial few minutes, thereafter, the rate of reduction in surface roughness becomes extremely low. After enough time (50 minutes in case of aluminium) of finishing, the improvement in surface roughness becomes almost asymptotic or, finishing rate becomes almost zero.
- In case of aluminium, material removed in 50 minutes is 1700 nm for 0% *KOH* and 1200 nm at 10% *KOH* and 0.5 mm of working gap.
- In case of silicon, material removed in 50 minutes is 750 nm for 0% *KOH* and 1100 nm at 10% *KOH* and 0.5 mm of working gap.
- It is also concluded that in CMMRF process, the chemical reaction helps in avoiding the possibilities of surface damage by creating hard layers on ductile materials, and soft layers on brittle materials followed by the removal of these layers.

------------X------------

Chapter-6

EXPERIMENTAL INVESTIGATIONS

6.1. Introduction

In chapter-5, mathematical modelling and FEA based simulation were carried out to study about the extent of material removal and prediction of the processing time to achieve the critical Ra value. This was investigated and the result was also reported for aluminium as ductile material and silicon as brittle material. However, value of critical Ra and surface quality could to investigated through macro-scale modelling in chapter-5. Whereas, chapter-3 deals the effect of working gap through zone-1 and zone-2 about the surface quality and chapter-4 deals that the chemical reaction plays a vital role to achieve better surface finish. In view of this, a series of experimentations are planned and conducted on aluminium as well silicon as workpiece material to experimentally validate the mathematical model of CMMRF and the effect of zone-1 and zone-2 to validate the outcome of chapter-3 as reported in Table 3.5. Further, a set of experiments are also carried out to validate the effect of chemically active abrasive particles as reported in section 4.4.2. of chapter-4 and it is also targeted to generate atomically finished surface in ductile material as well. In addition, another set of experimental study is also carried out for copper alloy to optimise CMMRF process in respect of the effect of chemical reaction to achieve better surface finish.

6.2. Experimental setup

To carry out experimental study and for validation of modelling work, a CMMRF set-up was designed and developed keeping in view the fundamental mechanisms of the process and basic functional requirements. A schematic of the process is shown in Fig.6.1.

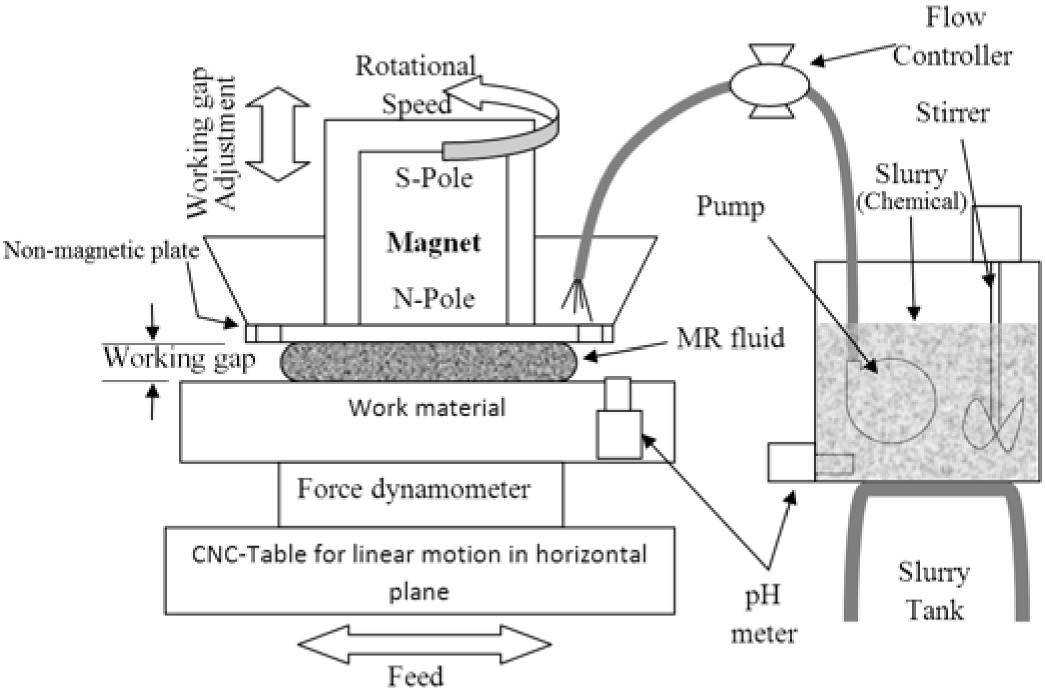

Fig.6.1: Schematic of CMMRF process

In this chapter a set of experimental study is planned to compare the experimental results with the mathematical model results of CMMRF process for aluminium alloy and single-crystal silicon. Moreover, another set of experiments are conducted to investigate the effect of chemicals on copper alloy.

The experimental set-up has been fabricated as shown in Fig. 6.2 to carry out CMMRF process on metals as well as non-metals. Main aspect of CMMRF set-up comprises flexible polishing pad with polishing slurry system under the specified precision movements (rotary and translator movements), and the entire CMMRF system is categorised in three units as follows.

1) Finishing head: It consists magnetic head with a rotary spindle.
2) Three axis stage: It is a CNC stage for motion along X, Y and Z directions.
3) Slurry system: It is used for continuous supplying of slurry to maintain chemical properties and fresh abrasive particles during nanofinishing.

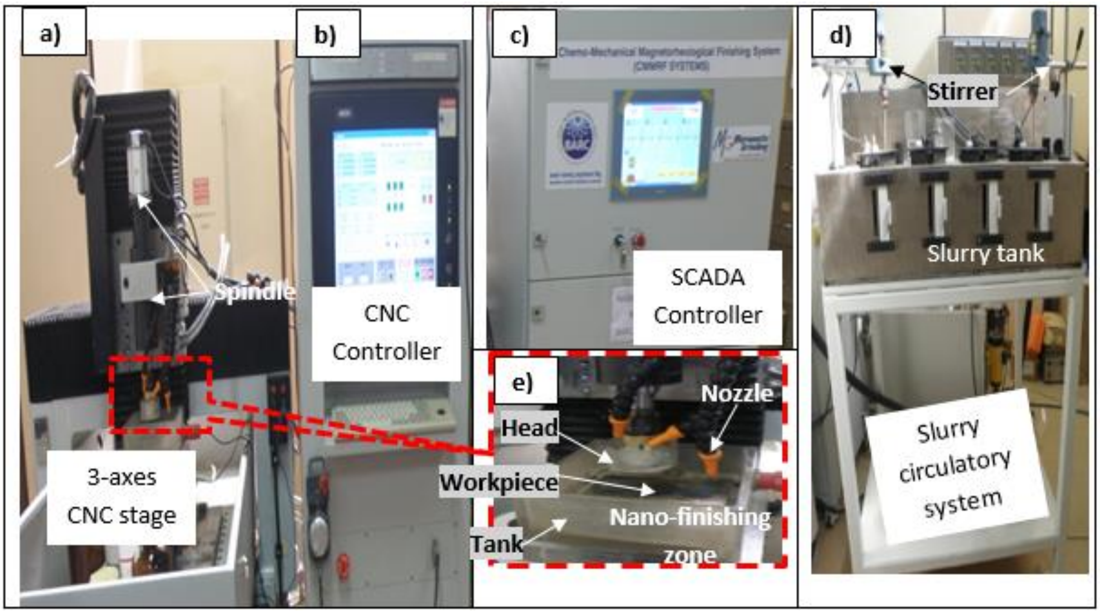

Fig.6.2: Experimental set-up for CMMRF operation. (a) 3-Axis CNC stage, (b) Controller of CNC stage, (c) Controller for slurry circulation, (d) Slurry circulatory system, and (e) Nano-finishing zone comprises finishing head, tank with pH meter, workpiece, and slurry delivery nozzles.

The finishing head is mounted on a precision linear movements of a computer numerical control (CNC) machine. This machine has positional accuracy of 2 μm and repeatability of 1 μm.

CMP process requires few parameters to be maintained within their acceptable working range such as polishing pressure, zeta potential and pH value of finishing medium. In view of this, CMMRF set up is also made with such provision so that unfavourable attributes of finishing medium can be avoided. These parameters are maintained by monitoring polishing pressure using force dynamometer (Make: KISTLER; Model no. 5070) along axial direction (to correlate with polishing pressure). Zeta potential is considered to be an effective parameter and it is controlled in the range of ±30 mV and pH value of finishing medium. Zeta value has been obtained by using additives in the slurry like glycol and glycerol. pH value is used to maintain concentration of chemical such as % of nitric acid, *KOH* and aqueous ammonia, which is measured by a pH meter (Make: HANNA instruments; Model: BL 931700-0). Rotational speed and feed rate were set to 250 rpm and 5 mm/min respectively. Working gap was set in the range of 0.3 to 1.5 mm (excluding thickness of PMMA sheet, i.e. 0.5 mm), and finishing time was set for 60 minutes.

Figs. 6.2 (a-e) show the details about the experimental setup in which three major units are shown. Fig. 6.2 (a) shows three axis CNC stage on which finishing head is mounted with a rotary spindle and it also includes nano-finishing tank to hold the workpiece with a suitable fixture. The CMMRF slurry is directed to the finishing zone using nozzles as shown in Fig. 6.2 (e). Fig. 6.2 (b) shows a CNC controller of the 3-axis CNC stage, which is used to programme the nanofinishing process by incorporating working gap, feed rate and area of finishing. Fig. 6.2 (d) shows the slurry circulatory system which consists slurry tank and stirrer with pH meters, and its controller as shown in Fig. 6.2 (c).

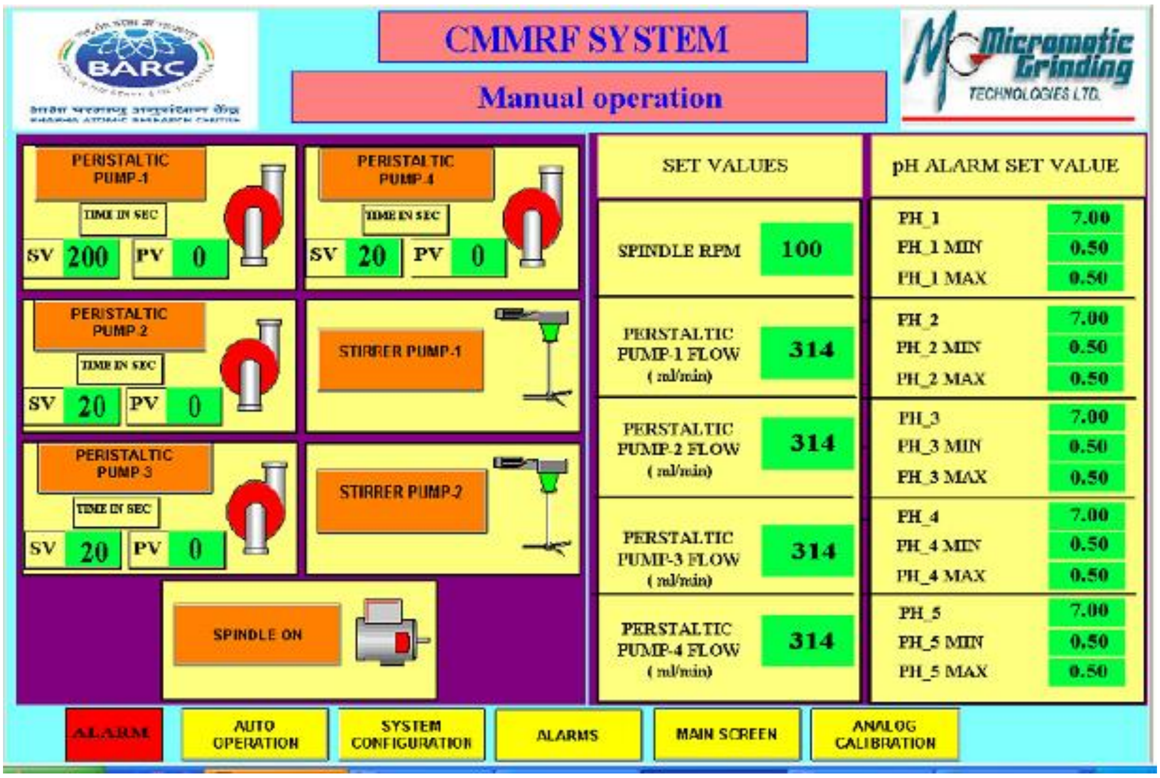
CMMRF SYSTEM

Manual operation

PERISTALTIC PUMP-1 — TIME IN SEC: SV 200 PV 0

PERISTALTIC PUMP-4 — TIME IN SEC: SV 20 PV 0

PERISTALTIC PUMP 2 — TIME IN SEC: SV 20 PV 0

PERISTALTIC PUMP 3 — TIME IN SEC: SV 20 PV 0

SET VALUES	
SPINDLE RPM	100
PERSTALTIC PUMP-1 FLOW (ml/min)	314
PERSTALTIC PUMP-2 FLOW (ml/min)	314
PERSTALTIC PUMP-3 FLOW (ml/min)	314
PERSTALTIC PUMP-4 FLOW (ml/min)	314

pH ALARM SET VALUE	
PH_1	7.00
PH_1 MIN	0.50
PH_1 MAX	0.50
PH_2	7.00
PH_2 MIN	0.50
PH_2 MAX	0.50
PH_3	7.00
PH_3 MIN	0.50
PH_3 MAX	0.50
PH_4	7.00
PH_4 MIN	0.50
PH_4 MAX	0.50
PH_5	7.00
PH_5 MIN	0.50
PH_5 MAX	0.50

Fig.6.3: Parameter setting for the CMMRF process which includes flow of slurry, time for slurry flow, stirrer of slurry, spindle speed, and pH values.

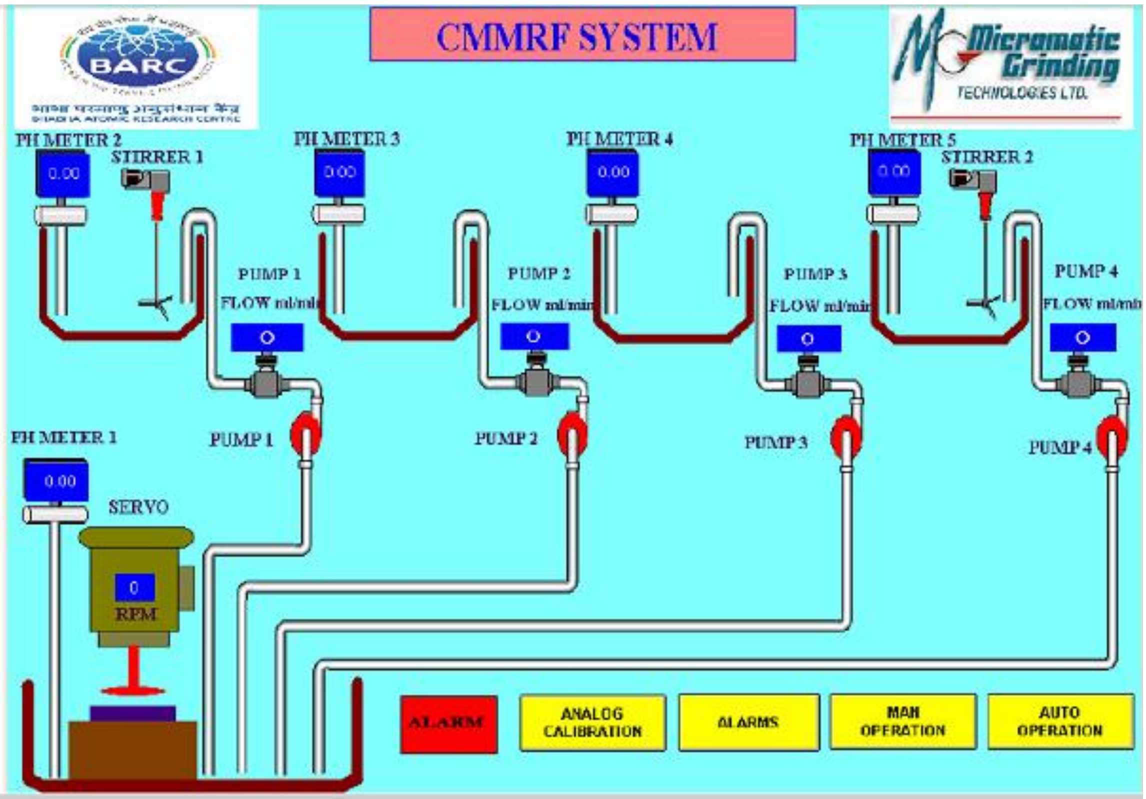

Fig.6.4: Monitoring window of CMMRF process.

The controller for the slurry system is made with a SCADA based control system which is used to monitor and control the CMMRF process parameters as shown in Figs. 6.3-6.4. This controller also includes an alarm system, so that, any variation on CMMRF process parameters due to time degradation can be identified and fixed. Details of the finishing head is presented in Fig.6.5, in which magnetic head is made to accommodate a permanent magnet with a magnetic strength equal to 0.6T (app.). In addition, this head also provides a passage to supply chemicals in the nano-finishing zone without disturbing the setup and working gap. Detailed schematic of magnetic head is shown in Figs. 6.5 (a-c). These figures show the magnetic head in two different orientations, and it also shows packaging of permanent magnet with suitable passage of slurry as labelled in this figure itself. Fig. 6.5 (c) shows the schematic in exploded view. Moreover, detailed schematic diagram, drawing and parameters of CMMRF system are presented in Figs. A1-A4 and Table A2 of Appendix.

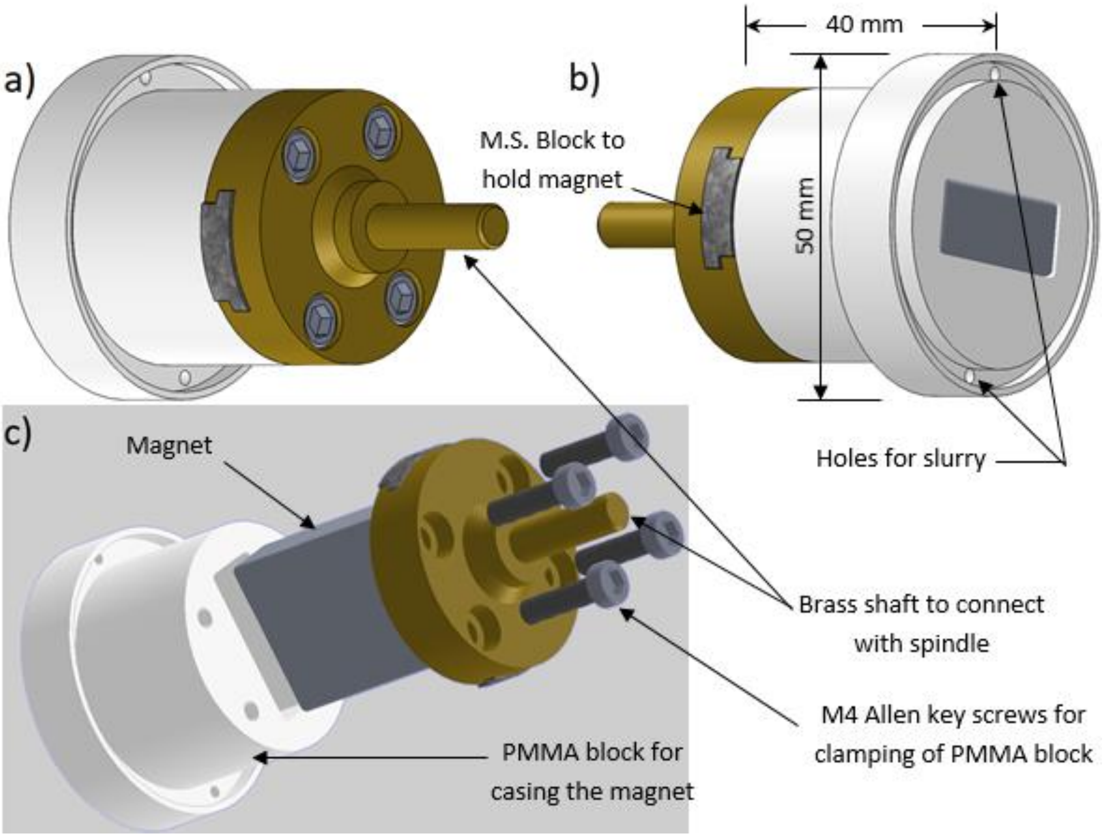

Fig.6.5: Details of finishing head. (a-b) Two different orientation of solid model. (c) Exploded view of parts of the magnetic head.

6.3. Plan of Experiments

The experiments are designed to investigate the influence of process variables on material removal and the improvement in surface finish, this work also includes validation of mathematical model. Two different materials of workpiece are selected for CMMRF experiments. These materials are used to investigate CMMRF capabilities to cover a wide range of engineering materials like ductile material and brittle material. In the present case, aluminium alloy is used as ductile material and silicon is used as brittle material. To plan the experiments, FEA, CFD, and MDS results are used from the previous chapters. For example, composition of MR fluid is obtained from preliminary experiments of Table 3.2 and addition of sodium stearate based on the section 3.5, range working gap is decided from FEA results of Fig. 3.20 and Table 3.5 and preliminary experiments of Fig. 3.22, and time for finishing is also obtained on basis of FEA results of Figs. 5.14 and 5.15. In addition, MDS results are used to select types of chemical (as per section 4.4 and Table 4.6) for a particular work material.

Preparation of workpiece: As CMMRF process does material removal at nanometric scale, hence the initial surface roughness of workpiece needs to maintain of the order of few tens of nanometer, otherwise the process becomes under-utilised due to the enormous time while processing of micro level finished surface. In view of this, workpieces are prepared using mechanical finishing suggested by MD simulation (steps-1 for rough finishing & step-2 for fine finishing of Table 4.7) as an essential prerequisite for CMMRF or any nano-finishing process. In addition, each workpiece has been provided with a micro-slot (specification of micro-slot with the dimensions of 0.2 mm width, 50 μm depth and 1.0 mm length) using micro-milling operation. The micro-slot is measured using optical profile-meter (Make: Taylor & Hobson, model: CCI with vertical resolution: 0.01 nm) which can measure at nanometric scale accurately. The depth of this micro-slot has been used to compute variation in depth of material removed with time during CMMRF operation as per following Eq. (6.1).

$$\text{Material removal at '}t\text{'} = (\text{depth of microslot at } t = 0) - (\text{depth of microslot at } t = t) \qquad (6.1)$$

6.3.1. Experiments on ductile material

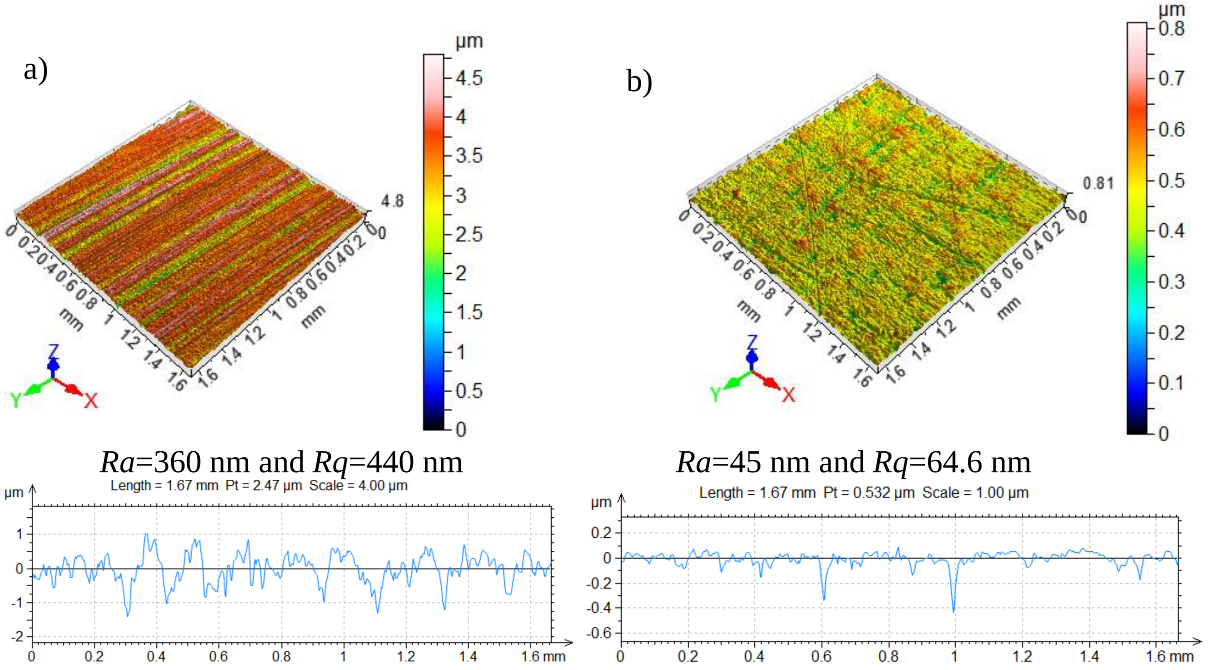

Ra=360 nm and *Rq*=440 nm

Ra=45 nm and *Rq*=64.6 nm

Fig.6.6: (a) Surface topography of raw surface which is made by conventional turning process. Surface finish *Ra*=360 nm, (b) Surface of prepared sample after lapping process. *Ra*=45 nm.

As far as ductile material of workpiece is concerned, few materials such as aluminium alloy, copper and stainless steel are used. However, parametric experiments are carried out on aluminium alloy to compare the mathematical model, thereafter parameters for CMMRF process are frozen to generate nano-finished surface on copper alloy as well.

6.3.1.1. Parametric experimental plan on aluminium alloy:6061-T6

Samples are prepared with micro-slot as discussed earlier for the computation of material removal in depth, and then the workpiece was finished with coarse abrasive of diamond particles (diameter = 8 μm) followed by fine particles (diameter = 0.25 μm). The surface topography of raw material and the prepared sample after mechanical finishing are presented in Figs. 6.6 (a-b).

Suitable chemicals for nanofinishing of aluminium alloy are selected as per the MD simulation, i.e. types of abrasive particles and chemicals of the finishing slurries. In the direction of experimental validation of the mathematical model, few parameters have been varied as follows. Parameters and their values for experiments are listed in Table 6.1.

Table 6.1: Variable parameters for experimental plan of CMMRF.

Sr. No.	**Parameters**	**Values**
1	Working gap to accommodate MR fluid between finishing head and workpiece.	0.5, 1.0, and 1.5 mm
2	Flanks of Potassium hydroxide in volume % or weight per *ml* of water.	0, 5% (100*mgs/ml*), 10% (200*mgs/ml*) and 15% (300*mgs/ml*)
3	Finishing time for CMMRF process	0, 5, 10, 15, 30, and 40 minutes.

There are some other fixed parameters as listed in Table 6.2. These parameters are continuously maintained during nano-finishing of aluminium alloy.

During the experiments of CMMRF process, workpiece (or work material) is clamped on the force dynamometer using a fixture, thereafter, MR fluid is placed underneath of the finishing head (Fig.6.5), and the chemical is fed continuously to the finishing zone through the holes of the finishing head using nozzle. After completion of finishing time, polishing head is retracted towards vertically upward direction and then workpiece is unloaded by unclamping the fixture.

Table 6.2: List of fixed parameters of CMMRF process.

Sr.No.	**Parameters**	**Values**	**Composition**
1	Diameter of magnetic particles (CIP)	1-5 µm	Mixing ratio of solid particles by weight: 60% CIP + 40% Al_2O_3
2	Diameter of abrasive particles (alumina)	5-6µm	
3	Chemicals for chemical reactions	Aqueous KOH	As per Table 6.1.
4	Additives to maintain properties of slurry and MR fluid	Glycerol + sodium stearate	Mixing ratio in volume: 90% chemical (i.e. aqueous KOH) + 8% sodium stearate + 2% glycerol.
5	Rotational speed of polishing head	250 rpm	-
6	Feed of the workpiece	5 mm/min	-
7	MR fluid preparation	Mixing of solid particles & additives	Mixing ratio in volume of 30% solid particles +70% additives.

6.3.2. Experiments on brittle material

This experimental plan was made to investing the behaviour of CMMRF process on brittle materials, and the parametric study is carried out on silicon for the validation of mathematical model. Experimental parameters for this study are used according to the earlier plan of aluminium as shown in the Tables 6.1-6.2.

Sample preparation: The surface finish of silicon is processed under two different categories of the finishing operations as shown in Table 4.7. The workpiece was prepared for CMMRF by carrying out rough finishing using coarse abrasive of diamond particles (diameter = 20 µm) followed by fine particles (diameter = 3 μm). Prior to finishing, micro-scratch is provided as discussed earlier for the computation of material removal in depth.

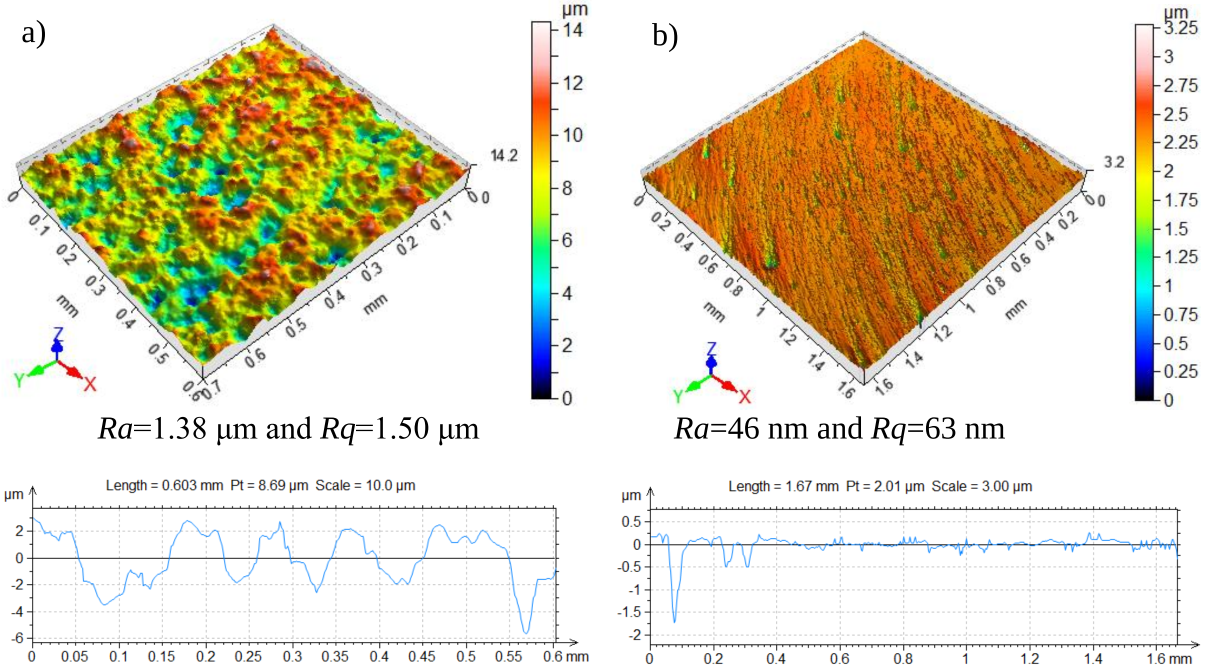

Ra=1.38 μm and *Rq*=1.50 μm

Ra=46 nm and *Rq*=63 nm

Fig. 6.7: (a) Surface topography of initial surface with *Ra*=1.38 μm (1380 nm). (b) Surface topography of sample which is generated by mechanical finishing, *Ra*=46 nm.

Surface topography of the raw sample and the prepared sample are shown in Figs. 6.7 (a-b). The prepared sample shows a texture which defines the direction of mechanical finishing, as shown in Fig. 6.7 (b).

6.4. Results and discussions

6.4.1. Results and discussion on Aluminium alloy workpiece

A series of experiments are conducted on aluminium alloy as per Table 6.1-6.2 and the results are presented in Table A3 of Appendix.

Experimental results are plotted against the simulated results of chapter 5, as shown in Figs. 6.8 (a-c) and 6.9 (a-c). These plots show good agreement with the simulated result. Effect of

CMMRF parameters are discussed in following section for surface roughness as well as material removal.

6.4.1.1 Effect of process parameters on surface roughness of aluminium alloy

Figs. 6.8 (a-c) show the effect of finishing time and the concentration of chemical at three different level of working gap.

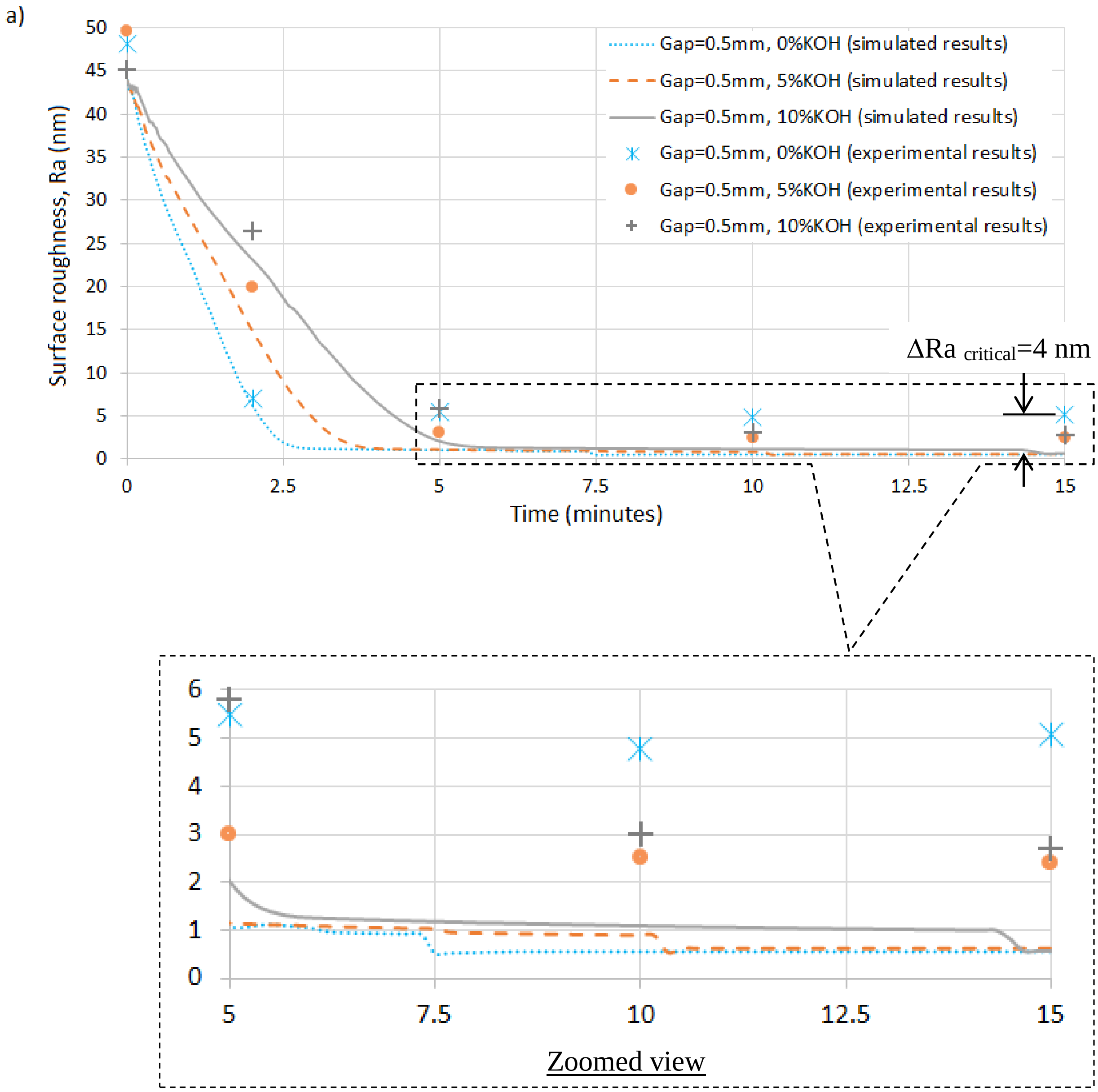

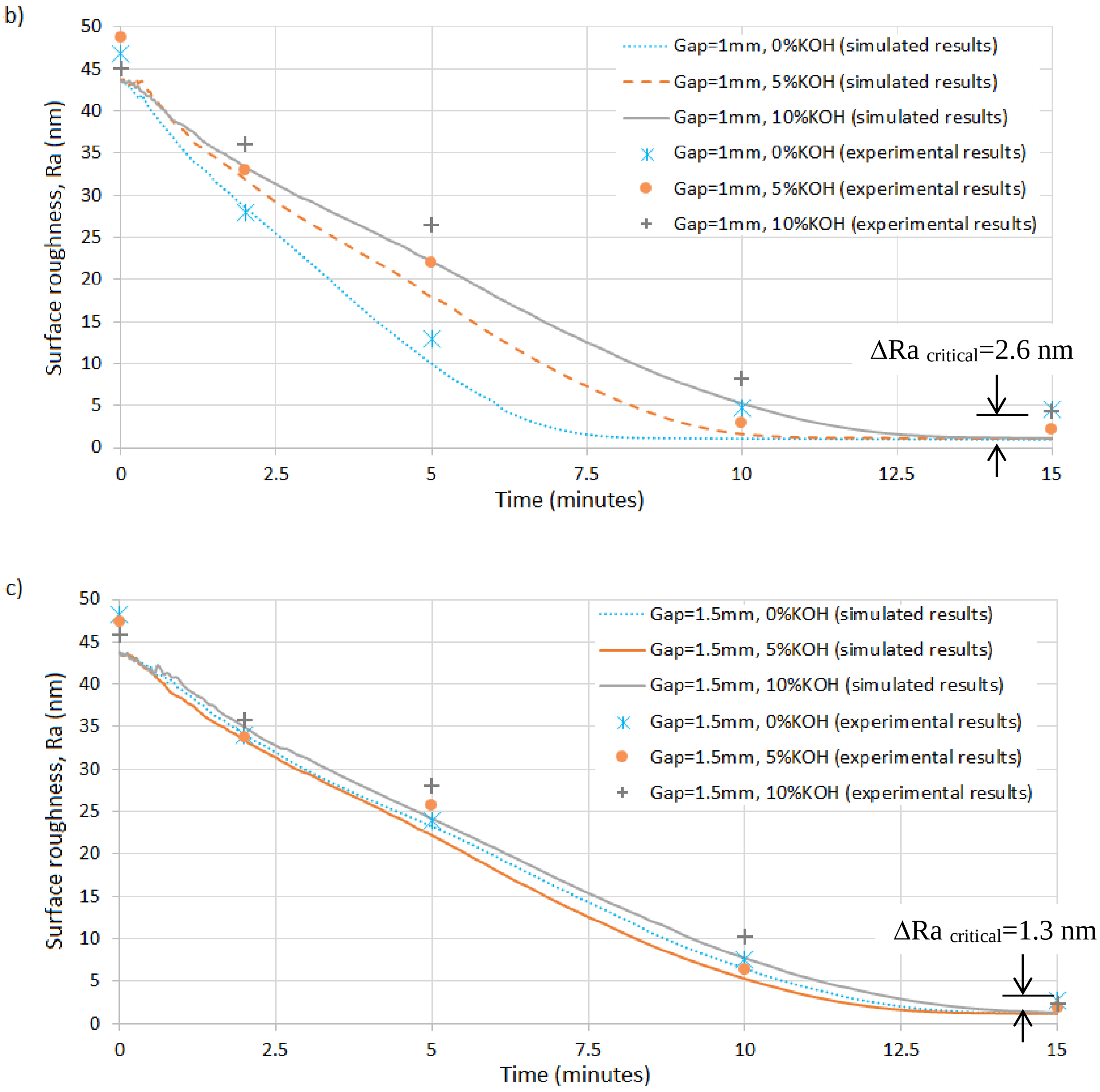

Fig. 6.8: Improvement in surface roughness of aluminium alloy with finishing time, and different levels of working gap and *KOH* concentration (i.e. %*KOH*). Working gap (a) 0.5mm, (b) 1.0mm, (c) 1.5mm.

6.4.1.2 Effect of finishing time on surface roughness

During initial time of finishing, reduction in surface roughness occurs exponentially as shown in Figs. 6.8 (a-c). Thereafter, the rate of reduction in surface roughness become extremely slow as shown in Fig. 6.8 (a) which shows almost asymptotic. This shows two zones of the improvement in surface roughness, the first zone belongs to the initial stage of finishing in which peaks and valleys of surface are comparable as shown in Figs. 5.11 (a-b), which offers more material to remove. When peaks and valleys of surface are comparable, material removal becomes easy as the shearing area becomes small, and this why the 1st zone shows more finishing rate. In the second zone, most of peaks get flattened with few valleys as shown in Fig. 5.11 (d). Thus the improvement in surface roughness becomes negligible in the second zone. After completion of the second zone of finishing, all valleys of surface also get vanished as shown in Fig. 5.11 (c), and therefore it is important to know the time required for completion of the second zone so that optimum surface finish can be achieved and over finishing of surface can be avoided. Figs. 6.8 (a-c) show good agreement between simulated results and experimental results as far as finishing time is concerned. However, there are some deviations in surface finish due to the surface damages at lesser working gap as ductile materials are amenable for zone-1 (gap < 0.5 mm).

6.4.1.3 Effect of KOH concentration on surface roughness

Effect of *KOH* is plotted in Figs. 6.8 (a-c) which shows that *KOH* resists in the reduction rate of surface roughness. In general, aqueous *KOH* forms aluminium hydroxide followed by the formation of alumina as shown in Fig. 4.44 of MD simulation. This oxide formation results in less material removal rate and it also prevents against unwanted indentation of abrasive particle on aluminium alloy, and scratches and digs formation are minimal. In case of chemical free abrasion, abrasive particle leads to excessive surface damages as shown in Fig. 4.18 (d). Thus the experimental results show higher roughness value than the simulated value in case of 0% *KOH* as shown in Figs. 6.8 (a-b). It is also observed that the effect of *KOH* becomes very small and difficult to distinguish if the working gap is higher or 1.5 mm as shown in Fig. 6.8 (c), this result shows the least effect of the chemical assisted mechanical finishing of CMMRF process as discussed in the chapter 4.

6.4.1.4 Effect of working gap on surface roughness

Figs. 6.8 (a-c) are plotted with gap equal to 0.5, 1.0 and 1.5 mm respectively. Reduction in the working gap increases polishing pressure which reduces the surface roughness faster and reaches the critical surface finish in less time. For example, the times to reach critical surface roughness are 5.5, 12.5 and 15 minutes for the working gap of 0.5, 1.0 and 1.5 mm, respectively. It is also observed that the effect of chemical reaction on the reduction of surface roughness is effective in case of low working gap, which means that the chemical reactions are stress dependent in the present case of CMMRF process. After achieving the critical roughness value, both simulated and experimental results are compared and it is found that there is a deviation of 4 nm, 2.6 nm and 1.3 nm at working gap equal to 0.5 mm (zone-1), 1 mm (zone-2) and 1.5 mm (zone-2), respectively. This deviation indicates that the experimental *Ra* is higher from the simulated *Ra* value when aluminium is processed at zone-1 which validates the conclusion made in Table 4.7 about the application of zone-2 for ductile materials. Hence, it is also experimentally validated that the zone-2 is suitable to process ductile materials and zone-1 damages more due to the formation of scratches on work-surface. In zone-2, i.e. at the working gap equal to 1.5 mm, the critical roughness obtained by experiment is 1.3 nm more, as the reactive-MDS shows that the material removal in aluminium occurs by breaking of parent bonds and results in 1-3 atomic layer deviations which would be 0.4-1.2nm. Therefore, the experimental results in zone-2 of CMMRF shows the critical *Ra* value of the order of few nanometer.

Figs. 6.9 (a-c) are plotted with simulated results for the material removal in aluminium alloy during different sets of CMMRF parameters. All these plots show a good agreement with the experimental results.

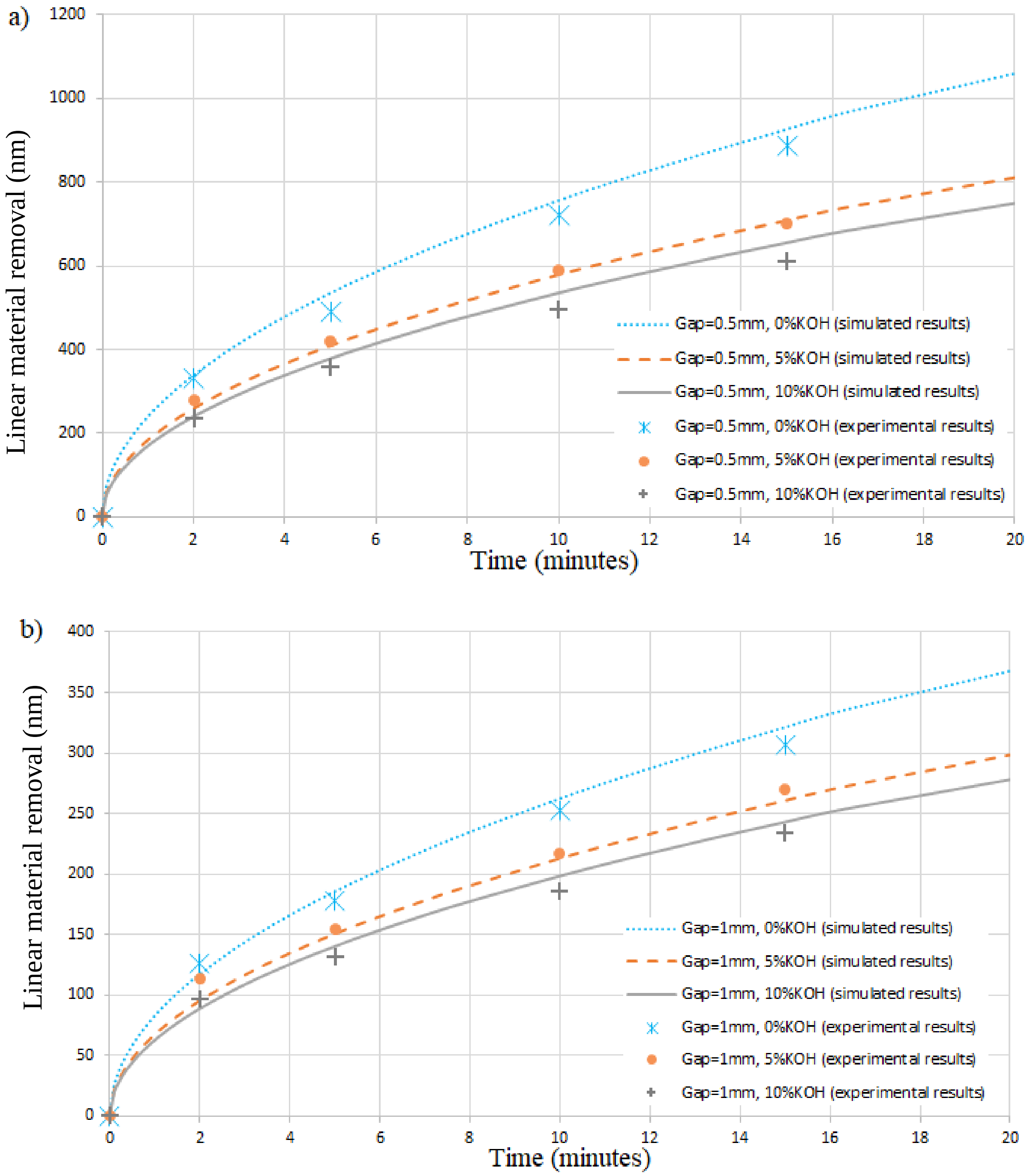
a)
Linear material removal (nm)
1200
1000
800
600
400
200
0
0
2
4
6
8
10
12
14
16
18
20
Time (minutes)
Gap=0.5mm, 0%KOH (simulated results)
Gap=0.5mm, 5%KOH (simulated results)
Gap=0.5mm, 10%KOH (simulated results)
Gap=0.5mm, 0%KOH (experimental results)
Gap=0.5mm, 5%KOH (experimental results)
Gap=0.5mm, 10%KOH (experimental results)
b)
Linear material removal (nm)
400
350
300
250
200
150
100
50
0
0
2
4
6
8
10
12
14
16
18
20
Time (minutes)
Gap=1mm, 0%KOH (simulated results)
Gap=1mm, 5%KOH (simulated results)
Gap=1mm, 10%KOH (simulated results)
Gap=1mm, 0%KOH (experimental results)
Gap=1mm, 5%KOH (experimental results)
Gap=1mm, 10%KOH (experimental results)

c)

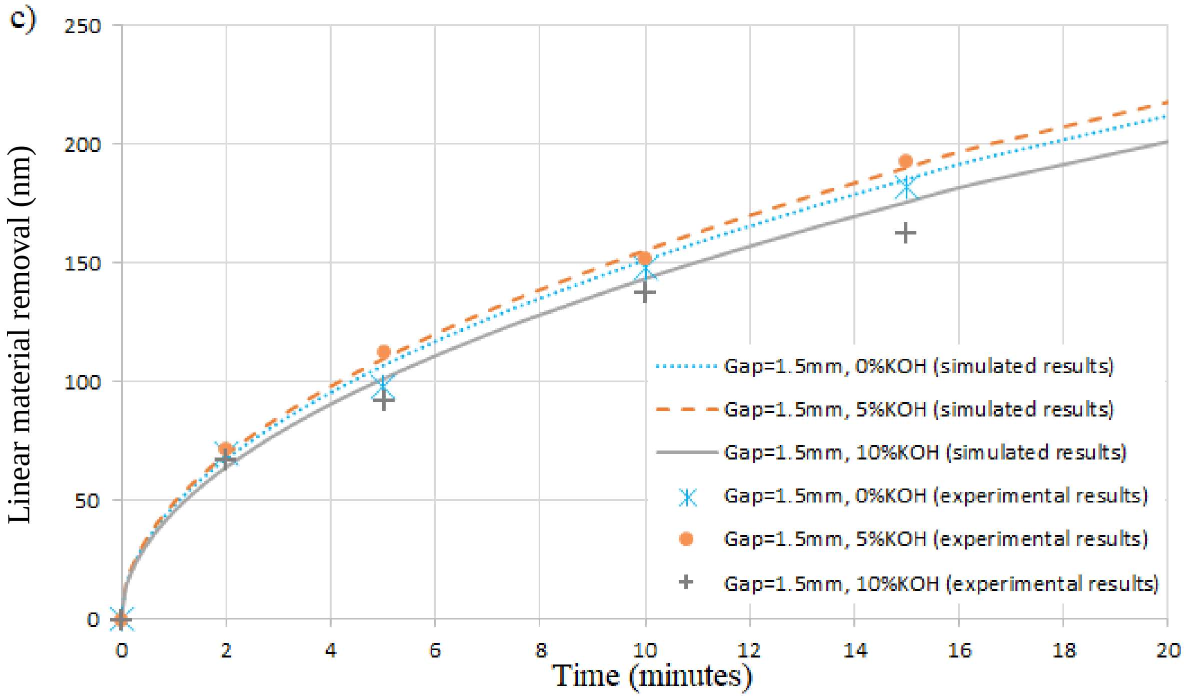

Fig. 6.9: Variation in the depth material removal on aluminium alloy with finishing time, and different levels of working gap and different *KOH* concentration. At working gap equal to (a) 0.5 mm, (b) 1.0 mm and (c) 1.5 mm.

6.4.1.5 Effect of finishing time on material removal

During initial time of finishing, the depth of material removal increases promptly and in non-linear fashion as shown in Figs. 6.9 (a-c). Afterward, the material removal become slow and almost linear relationship with time, as shown in Figs. 6.9 (a-c). In the beginning of finishing (t = 0), the peaks are sharp and the cross-sectional area of peaks to be sheared is quite small, hence, penetration rate (or, linear material removal rate) is quite high in Fig. 6.9. With time, as these peaks get sheared off, the cross-sectional area to be sheared off keeps on increasing. Hence, penetration rate keeps on decreasing which causes reduction in the slope of the linear material removal for some time, thereafter it becomes constant and material removal increases linearly with time, as shown in Figs. 6.9 (a-c).

6.4.1.6 Effect of KOH concentration on material removal

Effect of *KOH* on the material removal is plotted in Figs. 6.9 (a-c) which show that *KOH* resists the material removal. This effect is more in case of low working gap as compared between Fig. 6.9 (a) and Fig. 6.9 (c). This effect leads to the stress dependent surface oxidation by chemical reaction as shown in Fig. 4.45, and therefore, reduction in material removal is observed when *KOH* is added in the finishing medium.

6.4.1.7 Effect of working gap on material removal

Figs. 6.9 (a-c) are plotted with gap equal to 0.5, 1.0 and 1.5 mm respectively. Reduction in the working gap increases polishing pressure which increases the depth of material removal. For example, the depth of material removal in 15 minutes of 0% *KOH* are 886, 307 and 182 nm for the working gap of 0.5, 1.0 and 1.5 mm, respectively. It is also observed that the effect of chemical reaction on the material removal is effective in case of low working gap, which means that the chemical reactions are stress dependent in the present case of CMMRF process as discussed in chapter 4 of MD simulation.

Optical images of aluminium samples are captured and presented at three different states as shown in Figs. 6.10 (a-c). Fig. 6.10 (a) shows the sample of aluminium alloy which is generated by conventional turning process with feed of 0.12mm per revolution, in which the surface texture of machining feed marks is also visible, and this surface also shows non-reflectivity for the general optics application. Fig. 6.10 (b) shows a mechanically finished sample by using fine diamond abrasive particles with mean diameter of 0.25 μm, which shows reflectivity with haze. Fig. 6.10 (c) show the sample which is finished by CMMRF upto the critical roughness value and it shows clear reflectivity aspect of the surface for the general optics application.

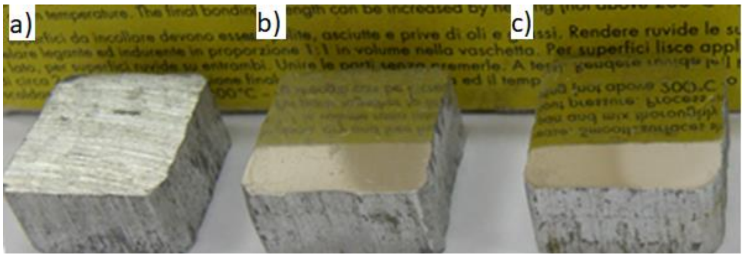

Fig.6.10: (a) Surface of aluminium after turning process, (b) Surface of aluminium after preparation for CMMRF process, and (c) CMMRF finished sample of aluminium at 5% *KOH* and working gap equal to 1 mm.

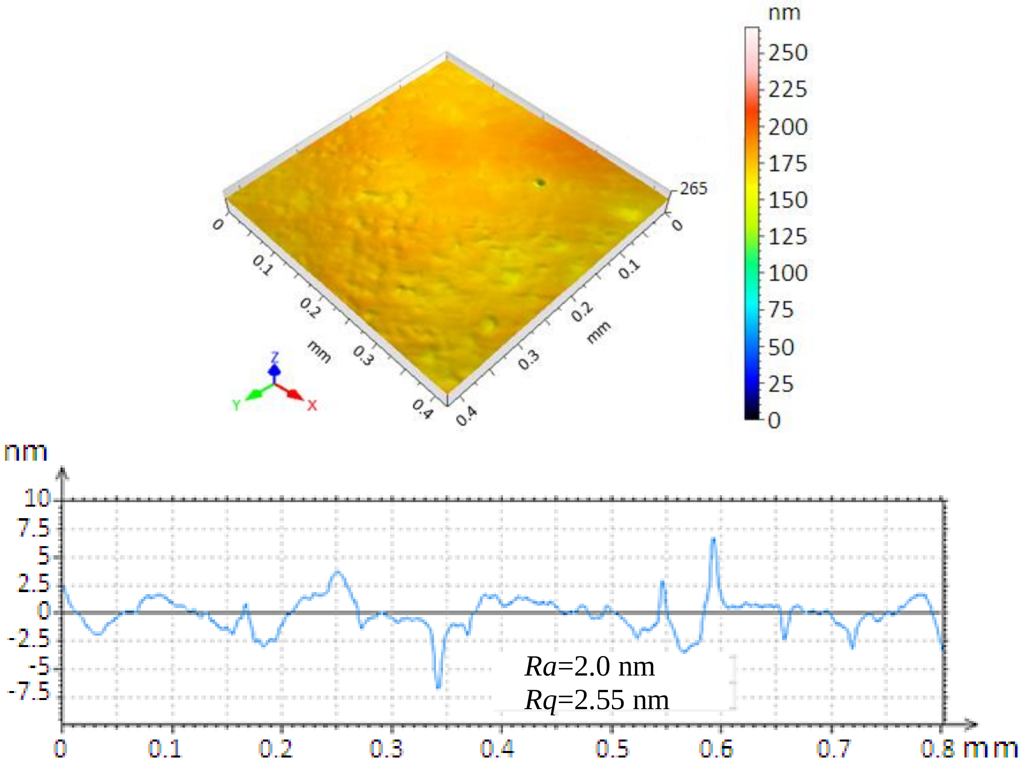

Fig.6.11: Surface topography in 3D which shows nanometric smooth surface and the 2D roughness profile shows *Ra* value equal to 2 nm.

Surface topography and the roughness profile of optimally finished surface of aluminium alloy is also presented in Fig.6.11.

6.4.2. Results and discussion on Silicon

A series of experiments are conducted on silicon substrate as per Table 6.1-6.2 and the results are presented in Table A4 of Appendix. Experimental results are plotted against the simulated results of chapter 5, as shown in Figs. 6.12 (a-c) and 6.13 (a-c). These plots show reasonably good agreement with the simulated results. Effects of CMMRF parameters are discussed in the following section for surface roughness as well as material removal.

6.4.2.1 Effect of process parameters on surface roughness of silicon substrate.

Before comparing the experimental and simulation results, critical surface roughness for the CMMRF model is set to 0.04 nm, as discussed in section 5.3.2 of chapter 5. Figs. 6.12 (a-c) show the effect of finishing time and the concentration of chemical at three different levels of working gap.

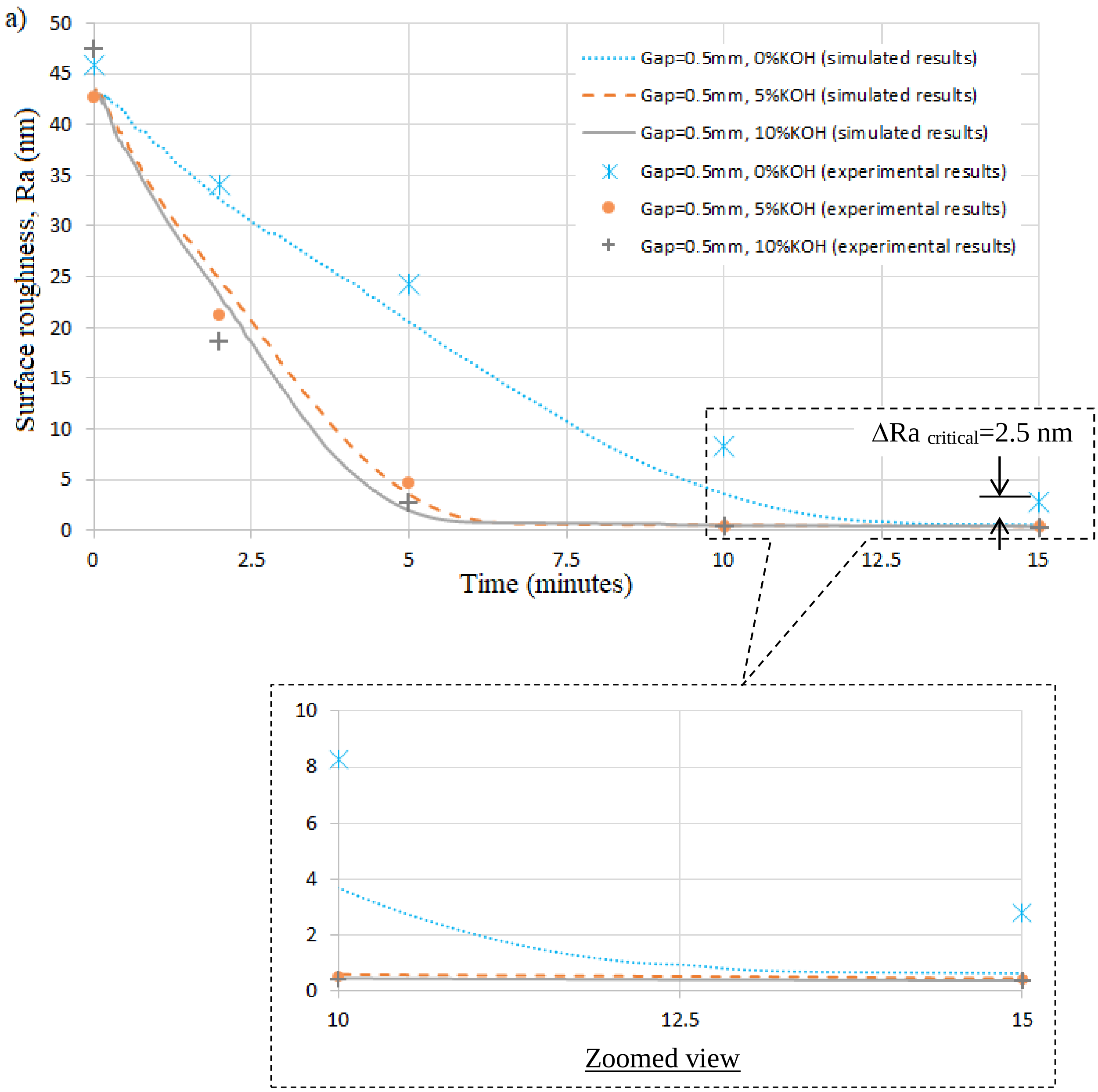

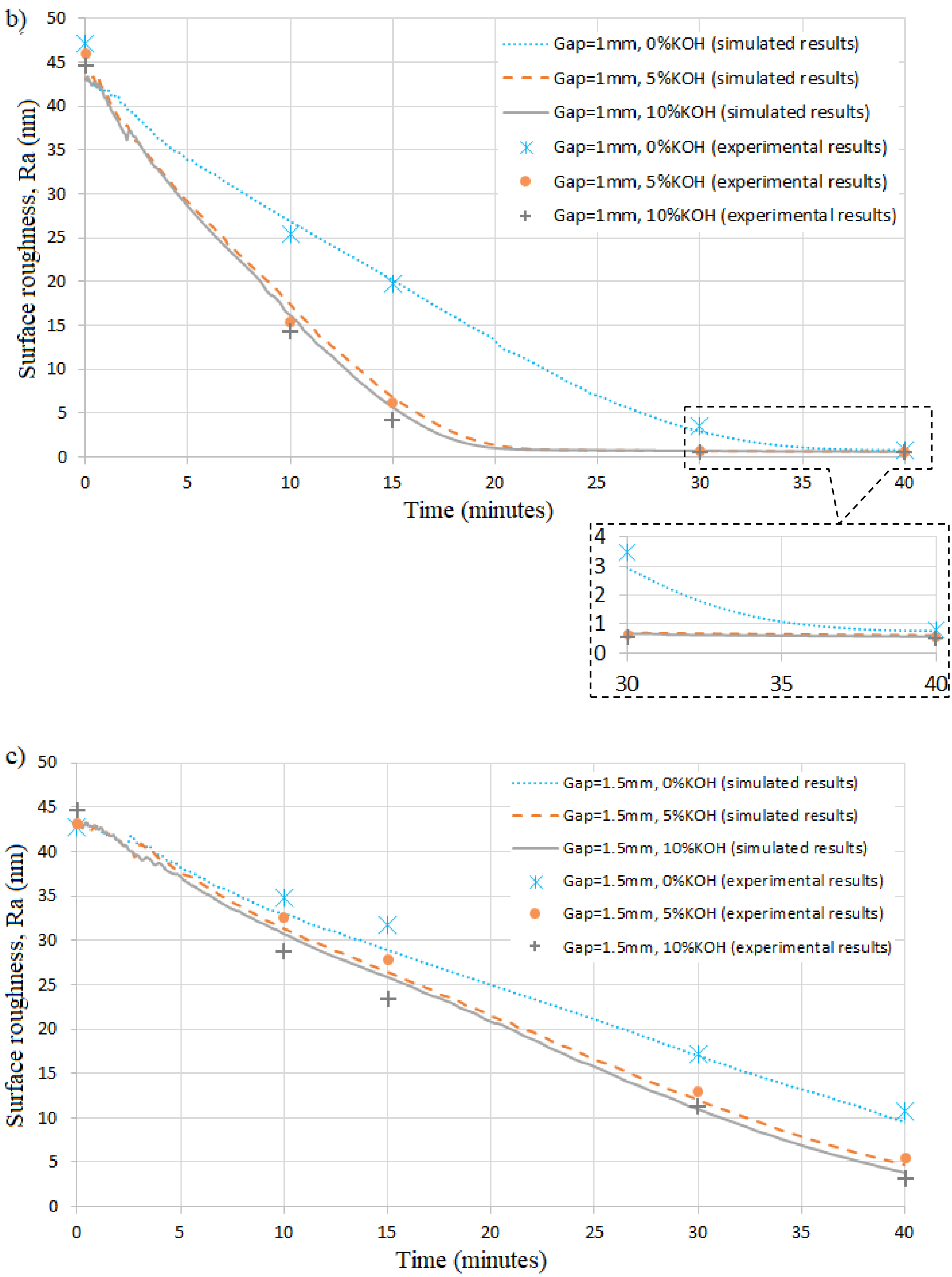

Fig. 6.12: Improvement in surface roughness on silicon substrate with finishing time, and different levels of working gaps and *KOH* concentration. At working gap equal to (a) 0.5 mm, (b) 1.0 mm and (c) 1.5 mm.

6.4.2.2 Effect of finishing time on surface roughness

During initial time of finishing, the reduction in surface roughness occurs exponentially as shown in Figs. 6.12 (a-c). Thereafter, the rate of reduction in surface roughness becomes extremely low which makes it almost asymptotic. This shows two zones of the improvement in surface roughness, which is similar to earlier results of aluminium as presented in section 6.4.1.2.

6.4.2.3 Effect of KOH concentration on surface roughness

Effect of *KOH* is also plotted in Figs. 6.12 (a-c) which shows that *KOH* helps in the reduction of surface roughness with time. Here, aqueous *KOH* chemically reacts with silicon and form hydroxide and oxide which are softer than silicon. Thus, the oxide formation results in more linear material removal rate and reduces the surface roughness faster as compared with 0% *KOH*. It is also observed that the improvement in surface roughness occurs by increasing percentage of *KOH* from 0% to 5%. By changing the *KOH* content from 5% to 10%, there is a marginal improvement. It is therefore considered that more *KOH* may be causing the surface damages at nanometric scale in forms of digs. Hence, % *KOH* needs to be small value so that the finished surface shall be free from mechanical as well as chemical defects.

6.4.2.4 Effect of working gap on surface roughness

Figs. 6.12 (a-c) are plotted with gap equal to 0.5, 1.0 and 1.5 mm respectively. Reduction in the working gap increases polishing pressure which reduces the surface roughness faster and reaches the critical surface finish in less time. For example, the time to reach critical surface roughness are 15, 40 and more than 40 minutes for the working gap of 0.5, 1.0 and 1.5 mm respectively. At low working gap (0.5 mm) and 0% *KOH*, it is observed that the finished surface results in more number scratches due to the mechanical abrasion of workpiece as seen in Fig. 6.7 (b), and hence, it yields in 2.5 nm higher value of critical *Ra* from the theoretical value. In addition, it is also noticed that the time required for critical *Ra* is much lesser at the working gap equal to 0.5 mm (zone-1) and zone-2 shows more time. Hence, the present study validates the effect of zone-1 and zone-2 for brittle material as presented in Table 3.5 of chapter-3.

Figs. 6.13 (a-c) are plotted with simulated results for the material removal in silicon substrate during different set of CMMRF parameters. All these plots are also discussed as follows.

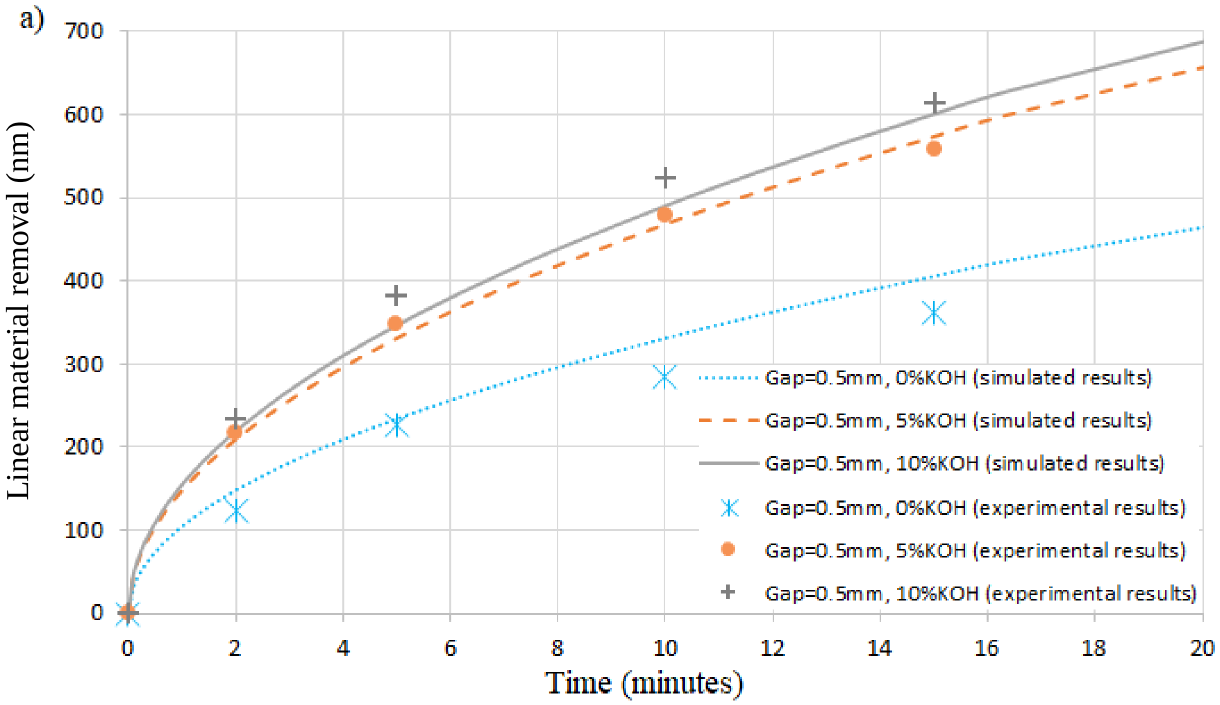

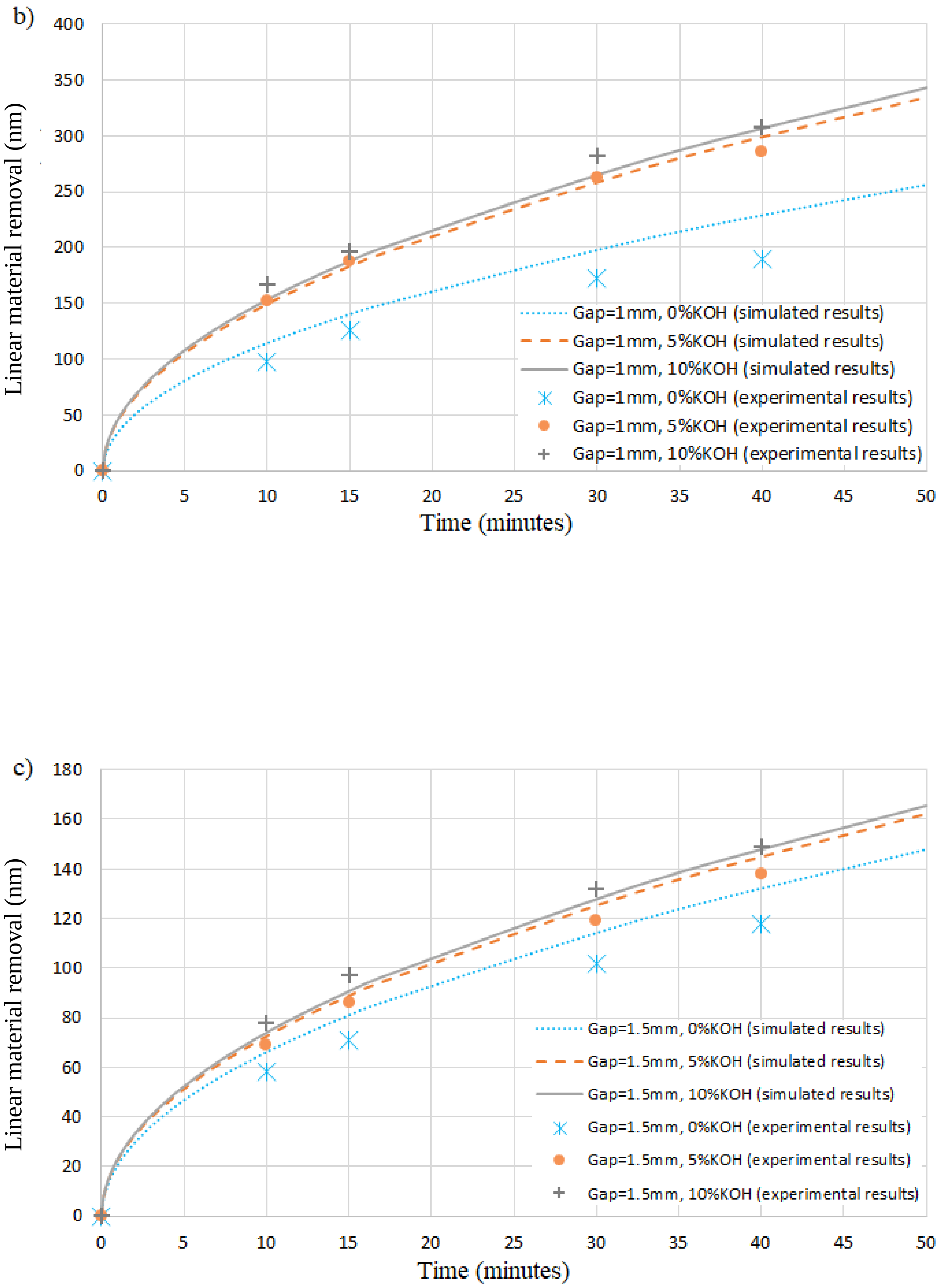

Fig. 6.13: Variation in the depth material removal on silicon substrate with finishing time, and different level of working gap and *KOH* concentration. (a) at working gap=0.5mm. (b) at working gap=1.0mm. (c) at working gap=1.5mm.

6.4.2.5 Effect of finishing time on material removal

Material removal with finishing time show the similar trend of aluminium in which the initial time of finishing removes material rapidly. Thereafter it becomes slow and almost linear relationship with time, as shown in Figs. 6.13 (a-c). During initial stage of finishing, sharp peaks get higher stress as the cross-sectional area to be sheared off becomes quite small, and this stress causes more chemical softening towards higher MRR. When 90% of peaks are removed then MRR becomes uniform and stable.

6.4.2.6 Effect of KOH concentration on material removal

Effect of *KOH* on the material removal is plotted in Figs. 6.13 (a-c) which show that *KOH* assists to increase the material removal. This effect is more in case of low working gap as compared between Fig. 6.13 (a), Fig. 6.13 (b) and Fig. 6.13 (c). This effect leads to the surface softening by oxidation due the chemical reaction, and this is why, there is an increase in material removal when extra *KOH* is added in finishing medium.

6.4.2.7 Effect of working gap on material removal

Figs. 6.13 (a-c) are plotted with gap equal to 0.5, 1.0 and 1.5 mm, respectively. Reduction in the working gap increases polishing pressure which increases the depth of material removal. For example, the depth of material removal in 15 minutes of 0% *KOH* are 361, 126 and 71 nm for the working gap of 0.5, 1.0 and 1.5 mm respectively. The experimental results show less material removal than simulated results when finishing time increases at 0% *KOH*. It is also observed that the effect of chemical reaction on the material removal is effective in case of low working gap, which means that the chemical reactions are stress dependent in present case of CMMRF process. These results reveal that the trends for material removal and surface finish are similar in both ductile and brittle except the phenomenon of hard passivation and soft passivation, respectively.

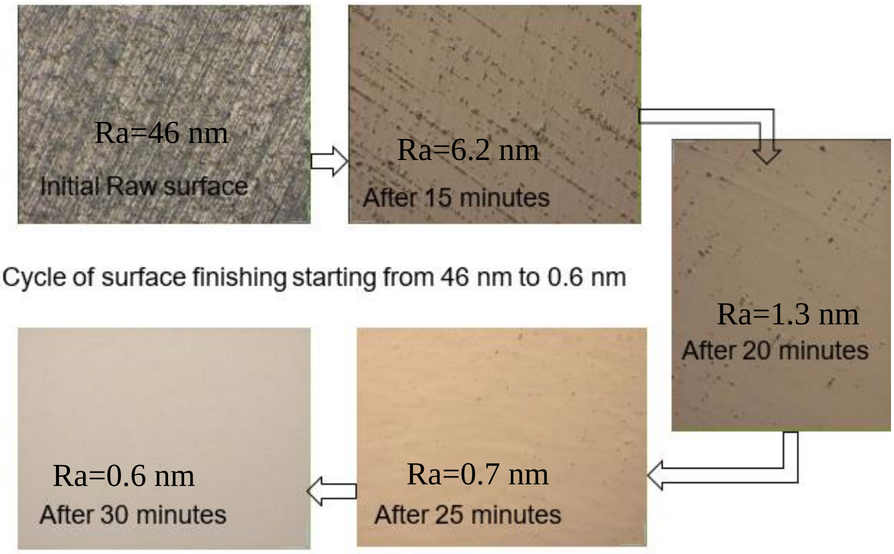

Fig. 6.14: Effect of finishing time at working gap=1mm, 5%*KOH* on silicon at initial *Ra*=46 nm. Magnification level of optics:100X.

In previous two cases, it is seen that the simulated results match well with experimental results except, the critical *Ra* value. The phenomenon of hard passivation is understood from Fig. 6.9 (a) in which it is observed that the addition of *KOH* reduces MRR. The phenomenon of soft passivation is understood from Fig. 6.13 (a) in which chemical reaction assists to increase MRR.

Surface texture of Fig. 6.12 (b) at 5% *KOH* is presented in Fig. 6.14 in which the texture is captured at different time so see the improvement in surface finish. Optical images of silicon samples are captured and presented at three different states as shown in Figs. 6.15 (a-c).

Fig. 6.15 (a) shows the initial sample of silicon substrate, which shows optically non-reflectivity for the general optics. Fig. 6.15 (b) shows a mechanically finished sample by using diamond abrasive particles with mean diameter of 3 μm, which shows reflectivity with haze. Fig. 6.15 (c) shows the sample which is finished by CMMRF upto the critical roughness value and it shows clear reflective image.

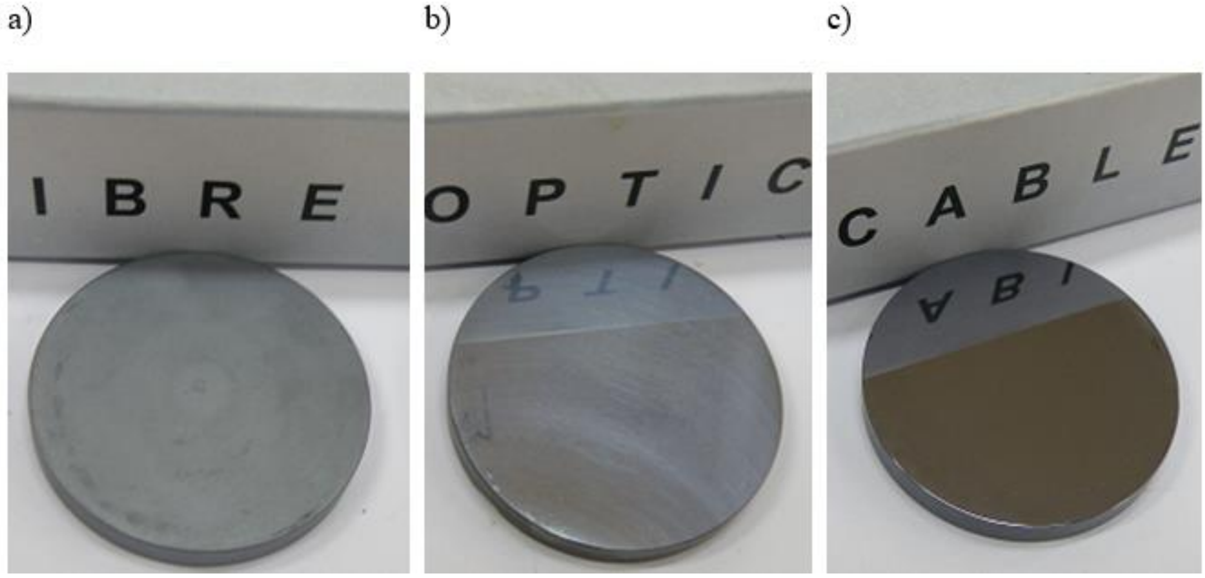

Fig.6.15: (a) Initial etched surface of silicon substrate, (b) Mechanically finished silicon blank, and (c) CMMRF finished surface of silicon which show good reflectivity as compared to the previous cases.

Surface topography and the roughness profile of optimally finished surface of silicon substrate is presented in Fig.6.16.

Now, it is well understood that the chemical has a great impact for getting better value of the critical surface finish. To validate this phenomenon further, one more set of experimental study is carried out on copper alloy by varying concentration and composition of chemical species. Experimental plan, results and discussions are presented in the following section.

6.5. Experiments on *SS304L*

The finishing parameters of this experimental study are designed as shown in Table 6.3, which are obtained on basis of the MDS observations (Table 4.7). There are some fixed parameters such as rotational speed: 300 rpm, working gap: 0.8 mm (i.e. zone-2 for tactful processing of ductile workpiece), feed rate: 10 mm/min and finishing time: 60 min.

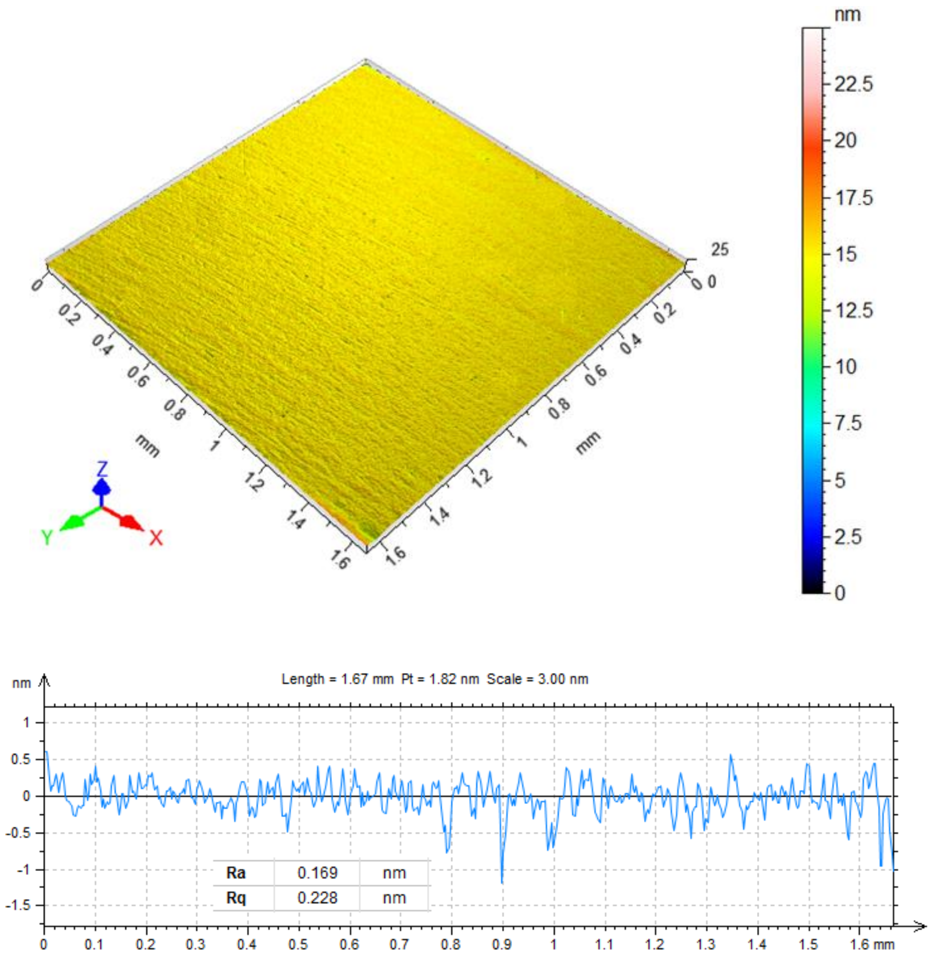

Fig.6.16: Surface topography in 3D which shows *Sa* value equal to 0.14 nm and the 2D roughness profile shows *Ra* value equal to 0.17 nm.

Table 6.3: Process parameters to finish *SS304L* using CMMRF experiments.

Stages of finishing	**Experimental parameters of CMMRF process**	**Condition of the sample (workpiece)**
1st step of finishing (Rough finishing)	Size of electrolytic iron (*Fe*) particles: 40 µm, Size of *SiC* abrasive particles: 25 µm, Mixture of MR fluid by volume: *Fe* (20 %), *SiC* (15 %), Glycine (3 %), Glycerol (2 %) and water (60 %).	Initial surface was taken with *Ra* equal to 298 nm. The nanofinished sample in this stage is used for 2nd step of finishing.
2nd step of finishing (Fine finishing)	Size if Carbonyl Iron particle (CIP): 1-5 µm, Size of Al_2O_3 abrasive particles: 5 µm, Mixture of MR fluid by volume: CIP (20 %), Al_2O_3 (15 %), Glycine (3 %), Glycerol (2 %) and water (60 %).	Initial roughness value for this operation was taken as the final roughness value of the surface at the end of 1st step. (*Ra*=125 nm).
3rd step of finishing (Precision finishing)	Size of CIP: 1-5 µm, Size of colloidal silica (SiO_2) abrasive particle: 0.1 µm,	Initial surface for this operation was taken as that of the sample prepared after 2nd step of finishing operation. (*Ra*=21 nm).

	Mixture of MR fluid by volume: CIP (20 %), SiO_2 (15 %), Glycine (3 %), Glycerol (2 %) and water (60 %).	
4th step of finishing	Size of CIP: 1-5 µm, Size of Al_2O_3 abrasive particle: 5 µm, Mixture of MR fluid by volume: CIP (20 %), Al_2O_3 (15 %), Glycine (3 %), Glycerol (2 %) and water (60 %).	Initial surface for this operation was taken as that of the sample prepared after 3rd step of finishing operation. (Ra=0.78 nm).
5th step of finishing (Ultra-precision finishing)	Size of CIP: 1-5 µm, Size of fumed Silica (SiO_2) abrasive particle with size =5 nm, Mixture of MR fluid by volume: CIP (20 %), SiO_2 (15 %), Glycine (3 %), Glycerol (2 %) and water (60 %).	Initial surface for this operation was taken as that of the sample prepared after 3rd step of finishing operation. (Ra=0.78nm).

Most of the workpiece are measured using optical profilometer (Make: Taylor & Hobson, model: CCI), like initial surface of 1st step, surface finished after 1st step, surface finished after 2nd step, surface finished after 3rd step. For remaining measurement, AFM (atomic force microscope) instrument (Agilent Technologies, Keysight Technologies, model: 5600LS AFM system; software: Pico Image, Elements7.2) is used like, surface finished after 4th step and the surface finished after 5th step.

6.5.1. Results and discussion

The experimental results are presented in Figs. 6.17 (a-k). The initial surface of workpiece is measured and characterised by CCI instrument and presented in Fig. 6.17 (a). The 3-D topography of this surface shows, surface irregularities in the form of sharp and large asperities. Therefore, 1st step of finishing process (as per Table 6.3) is used to reduce the surface roughness as presented in Fig. 6.17 (b). This 1st step of finishing process is carried out by mechanical abrasion, and hence the surface shows massive amount of scratches.

The surface roughness is further reduced by reducing material removal rate [141] that is by reducing the indentation depth. This mechanism is implemented as 2nd step of finishing process, wherein the indentation depth is reduced by taking fine abrasive particles (5 µm size). In this

2nd step of finishing process, the surface roughness comes down from 160 nm to 26.9 nm (rms). Since, the 2nd step utilises chemically inert abrasive particles, the finished surface shows nano-scratches, Fig. 6.17 (c). Figs. 6.17 (a)-(c) validate some mechanism which is derived after MDS work like material removal on rough surface and leads to nanofinished surface with defects (scratches and digs) during the mechanical abrasion based finishing process.

Figs. 6.17 (d)-(e) show the surface finished after 3rd step of finishing process. In this process, a chemically active abrasive particle (0.1 µm dia. of colloidal silica which is medium size of the abrasive) is used to generate defect free surface up to some extent. In this finishing process, the surface topography and surface roughness profile (in 2-D) indicate some sort of surface defects (scratch lines and digs). These types of minor defects in this process come because of medium size (0.1µm dia.) of silica particle which also induces mechanical damage due to the particle size. Furthermore, to validate the mechanical abrasion mechanism of MDS, experiment is carried out as per 4th step of finishing.

In this mechanical abrasion process, the surface generated by the experimentation illustrates about the material removal with more defects like scratches and digs as shown very clearly in Figs. 6.17 (f)-(g). Therefore, in the last stage of finishing operation (5th step of finishing), 5 nm size of colloidal fumed silica particles have been used as chemically active abrasive particles and it leads to almost defect free surface, Figs. 6.17 (h)-(i).

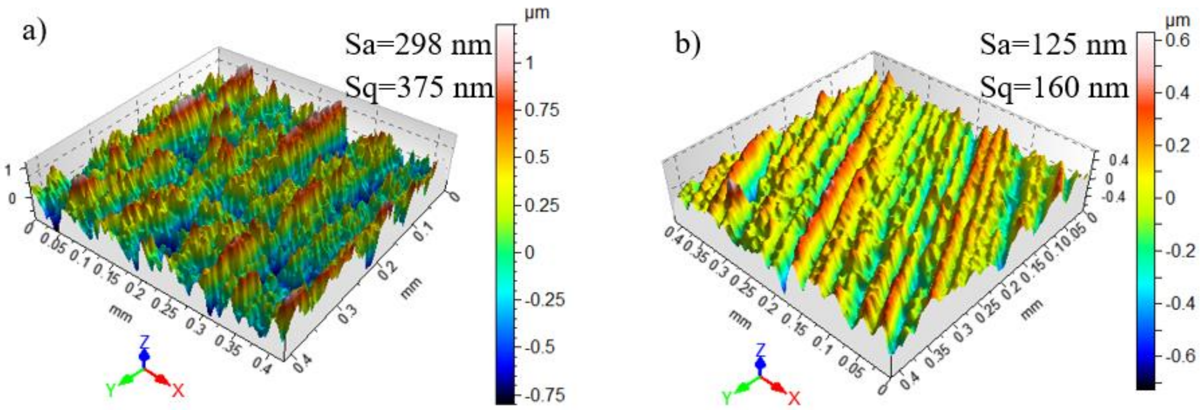

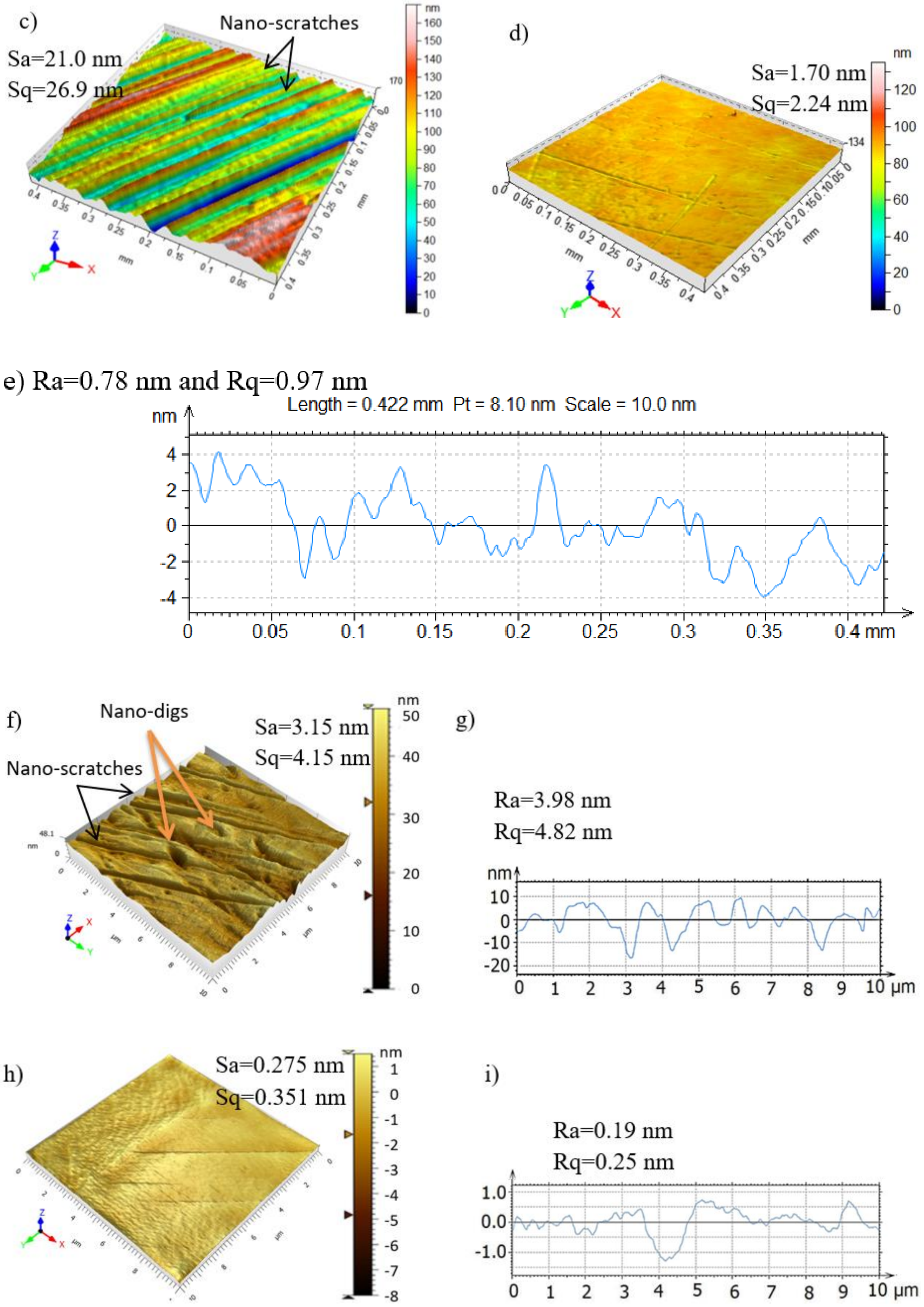
c)
Sa=21.0 nm
Sq=26.9 nm
Nano-scratches
nm
170
mm
d)
Sa=1.70 nm
Sq=2.24 nm
nm
134
mm
e) Ra=0.78 nm and Rq=0.97 nm
Length = 0.422 mm Pt = 8.10 nm Scale = 10.0 nm
nm
4
2
0
-2
-4
0
0.05
0.1
0.15
0.2
0.25
0.3
0.35
0.4 mm
f)
Nano-digs
Nano-scratches
Sa=3.15 nm
Sq=4.15 nm
nm
50
40
30
20
10
0
µm
g)
Ra=3.98 nm
Rq=4.82 nm
nm
10
0
-10
-20
0
1
2
3
4
5
6
7
8
9
10 µm
h)
Sa=0.275 nm
Sq=0.351 nm
nm
1
0
-1
-2
-3
-4
-5
-6
-7
-8
µm
i)
Ra=0.19 nm
Rq=0.25 nm
1.0
0.0
-1.0
0
1
2
3
4
5
6
7
8
9
10 µm

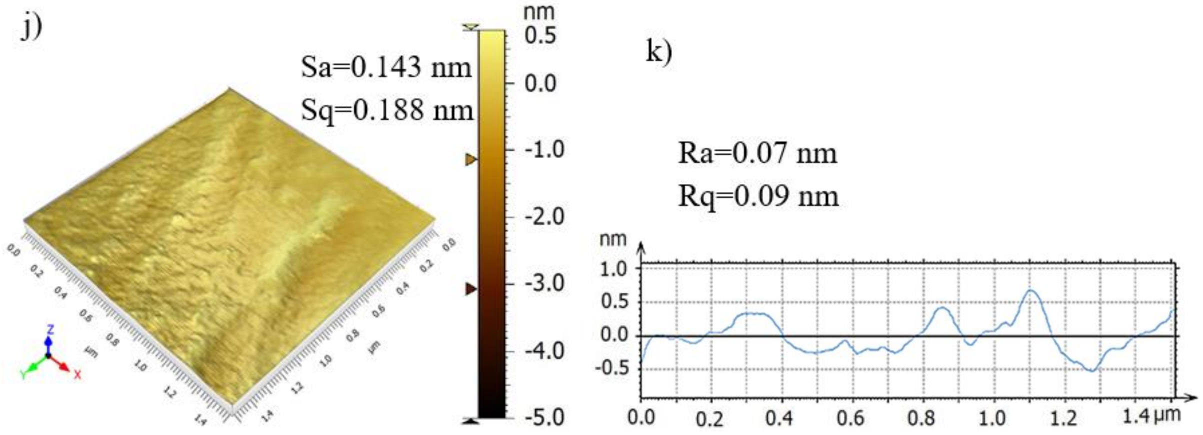

Fig. 6.17: CMMRF results on *SS304L*, (a) 3-D topography of initial surface, (b) 3-D topography of surface generated after 1st step of finishing operation, (c) 3-D topography of surface generated after 2nd step of finishing, (d)-(e) 3-D topography and 2-D profile of surface generated after 3rd step of finishing, (f)-(g) 3-D topography and 2-D profile of surface generated after 4th step of finishing, (h)-(i) 3-D topography and 2-D profile of surface of surface generated after 5th step of finishing. To characterise the surface which is finished by ultra-precision finishing (5th step), the AFM measurement was taken at small scanning area (1.51µmx1.51µm) as illustrated in (j)-(k). (a)-(e) are measured using CCI (coherent correlation interferometer) instrument, and (f)-(k) are measured by using AFM instrument.

To investigate the surface finish quality at atomic scale, AFM measurement is carried out on the same sample generated by 5th step of finishing process, and presented in Figs. 6.17 (j)-(k) in which scanning area was set to 1.51 µmx1.51 µm. The result shows the surface finish, *Ra* = 0.07 nm which is almost matching with ideal surface as per Eq. 5.19. This experimental work is an evidence of a foremost finding of the MDS work as shown in Table 4.7.

Thus, the present work of MDS is useful to understand and optimise an abrasive based finishing process for surface finish or material removal rate.

6.5.2. Comparison between simulation and experimental work

The MDS works of this paper are validated with experimental results, as presented in Table 6.4. In this study, it is found that the material removal with the help of chemically active abrasive particles is highly precise and it can be controlled from cluster of atoms to few numbers of atoms by reducing the depth of indentation during the finishing process. The experimental result (*Ra*=0.07 nm) is very close to the theoretical value (*Ra* =0.064 nm).

Table 6.4: Comparison between MDS and experimental works.

Step No.	**Finishing steps**	**MDS result**	**Experimental result**	**Remark**
1	Mechanical finishing-coarse abrasive	Material removal with surface damages in large scale, Fig.4.18 (d).	***Sq***: from 375 nm to 160 nm with massive scratches.	It indicates both aspects, material removal from the asperities and scratches on surface.
2	Mechanical finishing-fine abrasive		***Sq***: from 160 nm to 21 nm with massive nano-scratches.	
3	Chemo-mechanical finishing – medium size abrasive	Material removal with minimal surface damages. *Ra* can be at nanometric scale (1 nm) with few nano-scratches.	***Sq***: from 21 nm to 2.24 nm with few nano-scratches only.	It indicates that the chemical assisted material removal dominates over the mechanical scratching.
4	Chemical assisted mechanical finishing –fine abrasive	Generation of ideal surface with irregularities of 1-2 atomic layers. *Ra* can be 0.05-0.1 nm, Fig.4.54 (f) and Eq.5.19.	The finished surface shows ***Ra*** value equal to 0.07 nm.	Both, MDS and Experimental results are matching as 0.05<0.07<0.1

6.6. Experiments on copper alloy

Literature survey of *Cu*-CMP shows that the work was carried out with a wide range of polishing slurry such as alkaline slurry and acidic slurry in which nitric acid and ammonium hydroxide based slurry were extensively studied.

It was found that copper gets dissolved in nitric acid and the dissolution rate also depends on the concentration of nitric acid [142]. Dissolution of copper leads to the corrosion and it affects CMP process negatively due to localized and global corrosion defects. To avoid corrosion effects, corrosion inhibitors like BTA were also introduced to the CMP slurry which forms a protective film (for passivation of work-surface) over workpiece and prevents excessive corrosion and dissolution [143,144] [117,262] and due to this surface damages during CMP gets minimized.

Ammonium hydroxide has the ability to form complex compound on copper [145–149]. Therefore, copper can be passivated in alkaline medium without using acidic medium. A literature survey was carried out to use aqueous ammonia for the behavior of complexing agent and the dissolution mechanism [150].

Hence, CMMRF process is experimentally investigated on copper workpiece for both nitric acid and ammonium hydroxide medium. In addition, the process is also optimized for better surface finish and the same is reported and discussed to understand the process capability for copper workpiece also.

In this investigation, copper alloy (OFE grade) has been selected to explore the capability of CMMRF process for this material. Selection of chemical is one of the main aspect of CMMRF and based on literature survey it was found that nitric acid and aqueous KOH were used in CMP to see their effect on material removal rate. Hence, present work is focused to select suitable chemical, and in this direction, experiments are carried out as follows.

6.6.1. Plan of experiments

To study the effect of chemical, pH value of the medium is varied from 3.1 to 12.4 by changing the concentration of nitric acid and aqueous ammonia as shown in Table 6.5. In the present case, pH value is required to enhance polishing rate. It is measured by a pH meter (HANNA instruments BL 931700-0).

Table 6.5: Chemical composition, slurry in % volume.

Chemical	Deionised water	Glycerine	Ammonia	Nitric acid	Benzotriazole (BTA)	Alumina abrasive	CIPs
Value	56 to 66	1.9	0 to 10	0 to 10	0.1	10	20

Here, BTA is used as a corrosion inhibitor and, acidic as well as basic media, as polishing slurry have been explored to study final finishing value. The physical parameters are taken from earlier work {feed = 5 mm/min; RPM = 250 rpm; working gap = 1.5 mm; finishing time = 1 hr} and chemical aspects have been studied and optimised.

6.6.2. Results & discussion on copper

Table 6.6: Results of CMMRF on copper

Sr. No.	**pH value**	**Final surface roughness, *Ra* (nm)**
1	12.4	28.0
2	12.2	25.0
3	11.7	14.0
4	7.0	9.0
5	4.4	4.2
6	3.7	2.5
7	3.4	5.8
8	3.1	7.0

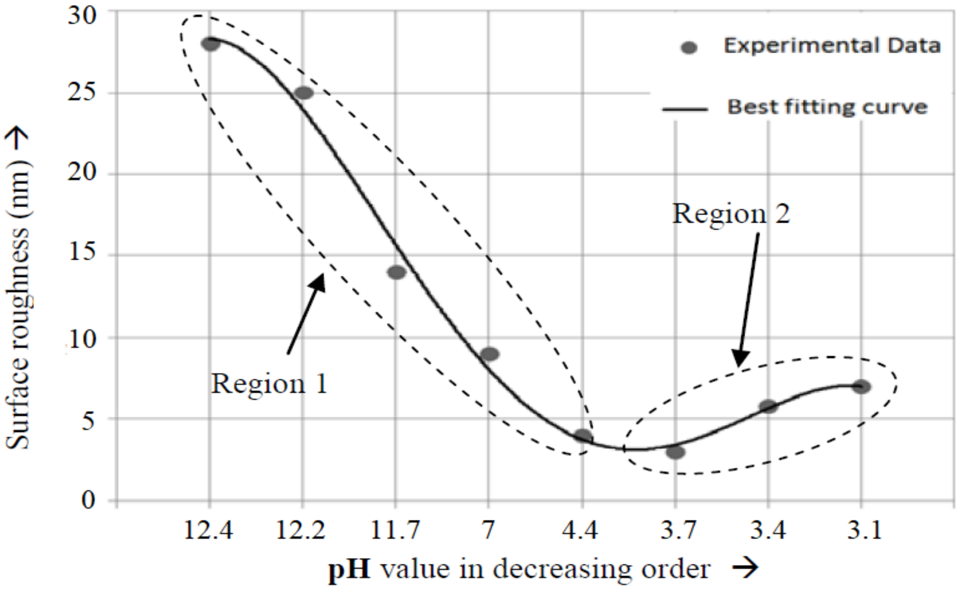

Fig.6.18: Effect of acidic and basic species on critical finishing value of CMMRF on copper.

Final roughness results after experiments are tabulated in Table 6.6. These results have also been plotted and presented in Fig. 6.18. It is seen that as the pH value decreases, the surface finish value improves and after reaching certain level, it starts deteriorating. Hence, the pH value plays an optimal characteristic for the perspective of surface finish. In the region 1 of Fig. 6.18, concentration of ammonia is used to change the pH value from 12.4 to 7.0 by varying it from 10% to 0%. Herein, ammonia degrades the surface integrity as the surface topography shows the generation of porous surface when high amount of aqueous ammonia (10%) is used, and it is presented in Fig. 6.19.

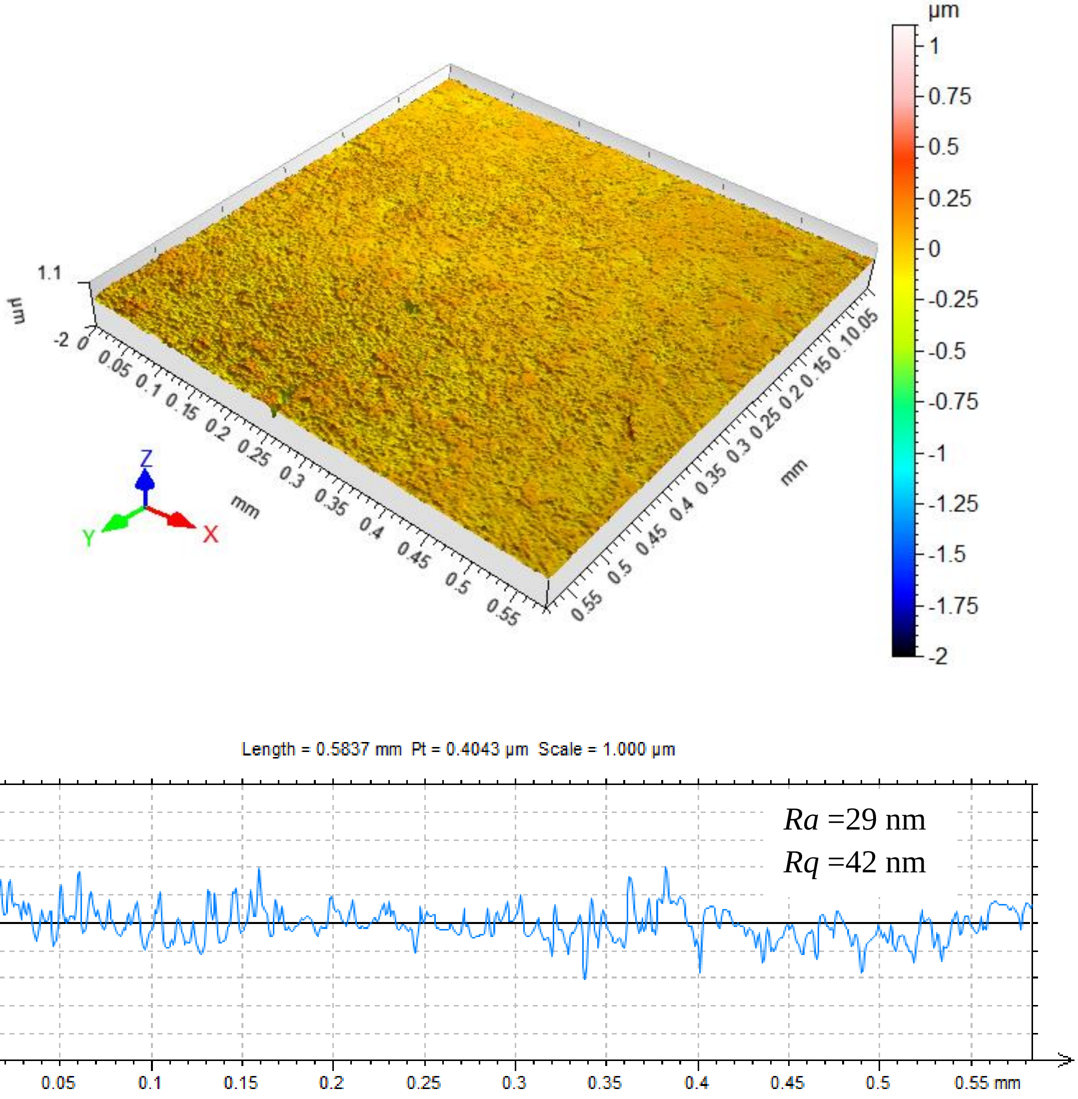

Fig.6.19: CMMRF finished copper (*Ra* = 28 nm) with 10% ammonia (Sr.N.1)

When percentage of ammonia reduced upto zero and pH value of slurry is maintained to 7.0 then the roughness value is reduced but the surface defects are found more in terms of scratches as shown in Fig.6.20. This is happening as finishing is done without any chemical reaction and superficial layer of surface gets exposed for pure abrasion by mechanical interaction with hard abrasive particles directly. Fig.6.20 shows few scratch lines, which are generated because of pure mechanical abrasion (without chemical reaction) on the superficial layer due to ductile failure (shearing action) as discussed in section 4.2.1 of chapter 4. These scratches belong to nano-scratches as their depth and width are few tens of nanometres.

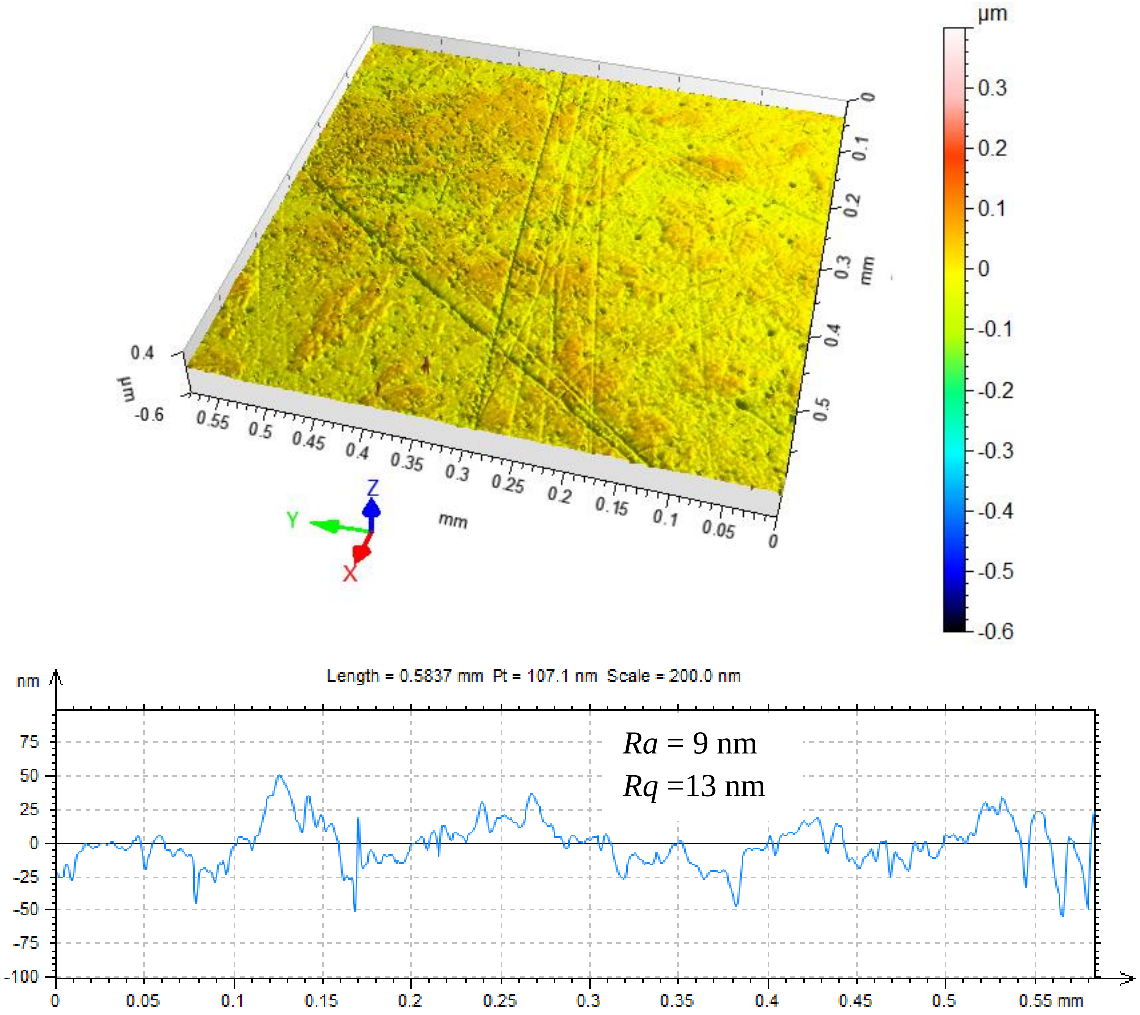

Fig.6.20: CMMRF finished copper (*Ra* = 9.0 nm) without ammonia and nitric acid (S.N.3)

In case of acidic media (or nitric acid), surface finish improves as shown in the region 2 of Fig.6.18. As acidic concentration increases, surface finish enhances upto some extent but surface becomes rougher beyond 0.4% of nitric acid (v/v), i.e., 3.78 pH value. The reason to get such nanometric surface finish in acidic medium is similar to the earlier case of aluminium. The surface topography of such copper surface is presented in Fig. 6.21.

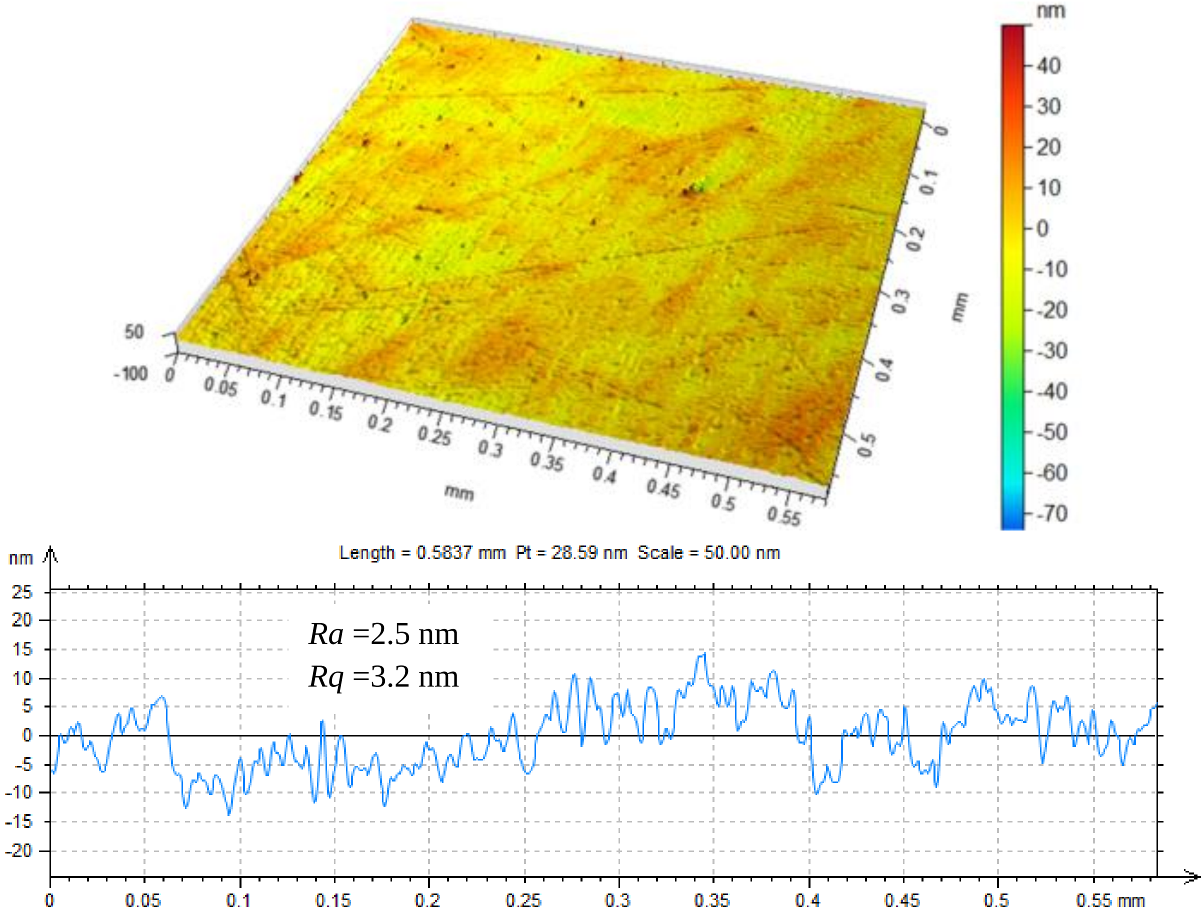

Fig.6.21: CMMRF finished copper (*Ra* = 2.5 nm) with 0.4% nitric acid (S.N.5)

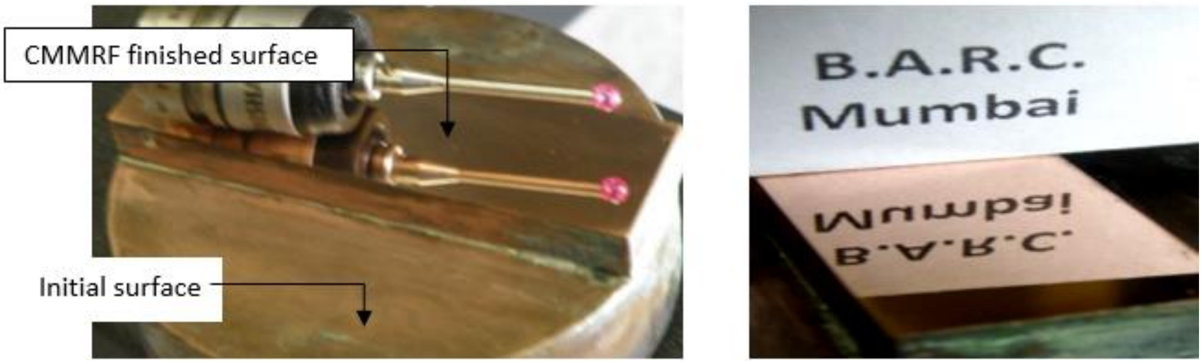

Fig.6.22: CMMRF finished copper (*Ra* = 2.5 nm) with 0.4% nitric acid. Nano-finished surface shows optical reflectivity as compared to initial surface.

Optical image of optimally finished workpiece of copper is presented in Fig.6.22. These samples show good quality of reflection for general optics application.

6.7. Summary

In this chapter, experimentations, results and discussion were reported on ductile as well brittle materials. Important aspects of these works are summarized as follows.

- During initial time of finishing, surface roughness reduces exponentially with respect to finishing time. Afterward, the rate of reduction in surface roughness becomes extremely slow and tends to be asymptotic in respect of the finishing time. This effect is observed because of the sharp peak for higher chemical reaction followed by mechanical abrasion. After removal of all peaks and valleys of the surface roughness profile, critical surface roughness gets maintained with time. This critical roughness depends CMMRF process parameters like hardness and size of abrasive particles, chemicals for chemical assisted mechanical finishing and other physical parameters like working gap, magnetic field, feed, and rotational speed.
- In case of ductile material like aluminium alloy, the chemical reaction of CMMRF process resists the material removal. However, brittle material like silicon gets higher material removal due to the chemical reaction. Hence, it can be stated that the ductile materials form hard passivation layer and brittle materials form soft passivation layer during CMMRF process.
- Aluminium shows more deviation of critical surface roughness from the theoretical value when it is processed in zone-1, i.e. 4 nm. This deviation comes down upto 1.3 nm when it is processed in zone-2. Experimental results also support to process ductile material in zone-2 and brittle material in zone-1 from efficient utilisation of CMMRF.

- Effect of chemical is also investigated on copper alloy and it is found that the pH value near to the acidic zone (0.4% of nitric acid) yield the surface finish better than 3.0 nm. However, high pH value leads to the formation of pores on the finished surface and the neutral solution of results in surface damages such as scratch lines.
- In this chapter, CMMRF is used to generate surface finish on three different materials with *Ra* value equal to 2 nm, 0.2 nm and 2.5 nm in poly-crystalline aluminium, single crystalline silicon and poly-crystalline copper.

----------X----------

Chapter-7

CONCLUSIONS AND SCOPE FOR FUTURE WORK

7.1 Conclusions

In the present work, CMMRF process is modelled and simulated at atomic scale and macroscopic scale followed by experimental validation. On the basis of modelling, simulation and experimental work done, following are the main conclusions drawn.

- CMMRF process is capable for defect-free finishing of ductile and brittle materials at nanometric scale.
- MR fluid stores magnetic energy under the influence of magnetic field, and it builds a flexible polishing pad in fraction of a second (<1 s). This MR fluid applies polishing pressure on the work surface under squeeze mode.
- Polishing pad of CMMRF has two zones of operation as far as working gap is concerned. These two zones have been identified to process a wide range of engineering materials. Wherein, hard and brittle materials can be processed in zone-1 which needs high precision machine to maintain consistent working gap in the band of 0.2 to 0.5 mm. Zone-2 (gap > 0.5 mm) is identified to process ductile and malleable materials in which machine accuracy and precision are not so critical.
- Sedimentation of MR fluid can be mitigated by sodium stearate for nano-coating on CIPs (studied by DFT modelling).
- Material removal at atomic scale happens by the principle of adhesion-de-bonding which also leads to the phase transformation towards the formation of sub-surface defects. These phase transformations are recoverable in case of ductile material like *Al*, and these phase transformations are irreversible in case of brittle material like *Si*.

Material's flow stress for abrasion becomes near to the theoretical value of shear strength, i.e. $G/2\pi$ irrespective of other properties of material (studied by MDS).

- Chemical reaction occurs in three stages viz. adsorption, absorption and finally passivation layer to stop further reaction. The passivation layer becomes soft or hard layers, which depends on the type of work material.
- During chemical assisted mechanical finishing (CAMF) of CMMRF, the chemical reaction increases by reducing working gap. Material removal in CMMRF process mainly depends on chemical reaction on the workpiece as the removed material belongs to the product made by chemical reaction. A model for this phenomenon at macroscopic scale is constructed based on the atomic scale model. This macroscopic model is helpful to understand the process.
- MDS result helps to bring down *Ra* value from 300 nm to 0.07nm on *SS304L* by applying rough finishing (with coarse and hard abrasive particles), fine finishing (with fine and hard abrasive particles), precision finishing (with micron size and chemically active abrasive particles), ultra-precision finishing (with nanometric size and chemically active abrasive particles).
- Chemically passivated layer helps to protect surface of parent material against mechanical damage in case of aluminium as a ductile material, and due to this MRR also reduces as the concentration of *KOH* chemical increases. However, in case of silicon as a brittle material, material removal increases with concentration of *KOH*. This effect enhances significantly when abrasion force increases by reducing working gap, and this is due to the fact that the ductile materials form hard passivation layer and brittle materials form soft passivation layer.
- CMMRF process has capability to generate surface finish near to the theoretical value on single crystalline as well poly-crystalline materials.

- The surface roughness reduces exponentially with finishing time during initial few minutes, thereafter, the reduction in surface roughness becomes extremely slow with respect to the earlier effect. After enough time (50 minutes in case of aluminium) of finishing, the improvement in surface roughness becomes almost asymptotic which is a deciding factor to stop and complete the processing of CMMRF process.
- In CMMRF process, surface damages are avoided due to the chemical reaction by creating hard layers on ductile materials, and soft layers on brittle materials.
- Critical surface roughness depends on the process parameters like hardness and size of abrasive particles, type of chemical and other physical parameters like working gap, magnetic field, feed, and rotational speed. To achieve the critical roughness near to the theoretical value, parameters of process need to be optimised.
- During nano-finishing of copper alloy in CMMRF process, acidic medium or low pH (0.4% of nitric acid) yields the surface finish better than 3.0 nm. However, alkaline medium or high pH value leads to the formation of pores on the finished surface, and the neutral solution results in surface damage such as scratch lines.

7.1.1 Scientific contribution

From the presented research work, following scientific contribution is made.

- A comprehensive understanding of CMMRF process is established from theoretical as well as experimental point of view. This process has unique capability to generate defect-less nanofinished (in some cases, sub-nanometer level) surface on both brittle as well as ductile materials.

- Physically stable MR fluid is synthesised by using sodium stearate in water base medium for CMMRF application.

- Two different zones, namely zone-1 and zone-2 of working gap are identified for nanofinishing of brittle and ductile materials respectively.

- Formation of soft passivation layers on brittle materials and hard passivation layers on ductile materials are identified by MDS during CMMRF process.

7.2 Scope for future work

As CMMRF is a new process developed, and the present work includes theoretical study of the process at atomic scale and macroscopic scale with few experimental study to understand the process mechanism and its capability. There is a scope for further research left out which is categorized and listed as follows.

7.2.1 Multi-scale modelling and simulation

In the present work, modelling of process is carried out using quantum chemical modelling, molecular dynamics modelling, computational fluid dynamics and finite element analysis separately. These modelling works are carried out in different time and space domain to understand the process behaviour right from atomic scale to macroscopic scale. Though, coupling of all these models will reveal some more scientific outcome of the process. Hence, applying and studying CMMRF process by using multi-scale modelling will be more accurate, and essential for the future work.

7.2.2 Optimization of CMMRF process: There is a scope to optimize this process from various aspects so that the surface finish can be achieved near to the theoretical value for various work-materials. The type of optimization is mentioned as follows.

1) Design of finishing head: Size and shape of magnet for the finishing head.
2) Design of MR fluid: Size and type of magnetic particle.

3) Steps of finishing: During MDS and experiments on *SS304L* it was observed that by implementing 4 steps of finishing with various parameters results surface finish near to the theoretical value. Hence, these steps and their types need to be optimised for various materials so that surface finish can be optimised.
4) Abrasive particle: Effect of the size and type of abrasive particle also need to be optimised for a particular work-material and a data bank shall be created for various materials.
5) Process parameters: All other process parameters like, speed, feed, time, working gap, chemical concentration, etc. also need to be optimised.

7.2.3 Experimental and theoretical study to finish 3D surface

CMMRF has capability to finish 3D surface as it utilises flexible pad made by MR fluid. Hence, there are some area which needs to be carried out towards development of CMMRF process for 3D finishing.

1) Design of polishing pad to generate similar amount of polishing pressure everywhere of the 3D surface. In this design centripetal force needs to be obtained by generating high magnetic flux density along a specified path to generate centripetal force due to the rotational speed of the finishing head. When the centripetal force is more than centrifugal force, will lead to flow particles of MR fluid in an elliptical path which can generate enough amount of polishing pressure everywhere in 2D as well as 3D surfaces.
2) Experimental study with various types of such polishing pad. An initial experiment was carried out on a corrugated diaphragm of stainless steel and it was found that the finishing rate becomes somewhat similar at crests and troughs of the diaphragm.
3) CFD simulation to understand the significant parameters for such 3D finishing and the design criteria to fabricate such polishing pad.

7.2.4 Sensitivity analysis of CMMRF: CMMRF does material removal because of finishing force or polishing pressure as shown in MDS result of Fig.4.41. Force is highly sensitive to the rate of change in working gap as shown in Fig. 3.5 in which sharp jump in force is observed when gap changes at a given feed along axial direction. Hence, experimental study of such aspect would be another part for the future work as follows.

1) Modeling and simulation of sensitivity of CMMRF due to working gap, feed rate magnetic field, and magneto-rheological property of MR fluid.
2) Effect of the sensitivity of CMMRF on surface quality by experimental study and mathematical modeling.

7.2.5. Theoretical and experimental study of shear stress in CMMRF: In present work, polishing pressure is used for finishing by assuming that the polishing pad of MR fluid is stiff enough. Hence, following future works are outlined.

1) Numerical simulation computation of shear stress using FEA-CFD integrated modeling.
2) Computation of shear stress during 3D finishing of un-even surface.
3) Experimental investigation.

----------X----------

REFERENCES

[1] J.F. Archard, Contact and rubbing of flat surfaces, J. Appl. Phys. 24 (1953) 981–988. doi:10.1063/1.1721448.

[2] N. Chandrasekaran, S. Ramarajan, W. Lee, G.M. Sabde, S. Meikle, Effects of CMP Process Conditions on Defect Generation in Low-k Materials, J. Electrochem. Soc. 151 (2004) G882. doi:10.1149/1.1810392.

[3] T.Y. Teo, W.L. Goh, V.S.K. Lim, L.S. Leong, T.Y. Tse, L. Chan, Characterization of scratches generated by a multiplaten copper chemical–mechanical polishing process, J. Vac. Sci. Technol. B Microelectron. Nanom. Struct. Process. Meas. Phenom. 22 (2004) 65–69. doi:10.1116/1.1634958.

[4] A.G. Evans, D.B. Marshall, Wear Mechanisms in Ceramics, in: Fundam. Frict. Wear Mater., 1981: pp. 439–452. http://books.google.ch/books?id=zp23AAAAIAAJ.

[5] Z.W. Zhong, Ductile or partial ductile mode machining of brittle materials, Int. J. Adv. Manuf. Technol. 21 (2003) 579–585. doi:10.1007/s00170-002-1364-5.

[6] A. Kumar, A. Kovalchenko, V. Pogue, E. Pashchenko, S.N. Melkote, Ductile Mode Behavior of Silicon during Scribing by Spherical Abrasive Particles, in: Procedia CIRP, 2016: pp. 147–150. doi:10.1016/j.procir.2016.02.341.

[7] V.K. Jain, P. Ranjan, V.K. Suri, R. Komanduri, Chemo-mechanical magneto-rheological finishing (CMMRF) of silicon for microelectronics applications, CIRP Ann. - Manuf. Technol. 59 (2010) 323–328. doi:10.1016/j.cirp.2010.03.106.

[8] T.Y. Kwon, M. Ramachandran, J.G. Park, Scratch formation and its mechanism in chemical mechanical planarization (CMP), Friction. 1 (2013) 279–305. doi:10.1007/s40544-013-0026-y.

[9] L. Zhong, J. Yang, K. Holland, J. Grillaert, K. Devriend, N. Heylen, M. Meuris, A static model for scratches generated during aluminum chemical-mechanical polishing process: Orbital technology, Japanese J. Appl. Physics, Part 1 Regul. Pap. Short Notes Rev. Pap. 38 (1999) 1932–1938.

[10] W. Lortz, A model of the cutting mechanism in grinding, Wear. 53 (1979) 115–128. doi:10.1016/0043-1648(79)90223-0.

[11] B. Denkena, J. Köhler, J. Kästner, Chip formation in grinding: An experimental study, Prod. Eng. 6 (2012) 107–115. doi:10.1007/s11740-011-0360-8.

[12] P. Puerto, R. Fernández, J. Madariaga, J. Arana, I. Gallego, Evolution of surface roughness in grinding and its relationship with the dressing parameters and the radial wear, in: Procedia Eng., 2013: pp. 174–182. doi:10.1016/j.proeng.2013.08.181.

[13] C. Yao, T. Wang, W. Xiao, X. Huang, J. Ren, Experimental study on grinding force and grinding temperature of Aermet 100 steel in surface grinding, J. Mater. Process. Technol. 214 (2014) 2191–2199. doi:10.1016/j.jmatprotec.2014.04.013.

[14] F.W. Preston, The theory and design of plate glass polishing machines, J. Soc. Glas. Technol. 11 (1927) 214–256.

[15] Y.P. Chang, M. Hashimura, D.A. Dornfeld, An Investigation of the AE Signals in the Lapping Process, CIRP Ann. - Manuf. Technol. 45 (1996) 331–334. doi:10.1016/S0007-8506(07)63074-1.

[16] X. Jiang, Z. Chen, J. Wolfram, Z. Wei, Y. Shen, Z. Yang, The impact of lubricants on the precision lapping process, Microsc. Microanal. 20 (2014) 1708–1714. doi:10.1017/S1431927614013397.

[17] C. Schmitt, D. Bähre, Analysis of the process dynamics for the precision honing of bores, in: Procedia CIRP, 2014: pp. 692–697. doi:10.1016/j.procir.2014.01.055.

[18] U. Moos, D. Bähre, Analysis of process forces for the precision honing of small bores, in: Procedia CIRP, 2015: pp. 387–392. doi:10.1016/j.procir.2015.03.066.

[19] F. Klocke, Manufacturing Processes 2. Grinding, Honing, Lapping, 2013. doi:10.1017/CBO9781107415324.004.

[20] Y. Xie, B. Bhushan, Effects of particle size, polishing pad and contact pressure in free abrasive polishing, Wear. 200 (1996) 281–295. doi:10.1016/S0043-1648(96)07275-4.

[21] L. Rhoades, Abrasive flow machining: a case study, J. Mater. Process. Tech. 28 (1991) 107–116. doi:10.1016/0924-0136(91)90210-6.

[22] R.E. Williams, K.P. Rajurkar, Stochastic Modeling and Analysis of Abrasive Flow Machining, J. Eng. Ind. 114 (1992) 74–81. http://dx.doi.org/10.1115/1.2899761.

[23] V.K. Jain, S.G. Adsul, Experimental investigations into abrasive flow machining (AFM), Int. J. Mach. Tools Manuf. 40 (2000) 1003–1021. doi:10.1016/S0890-6955(99)00114-5.

[24] T.R. Loveless, R.E. Williams, K.P. Rajurkar, A study of the effects of abrasive-flow finishing on various machined surfaces, J. Mater. Process. Tech. 47 (1994) 133–151. doi:10.1016/0924-0136(94)90091-4.

[25] R.K. Jain, V.K. Jain, P.M. Dixit, Modeling of material removal and surface roughness in abrasive flow machining process, Int. J. Mach. Tools Manuf. 39 (1999) 1903–1923. doi:10.1016/S0890-6955(99)00038-3.

[26] V.K. Jain, C. Ranganatha, K. Muralidhar, Evaluation of rheological properties of medium for AFM process, Mach. Sci. Technol. 5 (2001) 151–170. doi:10.1081/MST-100107841.

[27] G. Rajeshwar, J. Kozak, K.P. Rajurkar, Modeling and computer simulation of media flow in Abrasive Flow Machining process, Am. Soc. Mech. Eng. Prod. Eng. Div. PED. 68–2 (1994) 965–971. http://www.engineeringvillage.com/blog/document.url?mid=cpx_4946685&database=cpx.

[28] V.K. Gorana, V.K. Jain, G.K. Lal, Forces prediction during material deformation in

abrasive flow machining, Wear. 260 (2006) 128–139. doi:10.1016/j.wear.2004.12.038.

[29] G.Z. KREMEN, E.A. ELSAYED, J.L. RIBEIRO, MACHINING TIME-ESTIMATION FOR MAGNETIC ABRASIVE PROCESSES, Int. J. Prod. Res. 32 (1994) 2817–2825. doi:10.1080/00207549408957102.

[30] H.P. Coats, Method of and apparatus for polishing containers, US2196058A, 1940.

[31] T. Shinmura, K. Takazawa, E. Hatano, M. Matsunaga, T. Matsuo, Study on Magnetic Abrasive Finishing, CIRP Ann. - Manuf. Technol. 39 (1990) 325–328. doi:10.1016/S0007-8506(07)61064-6.

[32] G.W. Chang, B.H. Yan, R.T. Hsu, Study on cylindrical magnetic abrasive finishing using unbonded magnetic abrasives, Int. J. Mach. Tools Manuf. 42 (2002) 575–583. doi:10.1016/S0890-6955(01)00153-5.

[33] J.-D. Kim, Y.-H. Kang, Y.-H. Bae, S.-W. Lee, Development of a magnetic abrasive jet machining syste precision internal polishing of circular tubes, J. Mater. Process. Technol. 71 (1997) 384–393. doi:10.1016/S0924-0136(97)00103-9.

[34] J. Du Kim, M.S. Choi, Simulation for the prediction of surface-accuracy in magnetic abrasive machining, J. Mater. Process. Tech. 53 (1995) 630–642. doi:10.1016/0924-0136(94)01753-N.

[35] A.B. Khairy, Aspects of surface and edge finish by magnetoabrasive particles, J. Mater. Process. Technol. 116 (2001) 77–83. doi:10.1016/S0924-0136(01)00840-8.

[36] T. Mori, K. Hirota, Y. Kawashima, Clarification of magnetic abrasive finishing mechanism, in: J. Mater. Process. Technol., 2003: pp. 682–686. doi:10.1016/S0924-0136(03)00410-2.

[37] S.C. Jayswal, V.K. Jain, P.M. Dixit, Analysis of magnetic abrasive finishing with slotted magnetic pole, in: Proc. 8th Int. Conf. Numer. Methods Ind. Form. Process., 2004: pp. 1435–1440. doi:10.1063/1.1766730.

[38] S.C. Jayswal, V.K. Jain, P.M. Dixit, Modeling and simulation of magnetic abrasive finishing process, Int. J. Adv. Manuf. Technol. 26 (2005) 477–490. doi:10.1007/s00170-004-2180-x.

[39] J.S. Kwak, Enhanced magnetic abrasive polishing of non-ferrous metals utilizing a permanent magnet, Int. J. Mach. Tools Manuf. 49 (2009) 613–618. doi:10.1016/j.ijmachtools.2009.01.013.

[40] Z.-B. Hou, R. Komanduri, Magnetic Field Assisted Finishing of Ceramics—Part I: Thermal Model, J. Tribol. 120 (1998) 645–651. http://dx.doi.org/10.1115/1.2833761.

[41] Z.-B. Hou, R. Komanduri, Magnetic Field Assisted Finishing of Ceramics—Part II: On the Thermal Aspects of Magnetic Float Polishing (MFP) of Ceramic Balls, J. Tribol. 120 (1998) 652–659. http://dx.doi.org/10.1115/1.2833762.

[42] Z.-B. Hou, R. Komanduri, Magnetic Field Assisted Finishing of Ceramics—Part III: On the Thermal Aspects of Magnetic Abrasive Finishing (MAF) of Ceramic Rollers, J.

Tribol. 120 (1998) 660–667. http://dx.doi.org/10.1115/1.2833763.

[43] G. Kumar, V. Yadav, Temperature distribution in the workpiece due to plane magnetic abrasive finishing using FEM, Int. J. Adv. Manuf. Technol. 41 (2009) 1051–1058. doi:10.1007/s00170-008-1557-7.

[44] A. Misra, P.M. Pandey, U.S. Dixit, A. Roy, V. V Silberschmidt, Modeling of finishing force and torque in ultrasonic-assisted magnetic abrasive finishing process, Proc. Inst. Mech. Eng. Part B J. Eng. Manuf. (2017) 954405417737579. doi:10.1177/0954405417737579.

[45] H. Yamaguchi, T. Shinmura, Study on a new internal finishing process by the application of magnetic abrasive machining - Discussion of the roundness, Seimitsu Kogaku Kaishi/Journal Japan Soc. Precis. Eng. 62 (1996) 1617–1621. doi:10.2493/jjspe.61.996.

[46] D.K. Singh*, V.K. Jain, V. Raghuram, ON THE PERFORMANCE ANALYSIS OF FLEXIBLE MAGNETIC ABRASIVE BRUSH, Mach. Sci. Technol. 9 (2005) 601–619. doi:10.1080/10910340500398217.

[47] D.K. Singh, V.K. Jain, V. Raghuram, Experimental investigations into forces acting during a magnetic abrasive finishing process, Int. J. Adv. Manuf. Technol. 30 (2006) 652–662. doi:10.1007/s00170-005-0118-6.

[48] S. Ahmad, S. Gangwar, P.C. Yadav, D.K. Singh, Optimization of process parameters affecting surface roughness in magnetic abrasive finishing process, Mater. Manuf. Process. 32 (2017) 1723–1729. doi:10.1080/10426914.2017.1279307.

[49] V.K. Jain, V. Kumar, M.R. Sankar, V. Kumar, R. Sankar, Experimental study and empirical modelling of magnetic abrasive finishing on ferromagnetic and non-ferromagnetic materials) ’Experimental study and empirical modelling of magnetic abrasive finishing on ferromagnetic and non-ferromagnetic materials, Int. J. Precis. Technol. 3 (2012) 91–104. doi:10.1504/IJPTECH.2012.045991.

[50] L. Heng, Y.J. Kim, S.D. Mun, Review of Superfinishing by the Magnetic Abrasive Finishing Process, High Speed Mach. 3 (2017). doi:10.1515/hsm-2017-0004.

[51] W. Kordonski, S. Jacobs, Model of magnetorheological finishing, J. Intell. Mater. Syst. Struct. 7 (1996) 131–137. doi:10.1177/1045389X9600700202.

[52] S. Jacobs, I. Prokhorov, D. Golini, G. Gorodkin, T. Strafford, Deterministic Magnetorheological Finishing, U.S. Pat. 5,795,212 (1995).

[53] D.C. Harris, History of Magnetorheological Finishing, Wind. Dome Technol. Mater. XII. xxxx (2011) 80160N–80160N–22. doi:10.1117/12.882557.

[54] W. Kordonski, D. Golini, Progress Update in Magnetorheological Finishing, Int. J. Mod. Phys. B. 13 (1999) 2205–2212. doi:10.1142/S0217979299002320.

[55] S.D. Jacobs, F. Yang, E.M. Fess, J.B. Feingold, B.E. Gillman, W.I. Kordonski, H. Edwards, D. Golini, Magnetorheological finishing of IR materials, Opt. Manuf. Test. II. 3134 (1997) 258–269. doi:10.1117/12.295132.

[56] A. Sidpara, V.K. Jain, Analysis of forces on the freeform surface in magnetorheological fluid based finishing process, Int. J. Mach. Tools Manuf. 69 (2013) 1–10. doi:10.1016/j.ijmachtools.2013.02.004.

[57] P.B. Zantye, A. Kumar, A.K. Sikder, Chemical mechanical planarization for microelectronics applications, Mater. Sci. Eng. R Reports. 45 (2004) 89–220. doi:10.1016/j.mser.2004.06.002.

[58] Y. Li, Microelectronic Applications of Chemical Mechanical Planarization, 2007. doi:10.1002/9780470180907.

[59] Z. Yuan, Z. Jin, Y. Zhang, Q. Wen, Chemical Mechanical Polishing Slurries for Chemically Vapor-Deposited Diamond Films, J. Manuf. Sci. Eng. 135 (2013) 41006–41008. http://dx.doi.org/10.1115/1.4024034.

[60] J. Wang, G. Meng, Magnetorheological fluid devices: Principles, characteristics and applications in mechanical engineering, Proc. Inst. Mech. Eng. Part L J. Mater. Des. Appl. 215 (2001) 165–174. doi:10.1243/1464420011545012.

[61] M.R. Jolly, J.W. Bender, J.D. Carlson, Properties and applications of commercial magnetorheological fluids, J. Intell. Mater. Syst. Struct. 10 (1999) 5–13. doi:10.1106/R9AJ-XYT5-FG0J-23G1.

[62] R. Tao, Super-strong magnetorheological fluids, J. Phys. Condens. Matter. 13 (2001). doi:10.1088/0953-8984/13/50/202.

[63] J.D. Carlson, M.R. Jolly, MR fluid, foam and elastomer devices, Mechatronics. 10 (2000) 555–569. doi:10.1016/S0957-4158(99)00064-1.

[64] J. Rabinow, The Magnetic Fluid Clutch, Trans. Am. Inst. Electr. Eng. 67 (1948) 1308–1315. doi:10.1109/T-AIEE.1948.5059821.

[65] S. Jha, V.K. Jain, Modeling and simulation of surface roughness in magnetorheological abrasive flow finishing (MRAFF) process, Wear. 261 (2006) 856–866. doi:10.1016/j.wear.2006.01.043.

[66] M. Kciuk, R. Turczyn, Magnetorheological characterisation of carbonyl iron based suspension, J. Achiev. Mater. Manuf. Eng. 33 (2009) 135–141.

[67] Z. Parlak, T. Engin, Time-dependent CFD and quasi-static analysis of magnetorheological fluid dampers with experimental validation, Int. J. Mech. Sci. 64 (2012) 22–31. doi:10.1016/j.ijmecsci.2012.08.006.

[68] S. Jha, V.K. Jain, Design and development of the magnetorheological abrasive flow finishing (MRAFF) process, Int. J. Mach. Tools Manuf. 44 (2004) 1019–1029. doi:10.1016/j.ijmachtools.2004.03.007.

[69] S. Jha, V.K. Jain, Rheological characterization of magnetorheological polishing fluid for MRAFF, Int. J. Adv. Manuf. Technol. 42 (2009) 656–668. doi:10.1007/s00170-008-1637-8.

[70] M. Das, V.K. Jain, P.S. Ghoshdastidar, Estimation of magnetic and rheological

properties of MR polishing fluid and their effects on magnetic field assisted finishing process, Int. J. Precis. Technol. 4 (2014) 247–267. doi:10.1504/IJPTECH.2014.067740.

[71] A. Sidpara, V.K. Jain, Rheological properties and their correlation with surface finish quality in MR fluid-based finishing process, Mach. Sci. Technol. 18 (2014) 367–385. doi:10.1080/10910344.2014.925372.

[72] V.K. Jain, A. Sidpara, M.R. Sankar, M. Das, Nano-finishing techniques: a review, Proc. Inst. Mech. Eng. Part C J. Mech. Eng. Sci. 226 (2012) 327–346. doi:10.1177/0954406211426948.

[73] A. Sidpara, M. Das, V.K. Jain, Rheological characterization of magnetorheological finishing fluid, Mater. Manuf. Process. 24 (2009) 1467–1478. doi:10.1080/10426910903367410.

[74] X. Hu, Z. Song, W. Liu, F. Qin, Z. Zhang, H. Wang, Chemical mechanical polishing of stainless steel foil as flexible substrate, Appl. Surf. Sci. 258 (2012) 5798–5802. doi:10.1016/j.apsusc.2012.02.100.

[75] L. Jiang, Y. He, J. Luo, Chemical mechanical polishing of steel substrate using colloidal silica-based slurries, Appl. Surf. Sci. 330 (2015) 487–495. doi:10.1016/j.apsusc.2015.01.016.

[76] K. Saraswathamma, S. Jha, P. V. Rao, Experimental investigation into Ball end Magnetorheological Finishing of silicon, Precis. Eng. 42 (2015) 218–223. doi:10.1016/j.precisioneng.2015.05.003.

[77] N.K. Penta, Abrasive-free and ultra-low abrasive chemical mechanical polishing (CMP) processes, in: Adv. Chem. Mech. Planarization, 2016: pp. 1–227. doi:10.1016/B978-0-08-100165-3.00009-7.

[78] S. Kheradmand, M. Esmailian, A. Fatahy, A novel approach of magnetorheological abrasive fluid finishing with swirling-assisted inlet flow, Results Phys. 6 (2016) 568–580. doi:10.1016/j.rinp.2016.08.014.

[79] Y. Wang, Y. Zhang, Z. Feng, Analyzing and improving surface texture by dual-rotation magnetorheological finishing, Appl. Surf. Sci. 360 (2016) 224–233. doi:10.1016/j.apsusc.2015.11.009.

[80] J. Wen, T. Ma, W. Zhang, A.C.T. van Duin, X. Lu, Atomistic mechanisms of Si chemical mechanical polishing in aqueous H2O2: ReaxFF reactive molecular dynamics simulations, Comput. Mater. Sci. 131 (2017) 230–238. doi:10.1016/j.commatsci.2017.02.005.

[81] Z. Alam, S. Jha, Modeling of surface roughness in ball end magnetorheological finishing (BEMRF) process, Wear. 374–375 (2017) 54–62. doi:10.1016/j.wear.2016.11.039.

[82] A. Rajendran, Y. Takahashi, M. Koyama, M. Kubo, A. Miyamoto, Tight-binding quantum chemical molecular dynamics simulation of mechano-chemical reactions during chemical-mechanical polishing process of SiO2 surface by CeO2 particle, in: Appl. Surf. Sci., 2005: pp. 34–38. doi:10.1016/j.apsusc.2004.09.126.

[83] J.C. Slater, A simplification of the Hartree-Fock method, Phys. Rev. 81 (1951) 385–390. doi:10.1103/PhysRev.81.385.

[84] A. Szabo, N.S. Ostlund, Hartree-Fock Approximation, Phys. Rev. Lett. 84 (2000) 1–11. doi:10.1002/0471743984.vse3823.

[85] P. Geerlings, F. De Proft, W. Langenaeker, Conceptual Density Functional Theory, Chem. Rev. 103 (2003) 1793–1874. doi:10.1021/cr990029p.

[86] H. GrubmüLler, H. Heller, A. Windemuth, K. Schulten, Generalized verlet algorithm for efficient molecular dynamics simulations with long-range interactions, Mol. Simul. 6 (1991) 121–142. doi:10.1080/08927029108022142.

[87] T.P. Senftle, S. Hong, M.M. Islam, S.B. Kylasa, Y. Zheng, Y.K. Shin, C. Junkermeier, R. Engel-Herbert, M.J. Janik, H.M. Aktulga, T. Verstraelen, A. Grama, A.C.T. van Duin, The ReaxFF reactive force-field: development, applications and future directions, Npj Comput. Mater. 2 (2016) 15011. doi:10.1038/npjcompumats.2015.11.

[88] G. Sutmann, Classical Molecular Dynamics, Quantum Simulations Complex Many-Body Syst. From Theory to Algorithms. 10 (2002) 211–254. doi:10.1063/1.3481087.

[89] A. Vattré, B. Devincre, F. Feyel, R. Gatti, S. Groh, O. Jamond, A. Roos, Modelling crystal plasticity by 3D dislocation dynamics and the finite element method: The Discrete-Continuous Model revisited, J. Mech. Phys. Solids. 63 (2014) 491–505. doi:10.1016/j.jmps.2013.07.003.

[90] W.F. Van Gunsteren, H.J.C. Berendsen, Algorithms for brownian dynamics, Mol. Phys. 45 (1982) 637–647. doi:10.1080/00268978200100491.

[91] A. Voter, Introduction To the Kinetic Monte Carlo Method, Radiat. Eff. Solids. 235 (2007) 1–23. doi:10.1007/978-1-4020-5295-8_1.

[92] D. V. Hutton, Fundamentals of Finite Element Analysis, McGraw-Hill. (2004) 494. doi:10.1017/CBO9781107415324.004.

[93] M. Reis, Introduction, in: Fundam. Magn., First, Elsevier Inc., 2013: pp. 1–8.

[94] L. Hand, J. Finch, R.W. Robinett, Analytical Mechanics, Am. J. Phys. 68 (2000) 390. doi:10.1119/1.19451.

[95] J. Blazek, Governing Equations, in: Comput. Fluid Dyn. Princ. Appl., 3rd ed., Elsevier Ltd, Waltham, 2015: pp. 7–26.

[96] M. Das, V.K. Jain, P.S. Ghoshdastidar, Analysis of magnetorheological abrasive flow finishing (MRAFF) process, Int. J. Adv. Manuf. Technol. 38 (2008) 613–621. doi:10.1007/s00170-007-1095-8.

[97] T.M. Simon, F. Reitich, M.R. Jolly, K. Ito, H.T. Banks, The effective magnetic properties of magnetorheological fluids, in: Math. Comput. Model., 2001: pp. 273–284. doi:10.1016/S0895-7177(00)00244-2.

[98] A.K. Sikder, F. Giglio, J. Wood, A. Kumar, M. Anthony, Optimization of tribological

properties of silicon dioxide during the chemical mechanical planarization process, J. Electron. Mater. 30 (2001) 1520–1526. doi:10.1007/s11664-001-0168-y.

[99] H. Lu, Y. Obeng, K.A. Richardson, Applicability of dynamic mechanical analysis for CMP polyurethane pad studies, Mater. Charact. 49 (2002) 177–186. doi:10.1016/S1044-5803(03)00004-4.

[100] B.J. Hooper, G. Byrne, S. Galligan, Pad conditioning in chemical mechanical polishing, J. Mater. Process. Technol. 123 (2002) 107–113. doi:10.1016/S0924-0136(01)01137-2.

[101] Z. Parlak, T. Engin, İ. Çallı, Optimal design of MR damper via finite element analyses of fluid dynamic and magnetic field, Mechatronics. 22 (2012) 890–903. doi:10.1016/j.mechatronics.2012.05.007.

[102] J.S. Kim, K.H. and Kwak, Application of AE signal and neural network for monitoring the magnetic abrasive polishing process, in: 9th Int. Conf. Fract. Strength Solids, Jeju, Korea, 2013: pp. 9–13.

[103] A. Aharoni, Introduction to the Theory of Ferromagnetism, Oxford Sci. Publ. I (2007) 303. doi:10.1063/1.881916.

[104] B. Fegley, Chapter 3 – The First Law of Thermodynamics, in: Pract. Chem. Thermodyn. Geosci., Academic Press, 2013: pp. 41–80. doi:10.1016/C2009-0-22615-8.

[105] A.F. BAKUZIS, K. CHEN, W. LUO, H. ZHUANG, Magnetic body force, Int. J. Mod. Phys. B. 19 (2005) 1205–1208. doi:10.1142/S0217979205030074.

[106] F. Klocke, R. Zunke, Removal mechanisms in polishing of silicon based advanced ceramics, CIRP Ann. - Manuf. Technol. 58 (2009) 491–494. doi:10.1016/j.cirp.2009.03.120.

[107] H.K. Sung, C. Wang, N.Y. Kim, Ultra-smooth BaTiO3 surface morphology using chemical mechanical polishing technique for high-k metal-insulator-metal capacitors, Mater. Sci. Semicond. Process. 40 (2015) 516–522. doi:10.1016/j.mssp.2015.07.016.

[108] W. Cho, Y. Ahn, C.-W. Baek, Y.-K. Kim, Effect of mechanical process parameters on chemical mechanical polishing of Al thin films, Microelectron. Eng. 65 (2003) 13–23. doi:https://doi.org/10.1016/S0167-9317(02)00726-8.

[109] D. Zhao, Y. He, T. Wang, X. Lu, Comparative study of the lubricating behavior between 12-in. copper disk and wafer during chemical mechanical polishing, Tribol. Int. 105 (2017) 37–41. doi:10.1016/j.triboint.2016.09.019.

[110] N.J. Brown, P.C. Baker, R.T. Maney, Optical Polishing Of Metals, Proc. Soc. Photo-Optical Instrum. Eng. 306 (1982) 42–57. doi:10.1117/12.932717.

[111] N.A. Frankel, A. Andreas, On the viscosity of a concentrated suspension of solid spheres, Chem. Eng. Sci. 22 (1967) 847–853. doi:10.1007/BF01332611.

[112] P.M. Hinderliter, K.R. Minard, G. Orr, W.B. Chrisler, B.D. Thrall, J.G. Pounds, J.G. Teeguarden, ISDD: A computational model of particle sedimentation, diffusion and target cell dosimetry for in vitro toxicity studies, Part. Fibre Toxicol. 7 (2010) 36.

doi:10.1186/1743-8977-7-36.

[113] P. Ranjan, R. Balasubramaniam, V.K. Jain, Analysis of magnetorheological fluid behavior in chemo-mechanical magnetorheological finishing (CMMRF) process, Precis. Eng. 49 (2017) 122–135. doi:10.1016/j.precisioneng.2017.02.001.

[114] F. Neese, The ORCA program system, Wiley Interdiscip. Rev. Comput. Mol. Sci. 2 (2012) 73–78. doi:10.1002/wcms.81.

[115] A.K. Rappé, C.J. Casewit, K.S. Colwell, W.A. Goddard, W.M. Skiff, UFF, a full periodic table force field for molecular mechanics and molecular dynamics simulations, J. Am. Chem. Soc. 114 (1992) 10024–10035. doi:10.1021/ja00051a040.

[116] M.D. Hanwell, D.E. Curtis, D.C. Lonie, T. Vandermeerschd, E. Zurek, G.R. Hutchison, Avogadro: An advanced semantic chemical editor, visualization, and analysis platform, J. Cheminform. 4 (2012). doi:10.1186/1758-2946-4-17.

[117] Y.D. Liu, C.H. Hong, H.J. Choi, Polymeric colloidal magnetic composite microspheres and their magneto-responsive characteristics, Macromol. Res. 20 (2012) 1211–1218. doi:10.1007/s13233-012-0198-8.

[118] M.S. Cho, S.T. Lim, I.B. Jang, H.J. Choi, M.S. Jhon, Encapsulation of spherical iron-particle with PMMA and its magnetorheological particles, in: IEEE Trans. Magn., 2004: pp. 3036–3038. doi:10.1109/TMAG.2004.830413.

[119] O. Markovitch, N. Agmon, Structure and Energetics of the Hydronium Hydration Shells, J. Phys. Chem. A. 111 (2007) 2253–2256. doi:10.1021/jp068960g.

[120] J.M. Haile, Molecular Dynamics Simulation-Element Method, in: Mol. Dyn. Simulation-Element Method Elem. Methods, Wiley-Interscience, New York, 1997: pp. 332–339.

[121] K. Ueda, H. Fu, K. Manabe, Atomic scale level chip formation of amorphous metal investigated by using AFM and MD-RPFEM simulation, Mach. Sci. Technol. 3 (1999) 61–75. doi:10.1080/10940349908945683.

[122] R. Komanduri, N. Chandrasekaran, L.M. Raff, MD simulation of exit failure in nanometric cutting, Mater. Sci. Eng. A. 311 (2001) 1–12. doi:10.1016/S0921-5093(01)00960-1.

[123] S. Plimpton, LAMMPS-large-scale atomic/molecular massively parallel simulator, Sandia Natl. Lab. (2007).

[124] A. Stukowski, Visualization and analysis of atomistic simulation data with OVITO–the Open Visualization Tool, Model. Simul. Mater. Sci. Eng. 18 (2009) 15012. doi:10.1088/0965-0393/18/1/015012.

[125] M.I. Mendelev, D.J. Srolovitz, G.J. Ackland, S. Han, Effect of Fe segregation on the migration of a non-symmetric ∑5 tilt grain boundary in Al, J. Mater. Res. 20 (2005) 208–218. doi:10.1557/JMR.2005.0024.

[126] J. Tersoff, New empirical approach for the structure and energy of covalent systems,

Phys. Rev. B. 37 (1988) 6991–7000. doi:10.1103/PhysRevB.37.6991.

[127] G. Bonny, D. Terentyev, R.C. Pasianot, S. Poncé, A. Bakaev, Interatomic potential to study plasticity in stainless steels: the FeNiCr model alloy, Model. Simul. Mater. Sci. Eng. 19 (2011) 85008. doi:10.1088/0965-0393/19/8/085008.

[128] W. Huang, Y. Zhao, S. Yu, L. Zhang, Z. Ye, N. Wang, M. Chen, Structural Characterization of FeO–SiO2–V2O3 Slags Using Molecular Dynamics Simulations and FT-IR Spectroscopy, ISIJ Int. 56 (2016) 594–601. doi:http://dx.doi.org/10.2355/isijinternational.ISIJINT-2015-600.

[129] M.I. Baskes, J.E. Angelo, C.L. Bisson, Atomistic calculations of composite interfaces, Model. Simul. Mater. Sci. Eng. 2 (1999) 505–518. doi:10.1088/0965-0393/2/3A/006.

[130] A.K. Subramaniyan, C.T. Sun, Continuum interpretation of virial stress in molecular simulations, Int. J. Solids Struct. 45 (2008) 4340–4346. doi:10.1016/j.ijsolstr.2008.03.016.

[131] S. Goel, S.S. Joshi, G. Abdelal, A. Agrawal, Molecular dynamics simulation of nanoindentation of Fe3C and Fe4C, Mater. Sci. Eng. A. 597 (2014) 331–341. doi:10.1016/j.msea.2013.12.091.

[132] C.L. Kelchner, S.J. Plimpton, J.C. Hamilton, Dislocation nucleation and defect structure during surface indentation, Phys. Rev. B. 58 (1998) 11085–11088. doi:10.1103/PhysRevB.58.11085.

[133] K. Laidler, Chemical Kinetics, Harper Row. 1 (1987) 233–270. doi:10.1007/0-306-48390-4_2.

[134] W.R. French, C.R. Iacovella, P.T. Cummings, The Influence of Molecular Adsorption on Elongating Gold Nanowires, J. Phys. Chem. C. 115 (2011) 18422–18433. doi:10.1021/jp203837r.

[135] K.L. Joshi, G. Psofogiannakis, A.C.T. van Duin, S. Raman, Reactive molecular simulations of protonation of water clusters and depletion of acidity in H-ZSM-5 zeolite, Phys. Chem. Chem. Phys. 16 (2014) 18433–18441. doi:10.1039/C4CP02612H.

[136] A. Van Duin, C. Kimberly, ReaxFF Potential Functions, J. Phys. Chem. A. (2001) 1–10. doi:10.1021/jp709896w.

[137] V.K. Jain, A. Sidpara, M.R. Sankar, M. Das, Nano-finishing techniques: a review, Proc. Inst. Mech. Eng. Part C J. Mech. Eng. Sci. 226 (2011) 327–346. doi:10.1177/0954406211426948.

[138] J. Qu, A.J. Shih, Analytical surface roughness parameters of a theoretical profile consisting of elliptical arcs, Mach. Sci. Technol. 7 (2003) 281–294. doi:10.1081/MST-120022782.

[139] V.K. Jain, Magnetic field assisted abrasive based micro-/nano-finishing, J. Mater. Process. Technol. 209 (2009) 6022–6038. doi:10.1016/j.jmatprotec.2009.08.015.

[140] Y. Tarutani, M. Kudo, Atomic radii and lattice parameters of the A15 crystal structure,

J. Less-Common Met. 55 (1977) 221–229. doi:10.1016/0022-5088(77)90196-5.

[141] Y. Mori, K. Yamauchi, K. Endo, Elastic emission machining, Precis. Eng. 9 (1987) 123–128. doi:10.1016/0141-6359(87)90029-8.

[142] and D.S. Y. Ein-Eli, E. Abelev, E. Rabkin, The compatibility of copper CMP slurries with CMP requirements, J. Electrochem. Soc. 150 (2003) C646–C652.

[143] T.H. Tsai, S.C. Yen, Localized corrosion effects and modifications of acidic and alkaline slurries on copper chemical mechanical polishing, Appl. Surf. Sci. 210 (2003) 190–205. doi:10.1016/S0169-4332(02)01224-2.

[144] D.S. Y. Ein-Eli, E. Abelev, Electrochemical behavior of copper in conductive peroxide solutions, J. Electrochem. Soc. 151 (2004) G236–G240.

[145] T. Du, D. Tamboli, V. Desai, Electrochemical characterization of copper chemical mechanical polishing, Microelectron. Eng. 69 (2003) 1–9. doi:10.1016/S0167-9317(03)00222-3.

[146] R.J.G. J.M. Steigerwald, R. Zirpoli, S.P. Murarka, D. Price, Pattern geometry effects in the chemical–mechanical polishing of inlaid copper structures, Electrochem. Soc. Lett. 141 (1994) 2842–2848.

[147] J.M. Steigerwald, S.P. Murarka, R.J. Gutmann, D.J. Duquette, Effect of Copper Ions in the Slurry on the Chemical-Mechanical Polish Rate of Titanium, J. Electrochem. Soc. . 141 (1994) 3512–3516. doi:10.1149/1.2059362.

[148] R.J.G. J.M. Steigerwald, D.J. Duquette, S.P. Murarka, Electrochemical potential measurements during the chemical–mechanical polishing of copper thin films, J. Electrochem. Soc. 142 (1995) 2379–2385.

[149] J.M. Steigerwald, S.P. Murarka, R.J. Gutmann, D.J. Duquette, Chemical processes in the chemical mechanical polishing of copper, Mater. Chem. Phys. 41 (1995) 217–228. doi:10.1016/0254-0584(95)01516-7.

[150] E.B. Sandell, Colorimetric determination of traces of metals, Interscience, New York, 1950.

----------X----------

APPENDIX

Table A1: Sedimentation depth with varying time for different types of MR fluids. Where D.L. indicates the demarcation line.

MR fluid-1		MR fluid-2		MR fluid-3	
Time (s)	Position of D.L. (mm)	Time (s)	Position of D.L. (mm)	Time (s)	Position of D.L. (mm)
70	0.6	120	2	60	1
149	1.2	150	2.4	100	1.6
209	1.8	180	2.8	280	3
278	2.6	250	3	360	3.2
358	3	300	3.4	500	3.4
477	3.8	330	3.6	700	3.4
557	4	500	3.8	900	3.6
716	4.4	530	4	1380	3.6
955	4.6	680	4.2	2520	3.8
1193	4.8	860	4.4	4000	3.8
1670	5	1190	4.6	6000	3.8
2028	5.2	2980	5	7000	3.8
2983	5.6	6000	5.2	8000	3.8
4295	5.8	7000	5.2	9000	3.8
5170	5.9	8000	5.2	10000	3.8

A1: Details for the 'molecular simulation' packages used in this thesis

ORCA: 'ORCA version 3.0.3' program is used to conduct density functional theory (DFT) simulation towards studying the quantum chemical interactions between two different species. ORCA 3.0.3 program is an ab-initio, DFT, and semi-empirical SCF-MO package, which was developed by Frank Neese and his group at the Max Planck Institute for Chemical Energy Conversion. This is open-source software and available free of cost.

Avogadro: 'Avogadro version 1.2.0' is a free cross-platform molecular editor for molecule builder, editor and visualizer in the field of computational chemistry, molecular modelling, bioinformatics, materials science, and related areas. This software is used for building the molecule and atom files for DFT simulation. Avogadro software is also used to visualise and analyse the results obtained after DFT simulation.

VMD: Visual molecular dynamics (VMD), version 1.9.3, is a molecular modelling and visualization software developed by University of Illinois at Urbana-Champaign, and it is available free of charge. VMD is used in thesis to build multiple water molecule for reactive MDS, as water molecule is stored in the library of VMD software. VMD software is also used to visualise and analyse the results obtained after DFT simulation.

LAMMPS: Large-scale Atomic/Molecular Massively Parallel Simulator (LAMMPS) was developed by Sandia National Laboratories for classical molecular dynamics simulation and it is open-source software available free of charge. In this thesis, LAMMPS is used for classical MDS and reactive MDS.

A2: Details of Chemical building for reactive-MDS

Details about chemical building for MDS: Steps to build the data file for a specific chemical to simulate using LAMMPS, following steps have been implemented.

- Initialisation of a set of molecules under the specified geometric region in a box of XYZ by using VMD and modification using Avogadro.
- Optimisation of molecules structure in Avogadro, and building a XYZ file.
- Loading of the XYZ file in VMD followed by conversion of the Avogadro generated XYZ file to VMD generated XYZ file.
- Formatting of the final XYZ file needs to be re-arranged in following format using Microsoft Excel.

File name →(LAMMPS does not read this line)

Number atoms → (Number belongs to the total number of atoms in this data file)

TYPES atom types → (TYPES belongs to the total variety of atoms in this data file)

X1 X2 xlo xhi →(X1 & X2 are minima and maxima value along X-axis respectively)

Y1 Y2 ylo yhi →(Y1 & Y2 are minima and maxima value along Y-axis respectively)

Z1 Z2 zlo zhi →(Z1 & Z2 are minima and maxima value along Z-axis respectively)

Masses

TYPE# MASS → (TYPE# is type of atom ID in numeric, and MASS is their mass)

Atoms

SrNo TYPE# CHARGE X Y Z → (serial no, Atom ID, Charge value, & location)

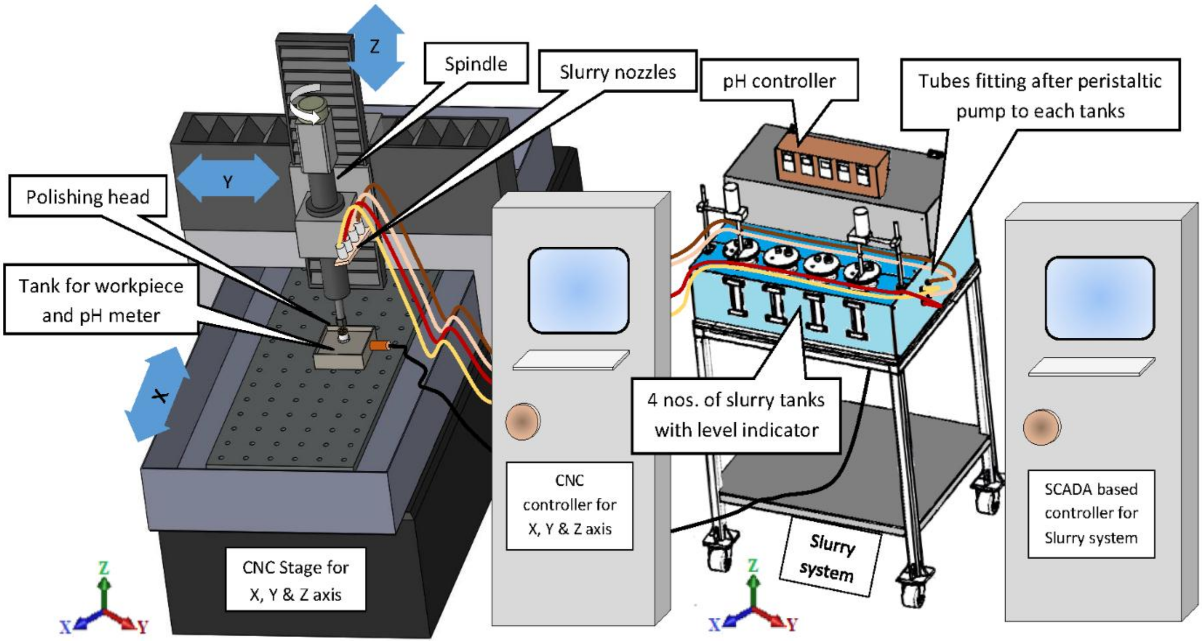

Fig. A1: Detailed schematic diagram of CMMRF system

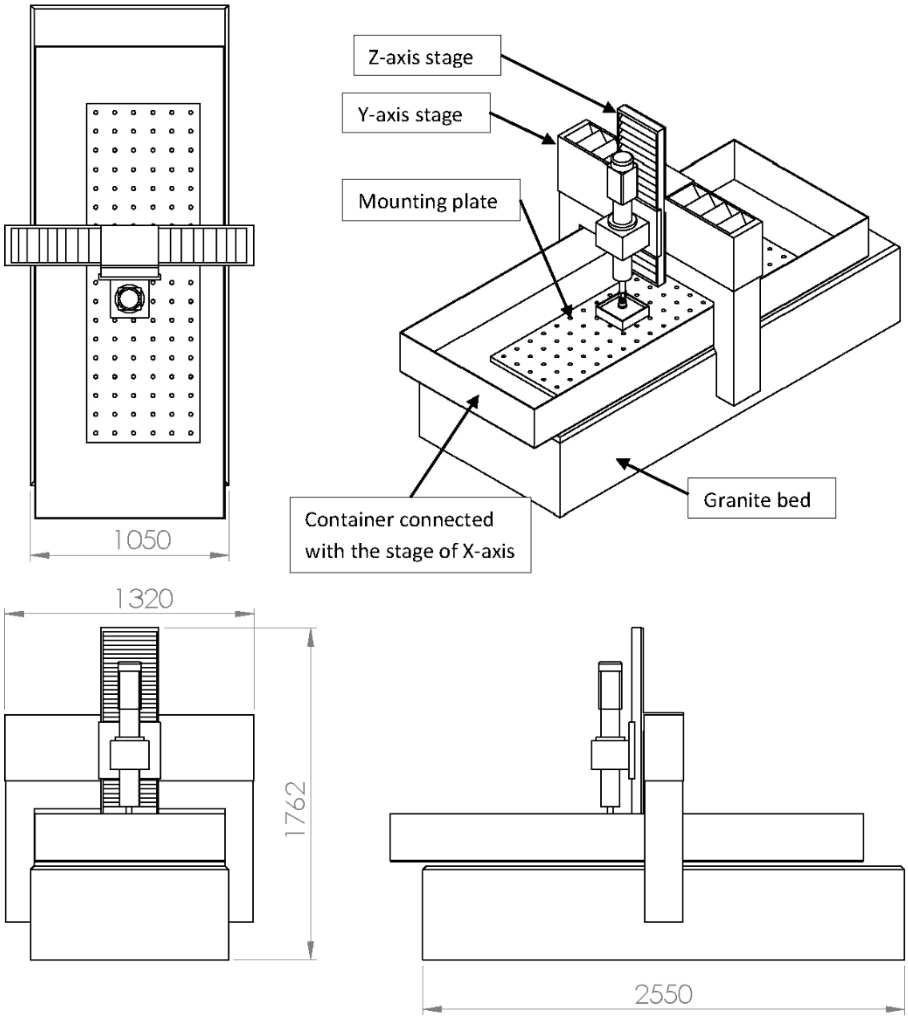

Fig. A2: Drawing of the CNC stages with overall dimension in ‘mm’.

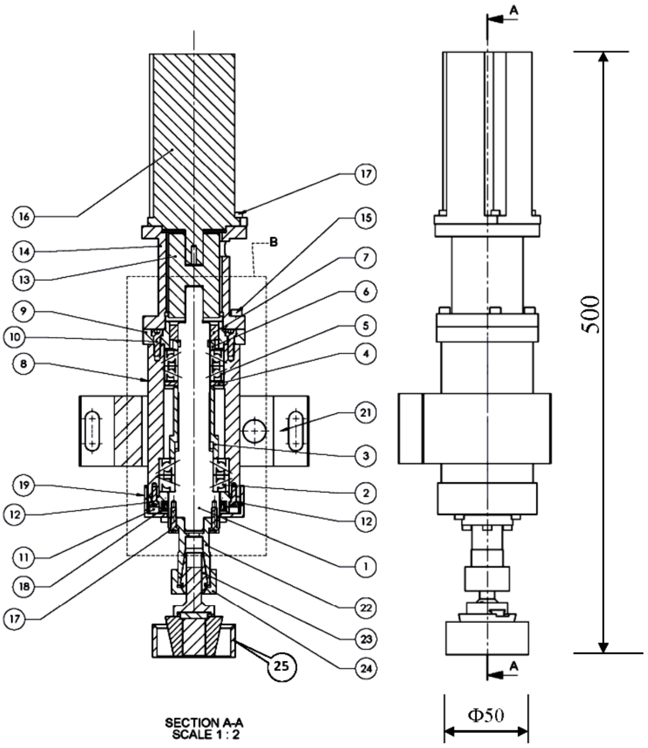

ITEM NO.	DESCRIPTION	QTY.
1	SPINDLE	1
2	ANGULAR CONTACT BEARING 7006 CTRDULP3 (RHP)	2
3	INNER SPACER	1
4	SPACER FOR ANGULAR CONTACT BEARING	1
5	ANGULAR CONTACT BEARING 7005 CTRDULP3 (RHP)	2
6	SPACER	1
7	PRECISION LOCK NUT YSR25X1.5	1
8	SPINDLE HOUSING	1
9	REAR COVER	1
10	ALLEN BOLT 5X16	4
11	OUTER COVER	1
12	ALLEN BOLT M 4 X 12 MM	4
13	COUPLING RobaE519/940.600.A14-14	1
14	MOTOR MTG. BRACKET	1
15	ALLEN BOLT 5X20	4
16	R88MG4003011-524600 WATTS SERVOMOTOR 3000RPM	1
17	ALLEN BOLT M 4 X 16 LPS	8
18	SEAL VS-RS19B 40X51X9.5	1
19	COVER	1
20	ALLEN BOLT M 4 X 16 LPS	4
21	HOUSING BKT.	1
22	COLLET ADAPTOR	1
23	COLLET ER20 Ø11.6	1
24	EX-20 COLLET NUT	1
25	ASSEMBLY OF POLISHING HEAD	1

Fig. A3: Drawing of the spindle assembly with overall dimension in ‘mm’.

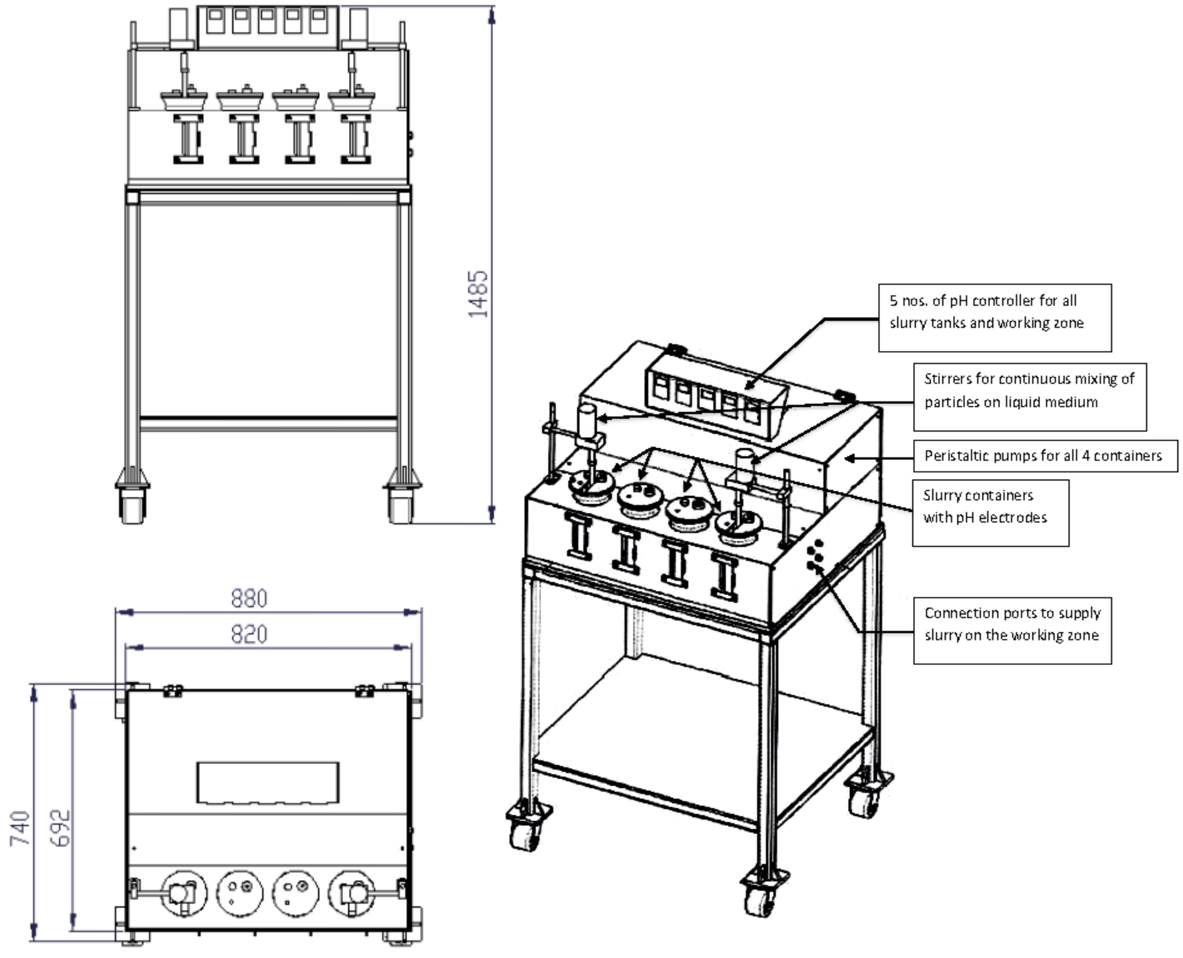

5 nos. of pH controller for all slurry tanks and working zone

Stirrers for continuous mixing of particles on liquid medium

Peristaltic pumps for all 4 containers

Slurry containers with pH electrodes

Connection ports to supply slurry on the working zone

Fig. A4: Drawing of the slurry circulatory system with overall dimension in ‘mm’.

Table A2: Detailed specifications of CMMRF system

Sr. No.	**Parameter**	**Value**
Controller for X, Y and Z stages		
1	Controller for X, Y and Z stages	Computer Numerical Control (CNC)
2	Accuracy of CNC stage	Within 5 µm
3	Repeatability of stages	Within 2 µm
4	Travelling capacity along X-axis	1500 mm
5	Travelling capacity along Y-axis	500 mm
6	Travelling capacity along Z-axis	200 mm
7	Operating platform for CNC	Windows XP
Controller for slurry circulatory system		
8	Controller for slurry circulatory system	Supervisory control and data acquisition (SCADA) based programmable logic controller (PLC)
9	Operating platform for CNC	Windows XP
10	Monitoring parameters	pH, Flow rate, flow pulses (on & off time), stirrer pump
11	Alarm	Based on the specified value of pH range
Parameters for CMMRF processing		
12	Spindle speed	0-2000 rpm
13	Power rating of spindle motor	0.4 kW
14	pH range of pH electrode	0-13 pH
15	Stirrer speed	5-550 rpm
16	Capacity of each tank of slurry	5 litre
17	Speed of peristaltic pump	10-196 rpm
18	Maximum pump flow	314 ml/min with 4mm of pipe ID
19	Pump pressure	1.96 bar
20	Magnet for polishing head	Nd-Fe-B Alloy with N50 grade
21	Slurry in-feed	Through orbital holes

Table A3: Experimental results of CMMRF on *Al 6061:T6*

Sr. No.	Working gap (mm)	%*KOH*	Time (minute)	Depth of material removal (nm)	Final surface finish (nm)
1	0.5	0	0	0	48.2
2	0.5	0	2	332	7
3	0.5	0	5	490	5.5
4	0.5	0	10	720	4.8
5	0.5	0	15	886	5.1
6	0.5	5	0	0	49.7
7	0.5	5	2	280	20
8	0.5	5	5	420	3
9	0.5	5	10	590	2.5
10	0.5	5	15	700	2.4
11	0.5	10	0	0	45.1
12	0.5	10	2	237	26.4
13	0.5	10	5	360	5.8
14	0.5	10	10	495	3
15	0.5	10	15	613	2.7
16	1	0	0	0	46.8
17	1	0	2	126	28
18	1	0	5	178	13
19	1	0	10	253	4.7
20	1	0	15	307	4.6
21	1	5	0	0	48.8
22	1	5	2	113	33
23	1	5	5	154	22
24	1	5	10	217	3
25	1	5	15	270	2.2
26	1	10	0	0	45
27	1	10	2	97	36
28	1	10	5	132	26.4
29	1	10	10	186	8.2
30	1	10	15	234	4.3
31	1.5	0	0	0	48.2
32	1.5	0	2	70	34
33	1.5	0	5	98	24
34	1.5	0	10	148	7.6
35	1.5	0	15	182	2.8
36	1.5	5	0	0	47.3
37	1.5	5	2	72	33.7
38	1.5	5	5	113	25.7
39	1.5	5	10	152	6.4
40	1.5	5	15	193	2.0
41	1.5	10	0	0	45.9
42	1.5	10	2	67	35.8
43	1.5	10	5	92	28
44	1.5	10	10	138	10.2
45	1.5	10	15	163	2.4

Table A4: Experimental results on Silicon substrate

Sr. No.	Working gap (mm)	%*KOH*	Time (minute)	Depth of material removal (nm)	Final surface finish (nm)
1	0.5	0	0	0	45.8
2	0.5	0	2	124	34
3	0.5	0	5	226	24.3
4	0.5	0	10	284	8.3
5	0.5	0	15	361	2.8
6	0.5	5	0	0	42.7
7	0.5	5	2	218	21.3
8	0.5	5	5	347	4.7
9	0.5	5	10	479	0.5
10	0.5	5	15	558	0.4
11	0.5	10	0	0	47.5
12	0.5	10	2	235	18.7
13	0.5	10	5	382	2.7
14	0.5	10	10	524	0.4
15	0.5	10	15	613	0.26
16	1	0	0	0	47.2
17	1	0	10	97	25.4
18	1	0	15	126	19.8
19	1	0	30	172	3.5
20	1	0	40	190	0.8
21	1	5	0	0	46
22	1	5	10	152	15.4
23	1	5	15	187	6.2
24	1	5	30	262	0.62
25	1	5	40	286	0.54
26	1	10	0	0	44.6
27	1	10	10	167	14.3
28	1	10	15	196	4.2
29	1	10	30	282	0.53
30	1	10	40	308	0.51
31	1.5	0	0	0	42.8
32	1.5	0	10	58	34.8
33	1.5	0	15	71	31.7
34	1.5	0	30	102	17.2
35	1.5	0	40	118	10.7
36	1.5	5	0	0	43.2
37	1.5	5	10	69	32.5
38	1.5	5	15	86	27.8
39	1.5	5	30	119	12.9
40	1.5	5	40	138	5.4
41	1.5	10	0	0	44.6
42	1.5	10	10	78	28.7
43	1.5	10	15	97	23.4
44	1.5	10	30	132	11.3
45	1.5	10	40	149	3.2